# EXPLORING THE REACTIVITY OF CATIONIC RHODIUM XANTPHOS COMPLEXES WITH AMINE-BORANES

Heather C. Johnson

A thesis submitted in partial fulfilment of the requirements for the degree of

Doctor of Philosophy at the University of Oxford






Magdalen College

January 2015

The work presented in this thesis was carried out between October 2011 and January 2015 under the supervision of Professor Andrew S. Weller. All of the work is my own, unless otherwise stated, and has not been submitted previously for any degree at this, or any other, university.

Heather C. Johnson

May 2015

# Acknowledgements

Firstly, I would like to thank Professor Andrew Weller. Without Andy's enthusiasm, advice and support, this thesis would not have been possible, and I consider myself extremely lucky to have worked in the Weller group. As well as the chemistry guidance, thanks for the many group days out, Scottish Cats on special occasions, entertaining stories, lab rules(!) and the opportunities to go to Canada (twice) and Singapore.

To all the postdocs who have worked in the group during my DPhil: Dr Miguel Huertos, Dr Rowan Young, Dr Tom Hooper, Dr Peng Ren, Dr Mark Chadwick and Dr Amparo Prades. Your help and advice has been invaluable, thank you. In particular, thanks to Miguel, for calling me the Little Kid, always being in Maxwells, and teaching me how to swear in Spanish. To Tom, for always being up for a tea break, and being incredibly chilled out. Happy birthday! To Mark, for being lots of fun and the promise of a sandwich party. I'm glad we eventually learnt how to fill the basebath. To Amparo, for being a great roommate in Singapore, the lovely Spanish chocolates and bringing glamour to the group.

Thank you also to the fellow DPhils that I have had the pleasure of working with. You have all been fantastic labmates and friends, and I learnt a lot from you. To Dr Rebekah Pawley, for reassuring me that it would all be fine, bright yellow catchpots, rowing chat, inviting us to your amazing wedding, and downing all the wine at Univ. To Dr Laura Sewell, for all the chemistry help in the early days, making me a perfectionist in the lab, love of dogs and celebrity gossip, hugs and tormenting Indreka. To Dr Indrek Pernik, for being The Pump Man, lunging, top notch chemistry advice, picking peppers out of CRL food, and teaching me many important life lessons. That's what she said. To Dr Seb Pike, for teaching me crystallography, Red October and being insistent on continuing Phil Collins Fridays. To Amit Kumar, for always smiling, being happy to help, cooking enormous portions of food for socials, and falling asleep after too many drinks. To Gemma Adams, for having so much enthusiasm for U.C. Fridays and group events, co-masterminding Where's Weller, being a fan of goats, and, of course, sharing the Trebor experience with me ("stop it!").

The Part IIs that have passed through the group during my time have each contributed to the great group atmosphere. Particular thanks to Becky Torry-Harris, my Part II, for the TMVS work and being a pleasure to teach, but mostly for your excellent company and Corrie chats. Thanks to Molly (the Mozzatron) for saying exactly what you think (vile!), Tim for complimenting my rendition of Starships, Mark for all the loving banter (I didn't ruin your rhodium Xantphos prep), Rosie for coxing chat, Lucy for always being keen for a Thatchers Gold and an excellent fumehood

partner. Thanks to Amy, Nick and Isobel for establishing the Part II bake-off and keeping me entertained whilst writing this year. Thanks also to the honorary Weller group members, Dr Michael Jones (Kiwi Mike) for all the good chats and pints, and Joe Abdalla for finding selfie sticks hilarious in Singapore ("whoopsie").

I have had the privilege of working with many excellent collaborators during my DPhil. Thanks to Professor Ian Manners, Dr George Whittell and Dr Erin Leitao for assistance and advice with GPC, and all the useful discussions at BrisOx meetings. Thanks to Professor Stuart Macgregor and Dr Claire McMullin for the calculations in Chapter 2. Thanks to Professor Guy Lloyd-Jones for the kinetic simulations and useful suggestions for the work in Chapter 4. Thanks to Dr J. Scott McIndoe for hosting my trip to UVic, Robin Theron for her patient help in the lab, and the McIndoe group (particularly Robin and Rhonda) for being so welcoming. Thank you to Laura Ortega for the work on phosphine-boranes. And thanks to Dr Silvia Mozo for being so fun to work with during the brief visit.

Thank you to all the CRL support staff who have helped. Particular thanks to Dr Nick Rees for NMR assistance and an introduction to Japanese pop music. Thanks to Dr Amber Thompson for the X-ray crystallography training and general X-ray help. Thanks to Colin Sparrow for helping me unblock the ESI-MS on several occasions, and for running GC-MS samples. Thank you to the workshop staff, particularly Alan and Jude, for being so happy to help whenever needed.

Outside the lab, thank you to my friends at Magdalen for all the fun times at dinners, Liquid Lounges and on the river. Particular thanks to Danielle Kaminski for being such a good friend throughout our time in College, with spontaneous Maxwells nights out, Nandos, hot chocolates and good gossiping sessions. To Paul Stevenson for your love and support, listening to my rants (and sometimes agreeing with me), reassuring me, disrupting most of your afternoons to chat, and trekking around lots of zoos and aquariums. Finally, a big thank you to my friends and family for their support.

# Abbreviations

| | |
|---|---|
| Å | Angstrom |
| atm | atmospheres |
| $[BAr^F{}_4]^-$ | $[B\{3,5\text{-}(CF_3)_2C_6H_3\}_4]^-$ |
| calc. | calculated |
| [cat.] | catalyst |
| cod | cyclooctadiene |
| Cp | cyclopentadienyl |
| Cp* | (pentamethyl)-cyclopentadienyl |
| Cy | cyclohexyl |
| Cyp | cyclopentyl |
| δ | chemical shift |
| ΔG | change in Gibb's free energy |
| DPEphos | *bis*(2-diphenylphosphinophenyl)ether |
| dpp2 | (1,2-diphenylphosphino)ethane |
| dpp3 | (1,2-diphenylphosphino)propane |
| dpp5 | (1,2-diphenylphosphino)pentane |
| EPR | electron paramagnetic resonance |
| eq. | equivalents |
| ESI-MS | electrospray ionisation mass spectrometry |
| Et | ethyl |
| EXAFS | Extended X-ray absorption fine structure |
| *fac* | facial |
| FWHM | full width at half maximum |
| GPC | gel permeation chromatography |
| HBCat | catecholborane |
| HBPin | pinacolborane |
| Hz | hertz |
| $^i$Bu | isobutyl |
| Imes | *N,N'-bis*(2,4,6-trimethylphenyl)imidazol-2-ylidene |
| $^i$Pr | isopropyl |
| IR | infrared |
| J | coupling constant |
| K | equilibrium constant |
| k | rate constant |
| KIE | kinetic isotope effect |
| Me | methyl |
| *mer* | meridional |
| Me-Xantphos | 9,9-dimethyl-4,5-*bis*(di-methylphosphino)xanthene |

| | |
|---|---|
| $M_n$ | number average molar mass |
| $M_w$ | weight average molar mass |
| m/z | mass to charge ratio |
| NBA | norbornane |
| NBD | norbornadiene |
| $^{n}$Bu | normal butyl |
| NMR | nuclear magnetic resonance |
| $[OTf]^-$ | triflate |
| PDI | polydispersity index |
| Ph | phenyl |
| ppm | parts per million |
| $^{s}$Bu | secondary butyl |
| σ-CAM | sigma Complex Assisted Metathesis |
| TBE | *tert*-butylethylene |
| $^{t}$Bu | tertiary butyl |
| $^{t}$BuPOCOP$^{t}$Bu | $\kappa^3_{P,C,P}$-1,3-(OP$^{t}$Bu$_2$)$_2$C$_6$H$_3$ |
| THF | tetrahydrofuran |
| TOF | turnover frequency |
| TON | turnover number |
| UV/Vis | ultraviolet/visible |
| Xantphos | 4,5-*bis*(diphenylphosphino)-9,9-dimethylxanthene |
| Xantphos* | [4-phenylphosphido-5-diphenylphosphino-9,9-dimethylxanthene]$^-$ |

# Abstract

This thesis explores the reactivity of amine-boranes with the {Rh(Xantphos)}$^+$ fragment, with the aim of gaining mechanistic insight into the catalytic dehydropolymerisation of the amine-borane $H_3B{\cdot}NMeH_2$ to yield the polyaminoborane $[H_2BNMeH]_n$.

Chapter 2 describes the synthesis of suitable $Rh^{III}$ and $Rh^{I}$ Xantphos precursors to be used in this investigation. Moreover, the first example of the dehydrogenative B—B homocoupling of the tertiary amine-borane $H_3B{\cdot}NMe_3$ to form $H_4B_2{\cdot}2NMe_3$ is reported.

The synthesis of the $Rh^{I}$ precatalyst introduced in Chapter 2 entails the hydroboration of *tert*-butylethylene by $H_3B{\cdot}NMe_3$. In Chapter 3, the ability of the {Rh(Xantphos)}$^+$ fragment to mediate this hydroboration in a catalytic manner is explored, and a mechanism is presented in which reductive elimination is proposed to be turnover-limiting. Other alkenes and phosphine-boranes are also trialled to determine the scope of the hydroboration.

Chapter 4 investigates the catalytic dehydrocoupling of $H_3B{\cdot}NMe_2H$ and $H_3B{\cdot}NMeH_2$ with {Rh(Xantphos)}$^+$ to form the dehydrocoupling products $[H_2BNMe_2]_2$ and $[H_2BNMeH]_n$, respectively, and the dehydrocoupling mechanisms are shown to be similar. Both involve an induction period in which the active catalyst is formed (thought to involve N—H activation), and saturation kinetics operate during the productive phase of catalysis. $H_2$ is shown to inhibit the dehydrocoupling, and lead to production of shorter chain $[H_2BNMeH]_n$. Conversely, using THF as the dehydropolymerisation solvent instead of $C_6H_5F$ results in longer chain $[H_2BNMeH]_n$.

Finally, Chapter 5 presents new dicationic {Rh(Xantphos)}-based dimers, the formation of which involves loss of a phenyl group from the Xantphos ligands by P—C activation. The dimers are produced by routes involving either dehydrogenative homocoupling of $H_3B{\cdot}NMe_3$, or dehydrocoupling of $H_3B{\cdot}NMe_2H$. One of these dimers was tested as a catalyst for the dehydrocoupling of $H_3B{\cdot}NMe_2H$, and the reaction kinetics appear closely related those obtained using {Rh(Xantphos)}$^+$, suggesting that the active catalysts in each system may be related.

# Contents

Declaration i
Acknowledgements ii
Abbreviations iv
Abstract vi
Contents vii

**1 Introduction 1**

1.1 Overview 1
1.2 Organotransition metal complexes 1
1.2.1 Catalysis using rhodium 1
1.3 Phosphine ligands 2
1.3.1 Monodentate phosphines 2
1.3.2 Chelating phosphines 3
1.3.3 Hemilabile ligands 6
1.4 Dehydrocoupling of amine-boranes 10
1.4.1 Generalised pathway of amine-borane dehydrocoupling 12
1.4.2 Aminoboranes: observation and trapping 13
1.4.3 Linear diborazanes 15
1.5 Metal catalysed dehydrocoupling of amine-boranes 16
1.5.1 Early examples of metal catalysed dehydrocoupling 16
1.5.2 Heterogeneous catalysts for the dehydrocoupling of amine-boranes 17
1.5.3 Transition metal-catalysed dehydrocoupling of $H_3B{\cdot}NH_3$ promoted by ionic liquids 20
1.5.4 Homogeneous dehydrocoupling of amine-boranes 21
1.5.5 Sigma complexes of amine-boranes 22
1.5.6 Comparison with H—H and C—H sigma complexes 24
1.5.7 Sigma complexes of aminoboranes 25
1.5.8 Boryl complexes 26
1.5.9 Main group catalysed dehydrocoupling of amine-boranes 27
1.5.10 Early transition metal catalysed dehydrocoupling of amine-boranes 28
1.5.11 Mid transition metal catalysed dehydrocoupling of amine-boranes 32
1.5.12 Late transition metal catalysed dehydrocoupling of amine-boranes 34
1.5.13 Dehydrocoupling of amine-boranes involving ligand cooperativity 40

1.5.14 Effect of solvent upon dehydrocoupling reactions ..... 46
1.5.15 Generic mechanism for the dehydrocoupling of $H_3B{\cdot}NMe_2H$ using transition metals ..... 48
1.5.16 Mechanistic studies upon the dehydropolymerisation of amine-boranes ..... 51
1.6 Summary ..... 63
1.7 References ..... 63
**2 Sigma complexes and dehydrogenative homocoupling of amine-boranes ..... 68**
2.1 Introduction ..... 68
2.2 Attempted formation of $[Rh(Xantphos)(\eta^6\text{-}C_6H_5F)][BAr^F{}_4]$ ..... 68
2.3 Formation of $[Rh(\kappa^3{}_{P,O,P}\text{-}Xantphos)(H)_2(\eta^1\text{-}H_3B{\cdot}NMe_3)][BAr^F{}_4]$ ..... 70
2.4 Reactivity of complex **3** ..... 75
2.4.1 Stability of complex **3** ..... 75
2.4.2 H/D exchange in complex **3** ..... 76
2.4.3 Addition of MeCN to complex **3** ..... 78
2.4.4 Addition of THF to complex **3** ..... 78
2.5 Synthesis and characterisation of a $Rh^I$ Xantphos complex ..... 80
2.5.1 Formation of $[Rh(\kappa^2{}_{P,P}\text{-}Xantphos)(\eta^2\text{-}H_2B(CH_2CH_2{}^tBu){\cdot}NMe_3)][BAr^F{}_4]$ ..... 80
2.5.2 Characterisation of complex **6** ..... 81
2.5.3 Hydrogenation of complex **6** ..... 83
2.6 Dehydrogenative homocoupling of $H_3B{\cdot}NMe_3$ ..... 84
2.6.1 Introduction ..... 84
2.6.2 Dehydrogenative homocoupling of $H_3B{\cdot}NMe_3$ by complex **6** ..... 90
2.6.3 Bonding interactions in complex **8** ..... 95
2.6.4 Addition of MeCN to the homocoupling mixture ..... 96
2.6.5 Mechanism of formation of complex **8** ..... 97
2.6.6 Role of cyclohexene in dehydrogenative homocoupling ..... 100
2.7 Conclusions ..... 102
2.8 References ..... 103
**3 Hydroboration of alkenes by $H_3B{\cdot}NMe_3$ ..... 105**
3.1 Introduction ..... 105
3.1.1 Non-catalysed hydroboration ..... 105
3.1.2 Metal catalysed hydroboration ..... 108

3.2 Catalytic hydroboration using **6** ..... 114
3.3 Hydroboration catalyst selection and formation ..... 115
3.4 Hydroboration using **9**: resting states ..... 118
3.5 Kinetic studies ..... 121
3.5.1 Initial rates experiments ..... 121
3.5.2 Role of **8** in the hydroboration ..... 125
3.5.3 Inhibition by **I** ..... 126
3.6 Labelling studies ..... 126
3.7 Proposed mechanism ..... 128
3.8 Hydroboration with other alkenes ..... 129
3.8.1 Cyclohexene ..... 129
3.8.2 2,3-dimethyl-2-butene ..... 131
3.8.3 1-hexene ..... 132
3.8.3.1 Hydroboration catalysis ..... 132
3.8.3.2 Characterisation of **10** ..... 133
3.8.3.3 Tentative structure of **11** ..... 135
3.8.3.3 Comparison with the hydroboration of TBE ..... 137
3.9 Hydroboration of TBE with phosphine-boranes ..... 137
3.9.1 Introduction ..... 137
3.9.2 Formation of [Rh($\kappa^3_{P,O,P}$-Xantphos)(H)$_2$($\eta^1$-$H_3B{\cdot}PCy_3$)][$BAr^F_4$] ..... 138
3.9.3 Formation of [Rh($\kappa^2_{P,P}$-Xantphos)($\eta^2$-$H_3B{\cdot}PCy_3$)][$BAr^F_4$] ..... 139
3.9.4 Hydroboration of TBE by **13** ..... 140
3.9.5 Attempted hydroboration using $H_3B{\cdot}PEt_3$ ..... 144
3.10 Conclusions ..... 144
3.11 References ..... 145
**4 Exploring the mechanism of the dehydrocoupling of amine-boranes with {Rh(Xantphos)}$^+$ ..... 147**
4.1 Introduction ..... 147
4.2 Stoichiometric reactivity of **6** with amine-boranes ..... 147
4.2.1 Reactivity with $H_3B{\cdot}NMe_2H$ ..... 147
4.2.2 Reactivity with $H_3B{\cdot}NMeH_2$ ..... 149
4.2.3 Conclusions on stoichiometric reactivity ..... 151
4.3 Dehydropolymerisation of $H_3B{\cdot}NMeH_2$ with **6** ..... 152

4.3.1 Role of $H_2B$=NMeH during dehydropolymerisation ..... 154
4.4 Polymer growth kinetics ..... 155
4.4.1 Temporal profile for the dehydropolymerisation ..... 155
4.4.2 Molecular weight *vs* conversion ..... 156
4.5 Effect of solvent upon dehydropolymerisation ..... 158
4.6 Role of $H_3B{\cdot}NMeHBH_2{\cdot}NMeH_2$ in dehydropolymerisation ..... 159
4.7 Dehydropolymerisation under closed conditions ..... 160
4.8 Catalytic dehydrocoupling of $H_3B{\cdot}NMe_2H$ with **6** ..... 162
4.8.1 Open conditions ..... 162
4.8.2 Catalysis in the presence of excess $[H_2BNMe_2]_2$ ..... 165
4.8.3 Role of **I** in dehydrocoupling ..... 165
4.8.4 Effect of [**6**] upon dehydrocoupling ..... 166
4.8.5 Effect of $[H_3B{\cdot}NMe_2H]$ upon dehydrocoupling: saturation kinetics ..... 166
4.8.6 Saturation kinetics in the dehydrocoupling of $H_3B{\cdot}NMeH_2$ ..... 170
4.8.7 Kinetic isotope effects ..... 170
4.8.8 Closed conditions ..... 171
4.9 Exploring rationale for the induction period ..... 175
4.9.1 Testing complex **3** as a dehydrocoupling catalyst ..... 175
4.9.2 Effect of using $D_3B{\cdot}NMe_2H$ and $H_3B{\cdot}NMe_2D$ upon the induction period ..... 176
4.9.3 Attempt to form a 'model' N—H activated complex ..... 177
4.9.4 Probing H/D exchange in **18** ..... 178
4.9.5 Aminoboryl complexes as the active catalyst ..... 180
4.9.5.1 B—H activation of $H_2B{=}N^iPr_2$ ..... 180
4.9.5.2 B—H activation of $H_2B{=}NMe_2$ ..... 183
4.9.5.3 Role of **23** in dehydrocoupling catalysis ..... 185
4.9.6 Induction period: conclusions ..... 185
4.10 Resting state experiments ..... 186
4.11 Proposed dehydrocoupling mechanism ..... 188
4.12 Conclusions and future work ..... 194
4.13 References ..... 195
**5 Synthesis and dehydrocoupling activity of P—C activated Rh Xantphos dimers ..... 198**
5.1 Introduction ..... 198

5.2 Formation of a P—C activated dimeric complex ..... 198
5.2.1 Synthesis and characterisation ..... 198
5.2.2 Exploring the formation of **24** ..... 203
5.2.3 Reactivity of **24** with $H_2$ and $D_2$ ..... 206
5.2.4 Reactivity of **24** with electrophiles ..... 209
5.2.5 Addition of MeCN to **24** ..... 209
5.2.6 Addition of $Ph_2PCH_2CH_2PPh_2$ to **24** ..... 210
5.2.6.1 Reaction between **6** and dpp2 ..... 213
5.2.7 Summary of the reactivity of **24** ..... 217
5.3 Formation of a Rh(Xantphos*) dimer *via* dehydrocoupling reactions ..... 217
5.3.1 Final product of **6**-catalysed dehydrocoupling of $H_3B{\cdot}NMe_2H$ ..... 217
5.3.2 Formation of **28** from **24** ..... 222
5.3.2.1 Addition of $Na[H_3B{\cdot}NMe_2{\cdot}BH_3]$ to **24** ..... 222
5.3.2.2 Dehydrocoupling of $H_3B{\cdot}NMe_2H$ ..... 223
5.4 Kinetic studies upon **24**-catalysed dehydrocoupling ..... 225
5.4.1 Catalytic dehydrocoupling of $H_3B{\cdot}NMe_2H$ by **24** ..... 225
5.4.2 Saturation kinetics ..... 226
5.4.3 Kinetic isotope effects ..... 228
5.4.4 Dehydrocoupling of $H_3B{\cdot}NMe_2H$ under sealed conditions ..... 228
5.4.5 Dehydropolymerisation of $H_3B{\cdot}NMeH_2$ by **24** ..... 230
5.4.6 Comparison of **24** and **6** as dehydrocoupling catalysts ..... 231
5.5 Conclusions and future work ..... 233
5.6 References ..... 234
**6 Summary and future outlook ..... 236**
**7 Experimental ..... 237**
7.1 Experimental techniques ..... 237
7.1.1 Nuclear Magnetic Resonance Spectroscopy ..... 237
7.1.2 Mass spectrometry ..... 237
7.1.3 Gel permeation chromatography (GPC) ..... 238
7.1.4 Elemental microanalysis ..... 239
7.1.5 X-ray crystallography ..... 239
7.1.6 General procedure for hydrogenation ..... 239
7.2 Synthesis and characterisation ..... 240

7.2.1 Starting materials ..... 240
7.2.2 Synthesis of new complexes ..... 240
7.3 Catalytic procedures ..... 260
7.3.1 General procedure for catalytic hydroboration ..... 260
7.3.2 General procedure for the dehydropolymerisation of $H_3B{\cdot}NMeH_2$ ..... 260
7.3.3 General procedure for the dehydrocoupling of $H_3B{\cdot}NMe_2H$ – open conditions ..... 261
7.3.4 General procedure for the dehydrocoupling of $H_3B{\cdot}NMe_2H$ – closed conditions ..... 261
7.4 Computational details ..... 261
7.5 References ..... 262
**8 Appendices ..... 263**
8.1 Crystallographic data ..... 263

# 1 Introduction

## 1.1 Overview

This thesis investigates the stoichiometric and catalytic reactivity of amine-boranes with the {Rh(Xantphos)}$^+$ fragment. This introduction provides a review of metal-catalysed amine-borane dehydrocoupling – focusing upon recent mechanistic insight – and covers the background to the ligand, Xantphos, chosen for this investigation.

## 1.2 Organotransition metal complexes

Organotransition metal complexes have been used widely as catalysts for various industrially important processes, including olefin hydrogenation,[1] hydroformylation,[2] Ziegler-Natta olefin polymerisation[3] and cross coupling reactions.[4] The majority of these processes focus on the creation of C—E (E = *e.g.* C, N, O) bonds with relatively few examples of the creation of other main group-main group bonds, as is the focus of this thesis.

### 1.2.1 Catalysis using rhodium

Rhodium (ground state electronic configuration [Kr]4d$^8$5s$^1$) is a group IX metal that has been widely used in many catalytic applications. For example, Wilkinson's catalyst [Rh(PPh$_3$)$_3$Cl] has been used in catalytic hydrogenations[1] and hydroformylation.[5] The most common oxidation states for rhodium are +I and +III, which enable rhodium to undergo oxidative addition and reductive elimination, common steps during catalytic cycles. During such cycles, intermediates with vacant sites are often proposed to form.[2] It has been suggested that vacant sites should be instead referred to as virtual coordination sites,[6] due to the likelihood of forming

weak bonds with the solvent or anion, or reactivity of an ancillary ligand.[7] The Weller group have studied various latent low-coordinate complexes of rhodium (Figure 1.1), which feature vacant site(s) stabilised by weak interactions, *e.g*. agostics or weakly coordinating solvents.[8-10] Understanding of these intermediate-like species can gain insight into the behaviour of potential catalytic intermediates. Rhodium phosphine complexes have also been used as precatalysts by the Weller group,[11-16] and others,[17-20] for the dehydrocoupling of amine-boranes (Section 1.5).

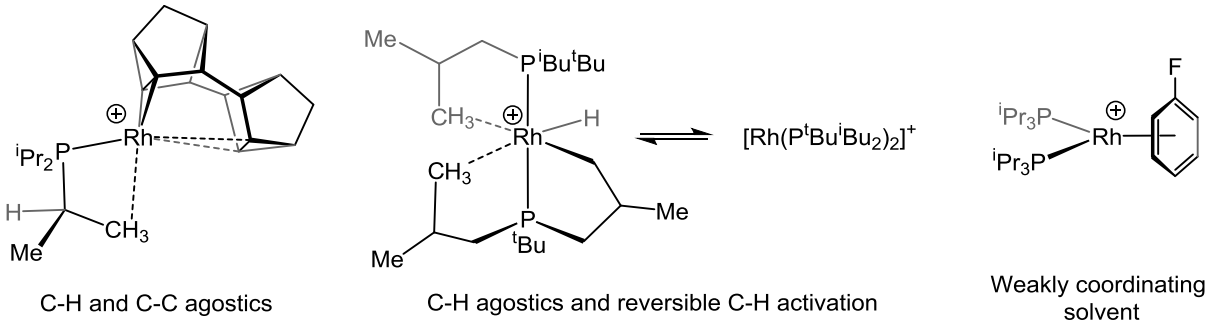



**Figure 1.1** Examples of latent low coordinate complexes of rhodium. $[BAr^F_4]^-$ anions not shown.

## 1.3 Phosphine ligands

### 1.3.1 Monodentate phosphines

Phosphines, $PR_3$, are one of the most common classes of organometallic ligands, used most often with late metals, including rhodium. Phosphines have a lone pair that can act as a σ donor to the metal. However, they also act as π-acids due to the vacant P—R σ* orbitals that accept electron density from filled metal-based dπ orbitals.[21] The extent of π-acidity can be readily tuned by altering the R groups.[22] More electronegative R groups result in lower energy P—R σ* orbitals, while also increasing the phosphorus contribution to the σ* orbital. These factors result in a

more accessible σ* orbital for back-donation, and hence increased π-acidity of the phosphine.[23] In $PF_3$, for example, the π-acidity is comparable with that of CO.[21] Electronic effects for a range of common tertiary phosphines were quantified by Tolman, who measured the C—O stretching frequencies in the complexes $LNi(CO)_3$ (L = phosphine). With greater π-acidity of the phosphine, the electron density at the metal centre is decreased. In turn, the degree of back-bonding to CO is decreased, and the C—O stretching frequency is increased.

Tolman also quantified the steric effects of altering the phosphine by devising the 'cone angle,' which is the angle defined by the outer edge of the phosphorus substituents and the metal centre in a space-filling model, where the metal-phosphorus distance is fixed at 2.28 Å and the metal is at the vertex (Figure 1.2).[24] An understanding of the steric and electronic factors of the phosphine can enable tailoring of the ligand environment for a desired purpose. For example, bulky phosphines may be used to isolate low-coordinate species.[21]

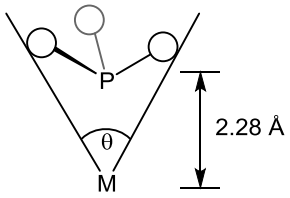



**Figure 1.2** Tolman cone angle (θ).

### 1.3.2 Chelating phosphines

Chelating phosphines – bidentate ligands in which phosphorus donors are connected by a bridge to another phosphorus donor – allow further tuning of the catalytic activity of the metal. Different chelating phosphines may have different geometry

preferences and therefore differing reactivity. Phosphines such as 1,2-bis(diphenylphosphino)ethane (dpp2) have a tether length such that a *cis*-P,P geometry is enforced upon complexation to a metal, whereas other phosphines (*e.g.* transphos)[25] encourage *trans*-P,P binding to the metal (Figure 1.3).[2]

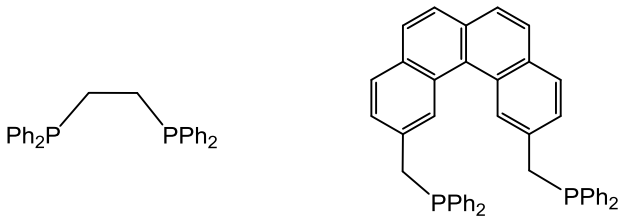



**Figure 1.3** The chelating phosphines dpp2 and transphos.

One of the methods used to quantify the properties of chelating diphosphine ligands is the preferred bite angle (Figure 1.4), developed by Casey and Whitaker and defined as the "preferred chelation angle determined only by ligand backbone constraints and not by metal valence angles."[26] The flexibility range for the ligand was defined as the range of bite angles with a strain energy within 3 kcal $mol^{-1}$ of the calculated bite angle.[27] Bite angles and flexibility ranges have been calculated for many bidentate ligands, and some relevant to this thesis are shown in Figure 1.4.

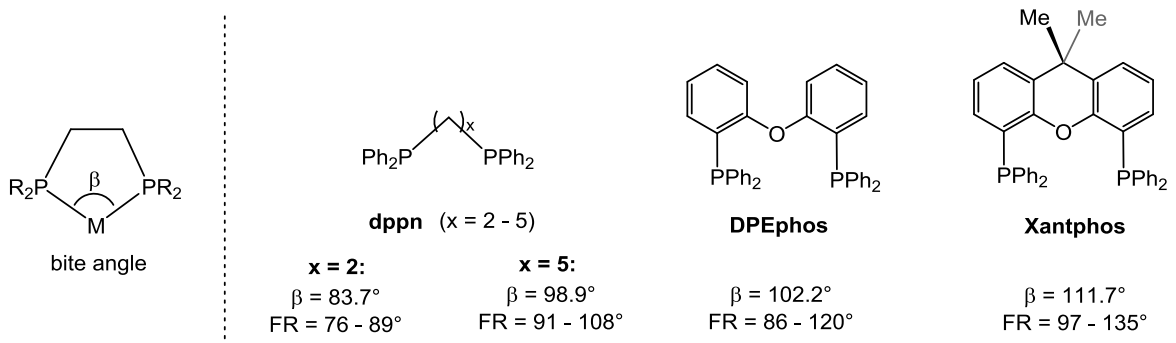
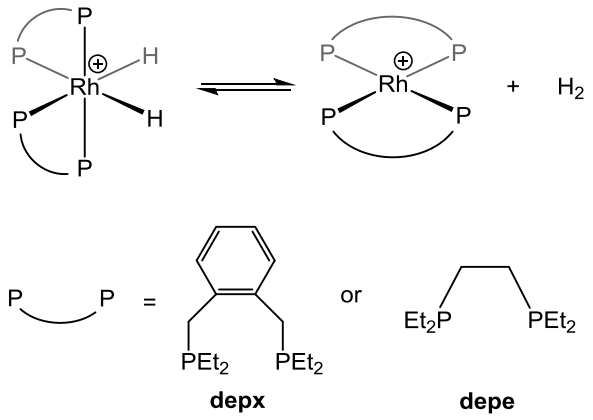



**Figure 1.4** Left: representation of the bite angle (β). Right: calculated bite angles and flexibility ranges (FR) for dpp2,[28] dpp5,[28] DPEphos[27] and Xantphos.[27]

The effects of bite angle upon the reactivity of metal complexes have been noted by many, with different effects observed with different systems. With group IX cationic complexes, for example, Dubois and co-workers have shown that the bite angle influences the propensity for the oxidative addition of dihydrogen to square planar $[Rh(diphosphine)_2][CF_3SO_3]$ complexes (Scheme 1.1).[29] Thermodynamic parameters were obtained for the equilibria with a variety of diphosphine ligands and showed that oxidative addition was favoured by ligands with large bite angles, small cone angles and electron donating substituents. Of these factors, the bite angle appeared dominant. For example, reductive elimination of $H_2$ from $[Rh(depe)_2(H)_2][CF_3SO_3]$ ($\beta = 86°$) was thermodynamically favourable ($\Delta G = -0.83$ kcal mol$^{-1}$) compared with the larger bite angle ($\beta = 100°$) complex $[Rh(depx)_2(H)_2][CF_3SO_3]$ ($\Delta G = +11.4$ kcal mol$^{-1}$).[30]




**Scheme 1.1** Oxidative addition of $H_2$ to $[Rh(disphosphine)_2][CF_3SO_3]$. $[CF_3SO_3]^-$ anions not shown.

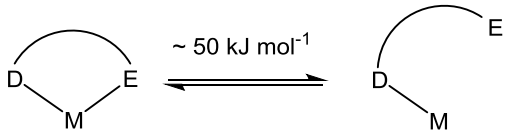
It is thought that this reliance on bite angle is due to tetrahedral distortion from square planar geometry in the complexes $[Rh(disphosphine)_2]^+$, which is more pronounced with a larger bite angle diphosphine. This distortion decreases the energy of the antibonding σ-acceptor $d_{xy}$ metal orbital and increases the energy of the

filled π-donor $d_{xz}$ and $d_{yz}$ orbitals, and the orbital energies are better optimised for interaction with the incoming dihydrogen.[29-31] As will be noted in Section 1.5.16, the rate of dehydrocoupling of $H_3B{\cdot}NMe_2H$ also correlated with bite angle in the system $[Rh(Ph_2P(CH_2)_xPPh_2)(\eta^6\text{-}C_6H_5)][BAr^F{}_4]$ (x = 3 – 5). The smallest bite angle (x = 3) gave the fastest turnover, possibly due to the instability of smaller bite angle $Rh^{III}$ dihydrides with respect to $H_2$ loss.[12]

Bite angles have been shown to affect the regioselectivity of various catalytic processes including hydroformylation[27,28] and cross couplings.[32,33] Furthermore, van Leeuwen and others have noted that increasing the bite angle increases the rate of reductive elimination of R—R' from square planar [(diphosphine)PdRR'] complexes.[34,35] The dependence of the rate of reductive elimination of $CH_3CN$ from $[(diphosphine)Pd(CH_3)(CN)]$ upon bite angle was found to be governed by electronics rather than sterics. The wide bite angle ligands destabilise the reactant by distorting the square planar geometry towards a linear geometry, but this distortion stabilises the transition state, and so the barrier to reductive elimination is lowered.[36]

### 1.3.3 Hemilabile ligands

Hemilabile ligands, first defined by Jeffrey and Rauchfuss,[37] contain at least two different types of chemical functionality capable of binding to the metal centre, where at least one donor (E) is substitutionally labile while the other donor group(s) (D) remain bound to the metal centre (Scheme 1.2). The labile donor E should be able to reversibly "open" and "close" and the energy differences between these geometries should be relatively small – often in the order of approximately 50 kJ $mol^{-1}$.[38]




**Scheme 1.2** Hemilabile ligand behaviour.

Hemilability can be classified into one of three categories. Type I hemilability involves spontaneous opening of the chelate and is often found when a complex (including multinuclear structures) has a variety of coordination modes available. Type II hemilability involves intramolecular competition between the E donor and another donor, and Type III hemilability involves intermolecular competition between E and an external reagent.[38] The hemilabile behaviour of many hybrid ligands (*e.g.* [N,P], [N,S] and [O,P] based ligands) has been reviewed.[39] This introduction will focus on P,O,P systems, in which the oxygen atom acts as a reversible donor to the metal centre, forming either $\kappa^2_{P,P}$ or $\kappa^3_{P,O,P}$ complexes.

One such ligand is Xantphos (9,9-dimethyl-4,5-*bis*-(diphenylphosphino)xanthene) (Figure 1.4). First synthesised by van Leeuwen,[27] Xantphos is a hemilabile ligand with versatile coordination modes and has been used widely in many catalytic applications including hydroformylation,[27,40] cross couplings[41] and hydrocyanation.[40,42] In 2011, Haynes and co-workers tabulated the bite angles and M—O distances of crystallographically characterised Xantphos complexes.[43] Contrasting initial molecular mechanics calculations by van Leeuwen,[27] they found that Xantphos has a wide bimodal range of bite angles (*ca.* 99 – 165°) that can be split roughly into *cis* (<120°) and *trans* (>143°) complexes. Their plot of P—M—P angle *vs* M—O bond distance is shown in Figure 1.5 and shows that, while *cis*-$\kappa^2_{P,P}$ coordination is the most common mode (black points), examples of *trans*-$\kappa^2_{P,P}$ (red points), *mer*-$\kappa^3_{P,O,P}$

(blue and orange points) and *fac*-$\kappa^3_{P,O,P}$ (green points) coordination geometries are also known.

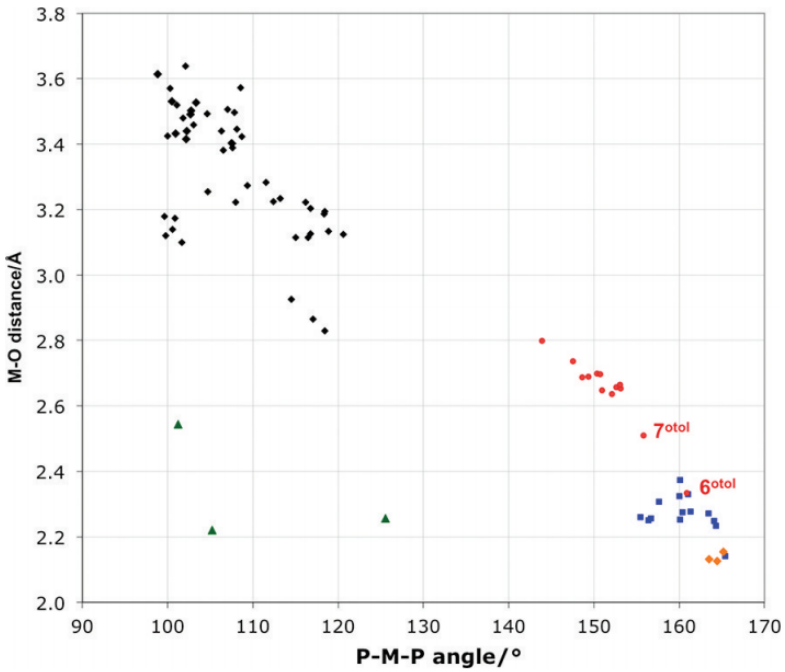
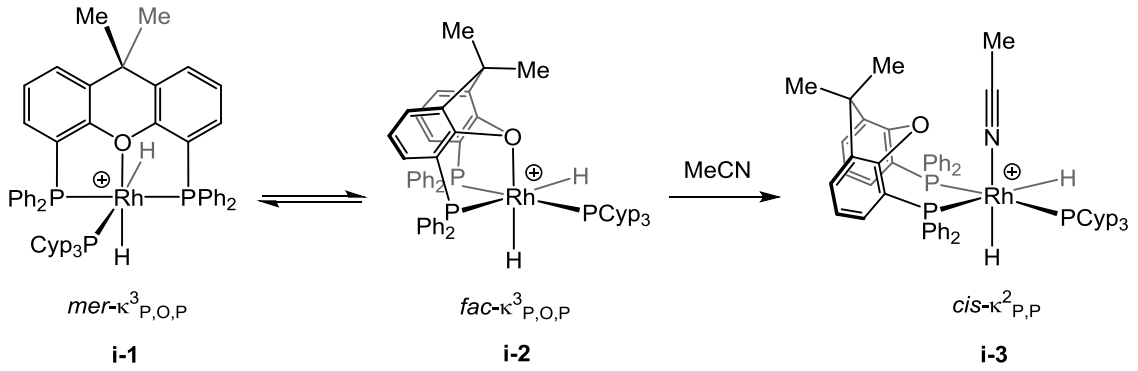


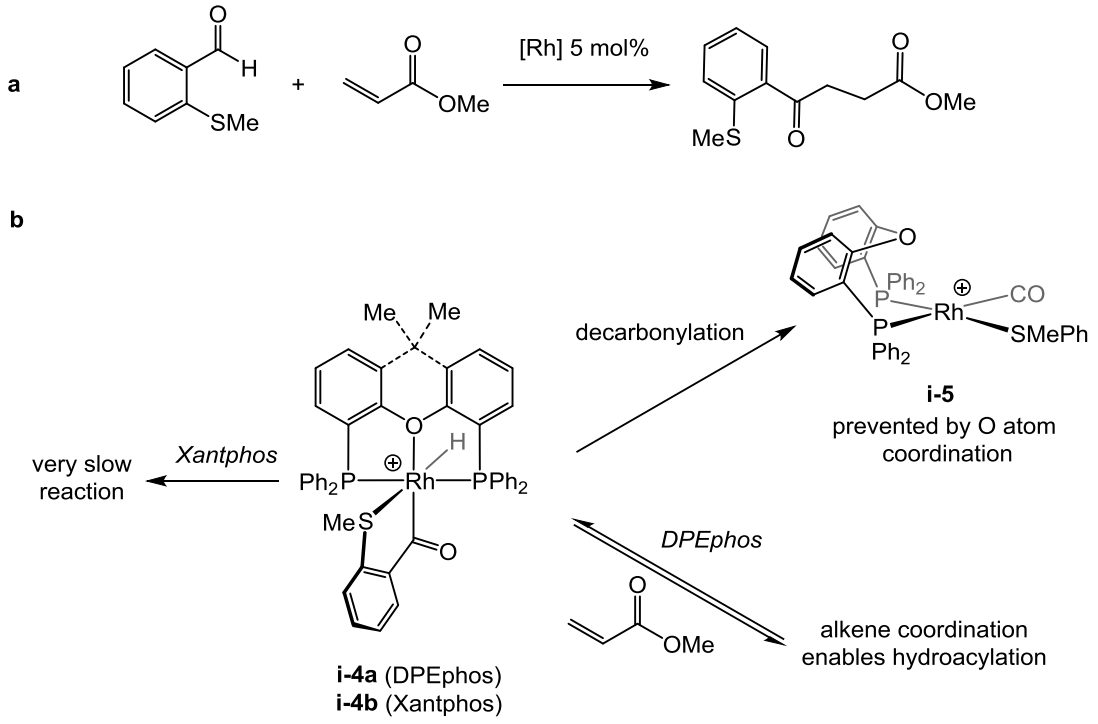

**Figure 1.5** Plot of P—M—P angle *vs* M—O distance of Xantphos complexes. Reprinted (adapted) with permission from G. L. Williams, C. M. Parks, R. Smith, H. Adams, A. Haynes, A. J. H. M. Meijer, G. J. Sunley, and S. Gaemers, *Organometallics*, **2011**, *30*, 6166-6179. Copyright 2011 American Chemical Society.

Reports by the Weller group upon the complex [Rh(Xantphos)$(H)_2$(PCyp$_3$)][BAr$^F_4$] (Cyp = cyclopentyl) demonstrated that, in this system, the *mer*-$\kappa^3$ (**i-1**) and *fac*-$\kappa^3$ (**i-2**) geometries are closely matched in energy with an equilibrium established between the two coordination geometries ($\Delta G$(298 K) = –1.9 ± 0.4 kJ mol$^{-1}$). Type III hemilabile behaviour was also demonstrated when the coordinated oxygen atom was displaced on addition of MeCN to form **i-3** (Scheme 1.3).[44]




**Scheme 1.3** Some coordination modes of Xantphos and demonstration of hemilabile behaviour. From **i-1** to **i-2**, ΔG(298 K) = –1.9 ± 0.4 kJ mol$^{-1}$. Cyp = cyclopentyl. [BAr$^F{}_4$]$^-$ anions not shown.

Weller and Willis have used the related hemilabile ligand DPEphos (*bis*(2-diphenylphosphinophenyl)ether) (Figure 1.4), first synthesised by Taube in 1985,[45] for the hydroacylation reaction of alkenes with β-S-substituted aldehydes.[46-48] Using the precatalyst [Rh(κ$^2$$_{P,P}$-DPEphos)(acetone)$_2$][BAr$^F{}_4$] (5 mol%), complete conversion to the hydroacylation product was achieved (Scheme 1.4a). The hemilability of DPEphos played a role in the mechanism. The hydroacylation intermediate **i-4a** (Scheme 1.4b) contains a vacant site masked by coordination of the DPEphos oxygen atom. If the atom were not coordinated, reductive decarbonylation to **i-5**, an undesired catalyst deactivation pathway, could occur. For productive catalysis, the DPEphos ligand in **i-4a** rearranges into a κ$^2$$_{P,P}$ geometry and the alkene coordinates to the vacant site. However, when using the Xantphos ligand instead, the reduced flexibility of Xantphos compared with DPEphos resulted in a significantly lower turnover frequency as the oxygen atom did not decoordinate from **i-4b** to allow alkene coordination.[46]




**Scheme 1.4 (a)** Hydroacylation. [Rh] = [Rh(κ$^2$$_{P,P}$-DPEphos)(acetone)$_2$][BAr$^F$$_4$]. **(b)** Pathways for reductive decarbonylation or hydroacylation from **i-4a** or **i-4b**. [BAr$^F$$_4$]$^-$ anions not shown.

## 1.4 Dehydrocoupling of amine-boranes

Dehydrocoupling is the formation of a new element-element bond with the concomitant release of $H_2$. Homonuclear and heteronuclear dehydrocoupling of many main group elements (*e.g.* Si, Ge and P) has revealed a range of new main-group oligomeric and polymeric materials.[49] This introduction will focus upon the dehydrocoupling of amine-boranes. These typical Lewis-acid/Lewis-base adducts, while isoelectronic with alkanes, possess hydridic B—H bonds and protic N—H bonds.[50] Resulting intra- or intermolecular B—H···H—N dihydrogen bonds can promote $H_2$ loss from amine-boranes much more readily than from their alkane analogues.[51,52] These interactions also explain the different physical properties of amine-boranes compared with their alkane analogues. For example, ethane is a gas at

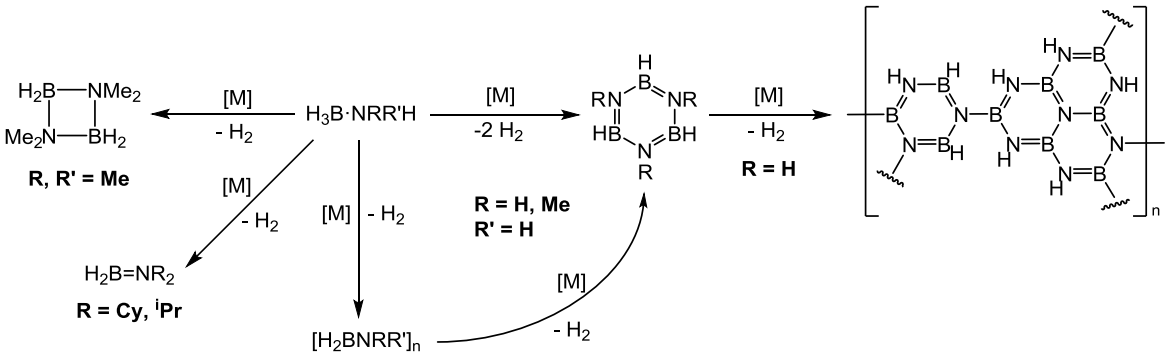
room temperature (melting point –183 °C), whereas the isoelectronic $H_3B{\cdot}NH_3$ is a solid (melting point 109 °C).[53]

Amine-borane dehydrocoupling has attracted much attention in recent years. The parent amine-borane, $H_3B{\cdot}NH_3$, has a gravimetric hydrogen content of 19.6 wt% and thus has been explored intensively as a hydrogen storage medium.[54-56] $H_2$ can be released from $H_3B{\cdot}NH_3$ thermally or catalytically (as discussed later in this Chapter) but, to be a viable $H_2$ storage candidate, energy efficient methods of regenerating $H_3B{\cdot}NH_3$ are required. Significantly, in 2010, Sutton reported the regeneration of $H_3B{\cdot}NH_3$ from polyborazylene 'spent fuel' by treatment with hydrazine in liquid ammonia.[57] This showed promise for $H_3B{\cdot}NH_3$ as a hydrogen storage system, although milder regeneration methods would be desirable. Other amine-boranes that can be regenerated from their spent fuel are discussed in Section 1.5.2.

An alternative focus of amine-borane dehydrocoupling is the production of B—N based materials. For example, high molecular weight $[H_2BNMeH]_n$ has been produced by the dehydrocoupling of $H_3B{\cdot}NMeH_2$ (Section 1.5.16). These materials – isoelectronic with ubiquitous polyolefins – have potential applications as piezoelectric materials or ceramic precursors to boron-nitride.[50] The formation of layers of hexagonal boron nitride films on graphene using $H_3B{\cdot}NH_3$ and Cu foil at 950 °C has also been reported.[58] Understanding of the mechanism of the formation of polyaminoboranes may ultimately enable the production of polyaminoboranes that are tailored for a particular purpose.

### 1.4.1 Generalised pathway of amine-borane dehydrocoupling

The general pathway for the dehydrocoupling of amine-boranes is shown in Scheme 1.5. $H_3B{\cdot}NH_3$ can also lose over two equivalents of hydrogen to form polyborazylene as well as often insoluble oligomeric and polymeric materials that arise from loss of less than two equivalents of $H_2$.[54] Primary amine–boranes, $H_3B{\cdot}NRH_2$, can lose one equivalent of hydrogen during dehydrocoupling to afford polyaminoboranes $[H_2BNRH]_n$ (R = H, Me, $^n$Bu). Borazines, $[HBNR]_3$ (R = H, Me, $^n$Bu), can result from the loss of two equivalents of dihydrogen and may be considered as the thermodynamic product of the dehydrocoupling of primary amine-boranes. Secondary amine-boranes $H_3B{\cdot}NR_2H$ can lose one equivalent of dihydrogen. The cyclic dimer $[H_2BNR_2]_2$ (R = *e.g.* Me, Et) is generally formed as the major dehydrocoupling product of $H_3B{\cdot}NR_2H$. With bulky N-substituents, *e.g.* $^i$Pr or Cy, dimerisation is prevented and instead the aminoborane $H_2B{=}NR_2$ results.[59,60]



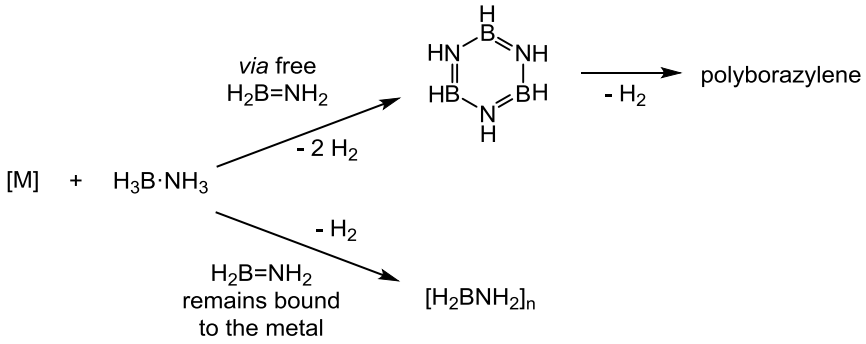

**Scheme 1.5** Generalised pathways for the dehydrocoupling of amine-boranes. Not all products and pathways shown.

Secondary amine-boranes dehydrocouple through generally soluble and well-defined intermediates; for $H_3B{\cdot}NMe_2H$, the most commonly observed are the transient aminoborane $H_2B{=}NMe_2$ and the linear diborazane $H_3B{\cdot}NMe_2BH_2{\cdot}NMe_2H$.

Consequently, $H_3B{\cdot}NMe_2H$ can be used as a model for the dehydrocoupling of $H_3B{\cdot}NH_3$ and $H_3B{\cdot}NMeH_2$,[16] the products of which are often insoluble or poorly defined polymeric or oligomeric materials.[61]

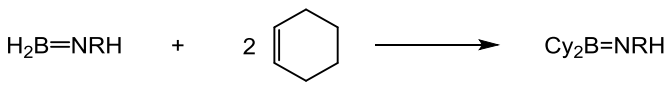
### 1.4.2 Aminoboranes: observation and trapping

The dehydrocoupling of amine-boranes is often proposed to proceed *via* initial dehydrogenation to form aminoboranes $H_2B{=}NRR'$. As noted above, $H_2B{=}NR_2$ (R = $^i$Pr or Cy) are stable as monomers. Less bulky aminoboranes, however, are transient species in dehydrocoupling reactions. For example, $H_2B{=}N^tBuH$ and $H_2B{=}NMe_2$ have been directly observed as intermediates in the catalytic dehydrocoupling of their respective amine-boranes.[62,63] The 'off-metal' dimerisation of $H_2B{=}NMe_2$ to form $[H_2BNMe_2]_2$ was found to be a second order process with a large negative entropy of activation.[64] The less bulky congeners $H_2B{=}NH_2$[65] and $H_2B{=}NMeH$,[20,66] have not been directly observed as intermediates in metal-catalysed dehydrocoupling of their respective amine-boranes, although $H_2B{=}NMeH$ has recently been observed as an intermediate in the formation of low molecular weight $[H_2BNMeH]_n$ from the reaction of $[H_2B(Et_2O){\cdot}NMeH_2][B(C_6F_5)_4]$ with 2,6-di-*tert*-butylpyridine.[67] Moreover, $H_2B{=}NH_2$ and $H_2B{=}NMeH$ have been observed coordinated to transition metal fragments (Section 1.5.7), being formed from dehydrogenation of the corresponding amine-borane.[68] In 2008, Baker, Dixon and co-workers proposed that $H_2B{=}NH_2$ liberated from the metal during dehydrocoupling results in the eventual production of borazine, whereas $H_2B{=}NH_2$ (or derivatives thereof) remaining bound to the metal results in oligomeric or polymeric products (Scheme 1.6).[69]




**Scheme 1.6** Baker and Dixon's generalised pathway for the outcome of dehydrocoupling, dependent upon whether the aminoborane is metal-bound or free.

To identify free aminoborane in dehydrocoupling reaction mixtures, cyclohexene was added. Cyclohexene can be hydroborated by $H_2B{=}NRH$ (R = H, Me), forming $Cy_2B{=}NRH$ (Scheme 1.7), thereby acting as a useful marker for free aminoboranes. When cyclohexene was added to a reaction mixture of $H_3B{\cdot}NH_3$ and $[Rh(1,5\text{-cod})(\mu\text{-Cl})]_2$, $Cy_2B{=}NH_2$ was the major product observed instead of the expected borazine (see Section 1.5.2).[70] However, upon addition of cyclohexene to a solution of $H_3B{\cdot}NH_3$ and catalyst $Ir(^tBuPOCOP^tBu)(H)_2$ ($^tBuPOCOP^tBu$ = $\kappa^3$-$_{PCP}$-1,3-$(OP^tBu_2)_2C_6H_3$), the same oligomeric products were observed as in the absence of cyclohexene (see Section 1.5.12),[71] *i.e.* no $Cy_2B{=}NH_2$ was observed. These observations support the proposal that free $H_2B{=}NH_2$ forms borazine, whereas bound $H_2B{=}NH_2$ forms oligomers.

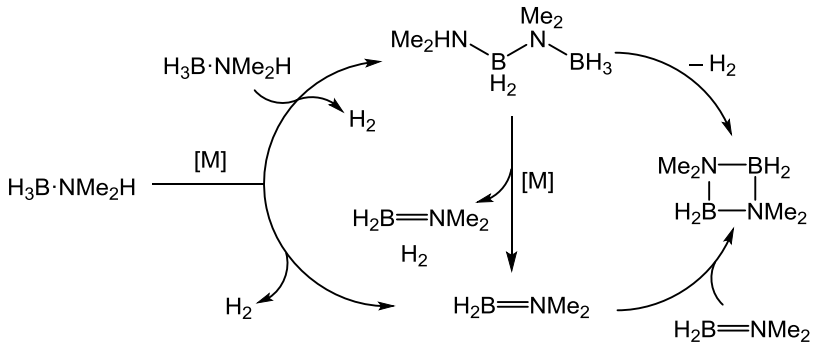



**Scheme 1.7** Trapping of aminoboranes by cyclohexene. R = Me, H.

Although cyclohexene trapping is still regarded as a useful method for detecting free aminoboranes, more recent studies have suggested that the absence of hydroboration does not necessarily reflect an absence of free aminoboranes. It has been suggested that, if borazine formation (from aminoborane trimerisation/dehydrogenation) or hydroboration of cyclohexene are not kinetically competitive with metal-based BN oligomerisation/polymerisation processes, $Cy_2B{=}NHR$ (R = Me, H) will not be observed even if aminoboranes are present.[65,72,73]

### 1.4.3 Linear diborazanes

Another intermediate often observed in the dehydrocoupling of $H_3B{\cdot}NMe_2H$ is the linear diborazane $H_3B{\cdot}NMe_2BH_2{\cdot}NMe_2H$.[59] Schneider has calculated that the thermodynamic pathway for B—N bond cleavage of $H_3B{\cdot}NMe_2BH_2{\cdot}NMe_2H$ to generate $H_3B{\cdot}NMe_2H$ and $H_2B{=}NMe_2$ is close to thermoneutral ($\Delta G = -2.3$ kcal mol$^{-1}$).[74] Therefore, if this process is reversible (*i.e.* as mediated by a catalyst), the position of the equilibrium (and hence whether $H_3B{\cdot}NMe_2BH_2{\cdot}NMe_2H$ is observed in catalysis) is likely to be dependent upon the relative concentrations and rates of formation of the BN species with a particular catalyst. A general pathway for the dehydrocoupling of $H_3B{\cdot}NMe_2H$ with Schneider's ruthenium catalysts (see Section 1.5.16) was developed (Scheme 1.8), with the kinetics suggesting that the formation of $H_3B{\cdot}NMe_2BH_2{\cdot}NMe_2H$ is a metal–based process. The role of this diborazane in the dehydrocoupling of $H_3B{\cdot}NMe_2H$ has been further discussed by others.[15,59,64,72,75]




**Scheme 1.8** Schneider's early model for metal catalysed dehydrocoupling of $H_3B{\cdot}NMe_2H$ to form $[H_2BNMe_2]_2$.

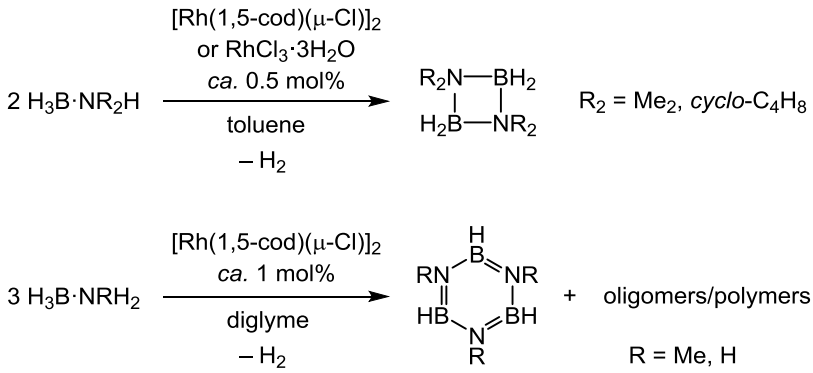
Weller and Manners have since reported that the diborazane $H_3B{\cdot}NMeHBH_2{\cdot}NMeH_2$ can be formed catalytically from the dehydrocoupling of $H_3B{\cdot}NMeH_2$,[76] and its role as a possible intermediate in dehydropolymerisation has been further explored (see Section 1.5.16).[72] Shore and co-workers have also reported the synthesis by stoichiometric methods of the $H_3B{\cdot}NH_3$ analogue, $H_3B{\cdot}NH_2BH_2{\cdot}NH_3$,[77] while Sneddon and co-workers have reported the synthesis of triborazanes such as $H_3B{\cdot}(NH_2BH_2)_2{\cdot}NH_3$ using non-catalytic methods.[78]

## 1.5 Metal catalysed dehydrocoupling of amine-boranes

### 1.5.1 Early examples of metal catalysed dehydrocoupling

Dehydrocoupling of amine-boranes can be thermally induced (*e.g.* $H_3B{\cdot}NH_3$ can lose two equivalents of $H_2$ on heating to 150 °C),[56] but metal catalysed dehydrocoupling is more efficient and controllable. The first example of transition metal catalysed dehydrocoupling of amine-boranes was reported in 1989 by Roberts and co-workers. The amine-borane $H_3B{\cdot}N^tBuMeH$ was dehydrogenated at 120 °C using 10% Pd on charcoal to form the aminoborane $H_2B{=}N^tBuMe$, which dimerised to form $[H_2BN^tBuMe]_2$.[79] In 2001 Manners and co-workers reported that $Rh^I$ or $Rh^{III}$

precursors catalytically dehydrocoupled secondary amine-boranes $H_3B{\cdot}NR_2H$ ($R_2$ = $Me_2$, *cyclo*-$C_4H_8$) to yield the corresponding cyclic dimer $[H_2BNR_2]_2$ (Scheme 1.9). The $Rh^I$ precursor was also an effective catalyst for the dehydrocoupling of $H_3B{\cdot}NH_3$ and $H_3B{\cdot}NMeH_2$ to form their respective borazines, although in both cases insoluble material, indicative of oligomeric chains, was also observed in the reaction mixtures.[70]




**Scheme 1.9** Dehydrocoupling of amine-boranes by $[Rh(1,5\text{-cod})(\mu\text{-Cl})]_2$ and $RhCl_3{\cdot}3H_2O$.

### 1.5.2 Heterogeneous catalysts for the dehydrocoupling of amine-boranes

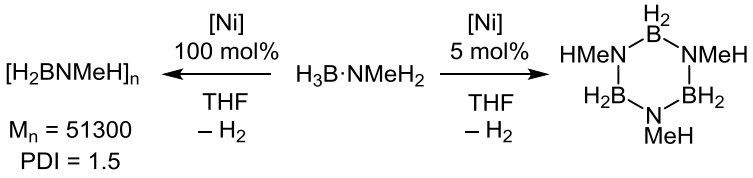
Various systems act as heterogeneous catalysts for amine-borane dehydrocoupling by the formation *in situ* of catalytically active nanoparticles, although the nature of the actual catalytic component can be the subject of debate. Nonetheless, heterogeneous catalysis is attractive due to facile separation of the products and catalyst. Manners' dehydrocoupling of $H_3B{\cdot}NMe_2H$ by $[Rh(1,5\text{-cod})(\mu\text{-Cl})]_2$ showed a reaction profile with an induction period, during which a black precipitate was observed to form. Tests, originally developed by Finke,[80] were performed to probe for heterogeneous catalysis. For example, both filtration and catalyst poisoning with mercury halted catalysis, suggesting a heterogeneous system in which the dehydrocoupling is

catalysed by rhodium nanoparticles.[81] Later EXAFS studies by Autrey and co-workers suggested that, instead, soluble $Rh_6$ clusters may be responsible for the dehydrocoupling activity in this system.[82] Interestingly, the catalytic dehydrocoupling of $H_3B{\cdot}PPh_2H$ with $[Rh(1,5\text{-cod})(\mu\text{-Cl})]_2$ to form $H_3B{\cdot}PPh_2BH_2{\cdot}PPh_2H$ was reported by Manners as a homogeneous process.[81]

Some heterogeneous systems are among the fastest reported dehydrocoupling catalysts. For example, the recently reported system $[Fe(NCMe)_2(PNNP)][BF_4]_2/KO^tBu$ [PNNP = $(PPh_2C_6H_4CH{=}NCH_2)_2$] by Morris and co-workers was highly active in the dehydrogenation of $H_3B{\cdot}NH_3$ with a turnover frequency (TOF) of approximately 2400 $h^{-1}$, yielding a mixture of products: borazine, polyborazylene, and B-N oligomers or partially cross-linked polyborazylene, as well as unreacted $H_3B{\cdot}NH_3$. The active species was proposed to be iron(0) nanoparticles stabilised by PNNP ligands.[83] Reasonable turnover frequencies (up to ~100 $h^{-1}$) have also been obtained with systems based upon ruthenium[84-86] and rhodium.[87]

Dehydropolymerisation of $H_3B{\cdot}NMeH_2$ by a skeletal nickel catalyst, produced from base-leaching a Ni/Al alloy, was reported by Manners and co-workers.[66] At a catalyst loading of 5 mol%, slow conversion (TOF ~0.2 $h^{-1}$) to form the cyclic triborazane $[H_2BNMeH]_3$ resulted. Interestingly, when using 100 mol% Ni, polyaminoborane $[H_2BNMeH]_n$ was formed ($M_n$ = 51 300 g $mol^{-1}$, PDI = 1.5), Scheme 1.10. These outcomes were attributed to initial dehydrogenation of $H_3B{\cdot}NMeH_2$ to form the monomer $H_2B{=}NMeH$, which is formed in higher concentrations with higher catalyst loadings, thus favouring polymerisation over cyclisation. Whether the polymerisation step is metal-mediated was not explored, although the recent report of $H_2B{=}NMeH$

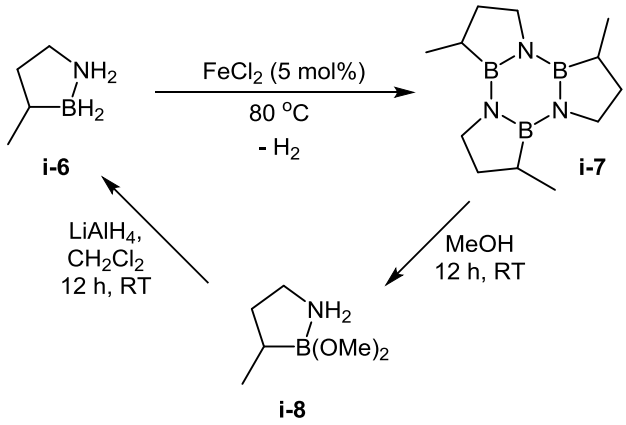
observation in non-metal catalysed $[H_2BNMeH]_n$ formation suggests the process could be off-metal.[67] $[H_2BNMeH]_n$ was also formed *via* the heterogeneous dehydrocoupling of $H_3B{\cdot}NMeH_2$ with $[CpFe(CO)_2]_2$ under photoirradiation after 3 hours ($M_n$ = 64 300 g $mol^{-1}$, PDI = 1.8). After 16 hours of irradiation, the borazine $[HBNMe]_3$ was the major product.[88] This work also illustrated that subtle changes in the ligand set can have significant effects upon whether the catalysis is homogeneous or heterogeneous; while $[CpFe(CO)_2]_2$ and $Cp_2Fe_2(CO)_3(NCMe)$ acted as heterogeneous catalysts, dehydrocoupling using CpFe(CO)I (under photoirradiation) was homogeneous.[89] The homogeneous mechanism is discussed in Section 1.5.12.




**Scheme 1.10** Dehydrocoupling of $H_3B{\cdot}NMeH_2$ with skeletal Ni.

An important result for the potential development of amine-boranes as hydrogen storage materials originated from Liu and co-workers using a heterogeneous system. The cyclic amine-borane BN-methylcyclopentane (**i-6**, Scheme 1.11), an air and moisture stable liquid at room temperature, released 2 equivalents of $H_2$ (4.7 wt%) at 80 °C to cleanly generate the trimer **i-7**, also a liquid, using 5 mol% loading of $FeCl_2$ as the catalyst in a neat solution of **i-6** (TOF 120 $h^{-1}$).[90] Significantly, **i-7** could be treated with MeOH, forming **i-8**, followed by $LiAlH_4$ to regenerate **i-6** in 92% yield. Although a more efficient regeneration method is desirable, these results illustrate the potential of this system as a hydrogen storage candidate, with the additional benefit of using cheap and abundant iron as the catalyst. The properties of **i-6** (*e.g.* viscosity, thermal

stability, purity) have been studied and the results suggest that **i-6** may be a viable liquid hydrogen storage carrier.[91] A related system was recently reported in which $MeH_2B{\cdot}NMeH_2$ is dehydrogenated by $CoCl_2$ (5 mol%, 80 °C, diglyme) to form the borazine product $[MeBNMe]_3$ in 71% yield. Subsequent treatment of $[MeBNMe]_3$ with HCOOH and then $LiAlH_4$ regenerated $MeH_2B{\cdot}NMeH_2$ in a 46% yield.[92]

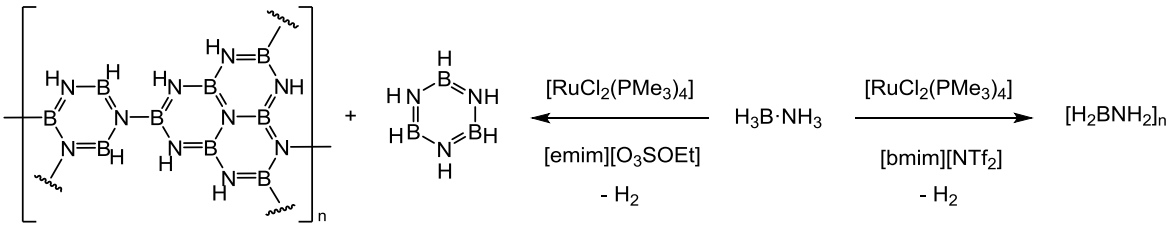



**Scheme 1.11** Dehydrogenation of **i-6** to yield **i-7**, and regeneration of **i-6** from **i-7**.

### 1.5.3 Transition metal catalysed dehydrocoupling of $H_3B{\cdot}NH_3$ promoted by ionic liquids

In 2006, Sneddon and co-workers noted that dissolving $H_3B{\cdot}NH_3$ in ionic liquids increased the rate and extent of thermal dehydrocoupling relative to that of solid $H_3B{\cdot}NH_3$.[93,94] In 2011, Baker and Sneddon sought to utilise this enhancement by combining transition metal catalysts with ionic liquid solvents. A range of transition metal catalysts were screened for the dehydrocoupling of $H_3B{\cdot}NH_3$ in the ionic liquid [bmim][Cl] (bmim = 1-butyl-3-methylimidazole),[95] all at 5 mol% loading, including $[Rh(1,5\text{-cod})(\mu\text{-Cl})]_2$, $Ru(1,5\text{-cod})Cl_2$, $RhCl_3$, $Ni(1,5\text{-cod})_2$ and $NiCl_2$. All showed enhanced dehydrocoupling activity at 65 °C compared with the analogous reaction in [bmim][Cl] in the absence of catalyst. However, increasing the temperature to 85 °C with the catalyst $[Rh(1,5\text{-cod})(\mu\text{-Cl})]_2$ led to lower total $H_2$ release than that in the

absence of catalyst. Different products were observed with changing the ionic liquid: catalysis with $[RuCl_2(PMe_3)_4]$ in $[emim][O_3SOEt]$ (emim = 1-ethyl-3-methylimidazole) resulted in borazine and polyborazylene, whereas the same reaction in $[bmim][NTf_2]$ resulted in $[H_2BNH_2]_n$ (Scheme 1.12).



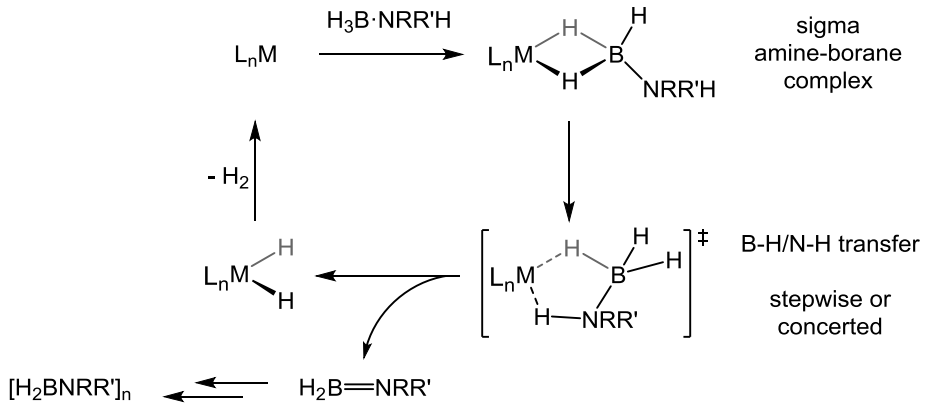

**Scheme 1.12** Different product distributions for the Ru-catalysed dehydrocoupling of $H_3B{\cdot}NH_3$ with different ionic liquids.

This selectivity was exploited by Baker in the dehydrocoupling of liquid fuel mixtures of $H_3B{\cdot}NH_3$ and *sec*-butylamine–borane, $H_3B{\cdot}N^sBuH_2$. Addition of $[RuCl_2(PMe_3)_4]$ (~1 mol%) to this neat mixture afforded $[HBN^sBu]_3$, $[HBNH]_3$, polyborazylene and insoluble $[H_2BNH_2]_n$. With $[emim][O_3SOEt]$ as co-solvent, no $[H_2BNH_2]_n$ was observed, making $H_3B{\cdot}N^sBuH_2/H_3B{\cdot}NH_3$ mixtures more appealing as potential liquid fuel cells.[96]

### 1.5.4 Homogeneous dehydrocoupling of amine-boranes

Although heterogeneous catalysts can produce high turnover frequencies, homogeneous systems have been more widely studied due to their well-defined coordination sites that can be tuned by modification of the metal and/or ligand. Homogeneous catalysts can operate *via* inner sphere or outer sphere mechanisms. Outer sphere mechanisms allow dehydrogenation of amine-boranes without the direct coordination to the metal centre, by using metal–ligand cooperativity (Section 1.5.13).[65,74,97-100] By contrast, inner sphere mechanisms involve initial coordination of

the amine-borane to the metal forming a sigma complex (Section 1.5.5), followed by dehydrogenation of the amine-borane (Scheme 1.13). Various mechanistic scenarios have been implicated for the mechanism of dehydrogenation and will be discussed in detail later in this Chapter.




**Scheme 1.13** Simplified pathway for inner-sphere dehydrogenation.

### 1.5.5 Sigma complexes of amine-boranes

Inner sphere mechanisms for the dehydrocoupling of amine-boranes often invoke coordination of an amine-borane to the metal *via* 3-centre-2-electron M-H-B interactions,[101] forming a sigma complex, [$L_nM$-$H_3B{\cdot}NR_3$]. These weak interactions arise primarily from donation from the σ B—H orbital to the metal; the B—H σ* orbital is high in energy, meaning that back-donation from the metal is negligible.[102,103] Often, sigma complexes are isolated using tertiary amine-boranes, *e.g.* $H_3B{\cdot}NMe_3$, as the lack of N—H bonds generally prevents further reactivity by N—H transfer. The first example of a simple amine-borane coordinated to a metal was reported by Shimoi and co-workers in 1999, in which [$M(CO)_5(\eta^1$-$H_3B{\cdot}NMe_3)$] (M = Cr, Mo, W) was formed through photolysis of [$M(CO)_6$] in the presence of $H_3B{\cdot}NMe_3$.[103] This 'end-on' $\eta^1$ binding of the amine-borane occurs through one B—H

bond, but the complexes are fluxional on the NMR timescale, showing rapid exchange between bridging and terminal H atoms. Various other $\eta^1$ sigma complexes of amine-boranes have since been reported (Figure 1.6a).[103-105] Amine-boranes can also bind to the metal centre through two B—H sigma bonds, resulting in $\eta^2$ complexes (Figure 1.6b).[12,17,64] Oligomeric species such as $H_3B{\cdot}NMe_2BH_2{\cdot}NMe_2H$ have also been observed to bind in this manner.[14,75,106]

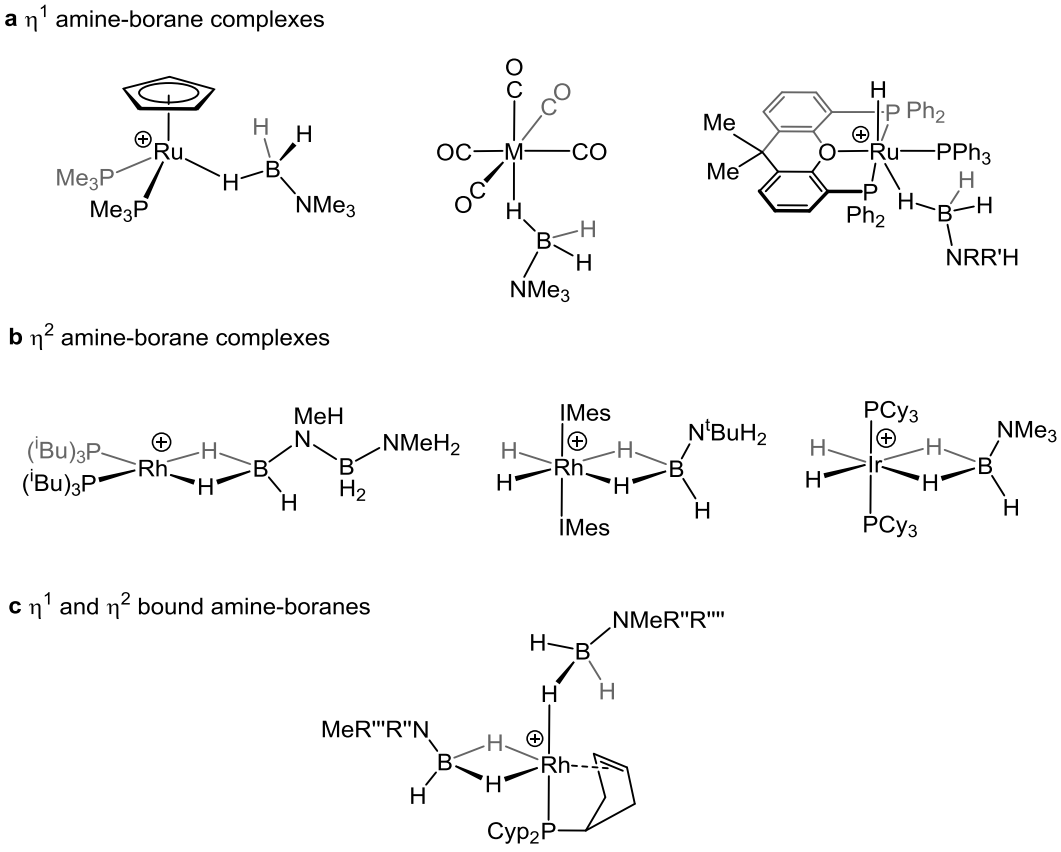



**Figure 1.6** $[BAr^F_4]^-$ anions not shown. **(a)** Selected examples of $\eta^1$ sigma amine-borane complexes. M = Cr, Mo or W. NRR'H = $N^tBuH_2$, $NMe_2H$ or $NH_3$. **(b)** Examples of $\eta^2$ sigma amine-borane complexes. IMes = *N*,*N*′-*bis*(2,4,6-trimethylphenyl)imidazol-2-ylidene, n = 1 – 3. **(c)** $\eta^1$ and $\eta^2$ bound amine-boranes. R'' = Me, H. R''' = Me, H.

Multiple amine-borane moieties bound to a metal centre have also been observed, and this is similar to intermediates often invoked in dimerisation and polymerisation mechanisms.[52,107,108] For example, $[Rh\{P(C_5H_9)_2(\eta^2\text{-}C_5H_7)\}(\eta^2\text{-}H_3B{\cdot}NMeRR')(\eta^1\text{-}$

$H_3B{\cdot}NMeRR')][BAr^F{}_4]$ (R, R' = Me, H), has two amine-boranes bound to the rhodium centre with $\eta^1$ and $\eta^2$ coordination (Figure 1.6c).[109]

### 1.5.6 Comparison with H—H and C—H sigma complexes

Since Kubas' seminal discovery of the dihydrogen complex $W(CO)_3(P^iPr_3)_2(\eta^2\text{-}H_2)$ (Figure 1.7),[110] many $\sigma\text{-}H_2$ complexes have been reported.[111,112] $H_2$ binds to the metal through synergic σ coordination to the metal and back donation from the metal to the σ* orbital of dihydrogen. As a result, 'side-on' binding is observed. If the extent of back donation is too great, oxidative cleavage occurs to form a dihydride complex.[21] By contrast, the sigma binding of amine-boranes is 'end on' due to the high energy B—H σ* orbital for amine-boranes, hydridic nature of the B—H bond, and steric factors.[102]

The polarity of B—H bonds *vs* C—H bonds also accounts for relative rarity of sigma complexes of alkanes compared with their isoelectronic amine-borane counterparts. Until relatively recently, direct observation of sigma alkane complexes was limited to infrared or NMR spectroscopy, often at low temperatures.[113-115] In 2012, Weller and Macgregor published the first crystallographically characterised true alkane complex, $[Rh(^iBu_2PCH_2CH_2P^iBu_2)(\eta^2\eta^2\text{–}C_7H_{12})][BAr^F{}_4]$ (Figure 1.7), formed by solid state hydrogenation of the norbornadiene precursor $[Rh(^iBu_2PCH_2CH_2P^iBu_2)(\eta^2\eta^2\text{–}C_7H_8)][BAr^F{}_4]$. The solid state structure showed predominantly 'end on' coordination of the alkane through two C—H bonds.[116]

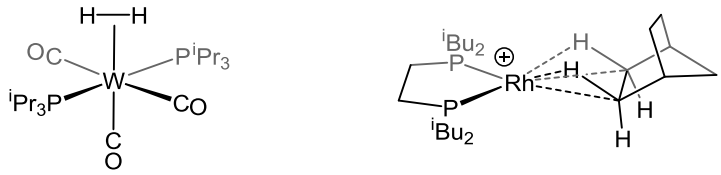



**Figure 1.7** Kubas' dihydrogen complex and Weller's alkane complex. $[BAr^F{}_4]^-$ anion not shown.

### 1.5.7 Sigma complexes of aminoboranes

Sigma complexes of aminoboranes have also been isolated, where donation from the B—H bonds into a vacant metal orbital is reinforced by π back-donation from the metal into the π* B-N orbital of the aminoborane.[117] Various examples have been characterised with rhodium,[14,16,117,118] iridium[62,64,117,119] and ruthenium,[68,117,120,121] and both $\eta^1$ and $\eta^2$ coordination modes have been observed.[122] A selection of aminoborane complexes are presented in Figure 1.8. Sabo-Etienne and Alcaraz have recently reported an unusual aminoborane complex exhibiting adjacent agostic B—H and C—H interactions (Figure 1.9).[123] Aminoboranes bound to the metal centre have been implicated in dehydrocoupling mechanisms, although often not observed directly.[52,124,125] Aminoborane complexes are closely related to transition metal complexes of three–coordinate boranes, *e.g.* $H_2BR$ or $HBR_2$, in which the vacant boron p orbital receives π-back donation from the metal.[126]

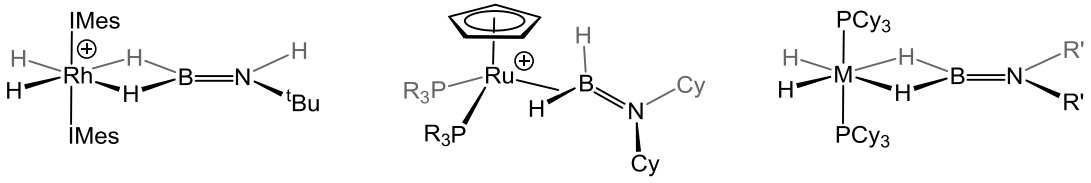



**Figure 1.8** Selected aminoborane complexes. $(PR_3)_2$ = $(Ph_3P)_2$ or $(Cy_2PCH_2CH_2PCy_2)$. M = Ru, R' = $^i$Pr, Me, H; M = $Rh^+$ or $Ir^+$, R' = $^i$Pr, Me. $[BAr^F{}_4]^-$ anions not shown.

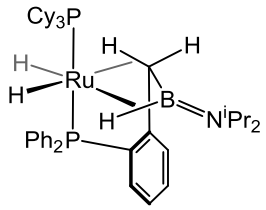



**Figure 1.9** Sabo-Etienne and Alcaraz's *bis*(agostic) phosphinobenzyl-(amino)borane ruthenium complex.

### 1.5.8 Boryl complexes

B—H activation of amine-boranes or aminoboranes at the metal centre results in the formation of base-stabilised boryl complexes. While boryl complexes resulting from the B—H activation of boranes (*e.g.* HBCat) are relatively common,[127] fewer examples of base-stabilised boryl complexes derived from the B—H activation of four coordinate base-stabilised boranes are known.[128] In 2010, Weller and co-workers reported a bimetallic species with two $\{Rh(PR_3)\}^+$ (R = $^i$Pr, Cy) fragments bridged by three $H_3B{\cdot}NMe_3$ ligands, two of which have undergone B—H activation to form base-stabilised boryls (Figure 1.10).[129] Aldridge and co-workers have isolated boryl complexes deriving from the B—H activation of aminoboranes (Figure 1.10).[119,130] Aldridge's complex $Ir(PMe_3)_3(H)Cl\{B(H)NR_2\}$ (R = $^i$Pr, Cy) underwent further B—H activation in the presence of $Na[BAr^F{}_4]$ to form the borylene dihydride complex [*fac*-$Ir(PMe_3)_3(H)_2(BNR_2)][BAr^F{}_4]$.[130]

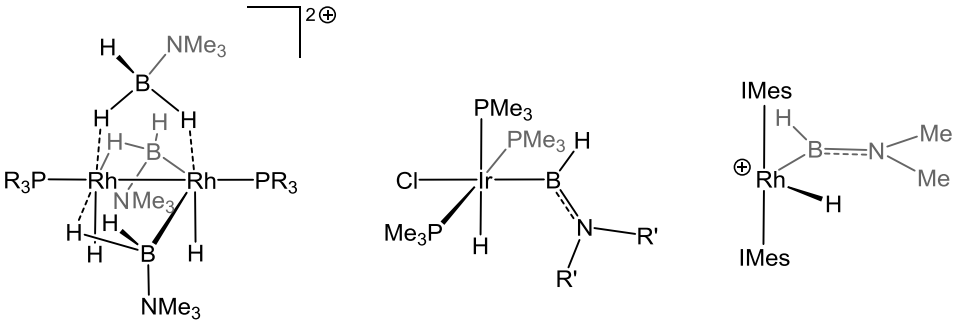
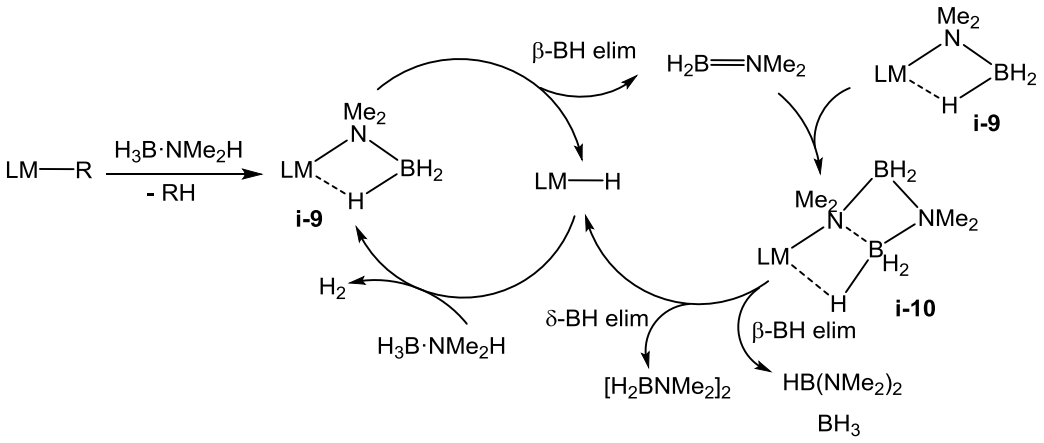


**Figure 1.10** Examples of boryl complexes. $[BAr^F_4]^-$ anions not shown. R = $^i$Pr, Cy. R' = $^i$Pr, Cy.

### 1.5.9 Main group catalysed dehydrocoupling of amine-boranes

Although most of the mechanistic studies on the dehydrocoupling of amine-boranes involve transition metals, main group catalysts have been reported based upon Al,[131,132] Mg,[133-135] Ca,[133,134,136] Y,[137] Sc,[137] La[138] and Sn.[139] These generally show much lower turnovers than the best transition metal catalysts, although a noteworthy exception is the yttrium complex $(C_5H_5BMe)_2YCH(SiMe_3)_2$, which dehydrocoupled $H_3B{\cdot}NMe_2H$ to form $[H_2BNMe_2]_2$ with an impressive TOF of 1015 $h^{-1}$.[140] Hill has proposed a mechanism (Scheme 1.14) for the group II catalysed dehydrocoupling of $H_3B{\cdot}NMe_2H$ to form $[H_2BNMe_2]_2$ using alkyl Mg and Ca precursors. During the dehydrocoupling, $H_2B{=}NMe_2$ and $HB(NMe_2)_2$ were observed, as well as the $[H_3BNMe_2BH_2NMe_2]^-$ anion bound to the metal. Stoichiometric reactions enabled the isolation of amidoborane complexes. These observations led to the mechanism proposed in Scheme 1.14, in which the metal remains in a constant oxidation state. Initial N—H activation (and concomitant protonation of the ligand) forms an amidoborane complex, **i-9**. This can undergo β-B—H elimination to form $H_2B{=}NMe_2$, which inserts into **i-9** to form the observed $LM[H_3BNMe_2BH_2NMe_2]$ (**i-10**) species. From here, either β-B—H elimination yields the observed $HB(NMe_2)_2$, or δ-B—H elimination forms $[H_2BNMe_2]_2$.

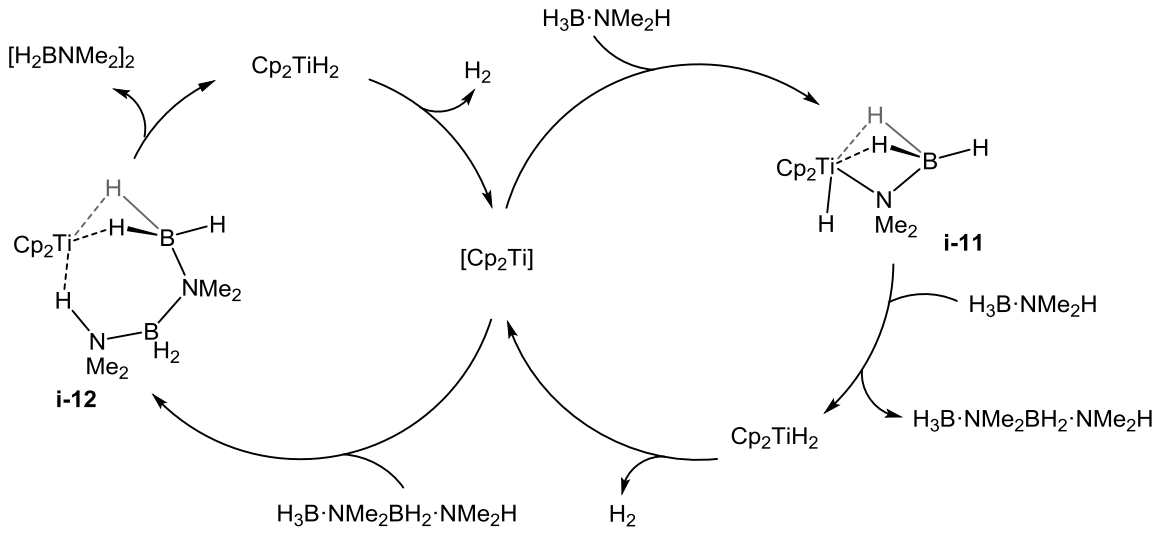



**Scheme 1.14** Proposed mechanism for the dehydrocoupling of $H_3B{\cdot}NMe_2H$ by Hill's group II catalysts.

### 1.5.10 Early transition metal catalysed dehydrocoupling of amine-boranes

In 2006, Manners demonstrated the first well–defined homogeneous catalytic dehydrocoupling of $H_3B{\cdot}NMe_2H$ to form $[H_2BNMe_2]_2$ by using the $[Cp_2Ti]$ fragment, generated *in situ* from $Cp_2TiCl_2/^nBuLi$.[141] After this initial report, calculations by Ohno and Luo suggested a stepwise mechanism for dehydrocoupling in which N—H bond activation is followed by B—H activation to form $H_2B{=}NMe_2$, which dimerises off-metal.[142] A more detailed kinetic mechanistic study by Manners, Lloyd-Jones and co-workers on the $[Cp_2Ti]$ system contradicted this mechanism. Significantly, the linear diborazane $H_3B{\cdot}NMe_2BH_2{\cdot}NMe_2H$ was identified as an intermediate in the dehydrocoupling reaction (2 mol% $[Cp_2Ti]$, TOF = 12.5 $h^{-1}$).[108] The proposed mechanism (Scheme 1.15) involves two cycles. Initial coordination of $H_3B{\cdot}NMe_2H$ to $[Cp_2Ti]$ to form $[Cp_2Ti(\eta^2\text{-}H_3B{\cdot}NMe_2H)]$ is followed by N—H activation of the protic hydrogen with the $Ti^{II}$ centre to yield the amidoborane $[Cp_2Ti(H)(NMe_2{\cdot}BH_3)]$, **i-11**. A second equivalent of $H_3B{\cdot}NMe_2H$ reacts with **i-11** resulting in B—N formation to give $Cp_2TiH_2$ with loss of $H_3B{\cdot}NMe_2BH_2{\cdot}NMe_2H$. The second cycle invokes reaction of $H_3B{\cdot}NMe_2BH_2{\cdot}NMe_2H$ with $[Cp_2Ti]$ to form **i-12**, which undergoes on-metal

dehydrocyclisation to form $[H_2BNMe_2]_2$ and $Cp_2TiH_2$. The proposed scheme is consistent with experimental and kinetic observations, in particular that reaction of independently prepared $H_3B{\cdot}NMe_2BH_2{\cdot}NMe_2H$ with $[Cp_2Ti]$ resulted in complete consumption of $H_3B{\cdot}NMe_2BH_2{\cdot}NMe_2H$ to form $[H_2BNMe_2]_2$, with only negligible amounts of $H_2B{=}NMe_2$ observed. This implies that $H_3B{\cdot}NMe_2BH_2{\cdot}NMe_2H$ is the sole intermediate in the formation of $[H_2BNMe_2]_2$ in this case, contrary to Luo and Ohno's mechanism. Interestingly, the same system was unreactive towards $H_3B{\cdot}NMeH_2$ (20 °C) and $H_3B{\cdot}PPh_2H$ (up to 40 °C). Zirconium analogues of amidoborane complexes such as **i-11** have been reported by Roesler and co–workers.[143]




**Scheme 1.15** Mechanism proposed by Manners and Lloyd-Jones for the dehydrocoupling of $H_3B{\cdot}NMe_2H$.

More recent work has found that paramagnetic $Ti^{III}$ species may play a significant role in the $[Cp_2Ti]$ system. Following the report of the isolation of the $Ti^{III}$ complex $[Cp_2Ti(NH_2{\cdot}BH_3)]$ by McGrady,[144] the analogous complexes $[Cp_2Ti(NMe_2{\cdot}BH_3)]$ (**i-13**) and $[Cp_2Ti(PPh_2{\cdot}BH_3)]$ (**i-14**) (Figure 1.11) were synthesised and employed as catalysts under the same conditions as with the titanocene fragment (2 mol%,

toluene).[145] **i-13** and **i-14** were shown to be effective catalysts, promoting 83% and 97% consumption of $H_3B{\cdot}NMe_2H$ after 2 hours, respectively. Similar to $[Cp_2Ti]$, both reaction profiles showed $H_3B{\cdot}NMe_2BH_2{\cdot}NMe_2H$ as an intermediate, followed by formation of $[H_2BNMe_2]_2$, with **i-13** showing comparable activity to $[Cp_2Ti]$ (TOF of 10.7 $h^{-1}$ for **i-13**, *cf.* 12.5 $h^{-1}$ for $[Cp_2Ti]$). Analysis by UV/Vis and EPR spectroscopies of reaction solutions using $[Cp_2Ti]$ and **i-13** as precatalysts resulted in spectra comparable with those of isolated **i-13**. These results imply that the $Ti^{III}$ complex **i-13** may be of importance in the catalytic dehydrocoupling by titanocene, in contrast to the $Ti^{II}/Ti^{IV}$ cycle depicted in Scheme 1.15. Rosenthal and co-workers used the alkyne complex $[Cp_2Ti(\eta^2\text{-}Me_3SiCCSiMe_3)]$ as a source of $[Cp_2Ti]$, which gave turnover frequencies of 3 $h^{-1}$ for the dehydrocoupling of $H_3B{\cdot}NMe_2H$.[146] The closely related precatalyst $[(\eta^5\text{-}C_5H_4{}^iPr)_2Ti(\eta^2\text{-}Me_3SiCCSiMe_3)]$ was explored shortly afterwards and showed improved dehydrocoupling activity (TOF = 32 $h^{-1}$ at 40 °C, 6 $h^{-1}$ at 24 °C).[147] The Cp* analogue, however, showed no dehydrocoupling activity, highlighting the importance of sterics in designing systems for dehydrocoupling with early transition metals.[146]

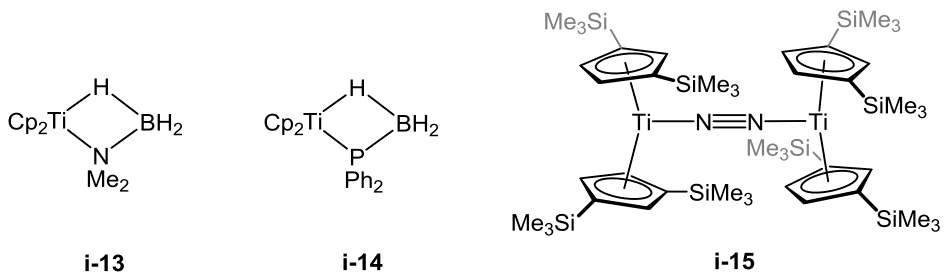
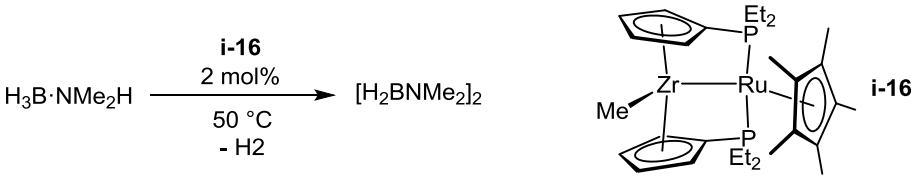



**Figure 1.11** $Ti^{III}$ complexes **i-13**, **i-14** and **i-15**.

The group IV systems with the fastest reported turnovers include Chirik's $Ti^{II}$ complex **i-15** (Figure 1.11), which dehydrocoupled $H_3B{\cdot}NMe_2H$ with a TOF of

420 $h^{-1}$.[148] Based on kinetic and isotopic labelling experiments, a mechanism was proposed that involved reversible B—H oxidative addition followed by β-H elimination of $H_2B{=}NMe_2$. A rapid $Zr^{IV}$ catalyst based on a frustrated Lewis pair (TOF ~600 $h^{-1}$) published by Wass is discussed further in Section 1.5.13.

Nishibayashi and co-workers reported the heterobimetallic group IV/VIII complex [ZrMe(μ-$\eta^5$:$\eta^1$-$C_5H_4PEt_2$)$_2$RuCp*], **i-16**, and showed that it was a slow catalyst for the dehydrocoupling of $H_3B{\cdot}NMe_2H$ to form $[H_2BNMe_2]_2$ (2 mol% **i-16**, TOF ~8 $h^{-1}$, 50 °C) (Scheme 1.16).[149] The system was less active for the dehydrocoupling of $H_3B{\cdot}NMeH_2$ and $H_3B{\cdot}NH_3$, reaching 92% and 56% completion, respectively, after 24 hours (10 mol% **i-16** at 50 °C) to form B-N oligomeric materials. Accordingly, mechanistic studies were conducted with $H_3B{\cdot}NMe_2H$, which suggested N—H activation by the Zr centre and B—H activation by the Ru centre are key in releasing $H_2B{=}NMe_2$.

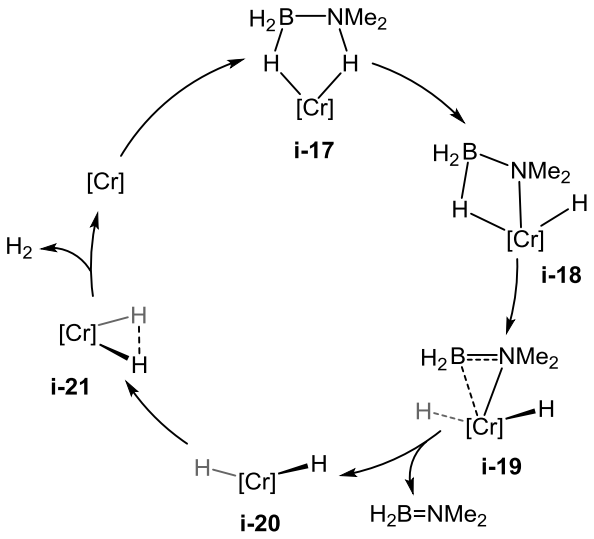



**Scheme 1.16** Dehydrocoupling of $H_3B{\cdot}NMe_2H$ using **i-16**.

This system highlights that the cooperative effect of two metals in close proximity could be of potential use in designing future catalysts, although the activity of **i-16** is only moderate compared with some other homogeneous systems.[12,65,100,124] Rousseau has also explored multimetallic dehydrocoupling of $H_3B{\cdot}NMe_2H$ with $Rh_4$ clusters.[150]

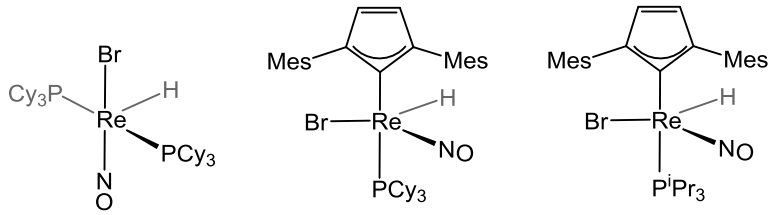
### 1.5.11 Mid transition metal catalysed dehydrocoupling of amine-boranes

Shimoi and co-workers have shown that photoactivated $[M(CO)_6]$ (M = Cr, Mo, W) act as dehydrocoupling catalysts yielding $[H_2BNMe_2]_2$ from $H_3B{\cdot}NMe_2H$ (TOF 19 $h^{-1}$ when M = Cr), and a mixture of $[HBNMe]_3$ and $[H_2BNMeH]_n$ from $H_3B{\cdot}NMeH_2$.[151] The mechanism of dehydrocoupling $H_3B{\cdot}NMe_2H$ with $[Cr(CO)_6]$ was investigated by DFT calculations, and suggested that the active species is the 14–electron $[Cr(CO)_4]$ fragment, which can coordinate $H_3B{\cdot}NMe_2H$ to form the sigma complex **i-17** (Scheme 1.17). From this, N—H activation to form an amidoborane complex (**i-18**) precedes B—H activation to release $H_2B{=}NMe_2$ from **i-19**. $[Cr(CO)_4]$ is regenerated by $H_2$ loss from $[Cr(CO)_4(H)_2]$ (**i-20**) (Scheme 1.17). Interestingly, although the sigma complex $[Cr(CO)_5(\eta^1\text{-}H_3B{\cdot}NMe_2H)]$ was observed in the reaction mixture it was calculated to sit outside the cycle, acting simply as a source of $[Cr(CO)_4]$.



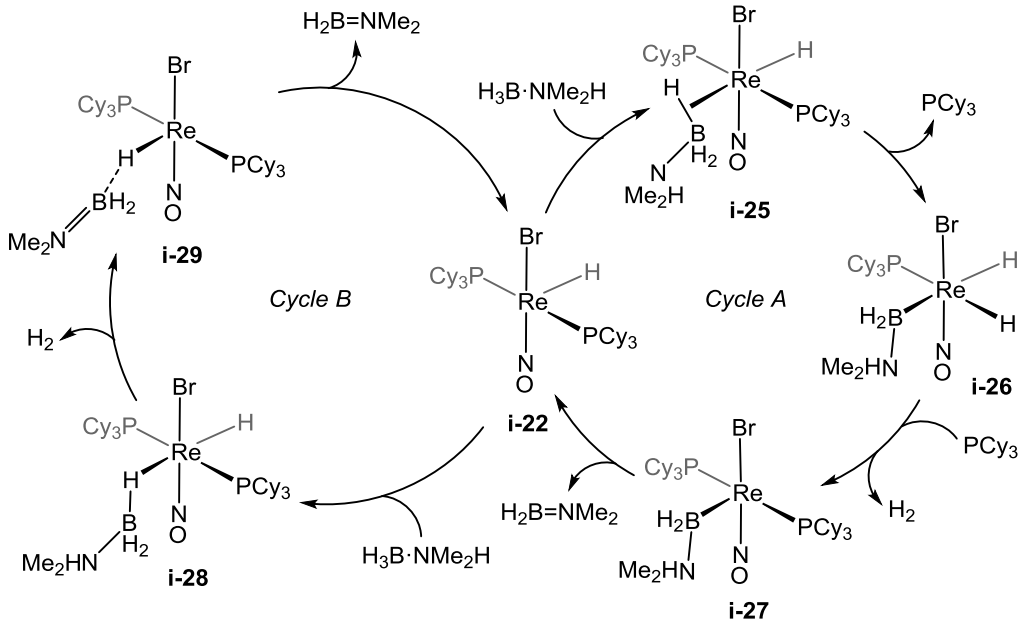

**Scheme 1.17** Shimoi's proposed mechanism for the dehydrocoupling of $H_3B{\cdot}NMe_2H$. [Cr] = $[Cr(CO)_4]$.

In 2009, Berke and co-workers explored a range of nitrosyl rhenium catalysts for the dehydrocoupling of $H_3B{\cdot}NMe_2H$ to form $[H_2BNMe_2]_2$.[125] The most active catalysts were **i-22**, **i-23** and **i-24** (Figure 1.12), showing turnover frequencies of 77, 100 and 92 $h^{-1}$, respectively. All three catalysts were also active for the transfer hydrogenation of *n*-octene using $H_3B{\cdot}NMe_2H$ as the hydrogen source. Two possible mechanisms for the dehydrocoupling reaction using **i-22** were suggested (Scheme 1.18). Cycle A involves coordination of $H_3B{\cdot}NMe_2H$ to the vacant coordination site in **i-22**, forming the sigma complex **i-25**. Loss of a $PCy_3$ ligand reveals a vacant coordination site, allowing B—H activation to form the base–stabilized boryl species **i-26**. Reductive elimination of $H_2$ forms **i-27**, from which a N—H proton transfer to the metal yields free $H_2B{=}NMe_2$ and reforms **i-22**. An alternative pathway (Cycle B) involves the formation of the sigma compound **i-28**, followed by N—H protonation of Re—H to form **i-29** and $H_2$. B—H cleavage then forms $H_2B{=}NMe_2$ and **i-22**. During catalysis, a dihydrogen complex $[ReBr(PCy_3)_2(H)(H_2)(NO)]$ was the observed resting state in the presence of hydrogen, being in equilibrium with the active species **i-22**.




**i-22** **i-23** **i-24**

**Figure 1.12** Rhenium catalysts for the dehydrocoupling of $H_3B{\cdot}NMe_2H$.




**Scheme 1.18** Suggested mechanisms for dehydrocoupling of $H_3B{\cdot}NMe_2H$ using **i-22**.

### 1.5.12 Late transition metal catalysed dehydrocoupling of amine-boranes

Despite early reports by Manners that some Rh systems were operating as heterogeneous catalysts (see Section 1.5.2), many late metal systems appear to be homogeneous in nature and have been studied mechanistically.[59,70] In 2006, Heinekey and Goldberg used Brookhart's catalyst Ir($^t$BuPOCOP$^t$Bu) catalyst (**i-30**, Figure 1.13) to efficiently dehydrocouple $H_3B{\cdot}NH_3$ to form the purported cyclic pentamer $[H_2BNH_2]_5$ ,[71] although this product was later reassigned by Manners and co-workers as $[H_2BNH_2]_n$ (n ~20).[20] At 1 mol% of **i-30**, an impressive TOF of 1500 $h^{-1}$ was recorded. At long reaction times a dormant new species was formed, assigned as the sigma–borane complex Ir($^t$BuPOCOP$^t$Bu)$H_2(BH_3)$ **i-31** (Figure 1.13),[152] which can be regenerated to form a catalytically active species on addition of $H_2$ . Related sigma complexes of **i-30** bound to pinacolborane and 9-BBN (9-borabicyclo[3.3.1]nonane) have also been reported. Hydrogen release experiments for the dehydrocoupling of $H_3B{\cdot}NH_3$ and $H_3B{\cdot}NMeH_2$ showed a first order dependence on [amine-borane] and

[**i-30**].[153] Interestingly, for this system, dehydrocoupling of $H_3B{\cdot}NMe_2H$ is sluggish at best. Calculations suggested a concerted process for B–H/N–H activation at the Ir centre.[154]

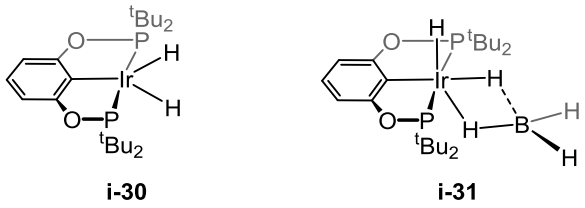
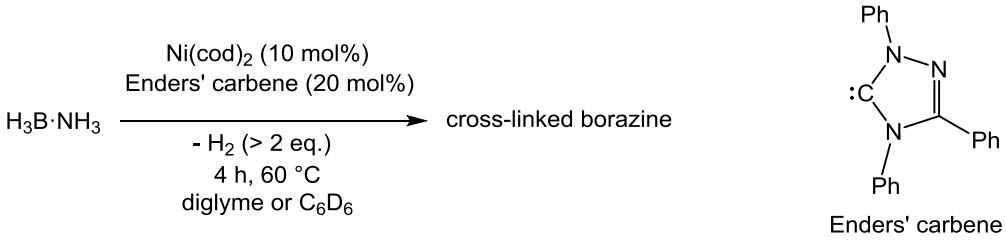


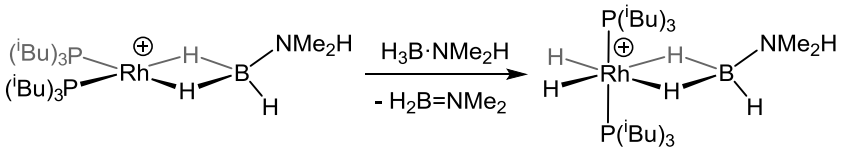

**Figure 1.13** The structures of complexes **i-30** and **i-31.**

In 2007, Baker reported that $Ni(NHC)_2$ systems were active catalysts for the dehydrogenation of ammonia–borane.[155] Enders' carbene (1,3,4-triphenyl-4,5-dihydro-1H-1,2,4-triazol-5-ylidene) resulted in the most active catalyst trialled (Scheme 1.19). First order consumption of $H_3B{\cdot}NH_3$ was observed, and kinetic isotope experiments indicated that both B—H and N—H bonds were being broken in the rate determining step(s). Computational studies were conducted on this system and revealed ligand cooperativity and free carbene are involved in the dehydrocoupling mechanism.[156-160]




**Scheme 1.19** Dehydrocoupling of $H_3B{\cdot}NH_3$ with $Ni(cod)_2$ and Enders' carbene.

In 2009, Weller and Hall conducted a detailed experimental and computational study on the dehydrocoupling of $H_3B{\cdot}NMe_2H$ by the latent low-coordinate complex $[Rh(P^iBu_3)_2][BAr^F{}_4]$[13] (5 mol%, TOF = 34 $h^{-1}$) to afford $[H_2BNMe_2]_2$.[14] $H_3B{\cdot}NMe_2BH_2{\cdot}NMe_2H$ was observed as an intermediate in catalysis, alongside small amounts of $H_2B{=}NMe_2$. Coordination of $H_3B{\cdot}NMe_2H$ to $[Rh(P^iBu_3)_2][BAr^F{}_4]$ forms the sigma complex $[Rh(P^iBu_3)_2(\eta^2\text{-}H_3B{\cdot}NMe_2H)][BAr^F{}_4]$ (**i-32**). This is short-lived in the presence of excess $H_3B{\cdot}NMe_2H$, rapidly forming $[Rh(P^iBu_3)_2(H)_2(\eta^2\text{-}H_3B{\cdot}NMe_2H)][BAr^F{}_4]$ (**i-33**, Scheme 19). A complex pathway was calculated for the lowest energy dehydrogenation of **i-32**. Either initial B—H activation and N—H transfer or initial N—H activation and B—H transfer occurs to form the $[Rh(P^iBu_3)_2(H)_2]^+$ fragment, *via* a $Rh^I$ dihydrogen intermediate, with concomitant loss of $H_2B{=}NMe_2$ (forming $[H_2BNMe_2]_2$). The $[Rh(P^iBu_3)_2(H)_2]^+$ fragment coordinates $H_3B{\cdot}NMe_2H$ to form **i-33**. A constant oxidation state $Rh^{III}$ cycle was also proposed, although this was a higher barrier process.

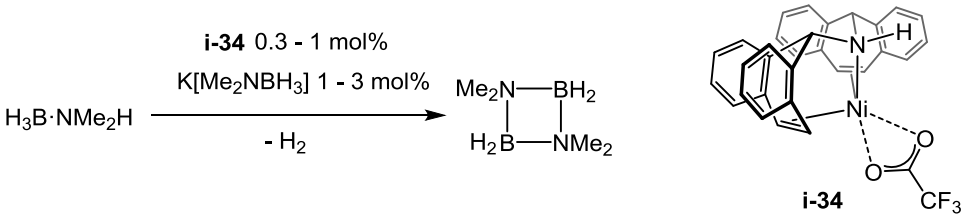



**i-32** **i-33**

**Scheme 1.20** Initial dehydrogenation of **i-32**. $[BAr^F{}_4]^-$ anions not shown.

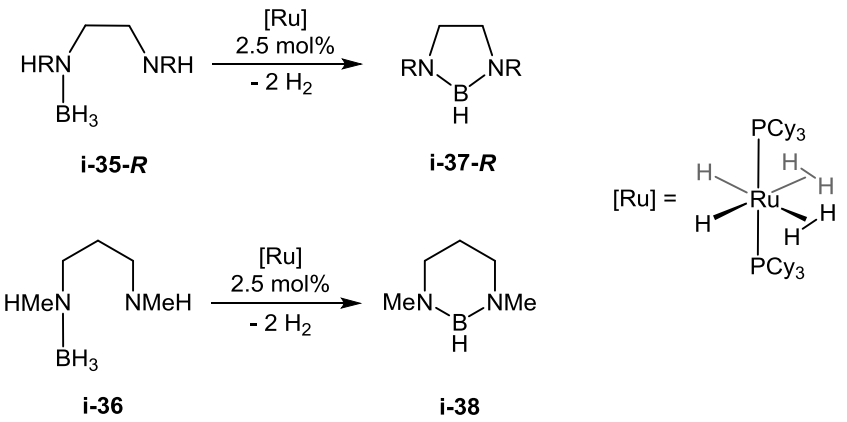
One of the fastest dehydrocoupling catalysts that has been reported is the $Ni^I$ species $[Ni(trop_2NH)(OOCCF_3)]$ ($trop_2NH$ = bistropylidenylamine) (**i-34**, Scheme 1.21).[161] At 0.3 mol% of **i-34**, one equivalent of hydrogen was released from a solution of $H_3B{\cdot}NMe_2H$ in less than 1 minute (TOF ~20 000 $h^{-1}$) to form $[H_2BNMe_2]_2$. Interestingly the amidoborane $K[NMe_2BH_3]$ is used as co-catalyst (1 – 3 mol%). Its

role was not commented upon, but hints that the active species may be a Ni–amidoborane complex. During dehydrocoupling, the aminoborane $H_2B{=}NMe_2$ was observed as an intermediate, although further mechanistic details were not reported.



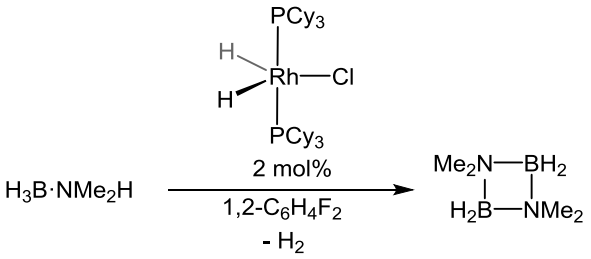

**Scheme 1.21** Dehydrocoupling of $H_3B{\cdot}NMe_2H$ with **i-34.**

Alcaraz and Sabo-Etienne reported the novel dehydrogenative cyclisation of the diamine-monoboranes **i-35-*Me***, **i-35-*$^i$Pr*** and **i-36** leading to cyclic diaminoboranes **i-37-*Me***, **i-37-*$^i$Pr*** and **i-38**, respectively, using the $[Ru(PCy_3)_2(H)_2(\eta^2\text{-}H_2)_2]$ catalyst at 2.5 mol% loading (Scheme 1.22).[162] The reaction was slower in the presence of bulkier N-substituents (3 hours for complete formation of **i-37-*Me*** *vs* 8 hours for complete formation of **i-37-*$^i$Pr***), but lengthening the alkyl chain length of the starting amine-borane (**i-35-*Me*** *vs* **i-36**) did not significantly affect the rate. $[Ru(PCy_3)_2(H)_2(\eta^2\text{-}H_2)_2]$ remained the resting state throughout catalysis, and could be reused twice.




**Scheme 1.22** Dehydrocyclisation of amine-boranes using $[Ru(PCy_3)_2(H)_2(\eta^2\text{-}H_2)_2]$. R = Me, $^i$Pr.

In 2013, Weller explored the mechanism of the dehydrocoupling of $H_3B{\cdot}NMe_2H$ with the neutral rhodium catalyst $Rh(PCy_3)_2(H)_2Cl$ after its catalytic activity had been implicated in an earlier study with $[Rh(PCy_3)_2][BAr^F{}_4]$ (see Section 1.5.15).[15,16] Investigations showed that $Rh(PCy_3)_2(H)_2Cl$ is a moderate catalyst for dehydrogenation of $H_3B{\cdot}NMe_2H$ (2 mol% [Rh], TOF = 28 $h^{-1}$) to form $H_2B{=}NMe_2$, which dimerises to form $[H_2BNMe_2]_2$ (Scheme 1.23).[15]

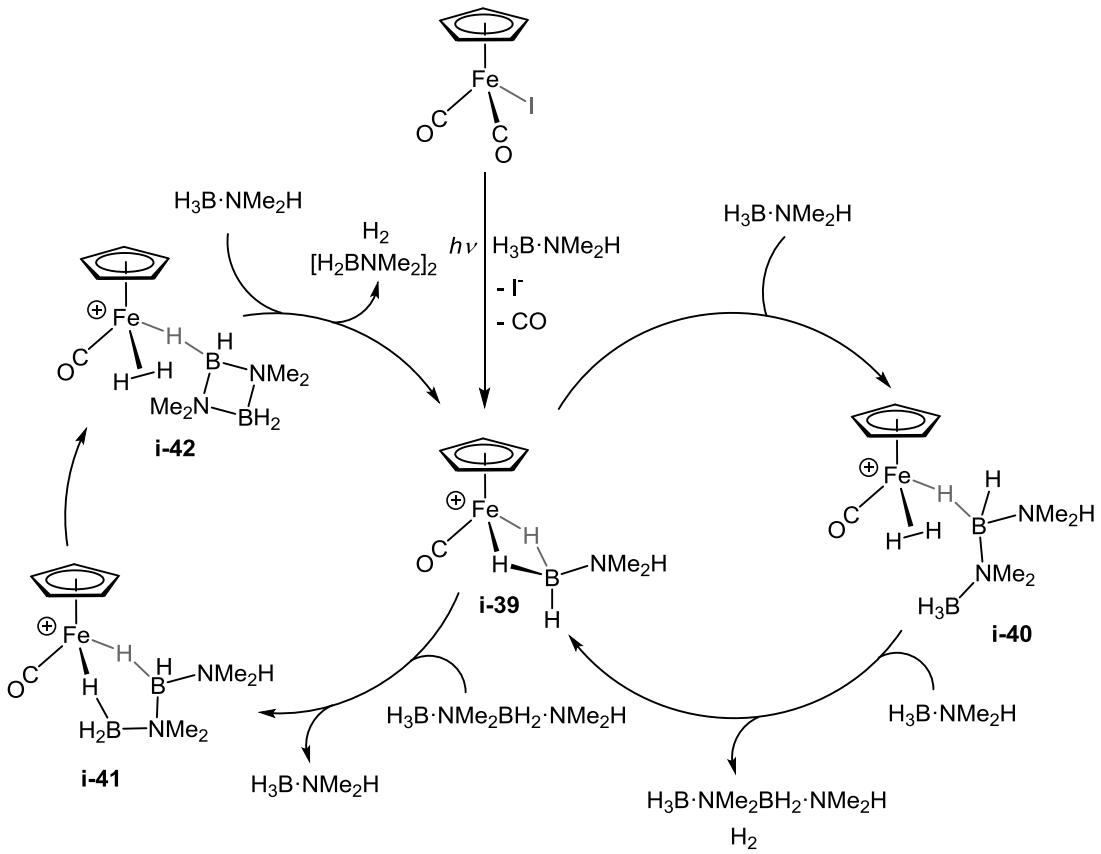



**Scheme 1.23** Dehydrocoupling of $H_3B{\cdot}NMe_2H$ with $Rh(PCy_3)_2(H)_2Cl$.

Mechanistic investigations indicated that N—H activation (either preceding or following B—H activation) is turnover-limiting in this system, indicated by a large primary kinetic isotope effect observed using $H_3B{\cdot}NMe_2D$. Kinetic analyses also

showed that the active catalyst, $Rh(PCy_3)_2(H)_2Cl$, is in an equilibrium with an off-cycle dimer, $[Rh(PCy_3)_2(H)_2Cl]_2$.

As introduced in Section 1.5.2, Manners and co-workers recently found that $[CpFe(CO)_2I]$, under conditions of photoirradiation, acts as a homogeneous catalyst in the dehydrocoupling of $H_3B{\cdot}NMe_2H$ to form $[H_2BNMe_2]_2$.[89] A two-stage mechanism was proposed for this system to account for the formation of $H_3B{\cdot}NMe_2BH_2{\cdot}NMe_2H$ and the on-metal dehydrocyclisation to yield $[H_2BNMe_2]_2$ (Scheme 1.24), similar to that invoked for $Cp_2Ti$ systems.[108] Experimental evidence and DFT calculations support initial coordination of $H_3B{\cdot}NMe_2H$ to the photogenerated $[FeCp(CO)]^+$ fragment, forming the sigma complex **i-39**. Addition of a second equivalent of $H_3B{\cdot}NMe_2H$ results in a B—N bond formation process to yield the bound $H_3B{\cdot}NMe_2BH_2{\cdot}NMe_2H$ complex **i-40**. $H_3B{\cdot}NMe_2BH_2{\cdot}NMe_2H$ and dihydrogen are displaced by $H_3B{\cdot}NMe_2H$ to reform **i-39**. The second cycle proposes that the just formed $H_3B{\cdot}NMe_2BH_2{\cdot}NMe_2H$ displaces $H_3B{\cdot}NMe_2H$ in **i-39** to form the chelate sigma complex **i-41**, similar to related isolated Rh complexes.[75] Subsequent on-metal dehydrocyclisation occurs to form $[H_2BNMe_2]_2$ sigma bound to the metal (**i-42**). $[H_2BNMe_2]_2$ and dihydrogen are displaced by $H_3B{\cdot}NMe_2H$, reforming **i-39**.



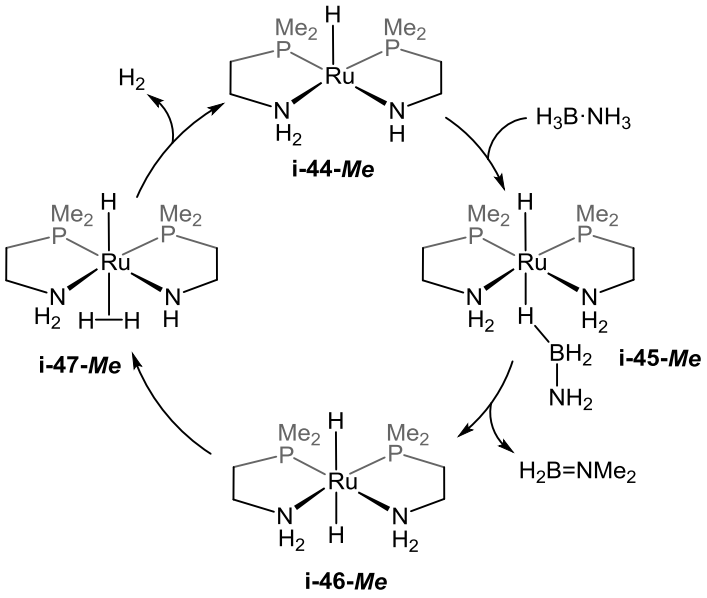

**Scheme 1.24** Proposed two stage mechanism for the homogeneous dehydrocoupling of $H_3B{\cdot}NMe_2H$ using $CpFe(CO)_2I$.

It was speculated that the electronegative iodide ligand enables heterolytic Fe—I cleavage under photoirradiation, maintaining an $Fe^{II}$ species. However, the dimeric complexes $[CpFe(CO)_2]_2$ and $Cp_2Fe_2(CO)_3(NCMe)$ formally are in the lower $Fe^{I}$ oxidation state and already have Fe—Fe interactions; these factors were suggested to aid nanoparticle formation, and hence heterogeneous catalysis is observed (Section 1.5.2).

### 1.5.13 Dehydrocoupling of amine-boranes involving ligand cooperativity

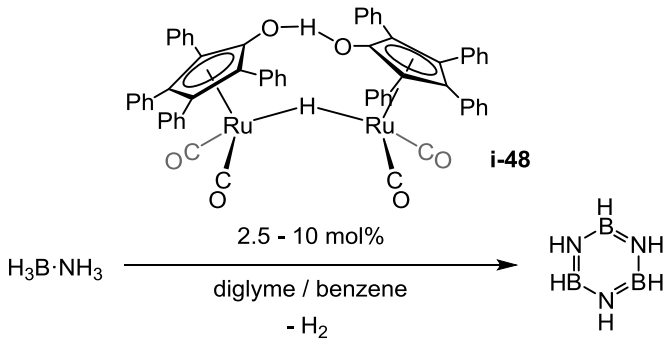
In 2008, Fagnou and co-workers reported the rapid dehydrogenation of $H_3B{\cdot}NH_3$ to form $[H_2BNH_2]_n$ with 0.03 mol% loadings of the catalyst $[Ru(P^iPr_2CH_2CH_2NH_2)_2Cl_2]$ (**i-43**), activated by 0.9 mol% $KO^tBu$ (TOF ~20 000 $h^{-1}$).[100] Furthermore, 0.5 mol% of

**i-43** could promote release of two equivalents of $H_2$ from $H_3B{\cdot}NMeH_2$ within ten minutes. An outer sphere mechanism was proposed using DFT calculations on the model complex [Ru($PMe_2CH_2CH_2NH_2$)($PMe_2CH_2CH_2NH$)H] (**i-44-*Me***), the product of activation of [Ru($PMe_2CH_2CH_2NH_2$)$_2Cl_2$] (**i-43-*Me***) with KO$^t$Bu (Scheme 1.25). The mechanism invokes protonation of the ligand by the amine (**i-45-*Me***), loss of $H_2B{=}NH_2$ to form **i-46-*Me***, and rate-limiting formation of the dihydrogen complex **i-47-*Me***.



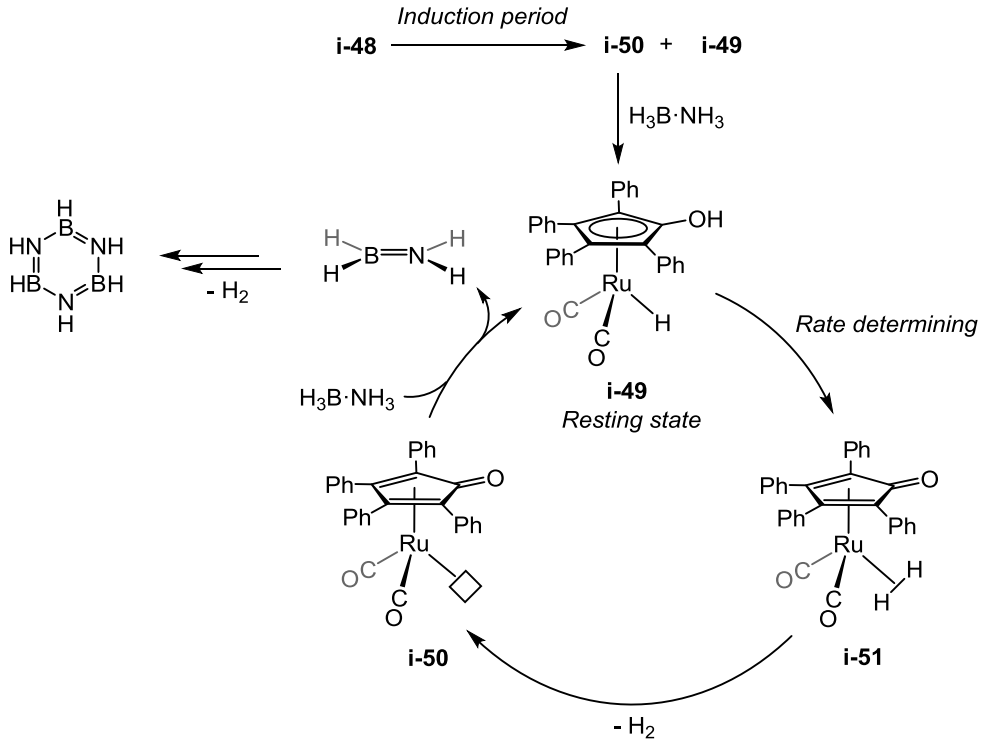

**Scheme 1.25** Proposed mechanism for the dehydrogenation of $H_3B{\cdot}NH_3$ by **i-44-*Me*.**

Williams also reported ligand cooperativity in the dehydrocoupling of $H_3B{\cdot}NH_3$ to yield borazine using Shvo's ruthenium catalyst, **i-48** (Scheme 1.26). The catalyst showed reasonable activity at 5 mol% **i-48** and 2 mol% EtOH (TOF ~18 $h^{-1}$ for release of 2 eq. $H_2$ at 70 °C).[99]



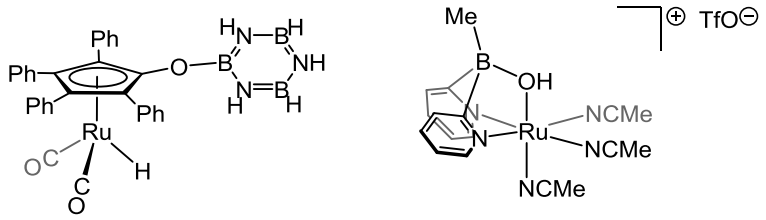

**Scheme 1.26** Dehydrocoupling of $H_3B{\cdot}NH_3$ by **i-48.**

$H_2$ release measurements (total 2 eq.) produced a kinetic profile with three regimes evident: *(i)* initiation period; *(ii)* fast catalysis showing a zero order decay of $[H_3B{\cdot}NH_3]$; *(iii)* slow catalysis showing a first order decay of $[H_3B{\cdot}NH_3]$. The induction period was attributed to the dissociation of **i-48** into **i-49** and **i-50** (Scheme 1.27). Fast dehydrogenation follows, in which H—H bond formation is the rate determining step, similar to Fagnou's mechanism,[100] and **i-49** is the resting state observed during catalysis.[99] At high [borazine], the third regime dominates. This is attributed to hydroboration of **i-50** by borazine to form **i-52** (Figure 1.14). $H_3B{\cdot}NH_3$ is required to convert **i-52** back into **i-49**, which is the rate-limiting step in this slow regime, and thus the reaction becomes first order in $[H_3B{\cdot}NH_3]$.[163]




**Scheme 1.27** Suggested catalytic cycle for the catalyst initiation and fast dehydrocoupling of $H_3B{\cdot}NH_3$ by Shvo's catalyst.

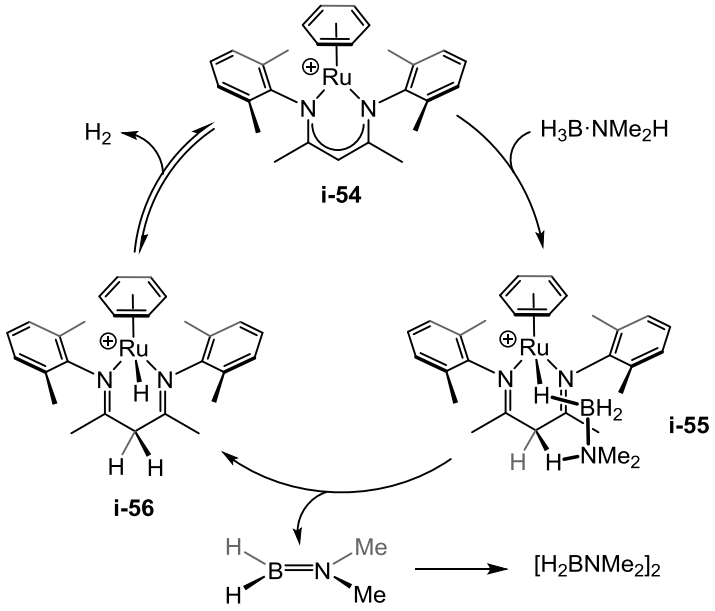
To avoid deactivation by borazine, the same group developed a catalyst with an oxygen atom already borylated, **i-53** (Figure 1.14). **i-53** catalysed the dehydropolymerisation of $H_3B{\cdot}NH_3$ to form a mixture of borazine and polyborazylene (2 mol%, 70 °C, TOF ~25 $h^{-1}$ for release of 2 equivalents of $H_2$ in a tetraglyme slurry). Significantly for potential practical applications, the catalysis could be conducted under air and the catalyst could be reused; four successive runs in a single reactor produced similar rates and quantities of $H_2$ loss in each run (2.1 – 2.3 eq.). To date, mechanistic details have not been unravelled, although a mechanism involving dual-site cooperativity is likely.[164]




**i-52** **i-53**

**Figure 1.14** Complexes **i-52** and **i-53**.

Phillips and co-workers recently reported the fast dehydrocoupling of $H_3B{\cdot}NH_3$ and $H_3B{\cdot}NMe_2H$ (TOF ~400 $h^{-1}$ for $H_3B{\cdot}NMe_2H$ at 42 °C in THF) using 0.5 mol% of the bifunctional $Ru^{II}$ β-diketiminato complex, **i-54** (Scheme 1.28).[165] Mechanistic studies focused on $H_3B{\cdot}NMe_2H$ as, under these reaction conditions, $H_3B{\cdot}NH_3$ can thermally release $H_2$ in the absence of catalyst. The proposed mechanism for initial dehydrogenation is that of hydride coordination from $BH_3$ at the $Ru^{II}$ centre, forming **i-55**. The acidic $NMe_2H$ proton can then protonate the β-carbon position of the β-diketiminato ligand, resulting in **i-56**. **i-54** had been previously shown to reversibly heterolytically cleave $H_2$ to yield **i-56**.[166] An induction period was observed in the dehydrocoupling, and the authors speculated that this is due to slow initial formation of **i-56**, which is the active catalyst for subsequent dehydrogenations. An experiment performed using a THF solution that had been saturated with $H_2$ resulted in faster dehydrogenation and a reduced induction period compared with the $N_2$-flushed THF used as the normal reaction solvent, suggesting the rate is dependent on the rate of formation of **i-56**.

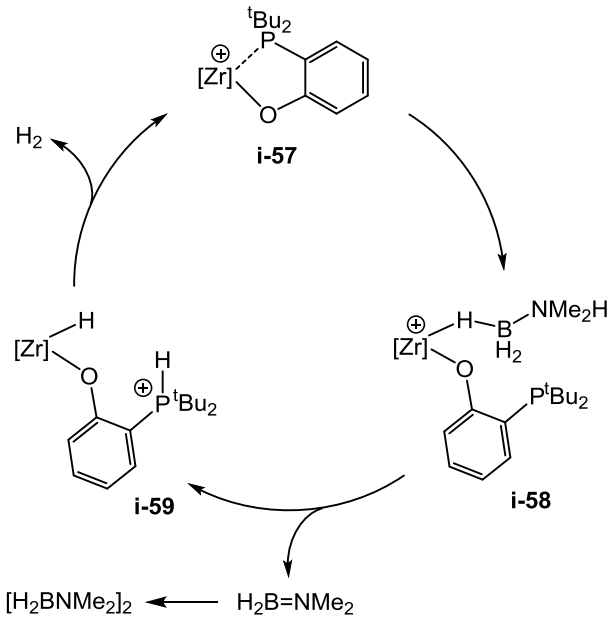



**Scheme 1.28** Proposed mechanism for the initial dehydrogenation of $H_3B{\cdot}NMe_2H$ using **i-54**. $[OTf]^-$ anions not shown.

Wass and co-workers reported a fast dehydrocoupling catalyst based upon a 'frustrated' Lewis pair, but where the Lewis acid (typically a fluorinated aryl borane) was replaced with an electrophilic $Zr^{IV}$ centre. The species $[Cp_2ZrOC_6H_4P^tBu_2][B(C_6F_5)_4]$ (**i-57**) dehydrocoupled $H_3B{\cdot}NMe_2H$ rapidly (1 mol% **i-57**, TOF ~600 $h^{-1}$), being the fastest reported group IV catalyst to our knowledge (Scheme 1.29).[167] Wass' proposed mechanism (Scheme 1.30) is different from those of other group IV metallocene catalysts (Section 1.5.4). Following sigma coordination of $H_3B{\cdot}NMe_2H$ to the $Zr^{IV}$ centre to form **i-58**, ligand-assisted dehydrogenation yields $H_2B{=}NMe_2$ and **i-59**. The loss of hydrogen from **i-59** is facile, regenerating **i-57**. The reaction using $[Cp_2ZrO^tBu][B(C_6F_5)_4]$ did not dehydrogenate $H_3B{\cdot}NMe_2H$, illustrating the importance of the phosphine in this cooperative system.



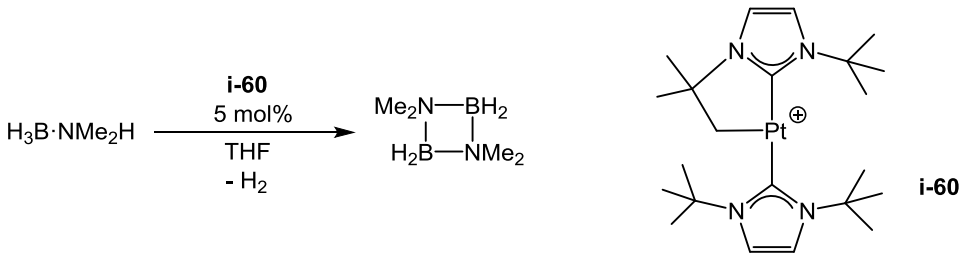

**Scheme 1.29** Dehydrocoupling of $H_3B{\cdot}NMe_2H$ with **i-57**. $[B(C_6F_5)_4]^-$ anion not shown.




**Scheme 1.30** Suggested mechanism for dehydrocoupling of $H_3B{\cdot}NMe_2H$ by **i-57**. [Zr] = $Cp_2Zr$. $[B(C_6F_5)_4]^-$ anions not shown.

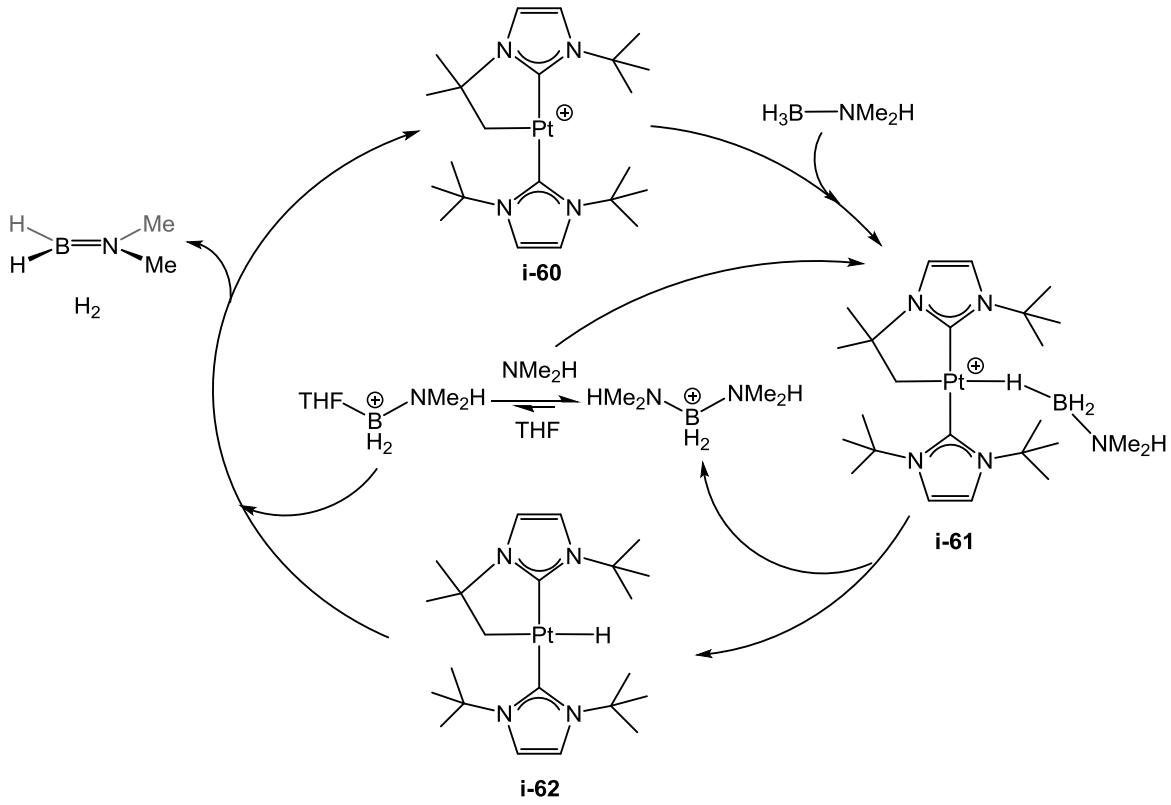
### 1.5.14 Effect of solvent upon dehydrocoupling reactions

Many dehydrocoupling reactions of amine-boranes are conducted in THF due to good solubility of $H_3B{\cdot}NMeH_2$ and $H_3B{\cdot}NH_3$ in this solvent.[20] A recent report by Conejero and López-Serrano, using $[Pt(I^tBu')(I^tBu)][BAr^F{}_4]$, **i-60** (Scheme 1.31) ($I^tBu$ = 1,3-di-*tert*-butylimidazol-2-ylidene, $I^tBu'$ = cyclometalated $I^tBu$), showed that THF is involved in the dehydrocoupling mechanism of $H_3B{\cdot}NMe_2H$ to form $[H_2BNMe_2]_2$.[168]




**Scheme 1.31** Dehydrocoupling of $H_3B{\cdot}NMe_2H$ with **i-60.**

The suggested mechanism (Scheme 1.32), supported by DFT calculations (in which $H_3B{\cdot}NH_3$ is used as the model amine-borane), involves the initial reaction of **i-60** with $H_3B{\cdot}NMe_2H$ to form a sigma complex, **i-61**. In the presence of $NMe_2H$ (thought to arise from B—N cleavage of $H_3B{\cdot}NMe_2H$[15,71,148]), **i-61** rearranges to form the neutral **i-62** with expulsion of the boronium cation $[(NMe_2H)_2BH_2]^+$. Calculations indicated that dehydrogenation of bound $H_3B{\cdot}NH_3$ to yield an aminoborane has a prohibitively high barrier of 42.5 kcal $mol^{-1}$ in this system. However, addition of a Lewis base such as THF or $NMe_2H$ ($Me_2O$ and $NH_3$ used as model analogues in the calculations) lowers the barrier to B—H activation. In THF solution, $[(NMe_2H)_2BH_2]^+$ and $[(NMe_2H)BH_2(THF)]^+$ are in an equilibrium. The THF adduct reacts with **i-62** to reform **i-60** and $H_2B{=}NMe_2$ with $H_2$ loss. Stoichiometric experiments showed that $[(NMe_2H)_2BH_2]^+$ reacted slowly with **i-62**, leading to unidentified products, whereas $[(NMe_2H)BH_2(THF)]^+$ reacted rapidly, producing $H_2B{=}NMe_2$ that dimerises to form $[H_2BNMe_2]_2$, supporting the proposed cycle.



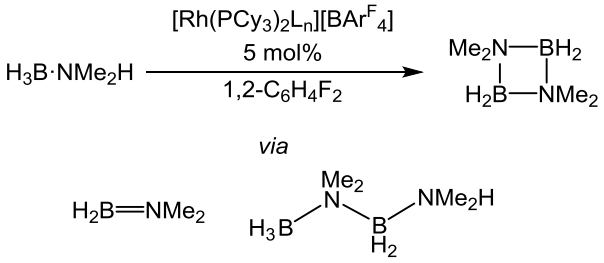

**Scheme 1.32** Proposed mechanism for the dehydrocoupling of $H_3B{\cdot}NMe_2H$ with **i-60**.

Solvent effects have also been noted in the off-metal dimerisation of $H_2B{=}NMe_2$, with the rate of dimerisation being accelerated in MeCN.[64,169]

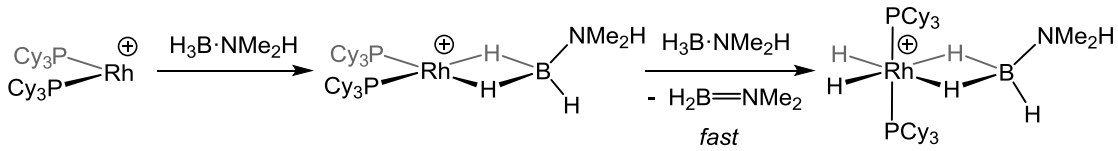
### 1.5.15 Generic mechanism for the dehydrocoupling of $H_3B{\cdot}NMe_2H$ using transition metals

In 2012, Weller and Lloyd-Jones conducted a thorough mechanistic study on the dehydrocoupling of $H_3B{\cdot}NMe_2H$ to form $[H_2BNMe_2]_2$ using the $\{Rh(PCy_3)_2L_n\}^+$ ($L_n$ = solvent or agostic interaction) fragment (Scheme 1.33).[16] During catalysis (5 mol% [Rh], TOF ~10 $h^{-1}$), both $H_2B{=}NMe_2$ and $H_3B{\cdot}NMe_2BH_2{\cdot}NMe_2H$ were observed to be formed as intermediates. Several important observations were noted for this system. Addition of 2 equivalents of $H_3B{\cdot}NMe_2H$ to $\{Rh(PCy_3)_2L_n\}^+$ led first to the $Rh^I$ sigma complex $[Rh(PCy_3)_2(\eta^2\text{-}H_3B{\cdot}NMe_2H)][BAr^F{}_4]$, which then rapidly formed the $Rh^{III}$

species $[Rh(PCy_3)_2(H)_2(\eta^2\text{-}H_3B{\cdot}NMe_2H)][BAr^F{}_4]$ with concomitant loss of $H_2B{=}NMe_2$ (Scheme 1.34). This species does not lose $H_2$ easily, implying the active catalyst (after the initial dehydrogenation) is a $Rh^{III}$, rather than a $Rh^{I}$, complex that operates in a constant $Rh^{III}$ oxidation state.



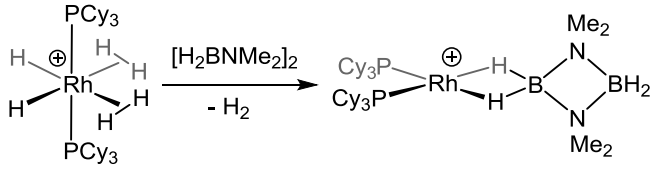

**Scheme 1.33** Catalytic dehydrocoupling of $H_3B{\cdot}NMe_2H$ by $[Rh(PCy_3)_2L_n][BAr^F{}_4]$.




**Scheme 1.34** Stoichiometric reactivity of $\{Rh(PCy_3)_2L_n\}^+$ with $H_3B{\cdot}NMe_2H$. $[BAr^F{}_4]^-$ anions not shown.

However, addition of the product $[H_2BNMe_2]_2$ to the $Rh^{III}$ species $[Rh(PCy_3)_2(H)_2(\eta^2\text{-}H_2)_2][BAr^F{}_4]$ resulted in the immediate formation of the $Rh^{I}$ complex $[Rh(PCy_3)_2(\eta^2\text{-}(H_2BNMe_2)_2)][BAr^F{}_4]$, indicating that $[H_2BNMe_2]_2$ can drive the reductive elimination of $H_2$ to reform a $Rh^{I}$ species (Scheme 1.35). Consistent with this, under catalytic conditions, $[H_2BNMe_2]_2$ was found to have an autocatalytic role in the dehydrocoupling catalysis by acting as a modifier to produce kinetically significant amounts of a $Rh^{I}$ catalytically active species alongside the $Rh^{III}$ species. Thus, the dehydrocoupling was shown to exist in both a constant oxidation state $Rh^{III}/Rh^{III}$ cycle (slow), and a $Rh^{I}/Rh^{III}$ cycle (faster). It was also shown that

$H_3B{\cdot}NMe_2BH_2{\cdot}NMe_2H$ is formed from $H_3B{\cdot}NMe_2H$ and $H_2B{=}NMe_2$ in a $Rh^{III}$ mediated equilibrium, the position of which depends upon the relative concentrations of the three species, consistent with Schneider's earlier calculations (Section 1.4.3).[74]

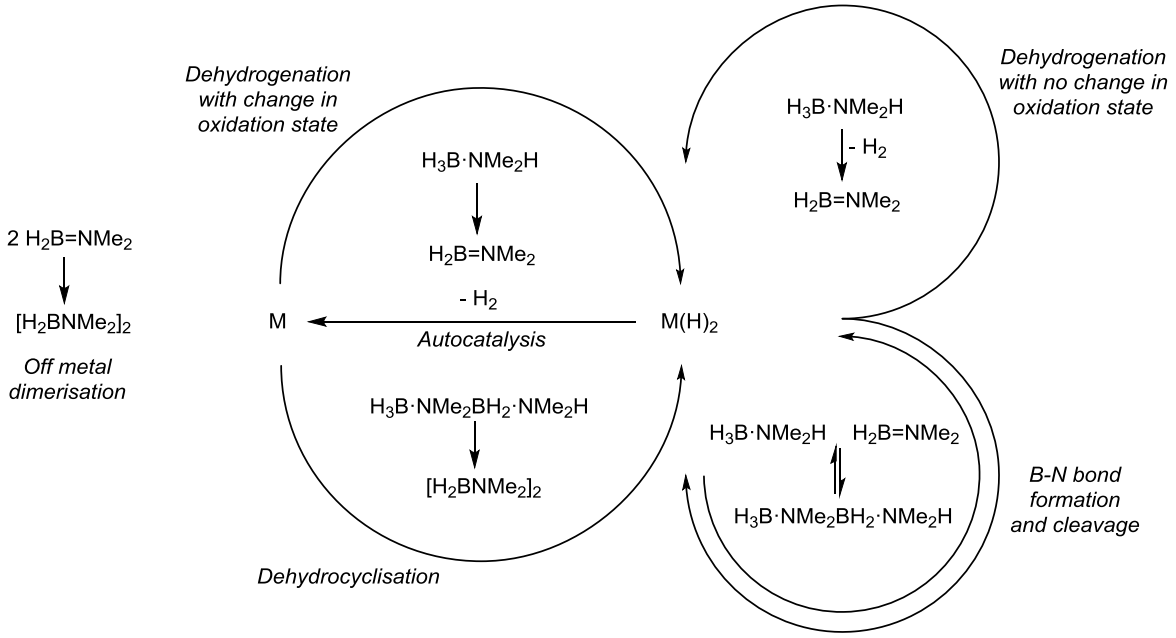



**Scheme 1.35** Reduction from $Rh^{III}$ to $Rh^{I}$ by addition of $[H_2BNMe_2]_2$. $[BAr^F{}_4]^-$ anions not shown.

Kinetic simulations indicated the presence of an additional catalyst present in constant (low) concentrations that promoted the first order dehydrogenation of $H_3B{\cdot}NMe_2H$ to give $H_2B{=}NMe_2$. Due to a constant concentration of chloride ions in solution (arising from the catalyst preparation method), it was suggested that the active catalyst was the neutral species $Rh(PCy_3)_2(H)_2Cl$, whose catalytic activity was separately examined (see Section 1.5.12).[15]

The observations led to a generalised mechanistic scenario for the dehydrocoupling of $H_3B{\cdot}NMe_2H$ (Scheme 1.36) simplified into several parts: *(i)* dehydrogenation of $H_3B{\cdot}NMe_2H$ with a change in the oxidation state of the catalyst; *(ii)* dehydrogenation of $H_3B{\cdot}NMe_2H$ with no change in the oxidation state of the catalyst; *(iii)* the formation and cleavage of $H_3B{\cdot}NMe_2BH_2{\cdot}NMe_2H$; *(iv)* dehydrocyclisation of $H_3B{\cdot}NMe_2BH_2{\cdot}NMe_2H$; *(v)* the off-metal dimerisation of $H_2B{=}NMe_2$ to give $[H_2BNMe_2]_2$. This cycle, or parts thereof, is generally applicable to various homogeneous transition-metal catalysed systems reported. For example, dehydrogenation with a change in oxidation state has been implicated for systems

based upon Ti,[108,145] Re,[125] Cr[151] and Rh.[12] Systems remaining in a constant oxidation state, however, include cationic Rh[14] and Ir[52,64] systems as well as bifunctional Ru catalysts.[65,100] The formation of $H_3B{\cdot}NMe_2BH_2{\cdot}NMe_2H$ from $H_3B{\cdot}NMe_2H$ and $H_2B{=}NMe_2$ has been observed with Ti,[108] Rh[14], Ir[64] and Ru[74] systems. These systems also catalyse the dehydrocyclisation of $H_3B{\cdot}NMe_2BH_2{\cdot}NMe_2H$ to form $[H_2BNMe_2]_2$. Manners has proposed related general dehydrocoupling pathways for $H_3B{\cdot}NH_3$ and primary and secondary amine-boranes.[50]

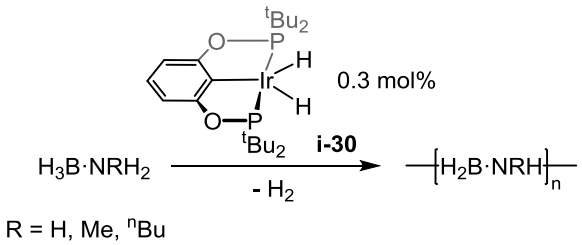



**Scheme 1.36** Weller and Lloyd-Jones' general mechanistic cycle for the dehydrocoupling of $H_3B{\cdot}NMe_2H$. M = metal catalyst.

### 1.5.16 Mechanistic studies upon the dehydropolymerisation of amine-boranes

While the cases discussed above address mostly the dehydrogenation of amine-boranes to form aminoboranes, or focus on the model $H_3B{\cdot}NMe_2H$, fewer studies have attempted to explore the B—N coupling event in the polymerisation of amine-boranes.

The first example of well–defined homogeneous catalytic dehydropolymerisation of amine-boranes was reported by Manners and co-workers in 2008.[61] The dehydropolymerisation of $H_3B{\cdot}NRH_2$ (R = H, Me, $^n$Bu) mediated by **i-30** formed $[H_2BNRH]_n$ (Scheme 1.37). With R = Me, high molecular weight $[H_2BNMeH]_n$ was isolated ($M_n$ = 55 200 g mol$^{-1}$, PDI = 2.9).

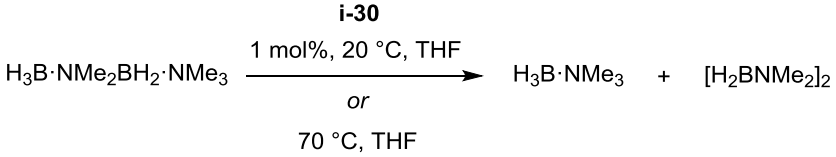



**Scheme 1.37** Catalytic dehydropolymerisation of amine-boranes using **i-30.**

In a detailed follow–up paper, on the basis of experiments including molecular weight *versus* conversion, a modified chain growth mechanism was proposed for this system, in which a slow initial dehydrogenation of $H_3B{\cdot}NMeH_2$ is followed by fast insertion of the resulting $H_2B{=}NMeH$.[20] Manners also demonstrated that a variety of other catalysts based on rhodium and ruthenium were active in dehydropolymerisation.[20] A recent computational study explored the mechanism of the polymerisation of $H_2B{=}NH_2$ by **i-30** (although concomitant dehydrogenation of the amine–borane was not probed) and also implicated a chain growth mechanism, as suggested experimentally by Manners. The proposed mechanism for propagation involves end chain growth from sigma complexes, rather than coordination insertion (*e.g.* in Ziegler-Natta olefin polymerisation); the lone pair on the $NH_2$ end of the chain interacts with the Lewis acidic $BH_2$ group of the entering $H_2B{=}NH_2$ molecule.[73]

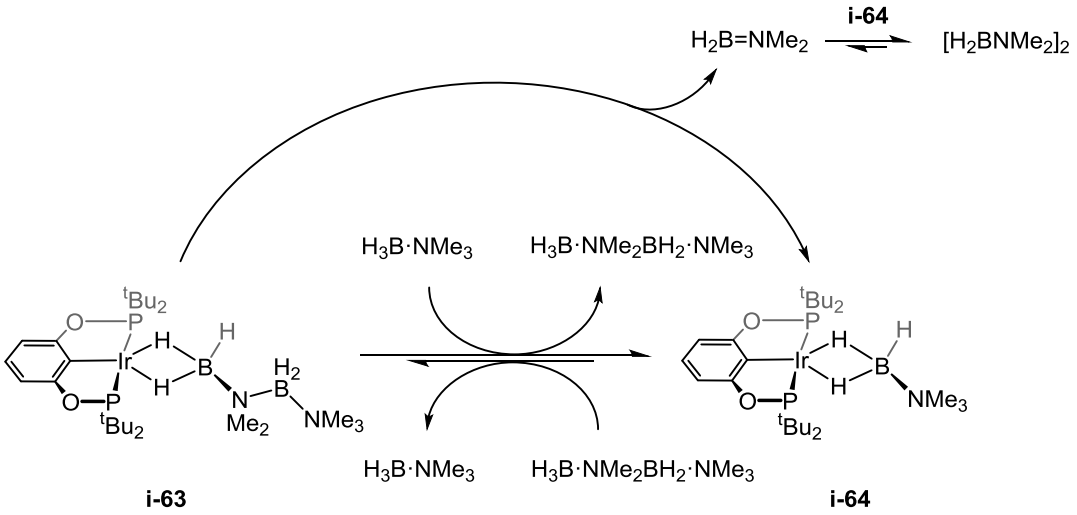
Whether the suggested sigma complexes could be displaced by excess $H_3B{\cdot}NH_3$ in the reaction mixture was not commented upon.

The role of **i-30** in the redistribution of linear diborazanes has also been investigated.[72,170] First, the diborazane $H_3B{\cdot}NMe_2BH_2{\cdot}NMe_3$ was used as a 'model' diborazane as it does not have a functional N—H group. This can undergo both thermal (70 °C, THF) and metal catalysed (20 °C, 1 mol% [Ir], THF) redistribution reactions to form $H_3B{\cdot}NMe_3$ and $[H_2BNMe_2]_2$ (Scheme 1.38).



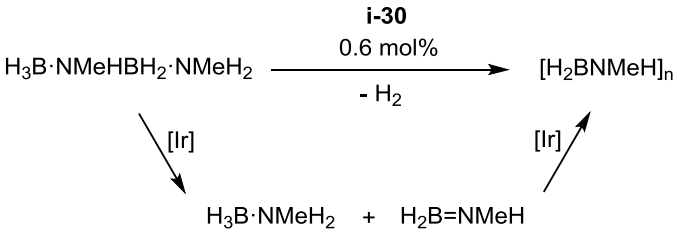

**Scheme 1.38** Hydrogen redistribution reaction of $H_3B{\cdot}NMe_2BH_2{\cdot}NMe_3$.

Kinetic analyses and simulations were used to probe the metal-catalysed pathway. The model suggested that **i-30** reacts with $H_3B{\cdot}NMe_2BH_2{\cdot}NMe_3$ to form a proposed sigma complex **i-63**, from which a direct redistribution reaction gives $H_2B{=}NMe_2$ and a sigma complex **i-64** (Scheme 1.39). Dimerisation of $H_2B{=}NMe_2$ affords $[H_2BNMe_2]_2$, and the kinetic simulations showed that, as well as the expected off-metal dimerisation, the dimerisation was also being catalysed by **i-64**, or a closely related fragment. Related to this, the pincer complex $[Pd(^tBuPCP^tBu)(OH_2)][PF_6]$ ($^tBuPCP^tBu$ = 2,6-$C_6H_3(CH_2P^tBu_2)_2$) has been shown to release one equivalent of $H_2$ on reaction with $H_3B{\cdot}NH_3$, and DFT modelling also suggested an on-metal cyclodimerisation to form $[H_2BNH_2]_2$.[171]



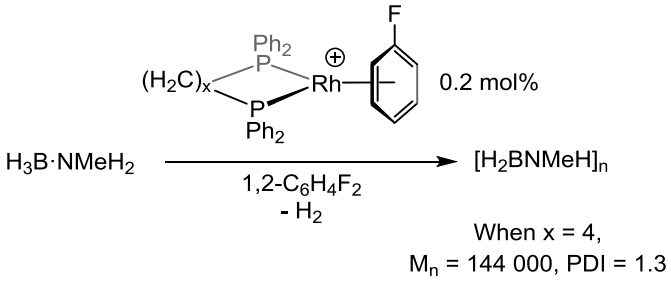

**Scheme 1.39** Model suggested for the metal-catalysed hydrogen redistribution reaction.

The redistribution chemistry of the more complex (*i.e.* containing N—H groups) linear diborazane $H_3B{\cdot}NMeHBH_2{\cdot}NMeH_2$, first noted by Weller and Manners as the product of a single oligomerisation of $H_3B{\cdot}NMeH_2$,[76] was also explored by Manners and co–workers. Treatment of $H_3B{\cdot}NMeHBH_2{\cdot}NMeH_2$ with 0.6 mol% **i-30** yielded high molecular weight $[H_2BNMeH]_n$ ($M_n$ = 67 400, PDI = 1.4), with the parent amine-borane $H_3B{\cdot}NMeH_2$ observed as an intermediate (Scheme 1.40). Hydroboration trapping experiments with cyclohexene (Section 1.4.2) did not lead to $Cy_2B{=}NMeH$. Nonetheless, the observation of $H_3B{\cdot}NMeH_2$ suggests that $H_2B{=}NMeH$ is formed, either remaining on-metal, or polymerising rapidly relative to the rate of hydroboration. By contrast, metal-free thermolysis of $H_3B{\cdot}NMeHBH_2{\cdot}NMeH_2$ at 70 °C in THF led to the formation of $H_3B{\cdot}NMeH_2$ and the cyclic trimer $[H_2BNMeH]_3$, presumed to arise from trimerisation of $H_2B{=}NMeH$. Addition of cyclohexene resulted in the formation of the trapping product $Cy_2B{=}NMeH$, implying free $H_2B{=}NMeH$ is present in solution and that hydroboration is kinetically competitive with trimerisation.[72,170]




**Scheme 1.40** Proposed mechanism for the metal-catalysed redistribution of $H_3B{\cdot}NMeHBH_2{\cdot}NMeH_2$.

In 2011, Weller and Manners reported that the dehydrocoupling of $H_3B{\cdot}NMeH_2$ with the cationic rhodium chelating phosphine system $[Rh(Ph_2P(CH_2)_xPPh_2)(\eta^6\text{-}C_6H_5F)][BAr^F{}_4]$ (x = 3 – 5) produced high molecular weight and narrow polydispersity polyaminoborane $[H_2BNMeH]_n$ (when x = 4, $M_n$ = 144 000 g $mol^{-1}$, PDI = 1.3) (Scheme 1.41).[12]

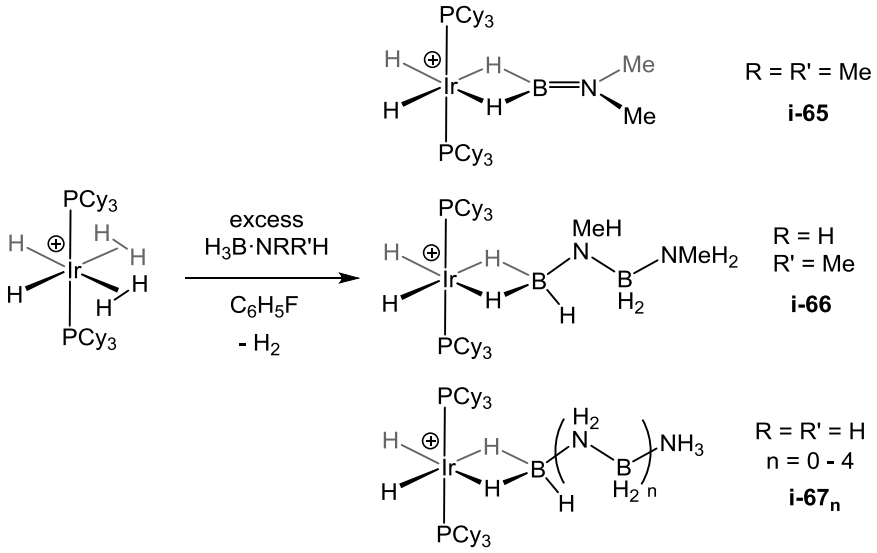



**Scheme 1.41** Dehydropolymerisation by $[Rh(Ph_2P(CH_2)_xPPh_2)(\eta^6\text{-}C_6H_5F)][BAr^F{}_4]$ (x = 3 – 5). $[BAr^F{}_4]^-$ anion not shown.

These catalysts were also efficient in dehydrocoupling $H_3B{\cdot}NMe_2H$ to form $[H_2BNMe_2]_2$ (fastest TOF ~1250 $h^{-1}$ when x = 3) following an induction period that was inversely proportional to catalyst concentration. The bite angle (see Section 1.3.2) correlated with binding strength in the related sigma complexes $[Rh(Ph_2P(CH_2)_xPPh_2)(\eta^2\text{-}H_3B{\cdot}NMe_3)][BAr^F{}_4]$ (x = 3 – 5); the smallest bite angle (x = 3) has the weakest sigma binding of $H_3B{\cdot}NMe_3$ and the fastest dehydrocoupling activity

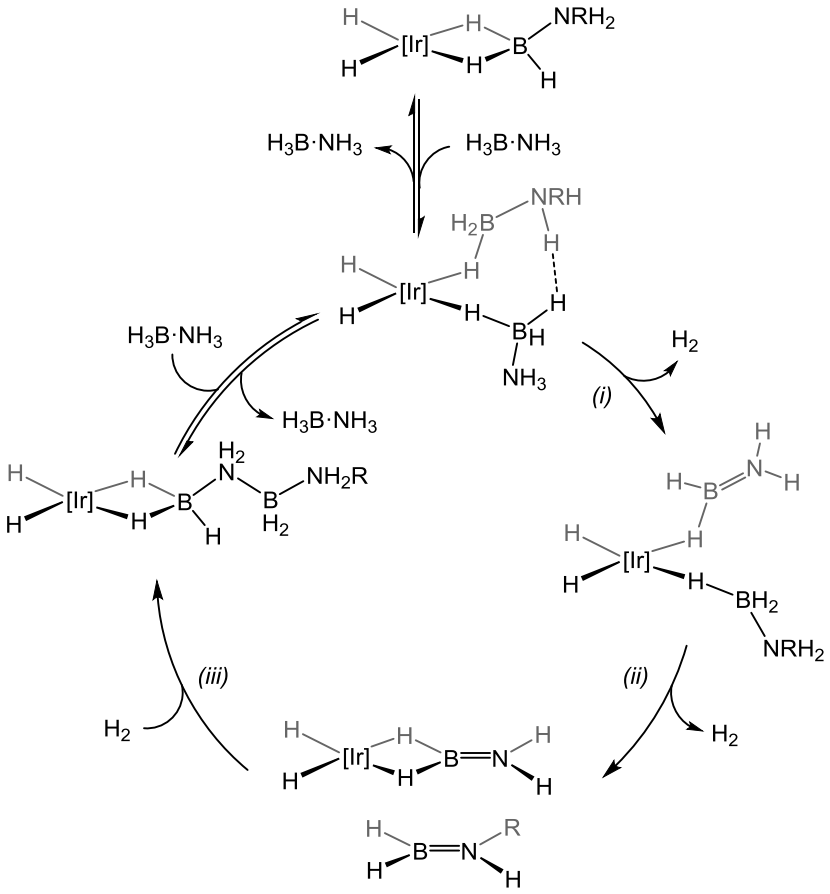
of $H_3B{\cdot}NMe_2H$. Tests indicated a homogeneous catalyst, and, although the reason for the induction period is yet to be deduced, it was speculated on the basis of ESI-MS experiments that this temporal profile was due to the formation of an initial inactive dimeric species, possibly in a slow equilibrium with an active monomeric species. Independent computational work on this system suggested that dimerisation forms an inactive hydridoboryl species, and the active catalyst is monomeric.[172]

The $\{Ir(PCy_3)_2(H)_2\}^+$ fragment has proved a useful, albeit slow (10-20 mol%, TOF ~0.1 $h^{-1}$), catalyst for the dehydrogenation and dehydrocoupling of $H_3B{\cdot}NMe_2H$,[64] $H_3B{\cdot}NMeH_2$,[76] and $H_3B{\cdot}NH_3$,[52] in which metal-bound products and intermediates can be observed, allowing direct comparisons between the different amine-boranes. Reaction of the *bis*–dihydrogen complex $[Ir(PCy_3)_2(H)_2(\eta^2\text{-}H_2)_2][BAr^F{}_4]$, a source of $\{Ir(PCy_3)_2(H)_2\}^+$, with $H_3B{\cdot}NMe_2H$ ultimately formed $[H_2BNMe_2]_2$, and the major metal-containing product is the bound aminoborane complex $[Ir(PCy_3)_2(H)_2(\eta^2\text{-}H_2B{=}NMe_2)][BAr^F{}_4]$ (**i-65**, Scheme 1.42). The mechanism of dehydrogenation of $[Ir(PCy_3)_2(H)_2(\eta^2\text{-}H_3B{\cdot}NMe_2H)][BAr^F{}_4]$ to form **i-65** was previously calculated to be sequential B—H activation, $H_2$ loss from the metal, and rate-limiting N—H activation.[64] By contrast, $H_3B{\cdot}NMeH_2$ catalytically undergoes an on–metal oligomerisation event to yield the diborazane $H_3B{\cdot}NMeHBH_2{\cdot}NMeH_2$, with the sigma complex $[Ir(PCy_3)_2(H)_2(\eta^2\text{-}H_3B{\cdot}NMeHBH_2{\cdot}NMeH_2)][BAr^F{}_4]$ (**i-66**) observed during the dehydrocoupling. $H_3B{\cdot}NH_3$ undergoes further oligomerisation events, yielding insoluble $[H_2BNH_2]_n$. During the dehydrocoupling, various species with bound oligomeric units, $[Ir(PCy_3)_2(H)_2(\eta^2\text{-}H_3B{\cdot}(NH_2BH_2)_n{\cdot}NH_3)][BAr^F{}_4]$ (**i-67$_n$**) (n = 0 – 4), were observed using ESI–MS techniques (Scheme 1.42).



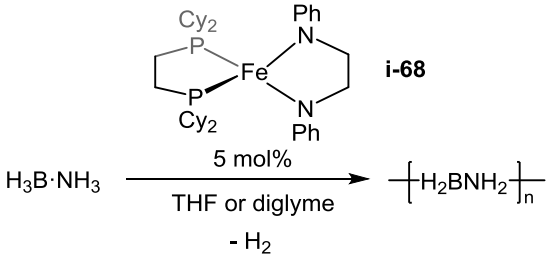

**Scheme 1.42** Metal-bound products in the reaction of excess amine-borane with $\{Ir(PCy_3)_2(H)_2\}^+$. $[BAr^F{}_4]^-$ anions not shown.

Calculations conducted on the model system $\{Ir(PMe_3)_2(H)_2\}^+$ for the dehydrogenation and oligomerisation of $H_3B{\cdot}NH_3$ propose a pathway (Scheme 1.43) involving: *(i)* initial dehydrogenation of the amine-borane; *(ii)* dehydrogenation of a second amine-borane; and *(iii)* B—N coupling. Step *(i)* was calculated to have the highest barrier, and the B—N coupling step *(iii)* had the lowest barrier. Calculations showed that subsequent oligomerisations were also viable for this system, as observed experimentally. With $H_3B{\cdot}NMeH_2$, the B—N coupling barrier for subsequent oligomerisations was significantly raised, consistent with the experimental observation of a single oligomerisation event. With the more sterically encumbered $H_3B{\cdot}NMe_2H$, the calculated B—N coupling barrier was prohibitively high, consistent with no experimental observation of linear diborazane. Although likely system-specific, this observed selectivity illustrates the potential importance of sterics in the dehydrocoupling of amine-boranes. Importantly, the calculations also suggested that outer sphere N–H···H–B interactions lower barriers to dehydrogenation. The impact of dihydrogen bonding upon dehydrocoupling has been reviewed by others.[51]



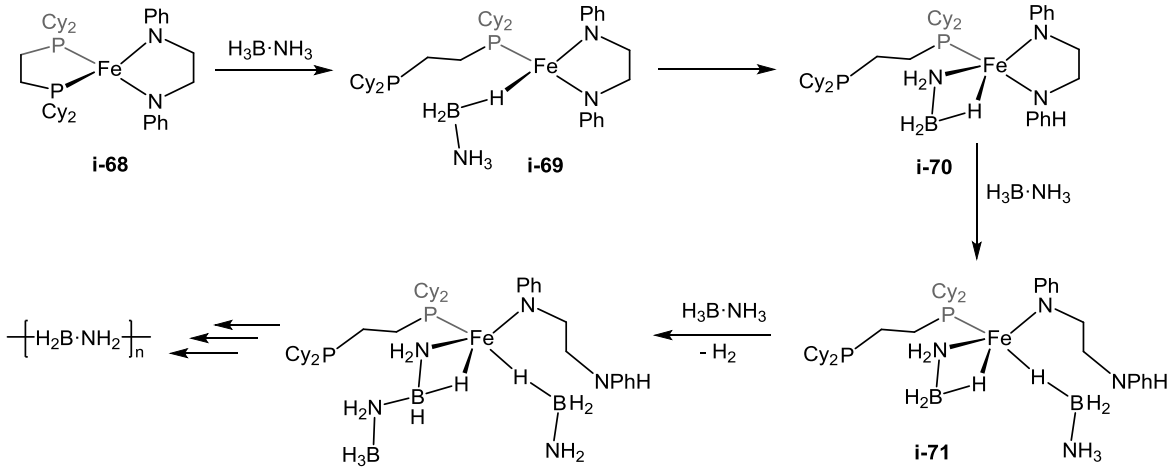
**Scheme 1.43** Calculated pathway by Macgregor and Weller for the dehydrogenation and coupling of $H_3B{\cdot}NH_3$. R = H (first oligomerisation), R = $BH_2NH_2$ (second oligomerisation). [Ir] = $\{Ir(PR'_3)_2\}^+$ (R' = Cy, experiment; Me, computation).

Systems involving ligand cooperativity have also provided mechanistic insight. In 2012, Gordon, Baker, *et al.* dehydrocoupled $H_3B{\cdot}NH_3$ to selectively form $[H_2BNH_2]_n$ using the [Fe($PCy_2CH_2CH_2PCy_2$)(NPh$CH_2CH_2$NPh)] catalyst (**i-68**) at 5 mol% loading (TOF ~80 $h^{-1}$) (Scheme 1.44).[107]



**Scheme 1.44** Dehydrocoupling of $H_3B{\cdot}NH_3$ by **i-68.**

The catalyst could not be recycled; a black precipitate – presumed to be iron metal – was observed during catalysis, indicating catalyst decomposition during dehydrocoupling. *In situ* NMR spectroscopy suggested de-coordination of one of the chelating phosphine arms occurred during catalysis, possibly responsible for the observed induction period (*ca.* 2 minutes). Two mechanisms were proposed to account for experimental observations, one of which is shown in Scheme 1.45.




**Scheme 1.45** A proposed mechanism for the dehydropolymerisation of $H_3B{\cdot}NH_3$ by **i-68**.

Initial dissociation of a phosphine arm enables coordination of $H_3B{\cdot}NH_3$ to form **i-69**. Protonation of one arm of the amido ligand by the amine-borane (affording a bound amido-borane, **i-70**) follows, and the resulting amino arm of the ligand can dissociate, allowing ligation of a second equivalent of $H_3B{\cdot}NH_3$ (**i-71**). From this, successive dehydrogenation and insertion steps yield $[H_2BNH_2]_n$. Throughout the proposed mechanism, no free $H_2B{=}NH_2$ is implicated, and experimentally $H_2B{=}NH_2$ was neither detected directly nor with cyclohexene trapping. This is consistent with previous work by some of the authors,[69] and others,[62] suggesting that $H_2B{=}NH_2$ must remain bound to the metal to oligomerise (Section 1.4.2), although other work has suggested

that cyclohexene trapping does not necessarily rule out the presence of free $H_2B{=}NH_2$ if the hydroboration is not kinetically competitive with oligomerisation.[65,72]

In 2009, Schneider and co-workers reported that the related bifunctional catalyst [Ru(PNP)(H)($PMe_3$)] (Figure 1.15, PNP = $N(CH_2CH_2P^iPr_2)_2$) (**i-72**, Figure 1.15) was extremely active in the dehydrocoupling of $H_3B{\cdot}NH_3$ to release approximately one equivalent of dihydrogen (TOF ~12 000 $h^{-1}$ at 0.1 mol% **i-72**) to form $[H_2BNH_2]_n$, with small amounts of borazine also observed.[98] $H_3B{\cdot}NMe_2H$ was also rapidly dehydrocoupled by **i-72** (2 mol%), forming $[H_2BNMe_2]_2$, until approximately 70% conversion (initial TOF ~3 600 $h^{-1}$); after this point, a much slower regime operates (TOF ~1.5 $h^{-1}$), suggesting a change in mechanism.[74] During the fast regime, the species *trans*-[Ru($PNP^H$)$(H)_2$($PMe_3$)] ($PNP^H$ = $HN(CH_2CH_2P^iPr_2)_2$) (**i-73**, Figure 1.15) was observed as the resting state and, indeed, starting catalysis with **i-73** showed very similar kinetics as with **i-72**. However, a new species evolved throughout the dehydrocoupling, [Ru($PNP^B$)$(H)_2$($PMe_3$)] ($PNP^B$ = $NMe_2BH_2N(CH_2CH_2P^iPr_2)_2$) (**i-74**, Figure 1.15), containing a four membered bora-metallacycle. The use of isolated **i-74** as the dehydrocoupling catalyst gave essentially the same catalytic activity as for the slow regime.

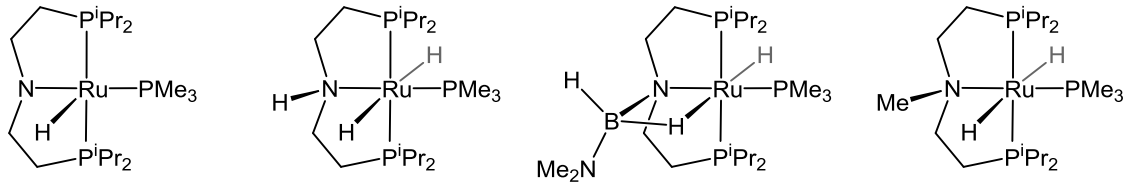
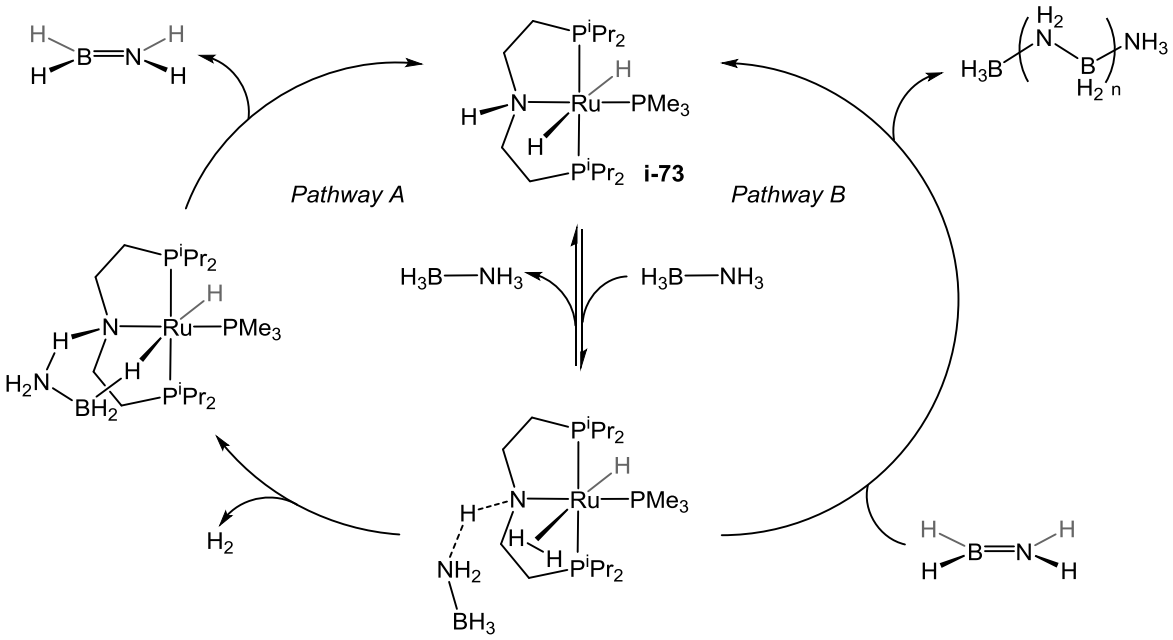



**Figure 1.15** Schenider's bifunctional ruthenium complexes.

A more detailed study published in 2013 focused on the catalytic dehydrocoupling of $H_3B{\cdot}NH_3$ with **i-72**, **i-73** and [Ru($^{Me}$PNP)(H)($PMe_3$)] ($^{Me}$PNP = $MeN(CH_2CH_2P^iPr_2)_2$) (**i-75**, Figure 1.15).[65] The methylation of the pincer nitrogen atom in **i-75** prevents the bifunctional reactivity that is thought to be key in rationalising the high activities of these complexes. Accordingly, catalysis using **i-75** exhibited a rate of $H_2$ evolution two orders of magnitude lower than with **i-72** or **i-73**, confirming the importance of amine cooperativity in these systems.

In contrast to the previous results, in which **i-72** and **i-73** appeared to operate within the same catalytic cycle,[74] on closer examination differences were found between the two, suggesting different mechanisms for each.[65] Both catalysts demonstrated first order kinetics for $H_2$ evolution on dehydrocoupling $H_3B{\cdot}NH_3$. On using the N-deuterated analogue $H_3B{\cdot}ND_3$, first order kinetics were retained with **i-73**. However, the $H_2$ evolution became zero order with **i-72**, implying a change in the turnover limiting step upon deuteration for this system. Additionally, some cross-linking of $[H_2BNH_2]_n$ was observed with **i-73**, which was not detected in $[H_2BNH_2]_n$ produced with **i-72**. For catalysis with **i-73**, a combination of DFT (using a $PMe_2$-truncated model) and experimental methods led to a proposed mechanism for the formation of $[H_2BNH_2]_n$ from $H_3B{\cdot}NH_3$, depicted in Scheme 1.46. The mechanism involves dehydrogenation of $H_3B{\cdot}NH_3$, *via* initial N—H activation, to form $H_2B{=}NH_2$ (Pathway A), which undergoes oligomerisation by catalytic insertion of $H_2B{=}NH_2$ into the N—H bond of the substrate (Pathway B). The barriers for dehydrogenation and B—N coupling were calculated to be very similar, implying that a low, steady-state concentration of $H_2B{=}NH_2$ is present during catalysis. Furthermore, experiments with $H_3B{\cdot}NMe_3$ and $Et_3B{\cdot}NH_3$ in the presence of 1 mol% **i-73** showed that 'head-to-tail'

coupling to yield $Et_3B{\cdot}NH_2BH_2{\cdot}NMe_3$ did not occur, indicating that proton and hydride transfer from the same substrate molecule to the catalyst is required in this system, as suggested in the proposed mechanism. Although the proposed cycles invoke free $H_2B{=}NH_2$, no trapping product $Cy_2B{=}NH_2$ was detected upon addition of cyclohexene to the mixture (Section 1.4.2). This suggests that, in this system, the hydroboration of cyclohexene is not kinetically competitive with B—N coupling.




**Scheme 1.46** Dehydrogenation and dehydrocoupling pathways proposed by Schneider and co-workers.

Overall, the insight garnered into the mechanisms of the dehydropolymerisation of amine-boranes indicates that the processes are complex and likely system-specific, particularly in the cases in which ligand cooperativity is key. Generally, however, chain growth dehydrogenation/coordination/insertion has been suggested, with $H_2B{=}NRH$ (R = Me, H), or related species, implicated as the monomers in polymerisation.

## 1.6 Summary

This thesis aims to elucidate mechanistic detail into the dehydropolymerisation of amine-boranes. The fragment {Rh(Xantphos)}$^+$ was selected as a suitable system to study. A *cis*-$\kappa^2_{P,P}$ geometry is closely related to the [Rh($Ph_2P(CH_2)_xPPh_2$)($\eta^6$-$C_6H_5F$)][$BAr^F_4$] system, whereas a *trans*-$\kappa^3_{P,O,P}$ geometry would somewhat resemble the Ir($^t$BuPOCOP$^t$Bu)$H_2$ scaffold, suggesting that {Rh(Xantphos)}$^+$ may be a suitable candidate for dehydropolymerisation reactions. The hemilability of the Xantphos ligand may also allow for the isolation of potential catalytic intermediates, as applied in the hydroacylation reaction with DPEphos.

In Chapter 2, the formation of suitable catalytic precursors using {Rh(Xantphos)}$^+$ is discussed, followed by the dehydrogenative homocoupling of the tertiary amine-borane $H_3B{\cdot}NMe_3$ by {Rh(Xantphos)}$^+$. $H_3B{\cdot}NMe_3$ has no N—H bond, so is unable to undergo B—H/N—H dehydrogenation. The {Rh(Xantphos)}$^+$ mediated hydroboration of alkenes by $H_3B{\cdot}NMe_3$ – pertinent to the formation of the chosen precatalyst – is explored in Chapter 3. In Chapter 4, a rigorous investigation into the {Rh(Xantphos)}$^+$ catalysed dehydrocoupling and dehydropolymerisation of $H_3B{\cdot}NMe_2H$ and $H_3B{\cdot}NMeH_2$, respectively, is undertaken. Finally, Chapter 5 presents the formation of novel dimeric species based upon {Rh(Xantphos)}$^+$, and the catalytic activity of these dimers is examined.

## 1.7 References

(1) Osborn, J. A.; Jardine, F. H.; Young, J. F.; Wilkinson, G. *J. Chem. Soc. A* **1966**, 1711.
(2) Hartwig, J. *Organotransition Metal Chemistry From Bonding to Catalysis*; University Science Books, 2010.
(3) Ziegler, K.; Holzkamp, E.; Breil, H.; Martin, H. *Angew. Chem.* **1955**, *67*, 541.
(4) Yin; Liebscher, J. *Chem. Rev.* **2006**, *107*, 133.
(5) Evans, D.; Osborn, J. A.; Wilkinson, G. *J. Chem. Soc. A* **1968**, 3133.

(6) Strauss, S. H. *Chem. Rev.* **1993**, *93*, 927.
(7) Verat, A. Y.; Pink, M.; Fan, H.; Tomaszewski, J.; Caulton, K. G. *Organometallics* **2007**, *27*, 166.
(8) Sewell, L. J.; Chaplin, A. B.; Abdalla, J. A. B.; Weller, A. S. *Dalton Trans.* **2010**, *39*, 7437.
(9) Chaplin, A. B.; Poblador-Bahamonde, A. I.; Sparkes, H. A.; Howard, J. A. K.; Macgregor, S. A.; Weller, A. S. *Chem. Commun.* **2009**, 244.
(10) Brayshaw, S. K.; Green, J. C.; Kociok-Köhn, G.; Sceats, E. L.; Weller, A. S. *Angew. Chem. Int. Ed.* **2006**, *45*, 452.
(11) Chaplin, A. B.; Weller, A. S. *Inorg. Chem.* **2010**, *49*, 1111.
(12) Dallanegra, R.; Robertson, A. P. M.; Chaplin, A. B.; Manners, I.; Weller, A. S. *Chem. Commun.* **2011**, *47*, 3763.
(13) Douglas, T. M.; Chaplin, A. B.; Weller, A. S. *J. Am. Chem. Soc.* **2008**, *130*, 14432.
(14) Douglas, T. M.; Chaplin, A. B.; Weller, A. S.; Yang, X.; Hall, M. B. *J. Am. Chem. Soc.* **2009**, *131*, 15440.
(15) Sewell, L. J.; Huertos, M. A.; Dickinson, M. E.; Weller, A. S.; Lloyd-Jones, G. C. *Inorg. Chem.* **2013**, *52*, 4509.
(16) Sewell, L. J.; Lloyd-Jones, G. C.; Weller, A. S. *J. Am. Chem. Soc.* **2012**, *134*, 3598.
(17) Tang, C. Y.; Thompson, A. L.; Aldridge, S. *J. Am. Chem. Soc.* **2010**, *132*, 10578.
(18) Sloan, M. E.; Clark, T. J.; Manners, I. *Inorg. Chem.* **2009**, *48*, 2429.
(19) Jaska, C. A.; Manners, I. *J. Am. Chem. Soc.* **2004**, *126*, 1334.
(20) Staubitz, A.; Sloan, M. E.; Robertson, A. P. M.; Friedrich, A.; Schneider, S.; Gates, P. J.; Gunne, J.; Manners, I. *J. Am. Chem. Soc.* **2010**, *132*, 13332.
(21) Crabtree, R. H. *The Organometallic Chemistry of the Transition Metals*; Wiley-Interscience, 2005.
(22) Orpen, A. G.; Connelly, N. G. *J. Chem. Soc., Chem. Commun.* **1985**, 1310.
(23) Dias, P. B.; de Piedade, M. E. M.; Simões, J. A. M. *Coord. Chem. Rev.* **1994**, *135–136*, 737.
(24) Tolman, C. A. *Chem. Rev.* **1977**, *77*, 313.
(25) DeStefano, N. J.; Johnson, D. K.; Lane, R. M.; Venanzi, L. M. *Helv. Chim. Acta* **1976**, *59*, 2674.
(26) Casey, C. P.; Whiteker, G. T. *Isr. J. Chem.* **1990**, *30*, 299.
(27) Kranenburg, M.; van der Burgt, Y. E. M.; Kamer, P. C. J.; van Leeuwen, P. W. N. M.; Goubitz, K.; Fraanje, J. *Organometallics* **1995**, *14*, 3081.
(28) Achord, P. D.; Kiprof, P.; Barker, B. *J. Mol. Struct-THEOCHEM* **2008**, *849*, 103.
(29) DuBois, D. L.; Blake, D. M.; Miedaner, A.; Curtis, C. J.; DuBois, M. R.; Franz, J. A.; Linehan, J. C. *Organometallics* **2006**, *25*, 4414.
(30) Wilson, A. D.; Miller, A. J. M.; DuBois, D. L.; Labinger, J. A.; Bercaw, J. E. *Inorg. Chem.* **2010**, *49*, 3918.
(31) Miedaner, A.; Haltiwanger, R. C.; DuBois, D. L. *Inorg. Chem.* **1991**, *30*, 417.
(32) Liron, F.; Fosse, C.; Pernolet, A.; Roulland, E. *J. Org. Chem* **2007**, *72*, 2220.
(33) Mo, J.; Ruan, J.; Xu, L.; Hyder, Z.; Saidi, O.; Liu, S.; Pei, W.; Xiao, J. *J. Mol. Catal. A: Chem.* **2007**, *261*, 267.
(34) Marcone, J. E.; Moloy, K. G. *J. Am. Chem. Soc.* **1998**, *120*, 8527.
(35) Brown, J. M.; Guiry, P. J. *Inorg. Chim. Acta* **1994**, *220*, 249.
(36) Zuidema, E.; van Leeuwen, P. W. N. M.; Bo, C. *Organometallics* **2005**, *24*, 3703.
(37) Jeffrey, J. C.; Rauchfuss, T. B. *Inorg. Chem.* **1979**, *18*, 2658.
(38) Braunstein, P.; Naud, F. *Angew. Chem. Int. Ed.* **2001**, *40*, 680.
(39) Zhang, W.-H.; Chien, S. W.; Hor, T. S. A. *Coord. Chem. Rev.* **2011**, *255*, 1991.
(40) Kamer, P. C. J.; van Leeuwen, P. W. N. M.; Reek, J. N. H. *Acc. Chem. Res.* **2001**, *34*, 895.
(41) Birkholz, M.-N.; Freixa, Z.; van Leeuwen, P. W. N. M. *Chem. Soc. Rev.* **2009**, *38*, 1099.
(42) Bini, L.; Muller, C.; Vogt, D. *Chem. Commun.* **2010**, *46*, 8325.
(43) Williams, G. L.; Parks, C. M.; Smith, C. R.; Adams, H.; Haynes, A.; Meijer, A. J. H. M.; Sunley, G. J.; Gaemers, S. *Organometallics* **2011**, *30*, 6166.
(44) Dallanegra, R.; Chaplin, A. B.; Weller, A. S. *Organometallics* **2012**, *31*, 2720.
(45) Dube, G.; Selent, D.; Taube, R. *Z. Chem.* **1985**, *25*, 154.
(46) Moxham, G. L.; Randell-Sly, H.; Brayshaw, S. K.; Weller, A. S.; Willis, M. C. *Chem. Eur. J.* **2008**, *14*, 8383.
(47) Moxham, G. L.; Randell-Sly, H. E.; Brayshaw, S. K.; Woodward, R. L.; Weller, A. S.; Willis, M. C. *Angew. Chem. Int. Ed.* **2006**, *45*, 7618.
(48) Pawley, R. J.; Huertos, M. A.; Lloyd-Jones, G. C.; Weller, A. S.; Willis, M. C. *Organometallics* **2012**, *31*, 5650.
(49) Clark, T. J.; Lee, K.; Manners, I. *Chem. Eur. J.* **2006**, *12*, 8634.

(50) Leitao, E. M.; Jurca, T.; Manners, I. *Nat. Chem.* **2013**, *5*, 817.
(51) Chen, X.; Zhao, J.-C.; Shore, S. G. *Acc. Chem. Res.* **2013**, *46*, 2666.
(52) Kumar, A.; Johnson, H. C.; Hooper, T. N.; Weller, A. S.; Algarra, A. G.; Macgregor, S. A. *Chem. Sci.* **2014**, *5*, 2546.
(53) Crabtree, R. H. *Science* **1998**, *282*, 2000.
(54) Stephens, F. H.; Pons, V.; Baker, R. T. *Dalton Trans.* **2007**, 2613.
(55) Hamilton, C. W.; Baker, R. T.; Staubitz, A.; Manners, I. *Chem. Soc. Rev.* **2009**, *38*, 279.
(56) Staubitz, A.; Robertson, A. P. M.; Manners, I. *Chem. Rev.* **2010**, *110*, 4079.
(57) Sutton, A. D.; Burrell, A. K.; Dixon, D. A.; Garner, E. B.; Gordon, J. C.; Nakagawa, T.; Ott, K. C.; Robinson, J. P.; Vasiliu, M. *Science* **2011**, *331*, 1426.
(58) Liu, Z.; Song, L.; Zhao, S.; Huang, J.; Ma, L.; Zhang, J.; Lou, J.; Ajayan, P. M. *Nano Lett.* **2011**, *11*, 2032.
(59) Jaska, C. A.; Temple, K.; Lough, A. J.; Manners, I. *J. Am. Chem. Soc.* **2003**, *125*, 9424.
(60) Pasumansky, L.; Haddenham, D.; Clary, J. W.; Fisher, G. B.; Goralski, C. T.; Singaram, B. *J. Org. Chem.* **2008**, *73*, 1898.
(61) Staubitz, A.; Soto, A. P.; Manners, I. *Angew. Chem. Int. Ed.* **2008**, *47*, 6212.
(62) Johnson, H. C.; Weller, A. S. *J. Organomet. Chem.* **2012**, *721*, 17.
(63) Garcia-Vivo, D.; Huergo, E.; Ruiz, M. A.; Travieso-Puente, R. *Eur. J. Inorg. Chem.* **2013**, 4998.
(64) Stevens, C. J.; Dallanegra, R.; Chaplin, A. B.; Weller, A. S.; Macgregor, S. A.; Ward, B.; McKay, D.; Alcaraz, G.; Sabo-Etienne, S. *Chem. Eur. J.* **2011**, *17*, 3011.
(65) Marziale, A. N.; Friedrich, A.; Klopsch, I.; Drees, M.; Celinski, V. R.; Guenne, J.; Schneider, S. *J. Am. Chem. Soc.* **2013**, *135*, 13342.
(66) Robertson, A. P. M.; Suter, R.; Chabanne, L.; Whittell, G. R.; Manners, I. *Inorg. Chem.* **2011**, *50*, 12680.
(67) Metters, O. J.; Chapman, A. M.; Robertson, A. P. M.; Woodall, C. H.; Gates, P. J.; Wass, D. F.; Manners, I. *Chem. Commun.* **2014**, *50*, 12146.
(68) Alcaraz, G.; Vendier, L.; Clot, E.; Sabo-Etienne, S. *Angew. Chem. Int. Ed.* **2010**, *49*, 918.
(69) Pons, V.; Baker, R. T.; Szymczak, N. K.; Heldebrant, D. J.; Linehan, J. C.; Matus, M. H.; Grant, D. J.; Dixon, D. A. *Chem. Commun.* **2008**, 6597.
(70) Jaska, C. A.; Temple, K.; Lough, A. J.; Manners, I. *Chem. Commun.* **2001**, 962.
(71) Denney, M. C.; Pons, V.; Hebden, T. J.; Heinekey, D. M.; Goldberg, K. I. *J. Am. Chem. Soc.* **2006**, *128*, 12048.
(72) Robertson, A. P. M.; Leitao, E. M.; Jurca, T.; Haddow, M. F.; Helten, H.; Lloyd-Jones, G. C.; Manners, I. *J. Am. Chem. Soc.* **2013**, *135*, 12670.
(73) Bhunya, S.; Malakar, T.; Paul, A. *Chem. Commun.* **2014**, *50*, 5919.
(74) Friedrich, A.; Drees, M.; Schneider, S. *Chem. Eur. J.* **2009**, *15*, 10339.
(75) Dallanegra, R.; Chaplin, A. B.; Tsim, J.; Weller, A. S. *Chem. Commun.* **2010**, *46*, 3092.
(76) Johnson, H. C.; Robertson, A. P. M.; Chaplin, A. B.; Sewell, L. J.; Thompson, A. L.; Haddow, M. F.; Manners, I.; Weller, A. S. *J. Am. Chem. Soc.* **2011**, *133*, 11076.
(77) Chen, X.; Zhao, J.-C.; Shore, S. G. *J. Am. Chem. Soc.* **2010**, *132*, 10658.
(78) Ewing, W. C.; Carroll, P. J.; Sneddon, L. G. *Inorg. Chem.* **2013**, 10690.
(79) Green, I. G.; Johnson, K. M.; Roberts, B. P. *J. Chem. Soc.-Perkin Trans. 2* **1989**, 1963.
(80) Widegren, J. A.; Finke, R. G. *J. Mol. Catal. A-Chem.* **2003**, *198*, 317.
(81) Jaska, C. A.; Manners, I. *J. Am. Chem. Soc.* **2004**, *126*, 9776.
(82) Chen, Y. S.; Fulton, J. L.; Linehan, J. C.; Autrey, T. *J. Am. Chem. Soc.* **2005**, *127*, 3254.
(83) Sonnenberg, J. F.; Morris, R. H. *ACS Catal.* **2013**, *3*, 1092.
(84) Duman, S.; Ozkar, S. *Int. J. Hydrog. Energy* **2013**, *38*, 10000.
(85) Zahmakiran, M.; Ayvali, T.; Philippot, K. *Langmuir* **2012**, *28*, 4908.
(86) Zahmakiran, M.; Philippot, K.; Ozkar, S.; Chaudret, B. *Dalton Trans.* **2012**, *41*, 590.
(87) Zahmakiran, M.; Ozkar, S. *Inorg. Chem.* **2009**, *48*, 8955.
(88) Vance, J. R.; Robertson, A. P. M.; Lee, K.; Manners, I. *Chem. Eur. J.* **2011**, *17*, 4099.
(89) Vance, J. R.; Schafer, A.; Robertson, A. P. M.; Lee, K.; Turner, J.; Whittell, G. R.; Manners, I. *J. Am. Chem. Soc.* **2014**, *136*, 3048.
(90) Luo, W.; Campbell, P. G.; Zakharov, L. N.; Liu, S. Y. *J. Am. Chem. Soc.* **2011**, *133*, 19326.
(91) Luo, W.; Neiner, D.; Karkamkar, A.; Parab, K.; Garner III, E. B.; Dixon, D. A.; Matson, D.; Autrey, T.; Liu, S.-Y. *Dalton Trans.* **2013**, *42*, 611.
(92) Campbell, P. G.; Ishibashi, J. S. A.; Zakharov, L. N.; Liu, S.-Y. *Aust. J. Chem.* **2014**, *67*, 521.
(93) Bluhm, M. E.; Bradley, M. G.; Butterick, R.; Kusari, U.; Sneddon, L. G. *J. Am. Chem. Soc.* **2006**, *128*, 7748.

(94) Himmelberger, D. W.; Alden, L. R.; Bluhm, M. E.; Sneddon, L. G. *Inorg. Chem.* **2009**, *48*, 9883.
(95) Wright, W. R. H.; Berkeley, E. R.; Alden, L. R.; Baker, R. T.; Sneddon, L. G. *Chem. Commun.* **2011**, *47*, 3177.
(96) Mal, S. S.; Stephens, F. H.; Baker, R. T. *Chem. Commun.* **2011**, *47*, 2922.
(97) Boulho, C.; Djukic, J.-P. *Dalton Trans.* **2010**, *39*, 8893.
(98) Kass, M.; Friedrich, A.; Drees, M.; Schneider, S. *Angew. Chem. Int. Ed.* **2009**, *48*, 905.
(99) Conley, B. L.; Williams, T. J. *Chem. Commun.* **2010**, *46*, 4815.
(100) Blaquiere, N.; Diallo-Garcia, S.; Gorelsky, S. I.; Black, D. A.; Fagnou, K. *J. Am. Chem. Soc.* **2008**, *130*, 14034.
(101) Kubas, G. J. *Metal Dihydrogen and σ-bond complexes*; Kluwer: New York, 2001.
(102) Alcaraz, G.; Sabo-Etienne, S. *Angew. Chem. Int. Ed.* **2010**, *49*, 7170.
(103) Shimoi, M.; Nagai, S.; Ichikawa, M.; Kawano, Y.; Katoh, K.; Uruichi, M.; Ogino, H. *J. Am. Chem. Soc.* **1999**, *121*, 11704.
(104) Ledger, A. E. W.; Ellul, C. E.; Mahon, M. F.; Williams, J. M. J.; Whittlesey, M. K. *Chem. Eur. J.* **2011**, *17*, 8704.
(105) Kawano, Y.; Hashiva, M.; Shimoi, M. *Organometallics* **2006**, *25*, 4420.
(106) Chaplin, A. B.; Weller, A. S. *Acta Crystallogr. Sect. C-Cryst. Struct. Commun.* **2011**, *67*, M355.
(107) Baker, R. T.; Gordon, J. C.; Hamilton, C. W.; Henson, N. J.; Lin, P. H.; Maguire, S.; Murugesu, M.; Scott, B. L.; Smythe, N. C. *J. Am. Chem. Soc.* **2012**, *134*, 5598.
(108) Sloan, M. E.; Staubitz, A.; Clark, T. J.; Russell, C. A.; Lloyd-Jones, G. C.; Manners, I. *J. Am. Chem. Soc.* **2010**, *132*, 3831.
(109) Dallanegra, R.; Chaplin, A. B.; Weller, A. S. *Angew. Chem. Int. Ed.* **2009**, *48*, 6875.
(110) Kubas, G. J.; Ryan, R. R.; Swanson, B. I.; Vergamini, P. J.; Wasserman, H. J. *J. Am. Chem. Soc.* **1984**, *106*, 451.
(111) Crabtree, R. H. *Angew. Chem. Int. Ed. Engl.* **1993**, *32*, 789.
(112) Kubas, G. J. *Chem. Rev.* **2007**, *107*, 4152.
(113) Young, R. D.; Hill, A. F.; Hillier, W.; Ball, G. E. *J. Am. Chem. Soc.* **2011**, *133*, 13806.
(114) Calladine, J. A.; Duckett, S. B.; George, M. W.; Matthews, S. L.; Perutz, R. N.; Torres, O.; Vuong, K. Q. *J. Am. Chem. Soc.* **2011**, *133*, 2303.
(115) Bernskoetter, W. H.; Schauer, C. K.; Goldberg, K. I.; Brookhart, M. *Science* **2009**, *326*, 553.
(116) Pike, S. D.; Thompson, A. L.; Algarra, A. G.; Apperley, D. C.; Macgregor, S. A.; Weller, A. S. *Science* **2012**, *337*, 1648.
(117) Alcaraz, G.; Chaplin, A. B.; Stevens, C. J.; Clot, E.; Vendier, L.; Weller, A. S.; Sabo-Etienne, S. *Organometallics* **2010**, *29*, 5591.
(118) Tang, C. Y.; Thompson, A. L.; Aldridge, S. *Angew. Chem. Int. Ed.* **2010**, *49*, 921.
(119) Tang, C. Y.; Phillips, N.; Bates, J. I.; Thompson, A. L.; Gutmann, M. J.; Aldridge, S. *Chem. Commun.* **2012**, *48*, 8096.
(120) Vidovic, D.; Addy, D. A.; Kramer, T.; McGrady, J.; Aldridge, S. *J. Am. Chem. Soc.* **2011**, *133*, 8494.
(121) MacInnis, M. C.; McDonald, R.; Ferguson, M. J.; Tobisch, S.; Turculet, L. *J. Am. Chem. Soc.* **2011**, *133*, 13622.
(122) These coordination modes are sometimes described as $\kappa^1$ and $\kappa^2$.
(123) Cassen, A.; Gloaguen, Y.; Vendier, L.; Duhayon, C.; Poblador-Bahamonde, A.; Raynaud, C.; Clot, E.; Alcaraz, G.; Sabo-Etienne, S. *Angew. Chem. Int. Ed.* **2014**, *53*, 7569.
(124) Johnson, H. C.; Leitao, E. M.; Whittell, G. R.; Manners, I.; Lloyd-Jones, G. C.; Weller, A. S. *J. Am. Chem. Soc.* **2014**.
(125) Jiang, Y. F.; Blacque, O.; Fox, T.; Frech, C. M.; Berke, H. *Organometallics* **2009**, *28*, 5493.
(126) Alcaraz, G.; Grellier, M.; Sabo-Etienne, S. *Acc. Chem. Res.* **2009**, *42*, 1640.
(127) Aldridge, S.; Coombs, D. L. *Coord. Chem. Rev.* **2004**, *248*, 535.
(128) Crossley, I. R.; Hill, A. F.; Willis, A. C. *Organometallics* **2005**, *24*, 1062.
(129) Chaplin, A. B.; Weller, A. S. *Angew. Chem. Int. Ed.* **2010**, *49*, 581.
(130) O'Neill, M.; Addy, D. A.; Riddlestone, I.; Kelly, M.; Phillips, N.; Aldridge, S. *J. Am. Chem. Soc.* **2011**, *133*, 11500.
(131) Cowley, H. J.; Holt, M. S.; Melen, R. L.; Rawson, J. M.; Wright, D. S. *Chem. Commun.* **2011**, *47*, 2682.
(132) Hansmann, M. M.; Melen, R. L.; Wright, D. S. *Chem. Sci.* **2011**, *2*, 1554.
(133) Liptrot, D. J.; Hill, M. S.; Mahon, M. F.; MacDougall, D. J. *Chem. Eur. J.* **2010**, *16*, 8508.
(134) Bellham, P.; Hill, M. S.; Kociok-Kohn, G.; Liptrot, D. J. *Chem. Commun.* **2013**, *49*, 1960.
(135) Spielmann, J.; Bolte, M.; Harder, S. *Chem. Commun.* **2009**, 6934.
(136) Bellham, P.; Hill, M. S.; Kociok-Köhn, G. *Organometallics* **2014**.

(137) Hill, M. S.; Kociok-Kohn, G.; Robinson, T. P. *Chem. Commun.* **2010**, *46*, 7587.
(138) Cui, P.; Spaniol, T. P.; Maron, L.; Okuda, J. *Chem. Eur. J.* **2013**, *19*, 13437.
(139) Erickson, K. A.; Wright, D. S.; Waterman, R. *J. Organomet. Chem.* **2014**, *751*, 541.
(140) Lu, E.; Yuan, Y.; Chen, Y.; Xia, W. *ACS Catal.* **2013**, *3*, 521.
(141) Clark, T. J.; Russell, C. A.; Manners, I. *J. Am. Chem. Soc.* **2006**, *128*, 9582.
(142) Luo, Y.; Ohno, K. *Organometallics* **2007**, *26*, 3597.
(143) Forster, T. D.; Tuononen, H. M.; Parvez, M.; Roesler, R. *J. Am. Chem. Soc.* **2009**, *131*, 6689.
(144) Wolstenholme, D. J.; Traboulsee, K. T.; Decken, A.; McGrady, G. S. *Organometallics* **2010**, *29*, 5769.
(145) Helten, H.; Dutta, B.; Vance, J. R.; Sloan, M. E.; Haddow, M. F.; Sproules, S.; Collison, D.; Whittell, G. R.; Lloyd-Jones, G. C.; Manners, I. *Angew. Chem. Int. Ed.* **2013**, *52*, 437.
(146) Beweries, T.; Hansen, S.; Kessler, M.; Klahn, M.; Rosenthal, U. *Dalton Trans.* **2011**, *40*, 7689.
(147) Beweries, T.; Thomas, J.; Klahn, M.; Schulz, A.; Heller, D.; Rosenthal, U. *ChemCatChem* **2011**, *3*, 1865.
(148) Pun, D.; Lobkovsky, E.; Chirik, P. J. *Chem. Commun.* **2007**, 3297.
(149) Miyazaki, T.; Tanabe, Y.; Yuki, M.; Miyake, Y.; Nishibayashi, Y. *Organometallics* **2011**, *30*, 2394.
(150) Rousseau, R.; Schenter, G. K.; Fulton, J. L.; Linehan, J. C.; Engelhard, M. H.; Autrey, T. *J. Am. Chem. Soc.* **2009**, *131*, 10516.
(151) Kawano, Y.; Uruichi, M.; Shimoi, M.; Taki, S.; Kawaguchi, T.; Kakizawa, T.; Ogino, H. *J. Am. Chem. Soc.* **2009**, *131*, 14946.
(152) Hebden, T. J.; Denney, M. C.; Pons, V.; Piccoli, P. M. B.; Koetzle, T. F.; Schultz, A. J.; Kaminsky, W.; Goldberg, K. I.; Heinekey, D. M. *J. Am. Chem. Soc.* **2008**, *130*, 10812.
(153) Dietrich, B. L.; Goldberg, K. I.; Heinekey, D. M.; Autrey, T.; Linehan, J. C. *Inorg. Chem.* **2008**, *47*, 8583.
(154) Paul, A.; Musgrave, C. B. *Angew. Chem. Int. Ed.* **2007**, *46*, 8153.
(155) Keaton, R. J.; Blacquiere, J. M.; Baker, R. T. *J. Am. Chem. Soc.* **2007**, *129*, 1844.
(156) Yang, X.; Hall, M. B. *J. Am. Chem. Soc.* **2008**, *130*, 1798.
(157) Yang, X.; Hall, M. B. *J. Organomet. Chem.* **2009**, *694*, 2831.
(158) Zimmerman, P. M.; Paul, A.; Musgrave, C. B. *Inorg. Chem.* **2009**, *48*, 5418.
(159) Zimmerman, P. M.; Paul, A.; Zhang, Z.; Musgrave, C. B. *Angew. Chem. Int. Ed.* **2009**, *48*, 2201.
(160) Ai, D.; Guo, Y.; Liu, W.; Wang, Y. *J. Phys. Org. Chem.* **2014**, *27*, 597.
(161) Vogt, M.; de Bruin, B.; Berke, H.; Trincado, M.; Grutzmacher, H. *Chem. Sci.* **2011**, *2*, 723.
(162) Wallis, C. J.; Dyer, H.; Vendier, L.; Alcaraz, G.; Sabo-Etienne, S. *Angew. Chem. Int. Ed.* **2012**, *51*, 3646.
(163) Lu, Z. Y.; Conley, B. L.; Williams, T. J. *Organometallics* **2012**, *31*, 6705.
(164) Conley, B. L.; Guess, D.; Williams, T. J. *J. Am. Chem. Soc.* **2011**, *133*, 14212.
(165) Schreiber, D. F.; O'Connor, C.; Grave, C.; Ortin, Y.; Muller-Bunz, H.; Phillips, A. D. *ACS Catal.* **2012**, *2*, 2505.
(166) Phillips, A. D.; Laurenczy, G.; Scopelliti, R.; Dyson, P. J. *Organometallics* **2007**, *26*, 1120.
(167) Chapman, A. M.; Haddow, M. F.; Wass, D. F. *J. Am. Chem. Soc.* **2011**, *133*, 8826.
(168) Rosello-Merino, M.; Lopez-Serrano, J.; Conejero, S. *J. Am. Chem. Soc.* **2013**, *135*, 10910.
(169) Leitao, E. M.; Stubbs, N. E.; Robertson, A. P. M.; Helten, H.; Cox, R. J.; Lloyd-Jones, G. C.; Manners, I. *J. Am. Chem. Soc.* **2012**, *134*, 16805.
(170) Robertson, A. P. M.; Leitao, E. M.; Manners, I. *J. Am. Chem. Soc.* **2011**, *133*, 19322.
(171) Rossin, A.; Bottari, G.; Lozano-Vila, A. M.; Paneque, M.; Peruzzini, M.; Rossi, A.; Zanobini, F. *Dalton Trans.* **2013**, *42*, 3533.
(172) Butera, V.; Russo, N.; Sicilia, E. *ACS Catal.* **2014**, *4*, 1104.

# 2 Sigma complexes and dehydrogenative homocoupling of amine-boranes

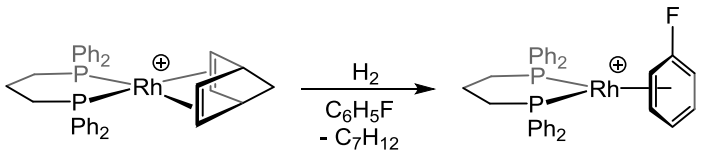
## 2.1. Introduction

As discussed in Chapter 1, the $\{Rh(Xantphos)\}^+$ fragment was targeted due to its similarity to the $[Rh(PPh_2(CH_2)_xPPh_2)(\eta^6\text{-}C_6H_5F)][BAr^F{}_4]$ (x = 3 – 5) complexes, which are proven catalysts for the production of high molecular weight $[H_2BNMeH]_n$ from the dehydrocoupling of $H_3B{\cdot}NMeH_2$.[1] It was also speculated that the hemilability of Xantphos may enable observation of intermediates during the catalysis, in order to deduce new insights into the mechanism of polymerisation. This Chapter involves the synthesis of 'model' $\{Rh(Xantphos)\}^+$ complexes using tertiary amine-boranes, and reports the first metal-mediated homocoupling of an amine-borane.

## 2.2. Attempted formation of $[Rh(Xantphos)(\eta^6\text{-}C_6H_5F)][BAr^F{}_4]$

A method employed by the Weller group to access latent low-coordinate $\{RhL_2\}^+$ complexes (L = phosphine or $L_2$ = bidentate phosphine) is the hydrogenation of a strained norbornadiene (NBD) precursor $[RhL_2(NBD)]^+$ in a weakly coordinating solvent, *e.g.* $C_6H_5F$ or 1,2-$C_6H_4F_2$, to yield $[RhL_2(\eta^6\text{-arene})]^+$ (Scheme 2.1, for example).[1] Weakly coordinating anions, *e.g.* $[BAr^F{}_4]^-$ ($Ar^F$ = 3,5-$(CF_3)_2C_6H_3$), are used to prevent competitive anion coordination to the metal or decomposition by anion reactivity. The arene solvent is bound $\eta^6$ to the metal and can be readily displaced, making them ideal for various catalytic applications including dehydrocoupling, hydroacylation, Suzuki-type couplings and C—S bond cleavage reactions.[1-9] Recently, Weller and McIndoe quantified the binding strengths of a range of $[Rh(L_2)(\eta^6\text{-arene})][BAr^F{}_4]$ complexes using ESI-MS and solution equilibrium measurements,

finding dependence upon the ligand substituents, ligand bite angle, and nature of the arene.[10]




**Scheme 2.1** Formation of $[Rh(Ph_2P(CH_2)_3PPh_2)(\eta^6\text{-}C_6H_5F)][BAr^F{}_4]$. $[BAr^F{}_4]^-$ anions not shown.

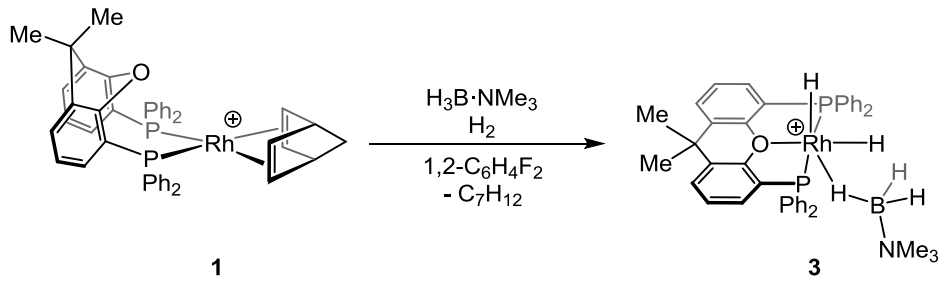
This strategy was employed in an attempt to form $[Rh(Xantphos)(\eta^6\text{-}C_6H_5F)][BAr^F{}_4]$, a potential $Rh^I$ precursor suitable for investigating the reactivity of the $\{Rh(Xantphos)\}^+$ fragment with amine-boranes. However, on hydrogenation (4 atm) of $[Rh(\kappa^2{}_{P,P}\text{-}Xantphos)(NBD)][BAr^F{}_4]$[11] (**1**) in $C_6H_5F$, a mixture of species was observed. The hydride region of the $^1H$ NMR spectrum showed a very broad signal at δ –19 and a broad multiplet at δ –20.8, while the $^{31}P\{^1H\}$ NMR spectrum showed multiple broad overlapping signals. No sensible molecular ion could be assigned by ESI-MS. No signals characteristic of an $\eta^6$-bound arene (approximately δ 5 – 5.5)[1] were observed by $^1H$ NMR spectroscopy. This contrasts the closely related complex $[Rh(\kappa^2{}_{P,P}\text{-}DPEphos)(NBD)][BAr^F{}_4]$, which rapidly forms $[Rh(\kappa^2{}_{P,P}\text{-}DPEphos)(\eta^6\text{-}C_6H_5F)][BAr^F{}_4]$ upon hydrogenation (4 atm) in $C_6H_5F$.[12] The apparent preferential formation of hydride complexes from **1** has been observed with other solvents. In acetone, for example, $[Rh(\kappa^3{}_{P,O,P}\text{-}Xantphos)(H)_2(acetone)][BAr^F{}_4]$ is formed,[11] whereas the analogous reaction using DPEphos forms $[Rh(\kappa^2{}_{P,P}\text{-}DPEphos)(acetone)_2][BAr^F{}_4]$.[13] Moreover, $[Rh(\kappa^3{}_{P,O,P}\text{-}Xantphos)(H)_2][BAr^F{}_4]$ was characterised by NMR spectroscopy as the sole product on hydrogenation of **1** in $CD_2Cl_2$.[14] The larger bite angle of Xantphos *vs* DPEphos may favour the formation of

dihydrides (see Chapter 1), and steric factors may play a role in hindering $\eta^6$ coordination of $C_6H_5F$.

## 2.3. Formation of [Rh(κ³P,O,P-Xantphos)(H)₂(η¹-H₃B·NMe₃)][BArᶠ₄]

Since the hydrogenation of **1** in $C_6H_5F$ yielded a mixture of products, an alternative route to $\{Rh(Xantphos)\}^+$ was required. As discussed in Chapter 1, sigma coordination of amine-boranes to a metal centre is generally weak. Thus, an amine-borane with no N—H functionality (to avoid dehydrocoupling) may prove to be an ideal 'masking' ligand for the $\{Rh(Xantphos)\}^+$ fragment. Additionally, the coordination of tertiary amine-boranes, *e.g.* $H_3B{\cdot}NMe_3$, to the metal centre can model the interactions of the metal with more reactive primary and secondary amine-boranes. Consequently, $[Rh(\kappa^2_{P,P}\text{-Xantphos})(\eta^2\text{-}H_3B{\cdot}NMe_3)][BAr^F_4]$ (**2**) was targeted. These complexes are known with other rhodium diphosphine fragments, $[RhL_2][BAr^F_4]$ ($L_2$ = $Ph_2P(CH_2)_xPPh_2$ (x = 3 – 5), DPEphos).[1,12]

Hydrogenation (4 atm) of **1** in the presence $H_3B{\cdot}NMe_3$ (1 eq.) in 1,2-$C_6H_4F_2$ or $C_6H_5F$ solution formed a single product (by NMR spectroscopy), assigned as $[Rh(\kappa^3_{P,O,P}\text{-Xantphos})(H)_2(\eta^1\text{-}H_3B{\cdot}NMe_3)][BAr^F_4]$ (**3**) (Scheme 2.2).




**Scheme 2.2** Formation of **3** from **1**. $[BAr^F_4]^-$ anions not shown.

Layering the pale yellow solution with $H_2$-saturated pentane at 5 °C yielded pale yellow oil-coated crystalline material free of norbornane (NBA) or excess $H_3B{\cdot}NMe_3$. In $CD_2Cl_2$ under $H_2$ (4 atm), the material was characterised by NMR spectroscopy. In the $^{31}P\{^1H\}$ NMR spectrum, a single environment at δ 43.6 (d, $^1J_{RhP}$ = 115 Hz) was seen, with a coupling constant indicative of a $Rh^{III}$ centre.[11] In the $^1H$ NMR spectrum (Figure 2.1), the hydride region shows three signals at δ –0.97, δ –14.69 and δ –19.11 with relative integrals of 3:1:1, respectively. The signal at δ –0.97 is quadrupolar broadened (FWHM = 145 Hz) and sharpens considerably upon $^{11}B$ decoupling (FWHM = 31 Hz), and thus was assigned as the $H_3B$ group, in which the bridging Rh—H—B and terminal B—H groups are exchanging rapidly compared with the NMR timescale. This behaviour has been observed in other $\eta^1$ amine-borane complexes.[15-17] At 218 K, this fluxionality is 'frozen out,' evident by a very broad signal at δ –6.23 of relative integral 1H, corresponding to the bridging Rh—H—B hydride. The signals for the terminal B—H hydrides were not observed; presumably they are broad and/or obscured by the aliphatic region (typical chemical shift values for terminal B—H resonances in $\eta^1$ complexes are of the range 0 – 3 ppm).[16,18] The $^{11}B$ NMR spectrum at 298 K is consistent with $\eta^1$-bound $H_3B{\cdot}NMe_3$; the signal for $H_3B{\cdot}NMe_3$ is a broad hump at δ –8.7, essentially unshifted compared with free $H_3B{\cdot}NMe_3$ in $CD_2Cl_2$ (δ –8.4, t, $J_{HB}$ = 97 Hz), implying weak interaction of the borane fragment with the metal. With a stronger M···B interaction, the electron density at the B atom is reduced, deshielding the nucleus and resulting in a more downfield $^{11}B$ chemical shift relative to the starting amine-borane (*cf.* $\eta^2$ amine-borane complexes, Section 2.5.2). The use of NMR spectroscopy in the characterisation of σ borane compounds has been previously discussed.[19]

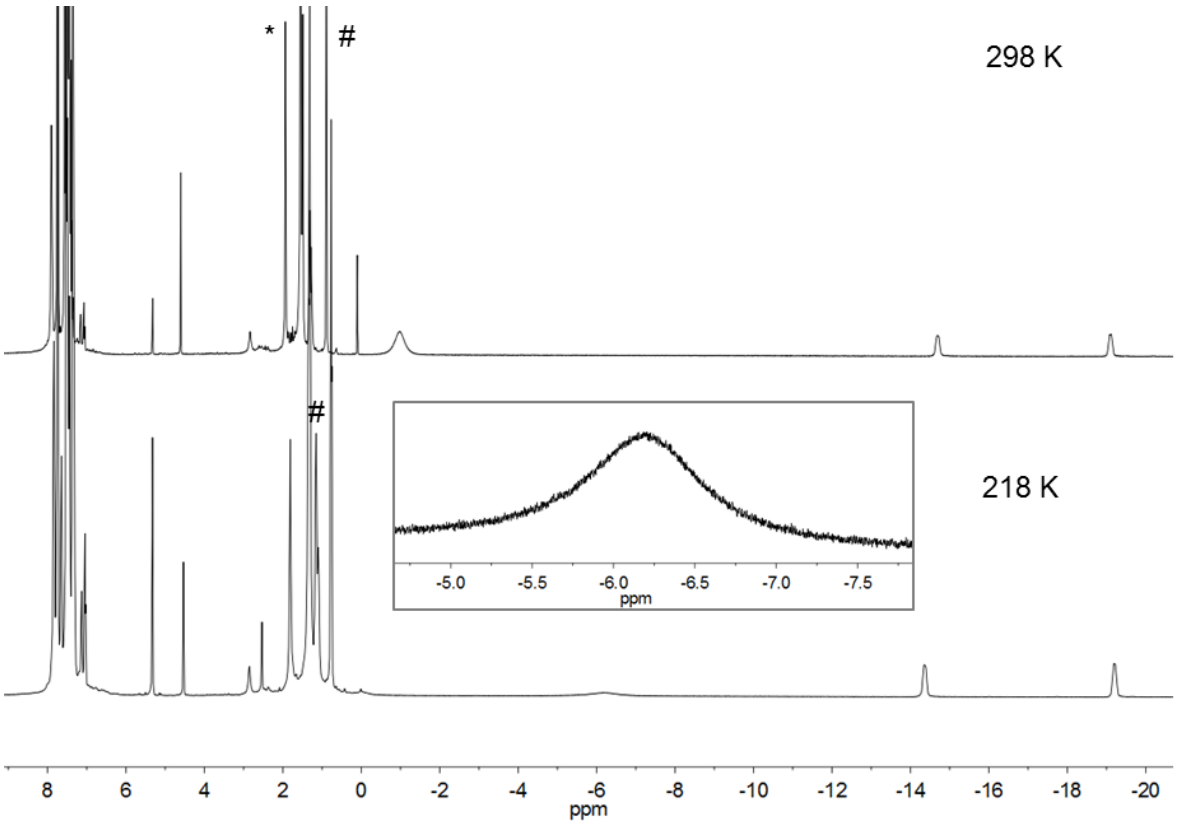



**Figure 2.1** $^{1}$H NMR spectrum of **3** in $CD_2Cl_2$ under $H_2$ at 298 K (upper) and 218 K (lower). Inset shows peak at δ –6.23 at 218 K. # = residual pentane; * = free $H_3B{\cdot}NMe_3$.

The Rh—H signals at δ –14.69 and δ –19.11 are each observed as overlapping doublets of triplets of doublets (Figure 2.2), indicating that each hydride couples to one rhodium atom, two phosphorus atoms and one hydride. Upon $^{31}$P decoupling, the signals collapse to doublets of doublets (for each, $^{1}J_{RhH}$ = 27 Hz, $^{2}J_{HH}$ = 7 Hz) (Figure 2.2). The magnitude of the $^{2}J_{HH}$ coupling constant implies the inequivalent hydrides are mutually *cis*.[11] The signal at δ –14.69 is broader than that at δ –19.11, but resolves somewhat on $^{11}$B decoupling (Figure 2.2), and a $^{2}J_{PH}$ coupling constant of 13 Hz can be observed. This implies that the signal at δ –14.69 is *trans* to the borane.[20] Upon selective $^{1}$H decoupling at δ –14.69, the signal at δ –19.11 collapses to a doublet of triplets ($^{2}J_{PH}$ = 14 Hz, $^{1}J_{RhH}$ = 27 Hz).

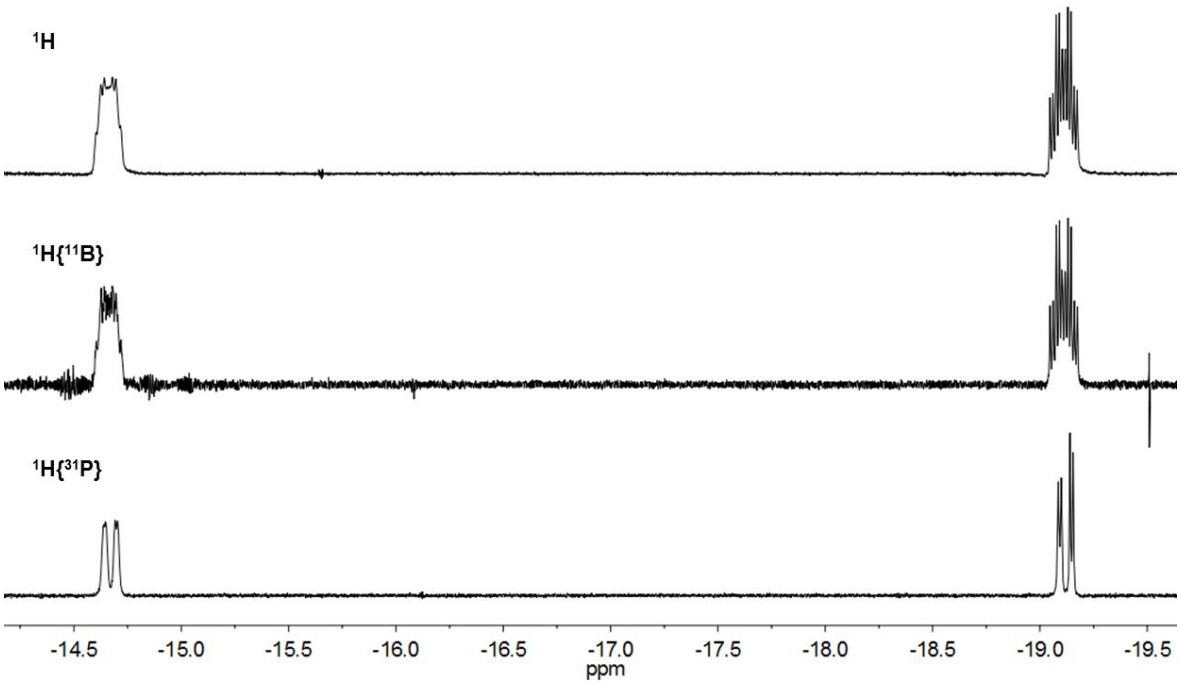



**Figure 2.2** $^{1}$H, $^{1}$H{$^{11}$B} and $^{1}$H{$^{31}$P} NMR spectra for the hydrides at δ –14.69 and δ –19.11 in **3**.

The data show that each hydride is *cis* to both $^{31}$P environments (hydrides *cis* to phosphines typically show $^{2}J_{PH}$ coupling constants of approximately 10 – 30 Hz, while hydrides *trans* to phosphines demonstrate larger coupling constants of approximately 90 – 160 Hz).[21] The structure of **3** is deduced to be in an octahedral arrangement around the rhodium atom, with the Xantphos ligand coordinated in a *mer*-$\kappa^{3}_{P,O,P}$ geometry. The Xantphos methyl signals are observed as two separate singlets in the $^{1}$H NMR spectrum at δ 1.93 and δ 1.49, each with relative integrals of 3H. These hydride resonances are very similar to those in the closely related complexes [Rh($\kappa^{3}_{P,O,P}$-Xantphos)$(H)_2$(acetone)][$BAr^{F}_4$] (at 225 K; the complex is fluxional at room temperature) and [Rh($\kappa^{3}_{P,O,P}$-Xantphos)$(H)_2$(MeCN)][$BAr^{F}_4$] (**4**).[11] ESI-MS of **3** was attempted but no sensible molecular ion was deduced, presumably due to decomposition in the spectrometer (even under anaerobic conditions).

Pure solid material of **3** could not be obtained due to its instability upon removal of the $H_2$ atmosphere. However, oil-covered single crystals were grown under $H_2$ (*vide supra*). The solid state structure contained two independent cations with similar structural metrics (Figure 2.3) and is consistent with the structure implied by the solution NMR data. The Xantphos ligand is coordinated *mer* with the oxygen atom bound to the metal centre; the Rh—O distance (2.199(3) Å) is slightly shorter than the analogous distances in the $Rh^{III}$ compounds **4** and [Rh($\kappa^3_{P,O,P}$-Xantphos)(H)($COCH_2CH_2SMe$)][$BAr^F_4$] (2.223(2) Å and 2.308(2) Å, respectively).[11] The P1-Rh1-P1' angle of 162.40(5)° is more compressed than the P-Rh-P angle in **4** of 164.31(3)°, possibly owing to the increased steric bulk of $H_3B{\cdot}NMe_3$ *vs* MeCN. Although the hydrides H1 and H2 were located on the Fourier map, they could not be refined sensibly and so were placed in calculated positions. Nonetheless, the hydrides around the $BH_3$ group were located and refined and indicate $\eta^1$ coordination of the $H_3B{\cdot}NMe_3$ unit. The Rh1-B1 bond length of 2.759(6) Å is also consistent with $\eta^1$ coordination, being slightly longer than the $\eta^1$ Rh—B distance in [Rh{$P(C_5H_9)_2(\eta^2\text{-}C_5H_7)$}($\eta^2$-$H_3B{\cdot}NMe_2H$)($\eta^1$-$H_3B{\cdot}NMe_2H$)]$BAr^F_4$] (2.661(3) Å).[22] Whittlesey's complex [Ru($\kappa^3_{P,O,P}$-Xantphos)($PPh_3$)($\eta^1$-$H_3B{\cdot}NH_3$)H][$BAr^F_4$] has a M—B distance of 2.94 Å,[16] longer than that in **3,** while the Ru—B distance in Shimoi's complex [$CpRu(PMe_3)_2(\eta^1\text{-}H_3B{\cdot}NMe_3)$][$BAr^F_4$] is shorter, 2.648(3) Å.[17] For comparison, the covalent radii of Ru and Rh are 1.46(7) Å and 1.42(7) Å, respectively.[23]

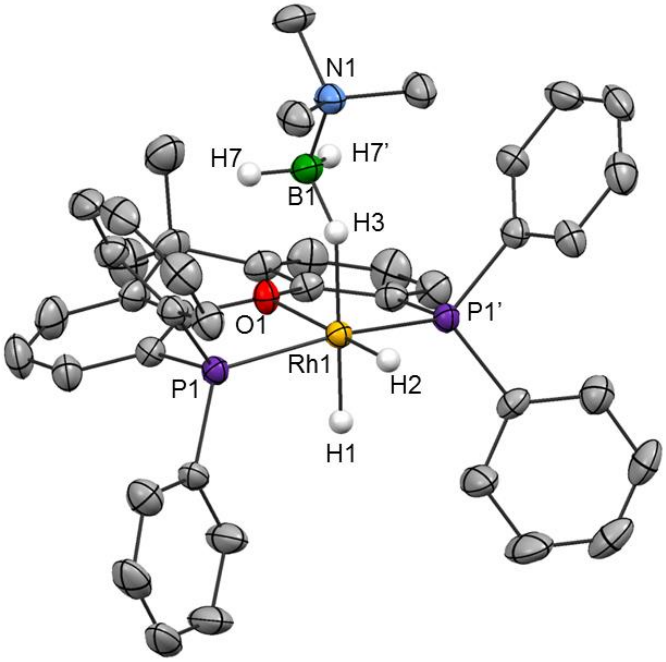



**Figure 2.3** Solid state structure of the cationic portion of **3**. Displacement ellipsoids are drawn at the 50% probability level. Only one of the two independent cations in the unit cell is shown. A crystallographically imposed mirror plane bisects each cation. All carbon bound H atoms are omitted for clarity. Selected bond lengths (Å) and angles (°): Rh1-P1, 2.2683(10); Rh1-O1, 2.199(3); Rh1-B1, 2.759(6); B1-N1, 1.609(8); P1-Rh1-P1, 162.40(5); P1-Rh1-B1, 93.70(3); N1-B1-Rh1, 133.5(4).

## 2.4. Reactivity of complex 3

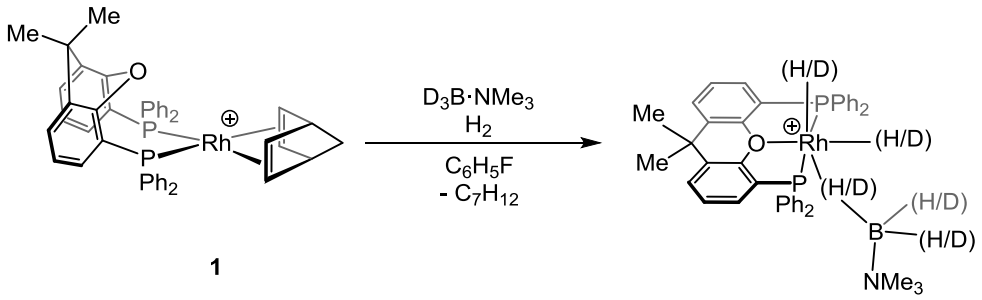
### 2.4.1. Stability of complex 3

**3** is not stable in 1,2-$C_6H_4F_2$ solution for prolonged periods in the absence of a $H_2$ atmosphere. Under argon, decomposition occurs to form a mixture of some known (**8**, *vide infra*) and some unidentified products (overall, ~50% decomposition of **3** within 24 hours, measured by $^{31}P\{^1H\}$ NMR spectroscopy). Under $H_2$, **3** does not appear to degrade within 24 hours. **3** also remains the sole organometallic product in the presence of excess $H_3B{\cdot}NMe_3$ under $H_2$ at room temperature.

### 2.4.2. H/D exchange in complex 3

Recently, Weller and Macgregor used $[M(PCy_3)_2(H)_2(\eta^2\text{-}H_3B{\cdot}NMe_3)][BAr^F{}_4]$ (M = Rh, Ir) to investigate, by computation and experiment, the fluxional processes in these $\eta^2$ complexes. They found that B—H bridging/terminal exchange was fast for both Ir and Rh, and rapid M—H/D mixing occurred on addition of exogenous $D_2$. A slower M—H/B—H exchange process was also observed, which was faster for Ir than Rh. This was attributed to a degree of $M^V$ character in the transition state for this exchange, which is more accessible for Ir.[24] B—H activation is key in the dehydrocoupling of amine-boranes and, as **3** provides a model for the behaviour of the more reactive $H_3B{\cdot}NMe_2H$ and $H_3B{\cdot}NMeH_2$ complexes (Chapter 4), the propensity for B—H and Rh—H activation in **3** was probed using $D_3B{\cdot}NMe_3$.

Complex **1** was hydrogenated (4 atm) in the presence of $D_3B{\cdot}NMe_3$ in $C_6H_5F$ solution to form $[Rh(\kappa^3{}_{P,O,P}\text{-Xantphos})(H)_2(\eta^1\text{-}D_3B{\cdot}NMe_3)][BAr^F{}_4]$ (**3a**). Immediate monitoring by NMR spectroscopy indicated that B—D/Rh—H mixing was rapidly occurring (Scheme 2.3).




**Scheme 2.3** Addition of $D_3B{\cdot}NMe_3$ and $H_2$ (4 atm) to **1**. $[BAr^F{}_4]^-$ anions not shown.

The $^1H$ NMR spectrum of this reaction after 2 minutes showed B—H resonances (δ –1.12, relative integral 1H) and Rh—H resonances (δ –14.53 and –18.98, each relative integral 0.4H). The $^2H$ NMR spectrum (Figure 2.4) is consistent with this, with

the B—D and two Rh—D signals being observed with relative integrals 2D:0.6D:0.6D, respectively, consistent with $B(H/D)_3$ and two Rh(H/D) groups overall.

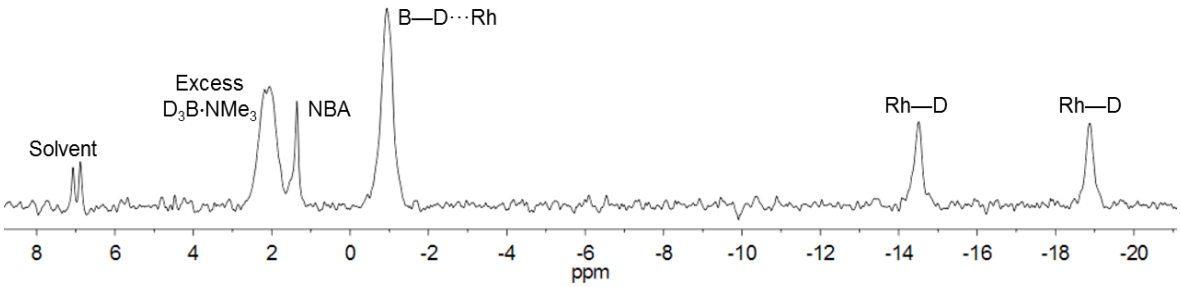
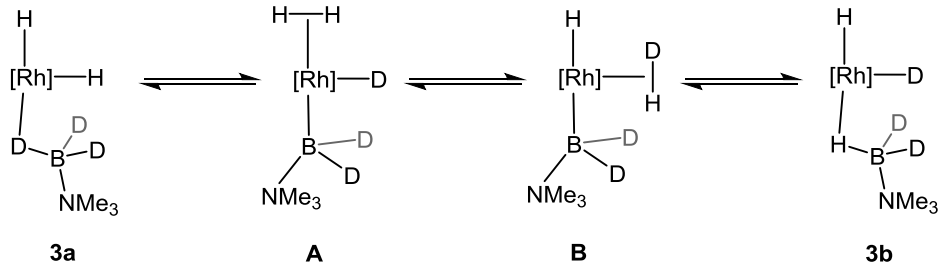



**Figure 2.4** $^2H$ NMR spectrum 2minutes after addition of $D_2$ to **1** in the presence of $D_3B{\cdot}NMe_3$ in $C_6H_5F$ solution.

These data indicate fast Rh—H/B—D exchange occurs in **3a**, which we suggest operates *via* a σ-CAM[25] type process in which B—D activation at the $Rh^{III}$ centre yields a rhodium dihydrogen base-stabilised boryl compound (*e.g.* **A**, Scheme 2.4). This can rearrange forming, for example, **B**, resulting in species such as **3b** as observed by NMR spectroscopy. Small amounts of HD (δ 4.49, t, $^1J_{DH}$ = 43 Hz) were observed in the $^1H$ NMR spectrum, which could arise from the displacement of HD from an intermediate akin to **B** by exogenous $H_2$.[24] No evidence for boryl intermediates (*e.g.* **A** or **B**) was observed by NMR spectroscopy.

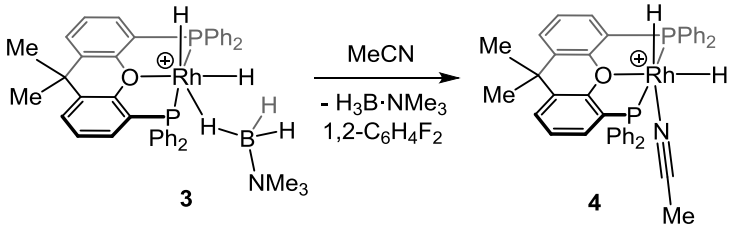



**Scheme 2.4** Proposed σ-CAM mechanism for Rh—H/B—D mixing in **3a**. [Rh] = [Rh(Xantphos)][$BAr^F_4$]. Not all pathways and H/D combinations shown.

The $^{2}H$ NMR spectrum also shows a peak at δ 1.32 (Figure 2.4). The origin of this peak is not clear; the region δ 1.30 – 1.35 in the $^{1}H$ NMR spectrum includes a Xantphos methyl group, the bound $NMe_3$ group and NBA (formed *in situ* from NBD hydrogenation) resonances. It is likely that the signal arises from deuteration on the *exo* face of norbornene[26] due to exchange occurring before all of **1** has been hydrogenated, but the origin of this peak has not been investigated further.

### 2.4.3. Addition of MeCN to complex 3

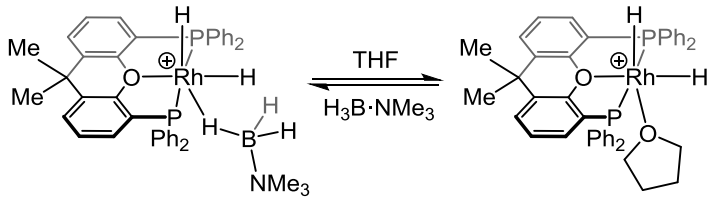
Addition of MeCN (~20 eq.) to **3** immediately formed the previously characterised MeCN complex **4**[11] and free $H_3B{\cdot}NMe_3$ (Scheme 2.5), measured by NMR spectroscopy. The weakly σ bound $H_3B{\cdot}NMe_3$ ligand in **3** is displaced by strong σ-donor (and reasonable π-acceptor) MeCN, and analogous behaviour has been observed previously on addition of MeCN to σ amine-borane complexes.[27-29]




**Scheme 2.5** Addition of MeCN to **3**. $[BAr^{F}_4]^-$ anions not shown.

### 2.4.4. Addition of THF to complex 3

Upon addition of 100 eq. THF to a 1,2-$C_6H_4F_2$ solution of **3**, a new species is observed that corresponds to the THF adduct, $[Rh(\kappa^3_{P,O,P}\text{-Xantphos})(H)_2(THF)][BAr^{F}_4]$ (**5**). Unlike with MeCN, a 45:55 mixture of **3**:**5** was established (measured by $^{1}H$ NMR spectroscopy), implying that $H_3B{\cdot}NMe_3$ can bind competitively with THF under these conditions (Scheme 2.6).




**3** 45% **5** 55%

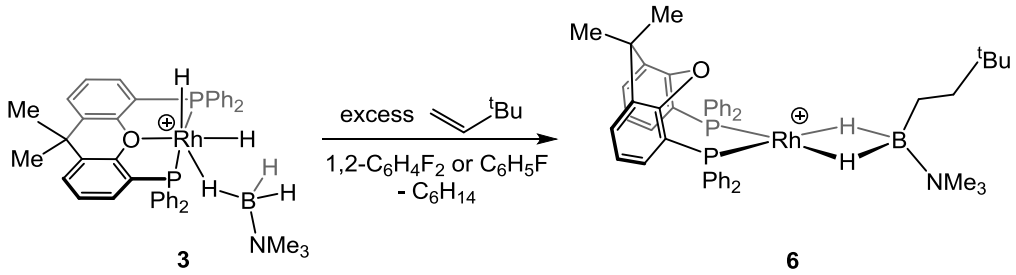
**Scheme 2.6** Addition of 100 eq. THF to **3** in 1,2-$C_6H_4F_2$. $[BAr^F{}_4]^-$ anions not shown.

**5** could also be formed quantitatively by hydrogenating **1** in THF. Layering the solution with pentane at 5 °C resulted in pale yellow crystals of **5**. While these crystals diffracted, the structure showed extensive disorder that we were unable to model. **5** in 1,2-$C_6H_4F_2$ solution shows similar NMR spectroscopic data to **3**, **4** and $[Rh(\kappa^3{}_{P,O,P}\text{-Xantphos})(H)_2(acetone)][BAr^F{}_4]$ at 225 K.[11] The $^{31}P\{^1H\}$ NMR spectrum of **5** consists of a doublet at δ 43.8 ($^1J_{RhP}$ = 118 Hz), indicative of a $Rh^{III}$ centre. Two hydride signals were observed at δ –19.01 and δ –19.88, each a broad doublet of triplet of doublets. A $^2J_{PH}$ coupling constant of 13 Hz was determined for each hydride. $^{31}P$ decoupling collapsed these signals to doublets of doublets: δ –19.01 ($^1J_{RhH}$ = 31 Hz, $^2J_{HH}$ = 8 Hz); δ –19.88 ($^1J_{RhH}$ = 29 Hz, $^2J_{HH}$ = 8 Hz). Since both hydrides are *trans* to an ether linkage in **5**, these have similar chemical shifts, compared with those in **3** that are *ca.* 5 ppm apart. Peaks corresponding to bound THF were observed at δ 2.90 (br, $CH_2$ groups at the 3 and 4 positions) and δ 0.84 (br, $CH_2$ groups at the 2 and 5 positions), each with relative integral 4H, showing that one molecule of THF is bound to the metal. Separate environments were seen for the Xantphos ligand at δ 1.92 and δ 1.49. ESI-MS is also consistent with the formulation of **5**, with peaks observed with *m/z* = 683.12 ($[Rh(Xantphos)(H)_2]^+$, calc. 683.11), and *m/z* = 755.18 (**5**$^+$, calc. 755.17). Many rhodium-THF complexes have been observed and characterised previously.[30-35]

## 2.5. Synthesis and characterisation of a $Rh^{I}$ Xantphos complex

### 2.5.1. Formation of $[Rh(\kappa^2_{P,P}\text{-Xantphos})(\eta^2\text{-}H_2B(CH_2CH_2{}^tBu)\cdot NMe_3)][BAr^F{}_4]$

To obtain the target $\{Rh(Xantphos)\}^+$ fragment, a method of reducing **3** to a $Rh^I$ species was required. As degassing the solution resulted in decomposition (Section 2.4.1), we turned to hydrogen acceptor 3,3-dimethylbut-1-ene (TBE)[36] to enable the reduction. Degassing a solution of **3** and quick addition of two equivalents of TBE led to a colour change from pale yellow to deep blue, and the formation of a new product was observed quantitatively by NMR spectroscopy within 10 minutes. The data for the new product were consistent with the formulation $[Rh(\kappa^2_{P,P}\text{-Xantphos})(\eta^2\text{-}H_2B(CH_2CH_2{}^tBu)\cdot NMe_3)][BAr^F{}_4]$ (**6**). **6** results from reduction to $Rh^I$, and the hydroboration of TBE by $H_3B\cdot NMe_3$ to form $H_2B(CH_2CH_2{}^tBu)\cdot NMe_3$ (**I**), which is σ bound to the metal centre with $\eta^2$ coordination (Scheme 2.7).




**Scheme 2.7** Addition of TBE (2 or more eq.) to **3** to form **6**. $[BAr^F{}_4]^-$ anions not shown.

**6** is closely related to $[Rh(P^iBu_2{}^tBu)_2(\eta^2\text{-}H_2B(CH_2CH_2{}^tBu)\cdot NMe_3)][BAr^F{}_4]$ (**i-77**), reported by Weller and co-workers in 2011, arising from the slow (3 days) hydroboration of TBE by $[Rh(P^iBu_2{}^tBu)_2(\eta^2\text{-}H_3B\cdot NMe_3)][BAr^F{}_4]$ (**i-76**).[37] During the formation of **6**, no intermediates such as **2** or $[Rh(\kappa^3_{P,O,P}\text{-Xantphos})(H)_2(\eta^1\text{-}H_2B(CH_2CH_2{}^tBu)\cdot NMe_3)][BAr^F{}_4]$ (**7**, Section 2.5.3) were observed by NMR

spectroscopy. See Chapter 3 for a thorough account of the catalytic hydroboration of TBE by $H_3B{\cdot}NMe_3$ in this system.

### 2.5.2. Characterisation of complex 6

The $^{31}P\{^1H\}$ NMR spectrum of **6** in $CD_2Cl_2$ consists of a doublet at δ 26.8 ($^1J_{RhP}$ = 182 Hz), consistent with Xantphos coordinated to a $Rh^I$ centre.[38] Two separate relative integral 3H signals are seen for the Xantphos methyl groups at δ 1.78 and δ 1.67. The hydride region shows a broad resonance at δ –6.91 of relative integral 2H. Upon $^{11}B$ decoupling, this signal appears as a broad virtual triplet ($^2J_{PtransH}$ ~36 Hz, $^1J_{RhP}$ ~36 Hz). Signals at δ 1.59 and δ 0.50 (each integral 2H) indicate that the anti-Markovnikov product of hydroboration has formed, as was reported with **i-77**.[37] No evidence for the Markovnikov product was observed, which would be expected to show two signals corresponding to the alkyl chain with relative integrals of 3H and 1H. The $^{11}B$ NMR spectrum contains a very broad signal at δ 36, consistent with an amine-borane bound $\eta^2$ to a $Rh^I$ centre; the signal is shifted 37 ppm downfield from that of free **I** ($\delta(^{11}B)$ = –0.8).[37] This change in chemical shift suggests M···B involvement in the bonding, unlike in the $\eta^1$ bound **3**. Marks has noted similarities in frontier orbitals and electron donation between $\eta^2$-bound $[BH_4]^-$ (and therefore ligands such as **I**) and $\eta^3$-allyl complexes.[39] Nonetheless, the binding of **I** is still weak as free **I** is observed immediately upon the addition of MeCN to **6**.

Layering a 1,2-$C_6H_4F_2$ solution of **6** with pentane at –30 °C yielded crystals suitable for X-ray diffraction, and the solid state structure obtained is consistent with the proposed connectivity (Figure 2.5).

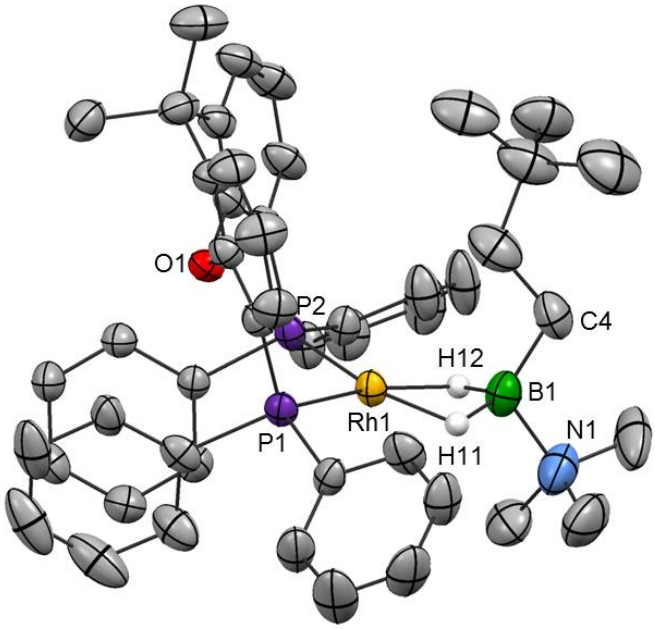
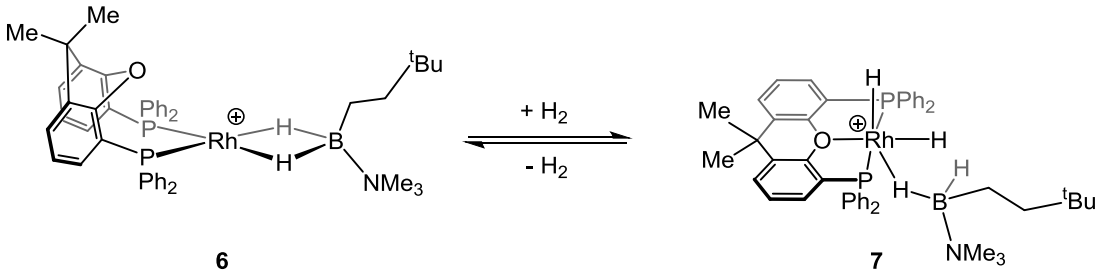



**Figure 2.5** Solid state structure of **6**. $[BAr^F_4]^-$ anion and all carbon-bound hydrogen atoms omitted for clarity. Displacement ellipsoids are drawn at the 50% probability level. Selected bond lengths (Å) and angles (°): Rh1-P1, 2.2678(12); Rh1-P2, 2.2494(12); Rh1-O1, 3.431(3); Rh1-B1, 2.162(5); B1-N1, 1.604(4); B1-C4, 1.585(8); P2-Rh1-P1, 101.49(4); Rh1-B1-C4, 118.5(3); Rh-B1-N1, 115.5(4); C4-B1-N1, 115.5(4).

During refinement of the structure of **6**, the bridging hydrides H11 and H12 were located, and reveal a *pseudo*-square planar geometry around rhodium with the Xantphos ligand in *cis*-$\kappa^2_{P,P}$ coordination mode. The oxygen atom is not bound to the metal centre, indicated by the Rh—O distance of 3.431(3) Å (*cf.* 2.199(3) Å in **3**), similar to the species $[Rh(\kappa^2_{P,P}\text{-DPEphos})(\eta^2\text{-}H_3B{\cdot}NMe_3)][BAr^F_4]$ that has an Rh—O distance of 3.547(2) Å.[12] The Rh—B distance in **6** (2.162(5) Å) is markedly shorter than in **3** (2.759(6) Å), consistent with stronger Rh···B interaction, as also implied by the solution $^{11}$B NMR spectroscopic data. ESI-MS also supports the formation of **6**, with a molecular ion observed with *m/z* = 838.31 (calc. 838.30) of the expected isotopic pattern. Unlike with **3**, **6** could be isolated as a pure solid in good yield (79%) and elemental analysis confirmed the bulk purity of the solid.

### 2.5.3. Hydrogenation of complex 6

Addition of $H_2$ (4 atm) to **6** in 1,2-$C_6H_4F_2$ in a high pressure NMR tube resulted in the formation (~90%, by $^1$H NMR spectroscopy) of [Rh($\kappa^3_{P,O,P}$-Xantphos)(H)$_2$($\eta^1$-$H_2B(CH_2CH_2{}^tBu)\cdot NMe_3$][$BAr^F{}_4$] (**7**), with ~10% **6** remaining in solution. Removal of the $H_2$ atmosphere and sealing the NMR tube under static vacuum ($10^{-2}$ mbar) resulted in an approximately 20:80 ratio **7**:**6**, implying the system is in equilibrium (Scheme 2.8).




**6** **7**

**Scheme 2.8** Equilibrium between **6** and **7**.

The NMR data for **7** are very similar to those of **3**. Unfortunately, spectra absent of **6** as a co-component could not be obtained, while attempts to crystallise **7** under $H_2$ resulted in reduction to **6** over the timescale of crystallisation. The $^{31}$P{$^1$H} NMR spectrum indicates equivalent phosphorus environments at a $Rh^{III}$ centre at δ 41.8 (d, $^1J_{RhP}$ = 116 Hz). The hydride region of the $^1$H NMR spectrum shows three environments: δ –1.82 (br, 2H, $H_2B$), –15.13 (br, 1H, RhH), and –19.70 (br, 1H, RhH). Upon decoupling to $^{31}$P, the signals at δ –15.13 and δ –19.70 sharpen to a broad apparent doublet ($^1J_{RhH}$ = 26 Hz, $^2J_{HH}$ not resolved) and a broad doublet of doublets ($^1J_{RhH}$ = 29 Hz, $^2J_{HH}$ = 5 Hz), respectively. As with **3**, this is consistent with two mutually *cis* hydrides. The signal at δ –1.82 sharpens upon $^{11}$B decoupling. The more upfield shift compared with the $BH_3$ signal in **3** (δ –0.97) is representative of the

bound/free B—H fluxionality being time-averaged over only two sites in **7** rather than three in **3**, although an additional factor is that **I** may bind more strongly than $H_3B{\cdot}NMe_3$ (see discussion in Section 2.6.5). Two resonances corresponding to the $CH_2$ groups in bound **I** are observed at δ 0.96 and δ –0.16 (each of relative integral 2H). The $^{11}B$ NMR spectrum contains a broad signal at δ –1.0, barely shifted from that of free **I** at δ –0.8.[37] This implies a weaker interaction of the boron atom in **I** with the metal centre than that in **6** and is also consistent with $\eta^1$ coordination.

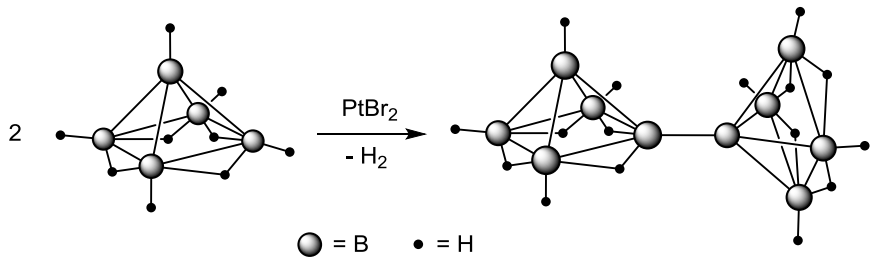
## 2.6. Dehydrogenative homocoupling of $H_3B{\cdot}NMe_3$

### 2.6.1. Introduction

The dehydrogenative homocoupling of main group elements provides a means to access molecular and macromolecular species potentially with a range of useful properties.[40] For example, the formation of polysilanes $[SiRR']_n$ has been extensively studied owing to their interesting optical and electronic properties as a result of σ electron delocalisation along the polymer chain. The first example of catalytic Si—Si bond formation, reported in 1985, involved the dehydrocoupling of $SiPhH_3$ with 1 mol% $Cp_2TiR_2$ (R = methyl or benzyl).[41] The reaction was inhibited by excess hydrogen. Polysilanes have also been formed by Wurtz-type routes involving the reduction of $SiRR'Cl_2$ by sodium.[42] Catalytic routes for the formation of other main group bonds *e.g.* P—P, Sn—Sn, As—As and Ge—Ge have also been reported.[40]

The formation of B—B bonds is comparatively rare. Although B—B bonds have a relatively high dissociation enthalpy of 293 kJ $mol^{-1}$ (*cf.* C—C, 345 kJ $mol^{-1}$ and Si—Si, 222 kJ $mol^{-1}$), strong bonds with heteroatoms (*e.g.* dissociation enthalpies: B—O, 536 kJ $mol^{-1}$; B—N 446 kJ $mol^{-1}$; B—C 372 kJ $mol^{-1}$) can encourage B—B cleavage.[43]

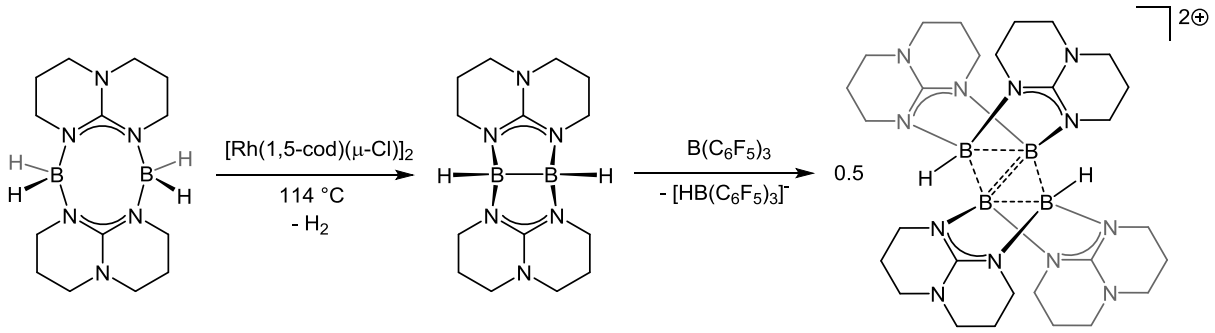
Kinetic difficulties in the formation of B—B single bonds arise from the vacant p orbitals on the borane precursors,[44] which are susceptible to nucleophilic attack.[43] Using π-basic heteroatoms on the boron can reduce the tendency for nucleophilic attack, however. Despite the challenges, some methods of B—B formation have been developed. The diborane(4) $(Me_2N)_2B\text{-}B(NMe_2)_2$[45] was prepared in good yields in 1960 by reaction of molten sodium with $BX(NMe_2)_2$ (X = Cl or Br).[46] $(Me_2N)_2B\text{-}B(NMe_2)_2$ can be converted into useful B—B containing reagents such as *bis*(pinacolato)diborane ($B_2Pin_2$) or *bis*(catecholato)diborane ($B_2Cat_2$).[47,48] $B_2Cat_2$ has also been prepared by reaction of ClBCat with Na/Hg.[49] However, the harsh conditions employed and multistep stoichiometric reactions mean that these preparation routes are not ideal. The first examples of the catalytic formation of B—B bonds by dehydrogenative homocoupling were reported by Sneddon in which boron hydride clusters were catalytically dehydrocoupled with $PtBr_2$ to form B—B linked polyhedral cages (Scheme 2.9).[50,51]




**Scheme 2.9** Formation of pentaborane(9) to form 1:2'-$[B_5H_8]_2$.

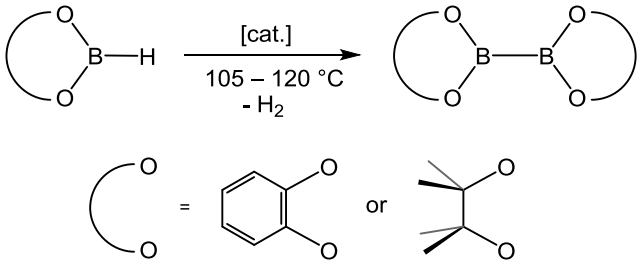
The doubly base-stabilised diborane(4) $[BH(hpp)]_2$ (hpp = 1,3,4,6,7,8-hexahydro-2*H*-pyrimido-[1,2-*α*]pyrimidinate) has been reported by Himmel to form through dehydrogenative B—B homocoupling, by heating a toluene solution of $[BH_2(hpp)]_2$ in the presence of catalytic amounts of $[Rh(1,5\text{-cod})(\mu\text{-Cl})]_2$ (Scheme 2.10). In $[BH_2(hpp)]_2$, the boron atoms are ideally positioned to form B—B bonds, aiding the

coupling.[52,53] Hydride abstraction of $[BH(hpp)]_2$ with the Lewis acid $B(C_6F_5)_3$ forms the dimeric dication $[B_4H_2(hpp)_2][HB(C_6F_5)_3]_2$ (Scheme 2.10), postulated to occur through a monomeric intermediate. The $B_4$ core has rhomboidal geometry and was calculated to consist of two B—B units connected by 3-centre-2-electron bonds sharing the short diagonal.[54]



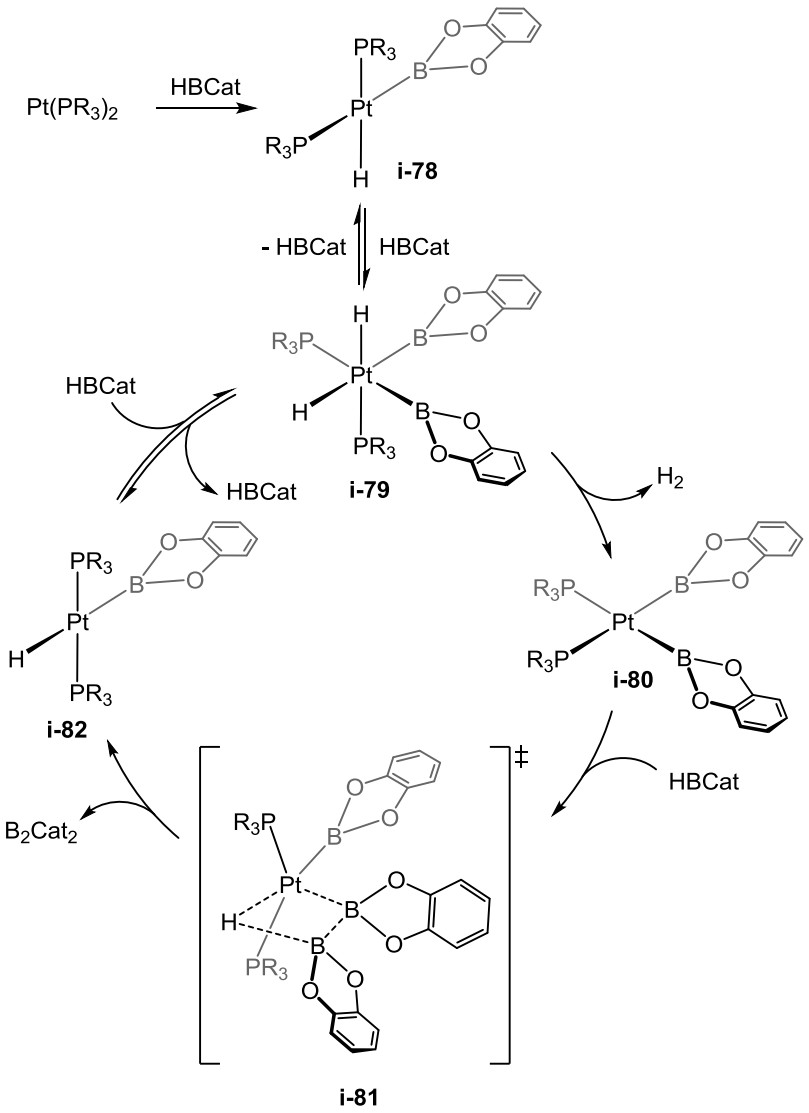

**Scheme 2.10** Formation of $[BH(hpp)]_2$ and subsequent formation of $[B_4H_2(hpp)_2][HB(C_6F_5)_3]_2$.

In 2011, Braunschweig reported the transition metal catalysed dehydrocoupling of pinacolborane (HBPin) and catecholborane (HBCat) to yield $B_2Pin_2$ and $B_2Cat_2$, respectively (Scheme 2.11). Both homogenous (*e.g.* $[Pt(dppm)Cl_2]$; dppm = *bis*(diphenylphosphino)methane) and heterogeneous (*e.g.* Pt on alumina) catalysts were trialled for the reaction and showed catalytic turnover. However, product formation appeared to inhibit turnover. The optimal dehydrocoupling conditions deduced were Pt on alumina (0.5 wt%) heated to 110 °C with continuous removal of the product, resulting in turnover numbers of around 11 600 for the formation of $B_2Cat_2$.[55] Group IV complexes, *e.g.* $Cp_2TiCl_2$, have also been shown to catalyse the formation of $B_2Cat_2$ from HBCat.[56]




**Scheme 2.11** Catalytic formation of $B_2Cat_2$ and $B_2Pin_2$.

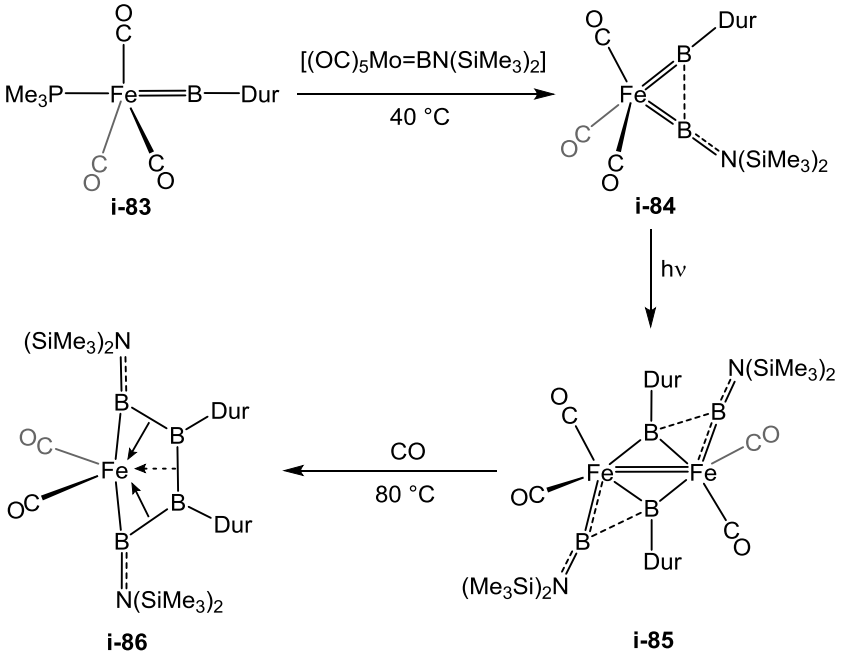
Platinum phosphine complexes were used to uncover mechanistic details for Braunschweig's homogeneous catalytic process. The complex $Pt(P\{CH_2Cy\}_3)_2$ formed $B_2Cat_2$ on addition of HBCat, and experimental observations and DFT calculations led to a proposed mechanism for the dehydrocoupling (Scheme 2.12). Oxidative addition of HBCat to $Pt(P\{CH_2Cy\}_3)_2$ forms the *cis* complex **i-78**. Addition of a further equivalent of HBCat forms the complex **i-79**, from which reductive elimination of $H_2$ yields the diboryl intermediate **i-80**. From **i-80**, σ-bond metathesis with another molecule of HBCat forms the *trans* complex **i-82** (*via* **i-81**, in which three BCat moieties are bound to Pt). **i-82** was calculated to be lower energy than the *cis* complex **i-78**.[57]




**Scheme 2.12** Proposed mechanism for the dehydrocoupling of HBCat by $Pt(PR_3)_2$. R = $CH_2Cy$.

Braunschweig and co-workers have developed other methods for B—B bond formation. For example, a chain of four boron atoms was produced in a stepwise manner (Scheme 2.13) starting with the borylene complex **i-83**,[58] *via* the *bis*-borylene complex **i-84** and the diiron tetraborylene complex **i-85**, culminating in complex **i-86**, which contains an approximately planar $FeB_4$ ring. This work indicates the potential for forming a B—B polymeric chain in a controlled manner.[59] The hydroboration of B=B bonds with HBCat has also been reported.[60] Extensive studies upon B—B double

bonds and even B—B triple bonds have been carried out, but shall not be elaborated upon here.[43,61]



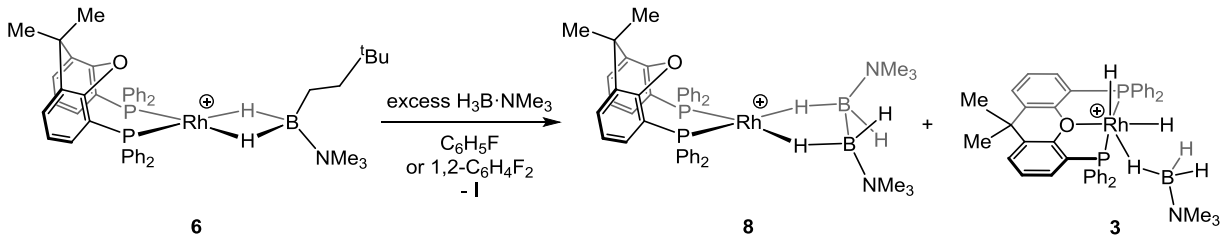

**Scheme 2.13** Braunschweig and co-workers' formation of $FeB_4$ ring. Dur = 2,3,5,6-tetramethylphenyl.

As discussed in Chapter 1, amine-boranes can readily undergo catalytic hetero-dehydrocoupling to yield B—N based oligomeric or polymeric material. Examples of the homocoupling of amine-boranes are scarce, although an alternative route to Himmel's $[HB(hpp)]_2$ complex involves heating $H_3B{\cdot}NMe_3$ and hppH for 20 hours at 110 °C.[62] Additionally, McGrady has shown through labelling experiments that both B—H···H—N and B—H···H—B interactions play a role in the thermal decomposition of $H_3B{\cdot}NH_3$.[63] The relative scarcity is likely due to the differences in B—B, N—N and B—N bond dissociation enthalpies of 293 kJ $mol^{-1}$, 167 kJ $mol^{-1}$ and 446 kJ $mol^{-1}$, respectively, so B—N bond formation is favoured.[64] No well-defined metal-mediated amine-borane homocoupling has been reported to our knowledge. Reaction of $CpRe(CO)_3$ with $H_3B{\cdot}NEt_3$ under photolysis was recently reported to form

$CpRe(CO)_2H_2$. The hydrides were thought to originate from $H_3B{\cdot}NEt_3$, but the resultant boron-containing product was not characterised.[65] Moreover, the catalyst $[Pd(NCMe)_4][BF_4]$ was reported to dehydrogenate $H_3B{\cdot}NH_3$ to form ill-defined polymeric materials with B—B bonds. IR studies on the material suggested no B—H bonds were present, and the total $H_2$ release was found to be dependent on the number of BH bonds in the starting amine-borane.[66]

### 2.6.2. Dehydrogenative homocoupling of $H_3B{\cdot}NMe_3$ by complex 6

On addition of 20 equivalents of $H_3B{\cdot}NMe_3$ to **6** in $C_6H_5F$, NMR spectroscopy indicated the formation of two products in approximately equal concentrations within one hour. One was recognised as **3**. Fractional recrystallisation of the reaction mixture enabled the other species to be identified as $[Rh(\kappa^2_{P,P}\text{-Xantphos})(\eta^2\text{-}H_4B_2{\cdot}2NMe_3)][BAr^F{}_4]$ (**8**) (Scheme 2.14) in which the diborane(4) $Me_3N{\cdot}BH_2BH_2{\cdot}NMe_3$ is bound to Rh. Thus, on-metal formation of $Me_3N{\cdot}BH_2BH_2{\cdot}NMe_3$ occurred *via* the dehydrogenative homocoupling of $H_3B{\cdot}NMe_3$, with the concomitant formation of **3**. Free **I** was also observed by $^{11}B$ NMR spectroscopy. $Me_3N{\cdot}BH_2BH_2{\cdot}NMe_3$ has been previously synthesised by treatment of $B_3H_7{\cdot}THF$ or $B_3H_7{\cdot}SMe_2$ with excess $NMe_3$, yielding mixtures of $Me_3N{\cdot}BH_2BH_2{\cdot}NMe_3$ and $H_3B{\cdot}NMe_3$.[67,68]




**Scheme 2.14** Addition of $H_3B{\cdot}NMe_3$ to form **8** and **3**.

Red crystals of **8** suitable for X-ray diffraction were obtained, and the solid state structure (Figure 2.6) shows that the Xantphos ligand has $\kappa^2_{P,P}$ geometry with the same bite angle (within error) and similar Rh—O distance to **6**. The hydrogen atoms were located and indicate that the diborane(4) is bound through two vicinal B—H atoms to give a *pseudo* square planar complex. The Rh—B distances (2.411(5) Å and 2.405(4) Å) are the same within error, as are the B—N distances (1.621(7) Å and 1.619(6) Å), indicating equal contribution from each bridging B—H to the σ bonding. The Rh—B distances lie between those for **6** and **3**, and the B—N distances in all three compounds are the same within error. The N1-B1-B2-N2 dihedral angle is 148.2°, and this anticlinal conformation is likely due to the steric bulk of the $NMe_3$ groups. The B1-Rh1-B2 plane is twisted 24.4° relative to the P2-Rh1-P1 plane, distorting the complex from square planar geometry. It is likely that this distortion is electronic in origin, rather than steric, as calculations performed by Dr Claire L. McMullin and Professor Stuart A. MacGregor (Heriot-Watt University) on a truncated MeXantphos model (MeXantphos = 9,9-dimethyl-4,5-*bis*(di-methylphosphino)xanthene) reproduce the distortion. The calculations are discussed further in Section 2.6.5.

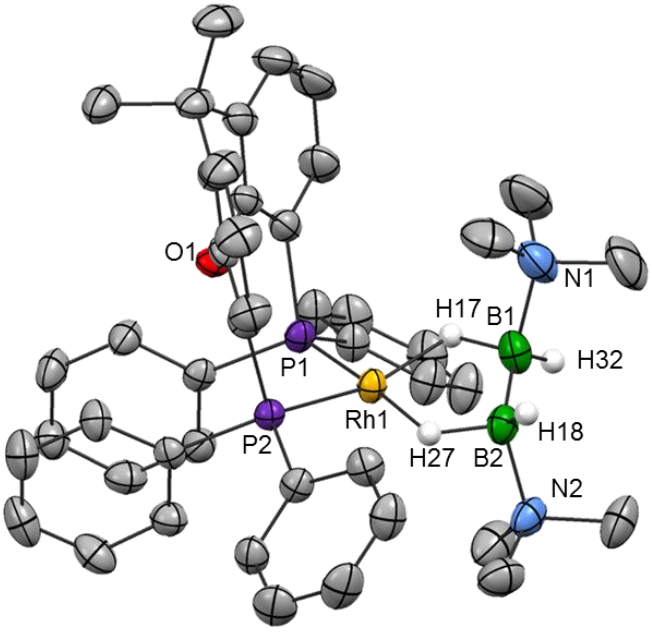



**Figure 2.6** Solid state structure of **8**. $[BAr^F_4]^-$ anion and all carbon-bound H atoms omitted for clarity. Displacement ellipsoids are drawn at the 50% level. Selected bond lengths (Å) and angles (°): Rh1-P1, 2.2834(9); Rh1-P2, 2.2720(10); Rh1-B1, 2.411(5); Rh1-B2, 2.405(4); B1-B2, 1.678(7); B1-N1, 1.621(7); B2-N2 1.619(6); Rh1-O1, 3.3044(25); P1-Rh1-P2, 101.56(4); P1-Rh1-B2, 147.79(12); P2-Rh1-B2, 110.58(12); P1-Rh1-B1, 109.42(13); P2-Rh1-B1, 145.76(12); B1-Rh1-B2, 40.77(17); N1-B1-B2, 115.1(4); B1-B2-N2, 116.7(4).

Shimoi and co-workers have used the related diborane(4) $PMe_3{\cdot}BH_2BH_2{\cdot}PMe_3$ (pre-formed by the addition of excess $PMe_3$ to $B_5H_9$[69]) to form complexes including $[Cu(\eta^2\text{-}H_4B_2{\cdot}2PMe_3)_2]I$[70] and $[ZnCl_2(\eta^2\text{-}H_4B_2{\cdot}2PMe_3)]$.[71] These complexes show similar structures to **8**, whereby the diborane(4) is bound in a bidentate fashion with anticlinal conformations. Interestingly, addition of $PMe_3{\cdot}BH_2BH_2{\cdot}PMe_3$ to $Cr(CO)_6$ under photolysis forms $[Cr(CO)_5(\eta^1\text{-}H_4B_2{\cdot}2PMe_3)]$ initially, bound only through one B—H interaction, and requires further irradiation and heat to form the bidentate complex $[Cr(CO)_4(\eta^2\text{-}H_4B_2{\cdot}2PMe_3)]$.[72] Solution data for the complex $[Ni(CO)_2(H_4B_2{\cdot}2PMe_3)]$ has also been reported.[73]

The solution NMR data of **8** in $CD_2Cl_2$ are consistent with the solid state structure. The $^{31}P\{^1H\}$ NMR spectrum at 298 K indicates a $Rh^I$ centre with equivalent $^{31}P$

environments in the Xantphos ligand (δ 26.2, d, $^{1}J_{RhP}$ = 172 Hz) (Figure 2.7). The methyl positions of Xantphos are also equivalent on the NMR timescale, evident by a relative integral 6H singlet at δ 1.74 in the $^{1}$H NMR spectrum (Figure 2.8). Furthermore, the $NMe_3$ groups of the diborane also appear equivalent on the NMR timescale (δ 2.24, s, 18H) as do the terminal (δ 1.51, v br, 2H) and bridging (δ –8.47, br, 2H) B—H resonances. Both B—H signals sharpen upon $^{11}$B decoupling. A broad resonance corresponding to the diborane is observed in the $^{11}$B NMR spectrum at δ –11.3. These data suggest inversion of the Xantphos ligand occurs in solution, rendering the discussed positions equivalent. This behaviour has been observed in related *cis*-$\kappa^2_{P,P}$-Xantphos complexes of Rh,[11] Ru[74] and Ir.[75]

On cooling the $CD_2Cl_2$ solution to 218 K, the Xantphos inversion had ceased on the NMR timescale. The $^{31}P\{^{1}H\}$ NMR spectrum reveals an ABX system of two overlapping doublets of doublets at δ 29.0 ($^{1}J_{RhP}$ = 164 Hz, $^{2}J_{PP}$ = 35 Hz) and δ 28.2 ($^{1}J_{RhP}$ = 168 Hz, $^{2}J_{PP}$ = 35 Hz) (Figure 2.7), indicating inequivalent mutually *cis* $^{31}$P environments, as expected from the solid state structure (Figure 2.6). In the $^{1}$H NMR spectrum, the Xantphos methyl signals are separated into two relative integral 3H singlets (δ 1.77 and δ 1.51). The environments in the diborane are also inequivalent at 218 K; separate signals are observed for the two $NMe_3$ groups and the bound B—H signals separate into two relative integral 1H broad doublets (δ –8.01, $^{2}J_{P\mathit{trans}H}$ = 42 Hz; δ –8.54, $^{2}J_{P\mathit{trans}H}$ = 41 Hz) (Figure 2.8). These doublets collapse into broad singlets upon $^{31}$P decoupling (inset, Figure 2.8). The terminal B—H signals were not observed at this temperature, possibly due to them being obscured by the aliphatic signals.

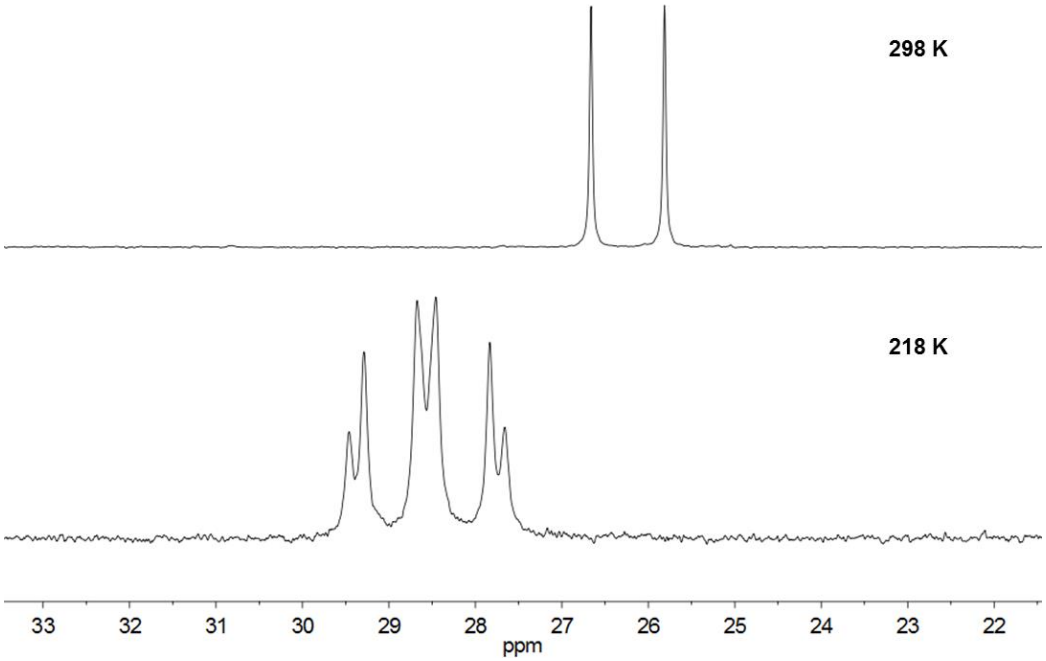



**Figure 2.7** $^{31}P\{^{1}H\}$ NMR spectrum of **8** at 298 K (upper) and 218 K (lower) in $CD_2Cl_2$.

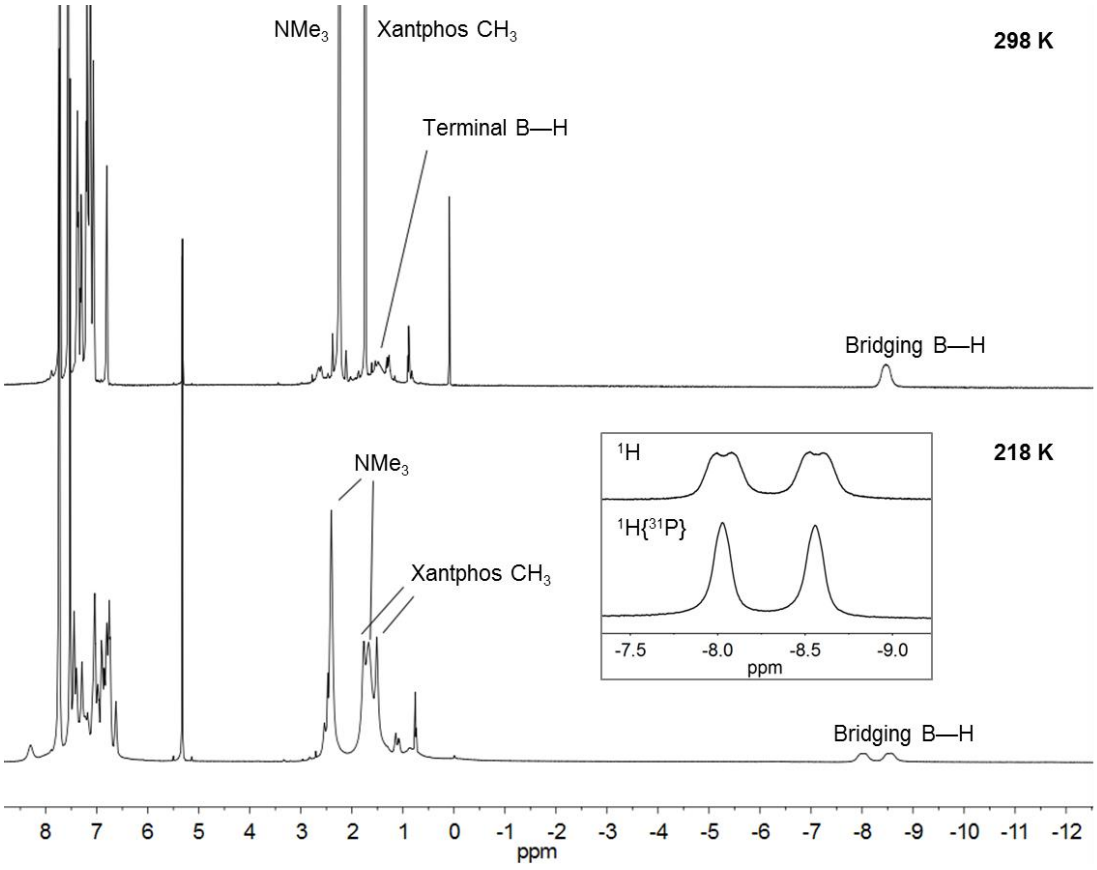



**Figure 2.8** $^{1}H$ NMR spectrum of **8** at 298 K (upper) and 218 K (lower) in $CD_2Cl_2$. Inset shows the bridging B—H signals at 218 K in the $^{1}H$ NMR spectrum (upper) and $^{1}H\{^{31}P\}$ NMR spectrum (lower).

ESI-MS is consistent with the formation of **8**, showing a molecular ion peak at *m/z* = 825.30 (calc. 825.30) of the expected isotopic pattern. Elemental microanalysis confirmed the bulk purity of the isolated solid.

### 2.6.3. Bonding interactions in complex 8

The upfield hydride chemical shift of δ –8.54 in the $^{1}$H NMR spectrum of **8** implies that the bonding arises predominantly from Rh—H—B interactions, rather than Rh···B—B bonding. In contrast, Himmel and co-workers investigated the binding of their [HB(hpp)]$_2$ ligand with metal fragments and found later metal complexes, *e.g.* [Rh(NCS)(cod){HB(hpp)}$_2$], were dominated by M···B—B interactions.[76] The Rh—B distances in [Rh(NCS)(cod){HB(hpp)}$_2$] (2.501(2) Å and 2.340(3) Å) indicate asymmetrical binding of the diborane to the metal. The Rh—B distances in **8** lie between these values. In [Rh(NCS)(cod){HB(hpp)}$_2$], the B—B bond length of 1.815(4) Å is lengthened compared with that of free [HB(hpp)]$_2$ (1.772(3) Å),[62] indicating significant B—B donation to the metal. Consistent with this, calculations upon the related [Rh(Cl)(cod){HB(hpp)}$_2$] system showed that the bonding involves strong donation from the B—B bond, and donation from only one B—H group to the metal. By contrast, the B—B bond length in Me$_3$N·BH$_2$BH$_2$·NMe$_3$ was calculated to shorten upon complexation in **8** (1.76 Å to 1.70 Å, Me-Xantphos system). To consolidate the M—H—B binding model in **8**, an Atoms in Molecules analysis was carried out upon **8** by Dr C. L. McMullin and Prof. S. A. Macgregor, and the results are shown in Figure 2.9.

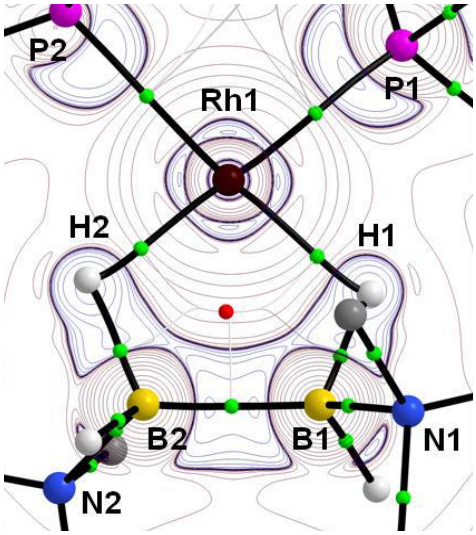
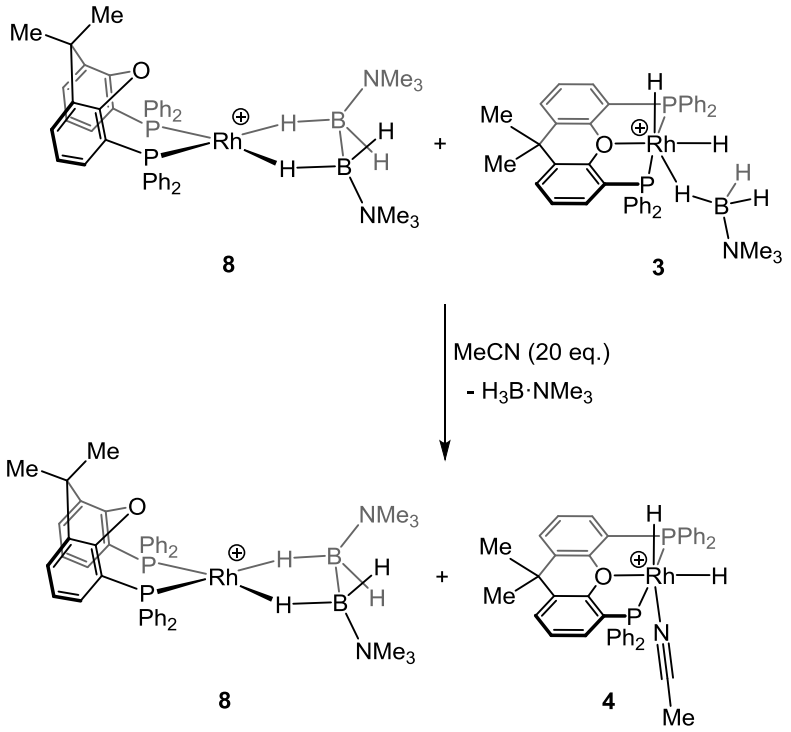



**Figure 2.9** Contour plot of the Laplacian electron density for the computed complex **8** in the $RhB_2$ plane. Bond critical points are shown in green, ring critical points are shown in red. Figure courtesy of Dr C. L. McMullin and Professor S. A. Macgregor and reproduced from *Angew. Chem. Int. Ed.* **2013**, *42,* 9776.

Bond critical points were located between Rh and the bridging H atoms, and no bond critical point was located between Rh and either B atom. A ring critical point was observed between the Rh atom and the B—B bond, confirming the chelate ring. These calculations support the primarily Rh—H—M bonding motif as suggested by experiment.

### 2.6.4. Addition of MeCN to the homocoupling mixture

Addition of 20 equivalents of MeCN to a mixture of **3** and **8** in $C_6H_5F$ (formed *in situ* from **6** and 20 eq. $H_3B{\cdot}NMe_3$) resulted in the immediate displacement of $H_3B{\cdot}NMe_3$ from **3** to form **4**. However, no change in the NMR spectrum of **8** was observed after 15 minutes and no evidence for free $Me_3N{\cdot}BH_2BH_2{\cdot}NMe_3$ was observed in the $^{11}B$ NMR spectrum.



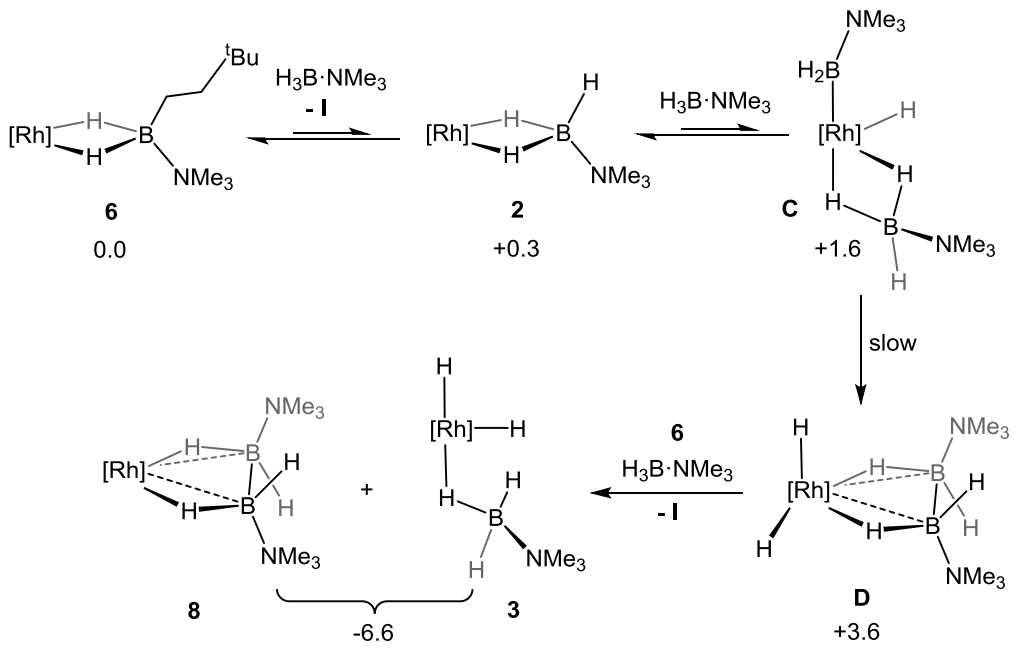

**Scheme 2.15** Addition of MeCN to a mixture of **8** and **3**.

After 24 hours, ~20% decomposition of **8** had occurred to form unidentified species. Nonetheless, the unfavourable displacement of $Me_3N{\cdot}BH_2BH_2{\cdot}NMe_3$ by MeCN indicates that $Me_3N{\cdot}BH_2BH_2{\cdot}NMe_3$ is strongly bound, possibly due to the chelate effect.[21] This also explains why the formation of $Me_3N{\cdot}BH_2BH_2{\cdot}NMe_3$ is not catalytic; once formed, it is not displaced by $H_3B{\cdot}NMe_3$ to undergo further homocoupling.

### 2.6.5. Mechanism of formation of complex 8

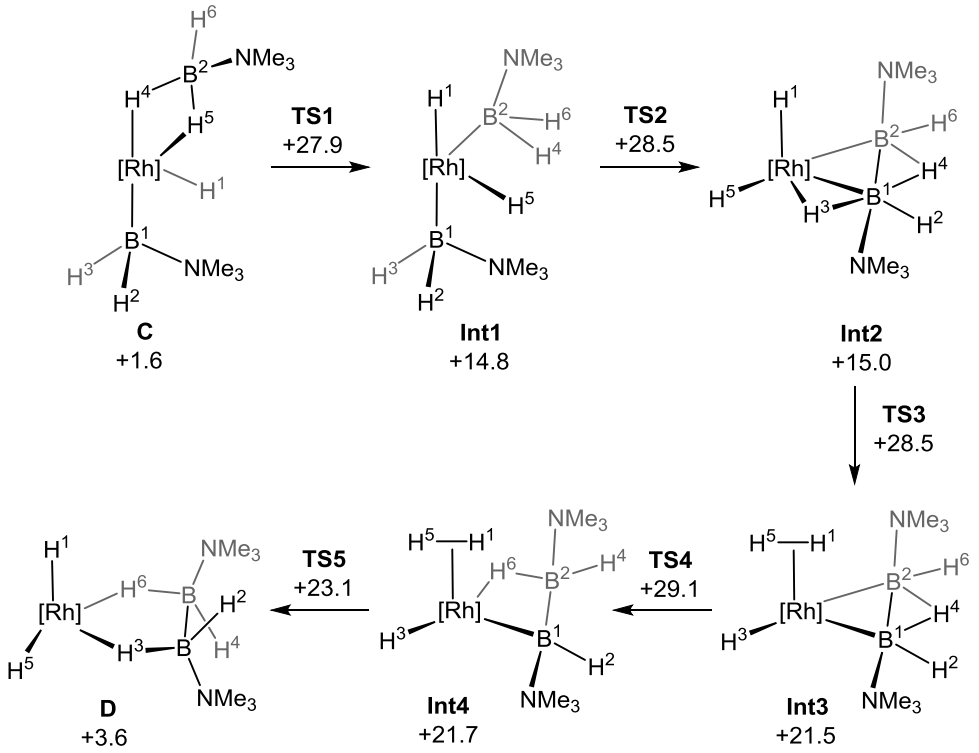
To verify that $H_3B{\cdot}NMe_3$ was the source of the hydrides in **3**, $D_3B{\cdot}NMe_3$ was added to **6** instead of $H_3B{\cdot}NMe_3$. As expected, $^2H$ NMR spectroscopy showed signals corresponding to $[Rh(\kappa^3_{P,O,P}\text{-Xantphos})(D)_2(\eta^1\text{-}D_3B{\cdot}NMe_3)][BAr^F_4]$ ($\delta$ –0.99, –14.45, –18.85; 3:1:1 relative integrals) and $[Rh(\kappa^2_{P,P}\text{-Xantphos})(\eta^2\text{-}NMe_3{\cdot}D_2B\text{-}BD_2{\cdot}NMe_3)][BAr^F_4]$ ($\delta$ 1.3, –8.51), indicating that the hydrides in **3** originate from $H_3B{\cdot}NMe_3$.

DFT calculations were performed by Dr C. L. McMullin and Prof. S. A. Macgregor to deduce mechanistic detail for the formation of **8** using the Me-Xantphos system. The computed pathway (Scheme 2.16) is consistent with experimental observations. Initial displacement of **I** by $H_3B{\cdot}NMe_3$ forms $[Rh(\kappa^2_{P,P}\text{-Xantphos})(\eta^2\text{-}H_3B{\cdot}NMe_3)][BAr^F{}_4]$ (**2**). Experimentally, **2** is not observed by NMR spectroscopy, consistent with a calculated equilibrium that favours the binding of **I**. B-alkylated amine-boranes have been previously shown to bind preferentially *vs* $H_3B{\cdot}NMe_3$. For example, addition of one equivalent of $H_3B{\cdot}NMe_3$ to **i-77** established an equilibrium between **i-77** and **i-76** that favoured the binding of **I** ($K_{298K}$ = 1.62).[37] Shimoi has also shown that alkylated boranes bind preferentially in the complexes $[M(CO)_5(\eta^1\text{-}BH_2R{\cdot}L)]$ (M = Cr, W; R = H or Me; L = $PMe_3$, $NMe_3$) as the electron-releasing substituent on boron stabilises the B—H—M interaction.[77] From **2**, a fast and reversible B—H activation, and trapping by excess $H_3B{\cdot}NMe_3$, forms **C**. The rate limiting step was calculated to be the slow formation of **D** from **C** *via* a second B—H activation and B—B coupling. Displacement of $NMe_3{\cdot}H_2B\text{-}BH_2{\cdot}NMe_3$ in **D** by $H_3B{\cdot}NMe_3$ was calculated to be unfavourable ($\Delta G$ = 10.7 kcal $mol^{-1}$). However, $H_2$ loss from **D**, forming **8** is favourable ($\Delta G$ = –2.6 kcal $mol^{-1}$), as is the reaction of $H_2$ with **2** to form **3** ($\Delta G$ = –7.9 kcal $mol^{-1}$), which gives in the observed product distribution. The end products were calculated to be 6.6 kcal $mol^{-1}$ lower in energy than the starting reactants.




**Scheme 2.16** Proposed mechanism for the formation of **3** and **8** from **6**. $[BAr^F_4]^-$ anions not shown. [Rh] = $\{Rh(Xantphos)\}^+$ (experimental) or $\{Rh(MeXantphos)\}^+$ (calculations). DFT-computed free energies indicated in kcal $mol^{-1}$, relative to **6** plus two $H_3B{\cdot}NMe_3$. Calculations performed by Dr C. L. McMullin and Professor S. A. Macgregor.

Additional calculations were performed to further elucidate the individual steps between the rate determining transformation of **C** to **D**. The calculated pathway is shown in Scheme 2.17. From **C** to **Int1**, $H^1$ moves from a position *trans* to a Xantphos arm and $H^5$ is transferred from $B^2$ to Rh. This places the two $\{BH_2NMe_3\}$ fragments *cis* to each other, enabling B—B coupling following $B^1$—$H^5$ activation. This forms a dihydride, **Int2**, in which the B—B moiety is established. A rearrangement occurs to form **Int3**; $B^1$—$H^3$ undergoes activation, while the *cis* hydrides $H^5$ and $H^1$ form a dihydrogen ligand. From **Int3**, $H^4$ is transferred from a bridging to terminal position on $B^2$ and $H^6$ forms a Rh—$H^6$—$B^2$ bridge (**Int4**). Finally, the $H^1$—$H^5$ dihydrogen ligand undergoes an oxidative addition and $H^3$ transfers to a bridging Rh—$H^3$—$B^1$ position, forming **D**.



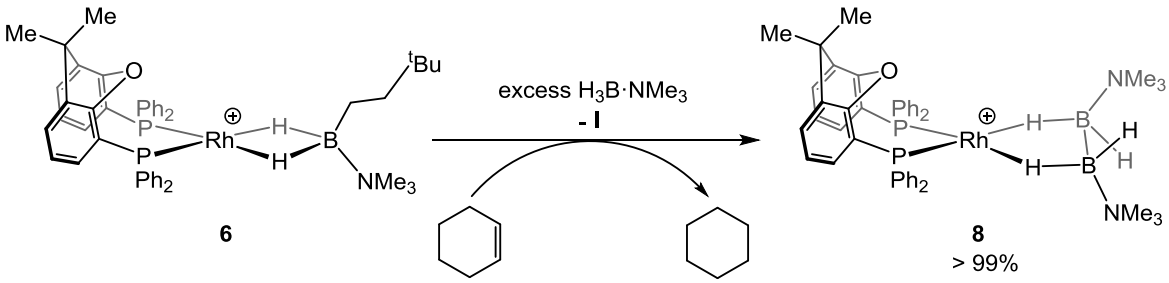

**Scheme 2.17** Proposed pathway for the multistep transformation of **C** to **D**. $[BAr^F_4]^-$ anions not shown. [Rh] = {Rh(MeXantphos)}$^+$. DFT-computed free energies indicated in kcal mol$^{-1}$, relative to **6** plus two $H_3B{\cdot}NMe_3$. Calculations performed by Dr C. L. McMullin and Professor S. A. Macgregor.

The highest calculated barrier (+29.1 kcal mol$^{-1}$) was that of **TS4**, the rearrangement of the $\{RhB_2H_6(NMe_3)_2\}$ unit, rather than the B—B coupling event itself. The rather high barrier is consistent with relatively slow reaction at room temperature, and it was speculated that the entropic contribution to the calculation may have been overestimated computationally.[78] Using 10 eq. $H_3B{\cdot}NMe_3$ also induced the transformation within ~1 hour, but with 2 eq. $H_3B{\cdot}NMe_3$, the reaction did not reach completion, as expected since 3 eq. $H_3B{\cdot}NMe_3$ are required to form **3** and **8** from **6**.

### 2.6.6. Role of cyclohexene in dehydrogenative homocoupling

From the mechanism, it is apparent that, once **3** forms, the homocoupling ceases since the $Rh^{III}$-dihydride cannot facilitate further coupling. Thus, to drive the reaction to a

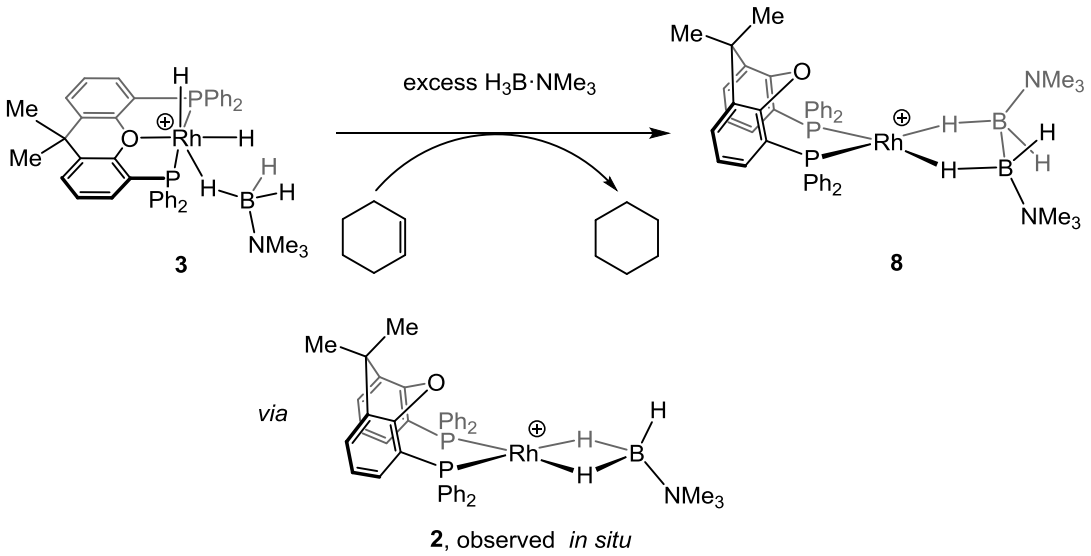
100% yield of **8**, a means of reducing **3** to **2** was required. TBE was ruled out since, although it is competent at reducing **3** to a $Rh^{I}$ species, it is hydroborated by $H_3B{\cdot}NMe_3$, forming **6**. As a bulkier alkene, and so less likely to undergo hydroboration, cyclohexene was used. Addition of cyclohexene (~20 eq.) at the start of the reaction formed > 99% **8** *in situ* within an hour (Scheme 2.18). Cyclohexene could also be added to the 50:50 mixture of **3** and **8** with the same results. Upon the addition of cyclohexene to the mixture, a green colour change was observed but no intermediates could be assigned as spectra were broad, possibly reflecting equilibria between the **6** (blue coloured, arising from residual **I** in solution) and the postulated **2**. The solution was red upon complete formation of **8**. Recrystallisation of the reaction mixture enabled pure solid **8** to be isolated in 67% yield.




**Scheme 2.18** Addition of cyclohexene (20 eq.) to the reaction mixture. $[BAr^{F}_4]^-$ anions not shown.

In an attempt to observe **2** in the formation of **8**, cyclohexene was added to a degassed solution of **3** (formed with approximately 2 eq. $H_3B{\cdot}NMe_3$) in 1,2-$C_6H_4F_2$ (Scheme 2.19). On addition of cyclohexene, the solution turned green. In the $^1H$ NMR spectrum, the major species contained a broad signal, relative integral ~5H at δ 0.10. The integral and chemical shift imply an equilibrium between $\eta^2$-bound and free $H_3B{\cdot}NMe_3$. Similarly, the $^{11}B$ NMR spectrum showed a broad signal at δ –1, also

suggesting a bound/free equilibrium. The $^{31}P\{^{1}H\}$ NMR spectrum showed a broad doublet at δ 26.7 ($^{1}J_{RhP}$ = 185 Hz), indicating a $Rh^{I}$ complex. These data support the formation of **2** and are similar to those observed in the formation of $[Rh(Ph_2P(CH_2)_xPPh_2)(\eta^2\text{-}H_3B{\cdot}NMe_3)][BAr^F{}_4]$ (x = 3 – 5) in the presence of excess $H_3B{\cdot}NMe_3$.[12] ESI-MS of the mixture showed a molecular ion at *m/z* = 754.20 corresponding to $\mathbf{2}^+$ (calc. 754.20, correct isotopic pattern). Within 10 minutes, **8** was observed by NMR spectroscopy, and the colour of the solution had changed to off-red. These observations of **2** substantiate the role of cyclohexene in reducing **3**.




**Scheme 2.19** Alternative route to **8**. $[BAr^F{}_4]^-$ anions not shown.

## 2.7. Conclusions

In this chapter, several new $Rh^{I}$ and $Rh^{III}$ Xantphos complexes have been synthesised. Of these, **6** represents the source of $\{Rh(Xantphos)\}^+$ that was targeted for exploration of the dehydrocoupling of amine-boranes (discussed in Chapter 4). In forming **6**, a selective and fast anti-Markovnikov hydroboration reaction occurs. The hydroboration is discussed in Chapter 3. Finally, the first well-defined example of the dehydrogenative homocoupling of an amine-borane was observed in the formation of

**8**. Using cyclohexene, **8** could be isolated as the sole product. While the reaction is not catalytic, and the barriers to the formation of **8** were computed to be high, future work in modifying the ligands or substrates to encourage the catalytic formation of $Me_3N{\cdot}BH_2BH_2{\cdot}NMe_3$ (or related boranes) would be worthy of exploration.

## 2.8. References

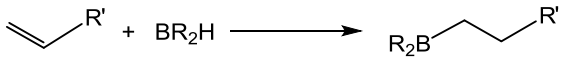

(1) Dallanegra, R.; Robertson, A. P. M.; Chaplin, A. B.; Manners, I.; Weller, A. S. *Chem. Commun.* **2011**, *47*, 3763.
(2) Chaplin, A. B.; Hooper, J. F.; Weller, A. S.; Willis, M. C. *J. Am. Chem. Soc.* **2012**, *134*, 4885.
(3) Douglas, T. M.; Brayshaw, S. K.; Dallanegra, R.; Kociok-Köhn, G.; Macgregor, S. A.; Moxham, G. L.; Weller, A. S.; Wondimagegn, T.; Vadivelu, P. *Chem. Eur. J.* **2008**, *14*, 1004.
(4) Douglas, T. M.; Chaplin, A. B.; Weller, A. S.; Yang, X.; Hall, M. B. *J. Am. Chem. Soc.* **2009**, *131*, 15440.
(5) Hooper, J. F.; Young, R. D.; Pernik, I.; Weller, A. S.; Willis, M. C. *Chem. Sci.* **2013**, *4*, 1568.
(6) Hooper, J. F.; Young, R. D.; Weller, A. S.; Willis, M. C. *Chem. Eur. J.* **2013**, *19*, 3125.
(7) Pernik, I.; Hooper, J. F.; Chaplin, A. B.; Weller, A. S.; Willis, M. C. *ACS Catal.* **2012**, *2*, 2779.
(8) Dallanegra, R.; Pilgrim, B. S.; Chaplin, A. B.; Donohoe, T. J.; Weller, A. S. *Dalton Trans.* **2011**, *40*, 6626.
(9) Hooper, T. N.; Huertos, M. A.; Jurca, T.; Pike, S. D.; Weller, A. S.; Manners, I. *Inorg. Chem.* **2014**, *53*, 3716.
(10) Pike, S. D.; Pernik, I.; Theron, R.; McIndoe, J. S.; Weller, A. S. *J. Organomet. Chem.*
(11) Pawley, R. J.; Moxham, G. L.; Dallanegra, R.; Chaplin, A. B.; Brayshaw, S. K.; Weller, A. S.; Willis, M. C. *Organometallics* **2010**, *29*, 1717.
(12) Dallanegra, R., DPhil Thesis, University of Oxford, 2011.
(13) Moxham, G. L.; Randell-Sly, H.; Brayshaw, S. K.; Weller, A. S.; Willis, M. C. *Chem. Eur. J.* **2008**, *14*, 8383.
(14) Pawley, R. J., DPhil Thesis, University of Oxford, 2012.
(15) Shimoi, M.; Nagai, S.-i.; Ichikawa, M.; Kawano, Y.; Katoh, K.; Uruichi, M.; Ogino, H. *J. Am. Chem. Soc.* **1999**, *121*, 11704.
(16) Ledger, A. E. W.; Ellul, C. E.; Mahon, M. F.; Williams, J. M. J.; Whittlesey, M. K. *Chem. Eur. J.* **2011**, *17*, 8704.
(17) Kawano, Y.; Hashiva, M.; Shimoi, M. *Organometallics* **2006**, *25*, 4420.
(18) Merle, N.; Koicok-Kohn, G.; Mahon, M. F.; Frost, C. G.; Ruggerio, G. D.; Weller, A. S.; Willis, M. C. *Dalton Trans.* **2004**, 3883.
(19) Alcaraz, G.; Sabo-Etienne, S. *Coord. Chem. Rev.* **2008**, *252*, 2395.
(20) Huertos, M. A.; Weller, A. S. *Chem. Sci.* **2013**, *4*, 1881.
(21) Crabtree, R. H. *The Organometallic Chemistry of the Transition Metals*; John Wiley & Sons, 2005.
(22) Dallanegra, R.; Chaplin, A. B.; Weller, A. S. *Angew. Chem. Int. Ed.* **2009**, *48*, 6875.
(23) Cordero, B.; Gomez, V.; Platero-Prats, A. E.; Reves, M.; Echeverria, J.; Cremades, E.; Barragan, F.; Alvarez, S. *Dalton Trans.* **2008**, 2832.
(24) Algarra, A. G.; Sewell, L. J.; Johnson, H. C.; Macgregor, S. A.; Weller, A. S. *Dalton Trans.* **2014**, *43*, 11118.
(25) Perutz, R. N.; Sabo-Etienne, S. *Angew. Chem. Int. Ed.* **2007**, *46*, 2578.
(26) Pike, S. D.; Thompson, A. L.; Algarra, A. G.; Apperley, D. C.; Macgregor, S. A.; Weller, A. S. *Science* **2012**, *337*, 1648.
(27) Johnson, H. C.; Robertson, A. P. M.; Chaplin, A. B.; Sewell, L. J.; Thompson, A. L.; Haddow, M. F.; Manners, I.; Weller, A. S. *J. Am. Chem. Soc.* **2011**, *133*, 11076.
(28) Chaplin, A. B.; Weller, A. S. *Angew. Chem. Int. Ed.* **2010**, *49*, 581.
(29) Chaplin, A. B.; Weller, A. S. *Inorg. Chem.* **2010**, *49*, 1111.
(30) Vigalok, A.; Uzan, O.; Shimon, L. J. W.; Ben-David, Y.; Martin, J. M. L.; Milstein, D. *J. Am. Chem. Soc.* **1998**, *120*, 12539.

(31) Doherty, M. D.; Grills, D. C.; Huang, K.-W.; Muckerman, J. T.; Polyansky, D. E.; van Eldik, R.; Fujita, E. *Inorg. Chem.* **2013**, *52*, 4160.
(32) Ingleson, M. J.; Brayshaw, S. K.; Mahon, M. F.; Ruggiero, G. D.; Weller, A. S. *Inorg. Chem.* **2005**, *44*, 3162.
(33) Douglas, T. M.; Notre, J. L.; Brayshaw, S. K.; Frost, C. G.; Weller, A. S. *Chem. Commun.* **2006**, 3408.
(34) Bergens, S. H.; Bosnich, B. *J. Am. Chem. Soc.* **1991**, *113*, 958.
(35) Zhang, Z.; Ojima, I. *J. Organomet. Chem.* **1993**, *454*, 281.
(36) Maguire, J. A.; Boese, W. T.; Goldman, M. E.; Goldman, A. S. *Coord. Chem. Rev.* **1990**, *97*, 179.
(37) Sewell, L. J.; Chaplin, A. B.; Weller, A. S. *Dalton Trans.* **2011**, *40*, 7499.
(38) Dallanegra, R.; Chaplin, A. B.; Weller, A. S. *Organometallics* **2012**, *31*, 2720.
(39) Marks, T. J.; Kolb, J. R. *Chem. Rev.* **1977**, *77*, 263.
(40) Leitao, E. M.; Jurca, T.; Manners, I. *Nat. Chem.* **2013**, *5*, 817.
(41) Aitken, C.; Harrod, J. F.; Samuel, E. *J. Organomet. Chem.* **1985**, *279*, C11.
(42) Koe, J. *Polym. Int.* **2009**, *58*, 255.
(43) Braunschweig, H.; Dewhurst, R. D. *Angew. Chem. Int. Ed.* **2013**, *52*, 3574.
(44) Osorio, E.; Olson, J. K.; Tiznado, W.; Boldyrev, A. I. *Chem. Eur. J.* **2012**, *18*, 9677.
(45) Urry, G.; Wartik, T.; Moore, R. E.; Schlesinger, H. I. *J. Am. Chem. Soc.* **1954**, *76*, 5293.
(46) Brotherton, R. J.; McCloskey, A. L. *J. Am. Chem. Soc.* **1960**, *82*, 6242.
(47) Ishiyama, M., Murata, M., Ahiko, T. A., Miyaura, N. *Org. Synth.* **2000**, *77*, 176.
(48) Welch, C. N.; Shore, S. G. *Inorg. Chem.* **1968**, *7*, 225.
(49) Anastasi, N. R.; Waltz, K. M.; Weerakoon, W. L.; Hartwig, J. F. *Organometallics* **2003**, *22*, 365.
(50) Corcoran, E. W.; Sneddon, L. G. *J. Am. Chem. Soc.* **1984**, *106*, 7793.
(51) Corcoran, E. W.; Sneddon, L. G. *J. Am. Chem. Soc.* **1985**, *107*, 7446.
(52) Ciobanu, O.; Kaifer, E.; Enders, M.; Himmel, H.-J. *Angew. Chem. Int. Ed.* **2009**, *48*, 5538.
(53) Wagner, A.; Litters, S.; Elias, J.; Kaifer, E.; Himmel, H.-J. *Chem. Eur. J.* **2014**, *20*, 12514.
(54) Litters, S.; Kaifer, E.; Enders, M.; Himmel, H.-J. *Nat. Chem.* **2013**, *5*, 1029.
(55) Braunschweig, H.; Guethlein, F. *Angew. Chem. Int. Ed.* **2011**, *50*, 12613.
(56) Braunschweig, H.; Claes, C.; Guethlein, F. *J. Organomet. Chem.* **2012**, *706–707*, 144.
(57) Braunschweig, H.; Brenner, P.; Dewhurst, R. D.; Guethlein, F.; Jimenez-Halla, J. O. C.; Radacki, K.; Wolf, J.; Zöllner, L. *Chem. Eur. J.* **2012**, *18*, 8605.
(58) Braunschweig, H.; Ye, Q.; Radacki, K. *Chem. Commun.* **2012**, *48*, 2701.
(59) Braunschweig, H.; Ye, Q.; Vargas, A.; Dewhurst, R. D.; Radacki, K.; Damme, A. *Nat. Chem.* **2012**, *4*, 563.
(60) Braunschweig, H.; Dewhurst, R. D.; Hörl, C.; Phukan, A. K.; Pinzner, F.; Ullrich, S. *Angew. Chem. Int. Ed.* **2014**, *53*, 3241.
(61) Braunschweig, H.; Dewhurst, R. D. *Organometallics* **2014**.
(62) Ciobanu, O.; Roquette, P.; Leingang, S.; Wadepohl, H.; Mautz, J.; Himmel, H.-J. *Eur. J. Inorg. Chem.* **2007**, *2007*, 4530.
(63) Wolstenholme, D. J.; Traboulsee, K. T.; Hua, Y.; Calhoun, L. A.; McGrady, G. S. *Chem. Commun.* **2012**, *48*, 2597.
(64) Huheey, J. E. K., E. A.; Keiter, R. L. *Inorganic Chemistry: Principles of Structure and Reactivity, 4th ed*; Harper-Collins, 1993.
(65) Muhammad, S.; Moncho, S.; Brothers, E. N.; Bengali, A. A. *Chem. Commun.* **2014**, *50*, 5874.
(66) Kim, S.-K.; Han, W.-S.; Kim, T.-J.; Kim, T.-Y.; Nam, S. W.; Mitoraj, M.; Piekoś, Ł.; Michalak, A.; Hwang, S.-J.; Kang, S. O. *J. Am. Chem. Soc.* **2010**, *132*, 9954.
(67) DePoy, R.; Kodama, G. *Inorg. Chem.* **1985**, *24*, 2871.
(68) Ishii, M.; Kodama, G. *Inorg. Chem.* **1990**, *29*, 2181.
(69) Hertz, R. K.; Denniston, M. L.; Shore, S. G. *Inorg. Chem.* **1978**, *17*, 2673.
(70) Shimoi, M.; Katoh, K.; Tobita, H.; Ogino, H. *Inorg. Chem.* **1990**, *29*, 814.
(71) Snow, S. A.; Shimoi, M.; Ostler, C. D.; Thompson, B. K.; Kodama, G.; Parry, R. W. *Inorg. Chem.* **1984**, *23*, 511.
(72) Shimoi, M.; Katoh, K.; Ogino, H. *J. Chem. Soc., Chem. Commun.* **1990**, 811.
(73) Snow, S. A.; Kodama, G. *Inorg. Chem.* **1985**, *24*, 795.
(74) Pingen, D.; Lebl, T.; Lutz, M.; Nichol, G. S.; Kamer, P. C. J.; Vogt, D. *Organometallics* **2014**, *33*, 2798.
(75) Pontiggia, A. J.; Chaplin, A. B.; Weller, A. S. *J. Organomet. Chem.* **2011**, *696*, 2870.
(76) Wagner, A.; Kaifer, E.; Himmel, H.-J. *Chem. Eur. J.* **2013**, *19*, 7395.
(77) Kawano, Y.; Yamaguchi, K.; Miyake, S.-y.; Kakizawa, T.; Shimoi, M. *Chem. Eur. J.* **2007**, *13*, 6920.
(78) Ardura, D.; López, R.; Sordo, T. L. *J. Phys. Chem. B* **2005**, *109*, 23618.

# 3 Hydroboration of alkenes by $H_3B{\cdot}NMe_3$

## 3.1 Introduction

Hydroboration is the addition of a B—H bond across an unsaturated C—C bond to form an alkylborane (Scheme 3.1). Hydroboration is tremendously useful in organic synthesis due to the further reactions the resulting alkylborane can undergo. For example, oxidation of the alkylborane with $H_2O_2$ produces alcohols.[1] Organoboranes are also used widely in Suzuki couplings.[2] The first example of hydroboration was reported by Brown in 1957, in which addition of diborane to alkenes including 1-pentene and 1-hexene yielded the trialkylboranes $B\{(CH_2)_4CH_3\}_3$ and $B\{(CH_2)_5CH_3\}_3$, respectively, as a result of three successive hydroborations.[3]

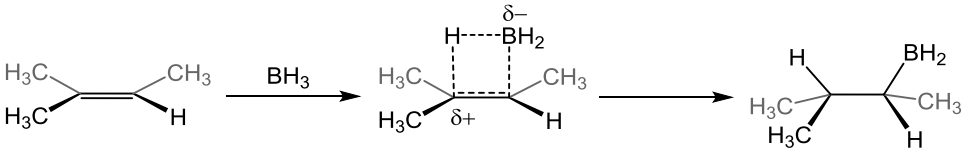



**Scheme 3.1** Hydroboration of an alkene.

### 3.1.1 Non-catalysed hydroboration

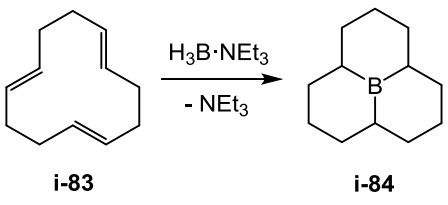
Non-metal catalysed hydroboration generally proceeds in an anti-Markovnikov fashion, whereby the borane adds to the least substituted carbon atom. This is thought to be due to a combination of steric and electronic factors. Sterically, the boron attaches to the less hindered carbon atom of the alkene. Electronically, the favoured four-membered transition state for hydroboration places a partial positive charge on the more substituted carbon atom (Scheme 3.2).[1] Typical borane reagents for non-catalysed hydroboration include $BH_3{\cdot}THF$ and $BH_3{\cdot}SMe_2$. However, $BH_3{\cdot}THF$ is only available in solutions of up to 1 M and, over time, the borane can react with THF, or must be stabilised by $NaBH_4$, potentially resulting in unwanted side

reactions.[4,5] $BH_3$·$SMe_2$ is more stable and is available at higher concentrations,[6] but is volatile and malodourous, and $SMe_2$ is released as a by-product of hydroboration.[4,7]




**Scheme 3.2** Mechanism for the hydroboration of 2-methylbut-2-ene by $BH_3$. Only the first hydroboration is shown.

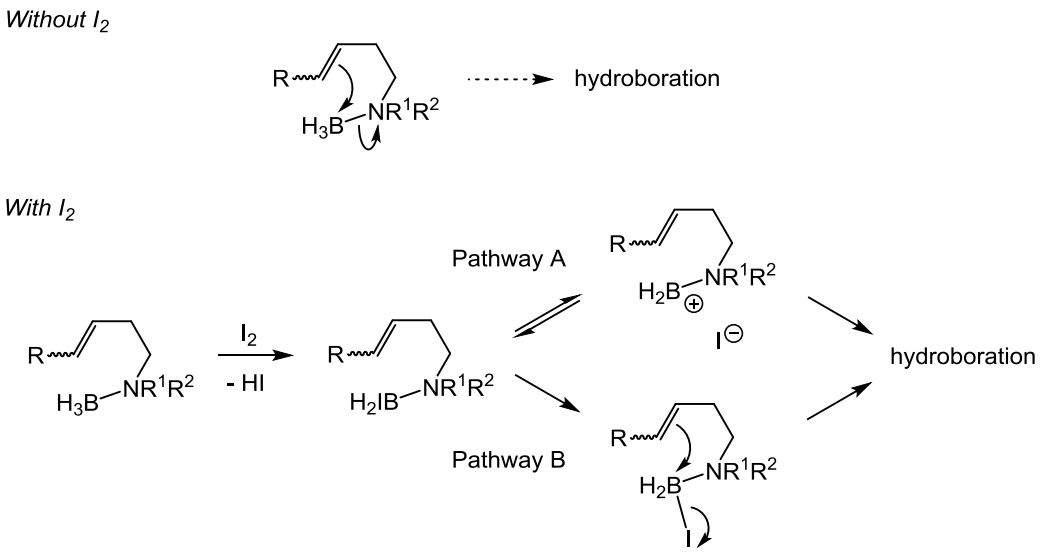
Amine-boranes offer a more stable source of $BH_3$ for hydroboration by B—N bond cleavage,[8] but the increased strength of the B—N dative bond compared with that in $BH_3$·THF or $BH_3$·$SMe_2$ means that amine-boranes are less active as hydroboration agents.[9] Thus, high temperatures are usually required for hydroboration using amine-boranes. However, *tert*-octyldiethylamine-borane has proved an especially reactive substrate for hydroboration, forming mono-, di- and tri-substituted boranes at room temperature with a range of alkenes.[10] Furthermore, the relatively sluggish hydroboration with amine-boranes has been utilised to form compounds such as **i-84** from the hydroboration of the cyclic triene **i-83** (Scheme 3.3), whereas di- or tri-boranes may result from using faster hydroborating agents.[11]




**Scheme 3.3** Hydroboration of a cyclic triene using $H_3B$·$NEt_3$.

Examples of the B—N bond remaining intact during hydroboration using amine-boranes are rare. Vedejs and co-workers reported that homoallylic amine-borane

complexes undergo intramolecular hydroboration, promoted by 10 mol% $I_2$.[12] To access the required four-membered transition state for hydroboration without $I_2$, the B—N bond must break (Scheme 3.4). This is unfavourable partly due to the strength of the B—N interaction, but primarily due to having an endocyclic leaving group relative to the cyclic transition state, which does not allow correct orbital overlap for an $S_N2$-like mechanism. With $I_2$, however, the formation of a weak B—I bond enables hydroboration through either an $S_N1$-like mechanism with a borenium cation (Scheme 3.4, Pathway A), or an $S_N2$-like mechanism that can occur with the exocyclic iodide leaving group (Scheme 3.4, Pathway B).[13] Hydroboration with amine-boranes has also been demonstrated to proceed *via* a radical pathway.[14]

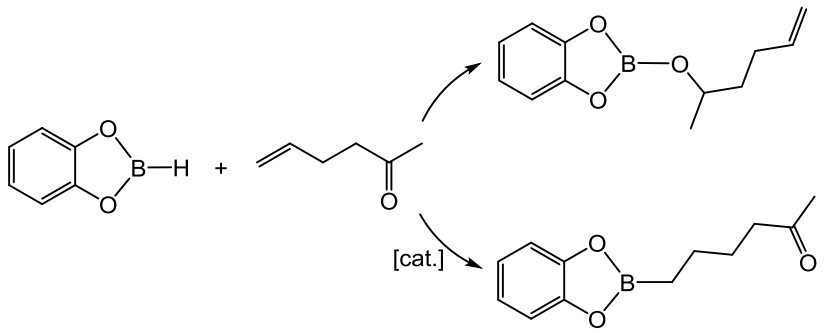



**Scheme 3.4** Potential pathways for intramolecular iodine-activated hydroboration of homoallylic amine-boranes.

Heteroatom-stabilised boranes, such as catecholborane or pinacolborane, are also fairly unreactive for uncatalysed hydroboration reactions,[15] although they have been shown to hydroborate alkynes at room temperature.[16] Generally, however, they are most commonly employed in catalysed transformations.[17]

### 3.1.2 Metal catalysed hydroboration

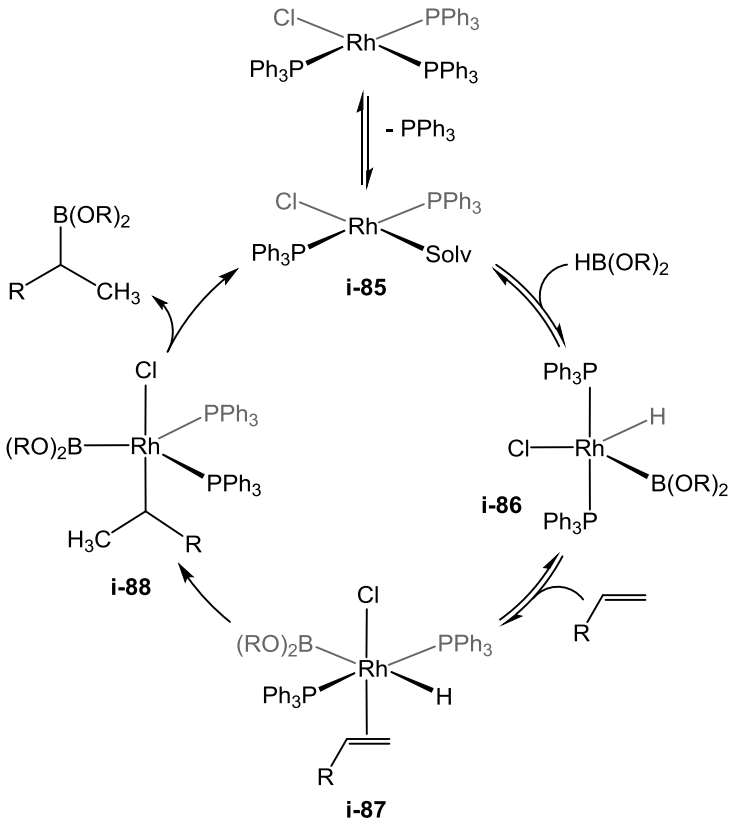
In 1985, Männig and Nöth reported the catalytic hydroboration of 5-hexen-2-one with catecholborane, and showed that the outcome of the reaction depends upon whether the reaction is catalysed or uncatalysed. Wilkinson's catalyst [$Rh(PPh_3)_3Cl$] was reported to catalyse hydroboration across the alkene, whereas the absence of catalyst led to addition of the borane across the ketone (Scheme 3.5). Other Rh-based complexes, *e.g.* [$Rh(\mu\text{-}Cl)_2(1,5\text{-cod})]_2$, showed reasonable activity, and Ru, Pd, Ir and Co complexes trialled showed little or no activity.[18]




**Scheme 3.5** Catalysed and non-catalysed hydroboration of 5-hexen-2-one. [cat.] = [$Rh(PPh_3)_3Cl$].

Metal-catalysed hydroboration can form either predominantly linear (anti-Markovnikov) or branched (Markovnikov) products depending upon the substrates and conditions used. The generally accepted mechanism for the hydroboration using Wilkinson's catalyst, similar to that first suggested by Männig and Nöth,[18] is shown in Scheme 3.6.[17] Initial decoordination of a phosphine ligand to form **i-85** enables the reversible oxidative addition of the borane, yielding a 16 electron boryl complex (**i-86**). This complex has been isolated with catecholborane,[19] and undergoes hydroboration upon the stoichiometric addition of alkenes.[18] Alkene coordination to **i-86** yields **i-87**, followed by hydride migration to the alkene, forming **i-88**. Reductive

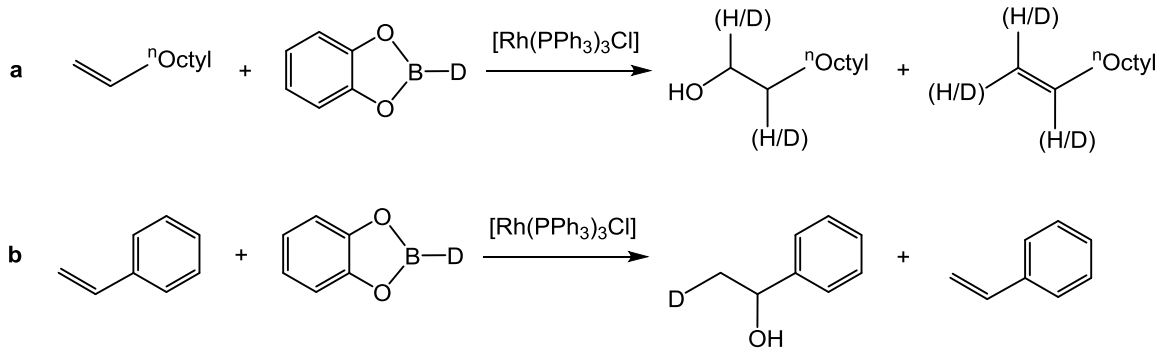
elimination from **i-88** yields the product of hydroboration and regenerates **i-85**. The linear:branched ratio of the product is determined by the hydride migration and reductive elimination steps.




**Scheme 3.6** General mechanism for the hydroboration of alkenes with Wilkinson's catalyst. Pathway leading to the branched product is shown. Hydride migration step (**i-87** to **i-88**) has been shown to be reversible in some systems.

Detailed mechanistic studies have been conducted upon this and related systems and show that the mechanisms are complex and likely consist of competing pathways.[20-24] For example, Evans and co-workers used deuterium labelled catecholborane, DBCat, to hydroborate a series of alkenes, catalysed by $[Rh(PPh_3)_3Cl]$. The alcohol products (post-oxidative work-up) were examined for deuterium incorporation to probe the reversibility of the alkene coordination, hydride migration and reductive elimination steps. With 1-decene, the anti-Markovnikov product was formed. Only the reductive

elimination step was irreversible, illustrated by the observation of deuterium in both the positions α and β to the alcohol in the product, as well as in the alkene signals of 'unreacted' starting 1-decene (Scheme 3.7a). For styrene, however, the Markovnikov product was formed, and deuterium was only observed in the product in the position β to the alcohol, and not observed in the starting alkene (Scheme 3.7b), suggesting that alkene coordination, hydride migration and reductive elimination are likely irreversible.[23] These results showed that the mechanistic detail of the hydroboration is highly dependent upon the nature of the alkene. Similarly, Sabo-Etienne has reported that the reaction of pinacolborane with various alkenes, catalysed by $[Ru(PCy_3)_2(H)_2(\eta^2\text{-}H_2)_2]$, results in either hydroboration or dehydrogenative borylation, with the outcome dependent upon the alkene.[25]



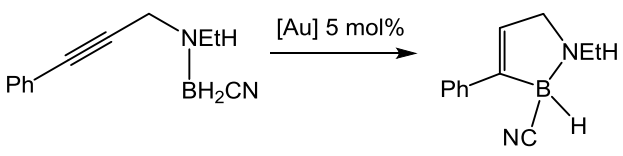

**Scheme 3.7** Evans' reaction of DBCat with **(a)** 1-decene and **(b)** styrene. The products are shown post-oxidative work-up.

In 2012, Leitner reported the selective hydroboration of terminal alkynes with pinacolborane to form *Z*-vinylborates using a ruthenium pincer catalyst. This contrasts the non-metal-catalysed hydroboration of terminal alkynes, in which *E*-vinylborates are produced through anti-Markovnikov *syn*-addition of the borane.[15] It was speculated that a 1,2-hydrogen shift from an $\eta^2$-alkyne forms an $\eta^1$-vinylidene complex, possibly due to steric interactions, and coupling of the vinylidene and

pinacolborates results in *Z* selectivity in this system.[26] $Fe_2(CO)_9$ has also been shown to catalyse the hydroboration of alkynes with pinacolborane, with the *E* or *Z* selectivity dependent upon the alkyne.[27]

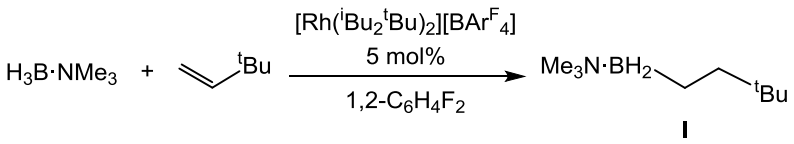
The regioselectivity of metal catalysed reactions has also been shown to vary with the nature of the borane, as well as with the metal, ligand and conditions.[28,29] For example, reaction of styrene and catecholborane, catalysed by Wilkinson's catalyst, produces exclusively the Markovnikov isomer.[23] $Cp_2TiMe_2$ as catalyst produces the anti-Markovnikov isomer, however.[30] Improved yields and selectivity in rhodium-catalysed hydroboration reactions have also been achieved by the addition of the Lewis acid $B(C_6F_5)_3$ as co-catalyst.[31] Furthermore, a range of lanthanide(III) complexes have been shown to catalyse the hydroboration of alkenes with catecholborane; it was speculated that the lanthanide operates as a Lewis acid to promote the hydroboration.[32]

Reports on metal catalysed hydroboration have generally focused upon catecholborane or pinacolborane,[17] and there are few examples of metal-mediated hydroboration of amine-boranes in which the B—N bond remains intact. Recently, Shi and co-workers described the synthesis of cyclic amine-boranes through gold-catalysed alkyne hydroboration (Scheme 3.8). [XPhosAu-TA][OTf] (TA = triazole) was found to be the most effective catalyst, achieving over 93% isolated yield (72 hours, 80 °C). It was assumed [Au] activates the alkyne and promotes the hydroboration.[33]



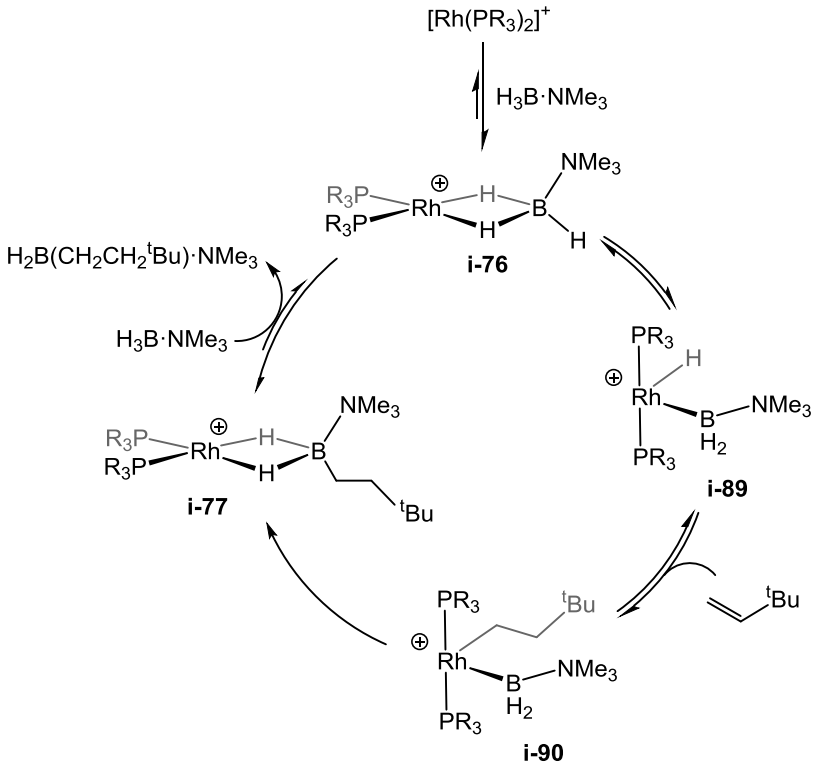

**Scheme 3.8** Gold-catalysed formation of cyclic amine-boranes.

As mentioned in Chapter 2, addition of TBE to **i-76** to form **i-77** was reported in 2011 by Weller and co-workers. Under catalytic conditions, starting with $[Rh(P^iBu_2{}^tBu)_2][BAr^F{}_4]$ (5 mol%), the anti-Markovnikov product of hydroboration $H_2B(CH_2CH_2{}^tBu)\cdot NMe_3$ (**I**) was formed exclusively (Scheme 3.9).[34] The control reaction between TBE and $H_3B\cdot NMe_3$ in the absence of catalyst resulted in no turnover. Previously, the hydroboration of TBE by $H_3B\cdot THF$, catalysed by $Rh^{III}$ or uncatalysed, formed a mixture of Markovnikov and anti-Markovnikov isomers.[35]



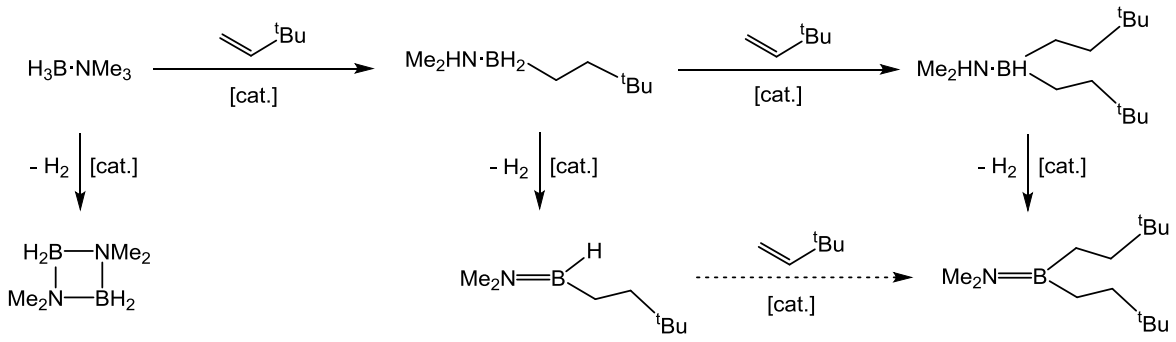

**Scheme 3.9** Hydroboration of TBE by $H_3B\cdot NMe_3$ catalysed by $[Rh(P^iBu_2{}^tBu)_2][BAr^F{}_4]$.

Although selective, the hydroboration with $[Rh(P^iBu_2{}^tBu)_2][BAr^F{}_4]$ was slow, reaching a maximum of ~70% conversion after 94 hours. This was thought to be due to product inhibition since **I** was demonstrated to compete effectively with $H_3B\cdot NMe_3$ for coordination to the metal centre. Initial rates[36] kinetic studies indicated that the reaction was first order in [Rh] and [TBE], and zero order in $[H_3B\cdot NMe_3]$. A catalytic cycle was proposed to account for these observations: initial fast, essentially irreversible, binding of $H_3B\cdot NMe_3$ to form **i-76** is followed by B—H activation to form base-stabilised boryl complex **i-89**, olefin insertion forms **i-90**, and reductive elimination forms **i-77** (Scheme 3.10). The cycle is similar to that proposed for the hydroboration using catecholborane and Wilkinson's catalyst (Scheme 3.6).




**Scheme 3.10** Proposed catalytic cycle for the hydroboration of TBE by $H_3B{\cdot}NMe_3$. $PR_3 = P^iBu_2{}^tBu$. $[BAr^F{}_4]^-$ anions not shown.

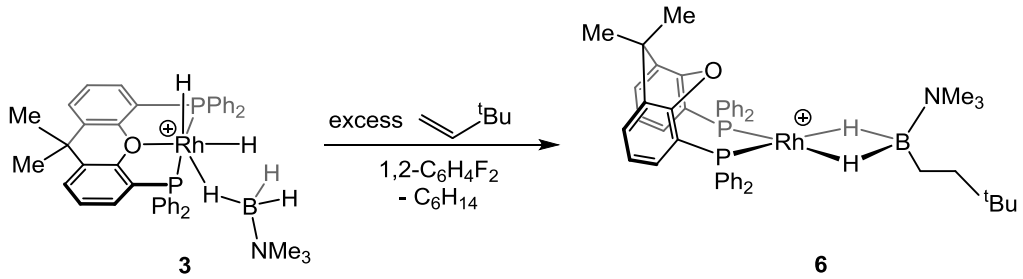
Interestingly, Weller also demonstrated tandem hydroboration and dehydrocoupling using this system. Reaction of $H_3B{\cdot}NMe_2H$ with TBE and $[Rh(P^iBu_2{}^tBu)_2][BAr^F{}_4]$ (5 mol%) resulted in the formation of three major products: $[H_2BNMe_2]_2$, $Me_2N{=}BH(CH_2CH_2{}^tBu)$ and $Me_2N{=}B(CH_2CH_2{}^tBu)_2$. A mechanism was suggested in which hydroboration of TBE by $H_3B{\cdot}NMe_2H$ can occur twice to form $Me_2H{\cdot}NBH(CH_2CH_2{}^tBu)_2$, but dehydrogenation is competitive at each stage (Scheme 3.11). Addition of excess TBE to $Me_2N{=}BH(CH_2CH_2{}^tBu)$ did not form $Me_2N{=}B(CH_2CH_2{}^tBu)_2$, suggesting that the formation of $Me_2N{=}B(CH_2CH_2{}^tBu)_2$ is not *via* hydroboration of $Me_2N{=}BH(CH_2CH_2{}^tBu)$. This system shows promise as a means of hydroboration with amine-boranes in which the B—N bond is retained, although the high catalyst loadings, product inhibition and long reaction times limit the broader applicability.



**Scheme 3.11** Tandem hydroboration and dehydrogenation. [cat.] = $[Rh(P^iBu_2{}^tBu)_2][BAr^F{}_4]$ (5 mol%).

## 3.2 Catalytic hydroboration using 6

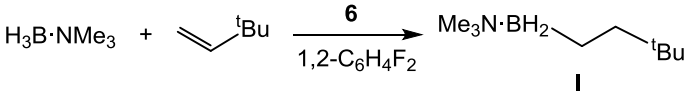
As introduced in Chapter 2, the fast reduction of **3** and the hydroboration of TBE by $H_3B{\cdot}NMe_3$ forms **6**, in which **I** is bound to $\{Rh(Xantphos)\}^+$. Only the anti-Markovnikov product was observed to form (Scheme 3.12). Conversion of **3** to **6** is fast (minutes) compared with the formation of **i-77** from **i-76** (3 days).[34] The fast stoichiometric reactivity in forming **6** encouraged exploration of the catalytic hydroboration of $H_3B{\cdot}NMe_3$ by TBE using the $\{Rh(Xantphos)\}^+$ fragment.



**Scheme 3.12** Formation of **6** from **3**. $[BAr^F{}_4]^-$ anions not shown.

Addition of **6** (5 mol% relative to $H_3B{\cdot}NMe_3$) to a mixture of $H_3B{\cdot}NMe_3$ (0.19 M) and TBE (0.38 M) in 1,2-$C_6H_4F_2$ resulted in the complete formation of **I** within three hours, as observed by $^{11}B$ NMR spectroscopy (Scheme 3.13). As previously reported,

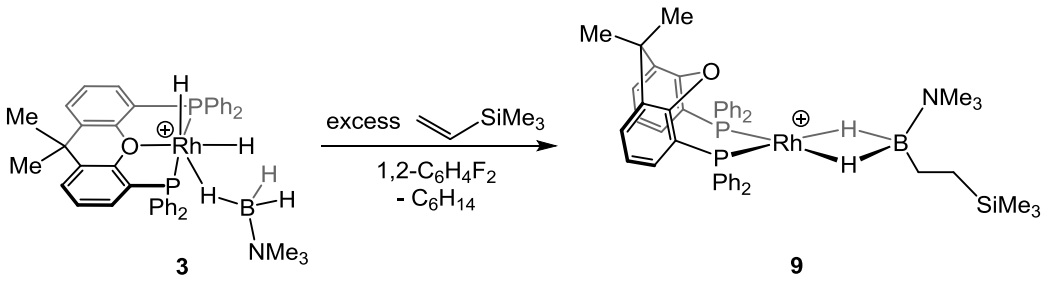
the $^{11}B$ NMR spectrum of **I** is a broad triplet at δ –0.83 ($^{1}J_{HB}$ = 96 Hz).[34] The sole formation of the anti-Markovnikov product was confirmed by $^{1}H$ NMR spectroscopy; two multiplet resonances were observed at δ 1.42 and δ 0.55, each relative integral 2H, corresponding to the signals in the alkyl chain, with no evidence of the branched isomer. A 2:1 ratio of TBE:$H_3B{\cdot}NMe_3$ was used in the hydroboration to avoid dehydrogenative homocoupling of $H_3B{\cdot}NMe_3$ to yield **8**, which can occur when an excess of $H_3B{\cdot}NMe_3$ is present (Chapter 2). During the reaction, the only metal-containing product observed by NMR spectroscopy was **6**.




**Scheme 3.13** Catalytic hydroboration of TBE by $H_3B{\cdot}NMe_3$ using **6** (5 mol%).

## 3.3 Hydroboration catalyst selection and formation

Although **6** is a competent catalyst for the hydroboration of TBE by $H_3B{\cdot}NMe_3$, a different source of {Rh(Xantphos)}$^{+}$ was sought. A complex with an amine-borane coordinated to {Rh(Xantphos)}$^{+}$ that is different, but related, to **I** would be expected to behave similarly to **6**, but show different spectroscopic properties. This would enable monitoring of the change in catalyst resting states during catalysis. Therefore, the complex [Rh($\kappa^2_{P,P}$-Xantphos)($\eta^2$-$H_2B(CH_2CH_2SiMe_3){\cdot}NMe_3$)][$BAr^F_4$] (**9**, synthesised and characterised by Part II student Rebecca Torry-Harris),[37] closely related to **6**, was used. In an analogous manner to the formation of **6**, addition of two equivalents of trimethyl(vinyl)silane (TMVS) to **3** resulted in reduction and hydroboration of TMVS to form **9** quantitatively within minutes (Scheme 3.14).




**Scheme 3.14** Formation of **9**. $[BAr^F{}_4]^-$ anions not shown.

Complex **9** shows very similar spectroscopic data to **6**. The $^1$H NMR spectrum indicates that $H_2B(CH_2CH_2SiMe_3)\cdot NMe_3$ is sigma bound to the metal centre in an $\eta^2$ fashion, evidenced by the 2H quadrupolar-broadened signal at δ –6.54, which collapses to an overlapping doublet of doublets (virtual triplet) on $^{11}$B decoupling ($^1J_{RhH}$ = 36 Hz, $^2J_{P\mathit{trans}H}$ = 36 Hz). As with **6**, only the anti-Markovnikov product of hydroboration was observed, with two relative integral 2H signals corresponding to the alkyl chain protons at δ 1.17 and δ 0.78. A $^{29}$Si–$^1$H HMBC NMR experiment showed a correlation between the signal at δ 1.17 and silicon ($\delta^{(29}Si)$ 2.1), indicating that these protons are α to silicon. The Xantphos methyl groups appear as separate relative integral 3H signals (δ 1.73 and δ 1.67). Similar to **6**, the $^{11}$B NMR spectrum shows the bound $H_2B(CH_2CH_2SiMe_3)\cdot NMe_3$ as a broad signal at δ 37.0, a *ca.* 37 ppm shift from that of the free borane (δ –0.5, t, $^1J_{HB}$ = 96 Hz, obtained by addition of MeCN to **9** in 1,2-$C_6H_4F_2$), typical for $\eta^2$ coordination to a $Rh^I$ centre.[38] The $^{31}$P{$^1$H} NMR spectrum shows one $^{31}$P environment at δ 26.7 ($^1J_{RhP}$ = 182 Hz). ESI-MS was consistent with the formation of **9** (*m/z* = 854.28, calc. 854.28) with the expected isotopic pattern. The solid state structure (Figure 3.1, crystals grown by R. Torry-Harris) supports the solution NMR data.

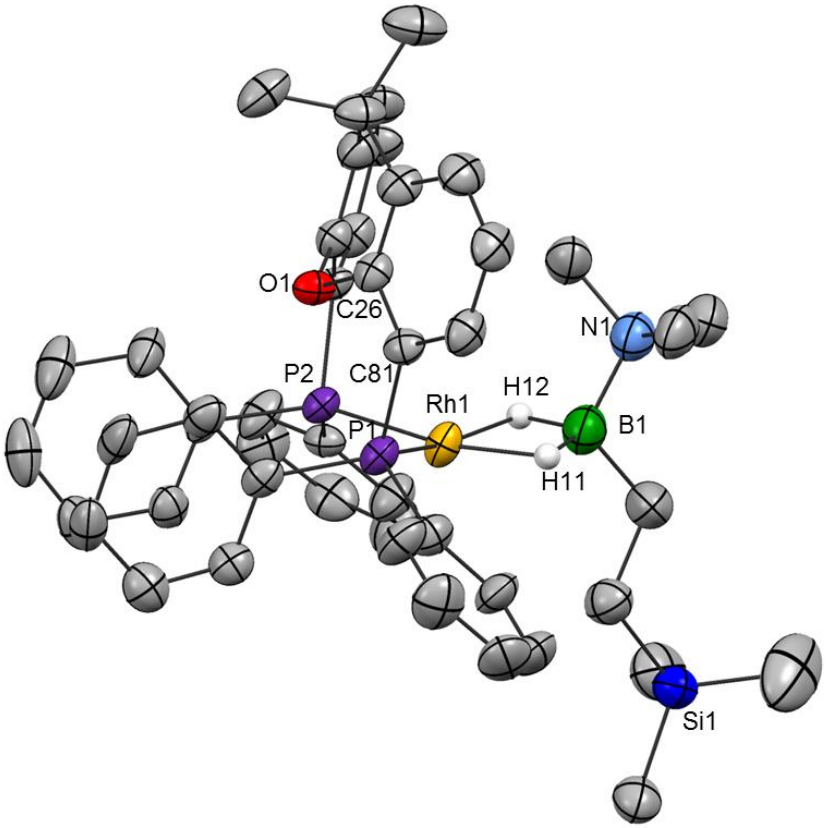



**Figure 3.1** Solid-state structure of the cationic portion of **9**. Displacement ellipsoids are drawn at the 50% probability level. All carbon-bound H atoms are omitted for clarity. Only the major component of the disordered $NMe_3$ and $SiMe_3$ groups are shown. Selected bond lengths (Å) and angles (°): Rh1–P1, 2.2398(18); Rh1–P2, 2.2670(17); Rh1–O1, 3.2342(73); Rh1–B1, 2.179(7); B1–N1, 1.603(4); P1–Rh1–P2, 98.23(6).

The solid state structure is similar to that of **6**, with Xantphos in $\kappa^2_{P,P}$ geometry. H11 and H12 were located on the Fourier map and show $\eta^2$ coordination of the borane. The Rh—B distances are the same (within error) for **9** and **6**, implying similar amine-borane binding strength. However, in **6**, the $CH_2CH_2{}^tBu$ group is *syn* to the Xantphos backbone whereas, in **9**, the $NMe_3$ group is *syn* to the Xantphos backbone, possibly due to steric or crystal packing effects. The different orientation of the borane induces slight differences in the Xantphos binding. In **9**, the angle between the P2-Rh1-P2 and mean C26-P2-P1-C81 planes is compressed (92.73°) compared with the analogous angle in **6** (114.33°) (Figure 3.2), which may be 'pushed' open due to the bulk of

$CH_2CH_2{}^tBu$ *vs* $NMe_3$. As a result, the Rh—O distance in **9** of 3.2342(73) Å is shorter than that in **6** (3.431(3) Å), although both distances are well within the range in which the hemilabile O atom is considered not coordinated to the metal.[39]

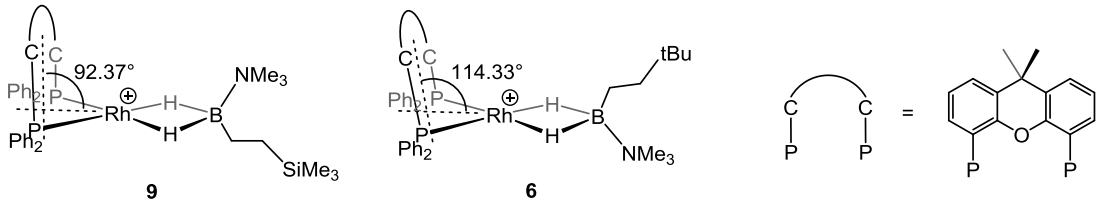
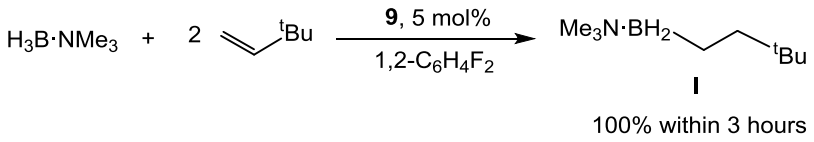



**Figure 3.2** Representation of the opening of the Xantphos backbone in **9** *vs* **6**. $[BAr^F{}_4]^-$ anions not shown.

Owing to its similarity with **6**, **9** appeared to be a viable alternative to **6** as a source of $\{Rh(Xantphos)\}^+$ for investigating the hydroboration mechanism.

## 3.4 Hydroboration using 9: resting states

Addition of **9** (5 mol%) to a 1,2-$C_6H_4F_2$ solution of TBE (0.38 M) and $H_3B{\cdot}NMe_3$ (0.19 M) formed **I** quantitatively within 3 hours (Scheme 3.15), as measured by $^{11}B$ NMR spectroscopy, a similar timescale to that observed with **6**.




**Scheme 3.15** Catalytic hydroboration using $H_3B{\cdot}NMe_3$ (0.19 M), TBE (0.38 M) and **9** ($9.5 \times 10^{-3}$ M).

At this concentration of **9**, $^1H$ and $^{31}P\{^1H\}$ NMR spectroscopies could be used to observe the metal species. With **6** as the precatalyst, **6** was the only species observed by NMR spectroscopy (Section 3.2). However, using **9** enabled a change in the resting state to be observed; initially, at conversions of approximately 20%, a mixture of **9** and **6** is apparent by broad overlapping hydride signals in the $^1H$ NMR spectrum (**6**:

δ –6.85; **9**: δ –6.54 in 1,2-$C_6H_4F_2$). As the reaction progressed, the signal sharpened until the exclusive metal-containing product observed by NMR spectroscopy was **6**. Thus, as more **I** is produced, $H_2B(CH_2CH_2SiMe_3)\cdot NMe_3$ is displaced from the metal.

The change in the resting state was probed in more detail using the pressurised sample infusion (PSI) ESI-MS technique in collaboration with Dr J. Scott McIndoe (University of Victoria, Canada).[40-42] This technique uses an overpressure of argon gas (1.5 psi in this case) to continuously feed the reaction mixture into the mass spectrometer (see Figure 3.3 for experiment setup), allowing for 'real time' monitoring of the reaction.

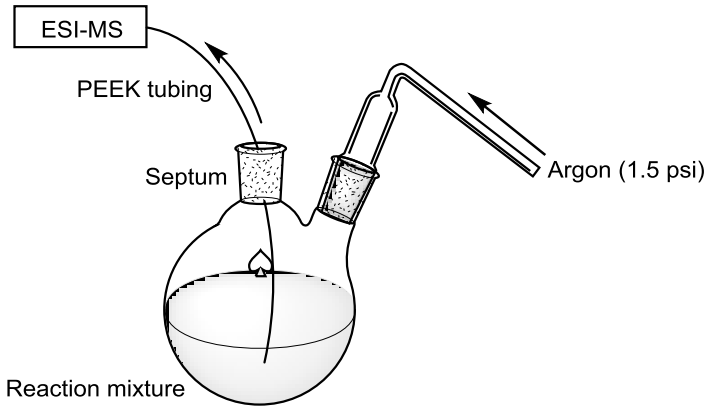



**Figure 3.3** Diagram depicting the experimental setup for the PSI ESI-MS technique.

PSI ESI-MS allows a high data density to be collected over a wide dynamic range and provides a temporal profile of the cationic species present during the course of the reaction. Due to the necessarily low concentrations of $[M]^+$ used for ESI-MS analysis, a high catalytic loading of 15 mol% **9** (0.001 M) was required, with $[TBE]_0$ = 0.013 M and $[H_3B\cdot NMe_3]_0$ = 0.006 M. The reaction solution was continuously monitored by ESI-MS for 1 hour, from which a plot of the normalised intensities of each species *vs* time was obtained (Figure 3.4). Periodic sampling of the reaction mixture for analysis

by $^{11}B$ NMR spectroscopy indicated that catalysis had reached approximately 80% completion after 1 hour.

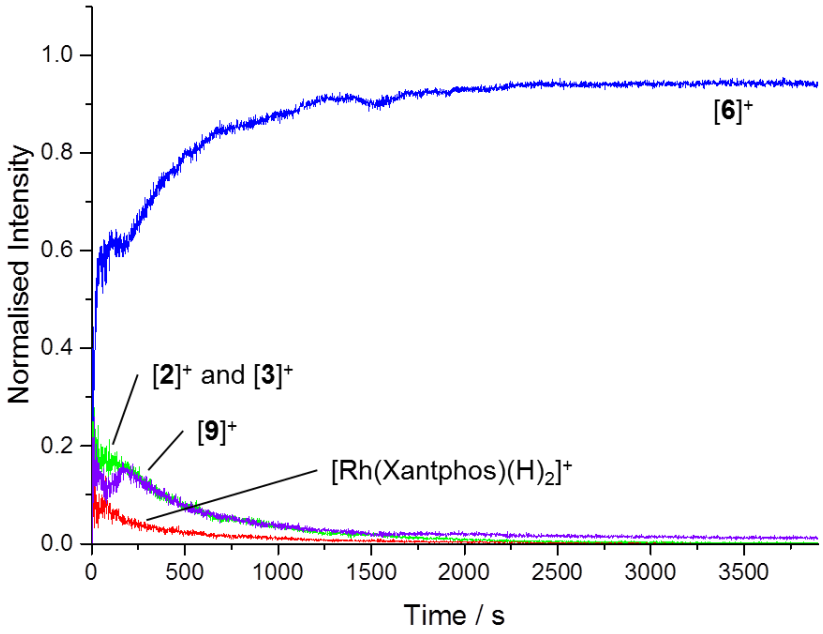



**Figure 3.4** ESI-MS of the metal-containing species observed in the reaction of TBE (0.013 M), $H_3B{\cdot}NMe_3$ (0.006 M) and **9** (0.001 M) in 1,2-$C_6H_4F_2$ under PSI conditions. Hydroboration proceeded to 80% conversion after 3600 s.

The plot of intensities *vs* time shows that [**6**]$^+$ rapidly grows in with decay of [**9**]$^+$ as the reaction progresses, consistent with the NMR experiments at 5 mol% loading. Peaks corresponding to [**2**]$^+$ and [**3**]$^+$ were also observed; as the molecular ions for these species appear only 2 mass units apart, their isotopic patterns overlapped and so could not be plotted separately. The presence of [**2**]$^+$ at early reaction times shows that initial displacement of **I**/$H_2B(CH_2CH_2SiMe_3){\cdot}NMe_3$ by $H_3B{\cdot}NMe_3$ is a likely first step in the reaction. No evidence for [Rh(Xantphos)(TBE)]$^+$ was observed either by ESI-MS or NMR experiments; TBE has been shown to have a low affinity for the related pincer fragment {Ir($^t$BuPOCOP$^t$Bu)}$^+$, possibly due to sterics.[43] The less bulky alkene complex [Rh($\kappa^3{}_{P,O,P}$-Xantphos)($\eta^2$-$H_2C$=CHCOOMe)][$BAr^F{}_4$] has been

previously characterised in solution, however.[44] The presence of [**3**]$^+$ and [Rh(Xantphos)(H)$_2$]$^+$ may be due to parallel homocoupling, in which **3** forms alongside **8**. Under a two-fold excess of TBE, neither **8** nor **3** are observed by NMR spectroscopy, implying that ESI-MS may be particularly sensitive to the observation of these species. These intermediates decay at a similar rate to **9**, suggesting that **I** may bind preferentially to the metal, forming **6**, and implying that product inhibition in this system is likely.

## 3.5 Kinetic Studies

### 3.5.1 Initial rates experiments

Due to the potential for product inhibition in this system,[34] as well as potential homocoupling reactivity with excess $H_3B{\cdot}NMe_3$, initial rates methods[36] were selected to study the kinetics of the hydroboration in more detail. $^{11}$B NMR spectroscopy was used to monitor conversion of $H_3B{\cdot}NMe_3$ to **I**. Although a catalyst loading of 5 mol% (catalyst = **6** or **9**) enabled observation of the catalyst by NMR spectroscopy, the reaction was too fast for meaningful kinetic data to be gleaned, with approximately 50% conversion to **I** within the first 300 s. With a reduced loading of 0.5 mol% of **6** or **9**, however, catalysis reached approximately 80% completion within 12 hours (with 20% $H_3B{\cdot}NMe_3$ remaining unreacted), and approximately 10% completion within the first 300s. Some representative $^{11}$B NMR spectra are shown in Figure 3.5.

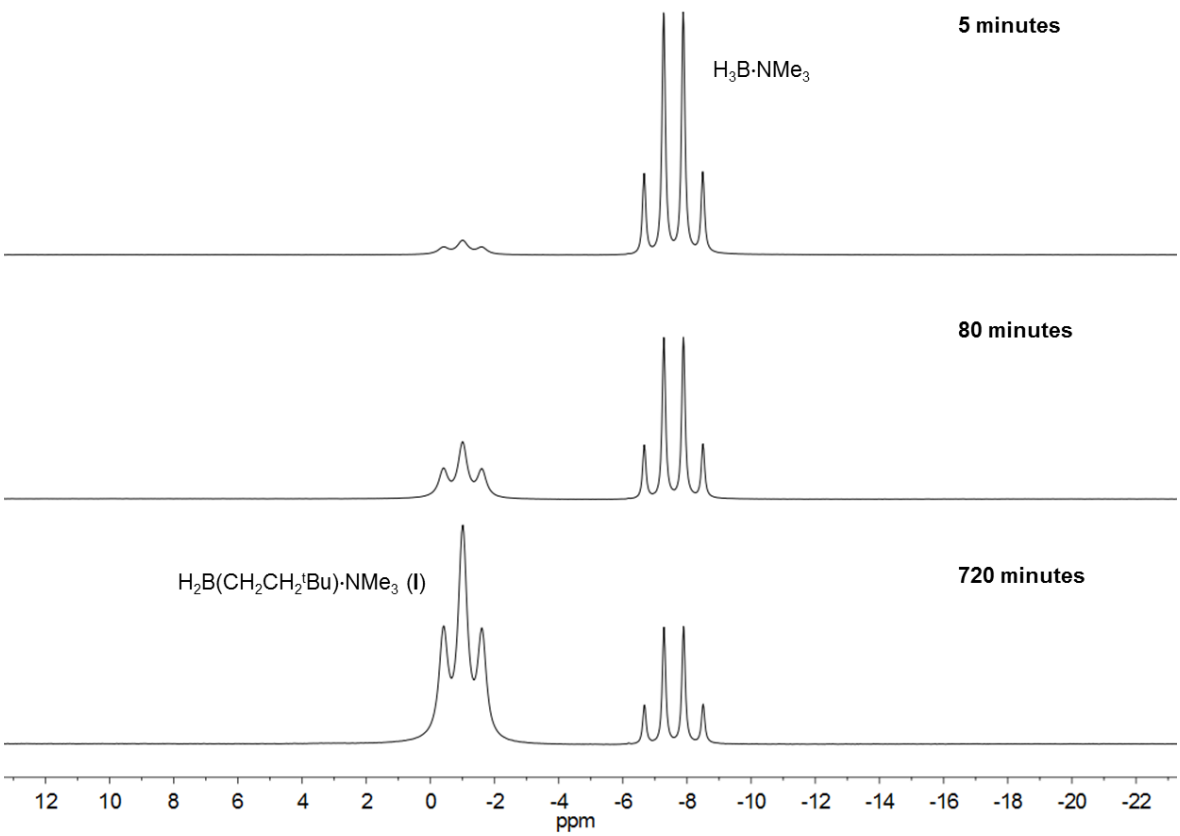



**Figure 3.5** Back-linear predicted $^{11}B$ NMR spectra of the hydroboration reaction at 5, 80 and 720 minutes. $[H_3B{\cdot}NMe_3]_0$ = 0.19 M, $[TBE]_0$ = 0.38 M, [**9**] = 9.5 x $10^{-4}$ M, 1,2-$C_6H_4F_2$ solvent, 295 K.

These timescales indicated that a 0.5 mol% loading of **9** was appropriate for initial rates investigations. To probe the orders of the reactants in the hydroboration reaction, the starting concentrations of $H_3B{\cdot}NMe_3$, TBE and **9** were systematically varied and the initial rates were calculated from integration of the $^{11}B$ NMR signals over the zero order region of catalysis (*ca.* first 300 s). The initial rates obtained are shown in Table 3.1. **9** was used as the catalyst for these studies; using **9** or **6** as the catalyst resulted in the same initial rate, within error (Entries 1 and 8, Table 3.1). The data from Entries 1, 2 and 3 (Table 3.1) indicate that the reaction is first order in [TBE]; a plot of initial rate *vs* $[TBE]_0$ gives a straight line (Figure 3.6), confirming this. The reaction is first order in [**9**] also (Entries 1 and 4 and Figure 3.7).

**Table 3.1** Initial rates data on altering the starting concentrations of $H_3B{\cdot}NMe_3$, TBE and **9**. Initial rates obtained from $^{11}B$ NMR spectroscopy integrals over the first 300 s of reaction (*pseudo* zero order region). Solvent = 1,2-$C_6H_4F_2$. [a]With an additional 70 eq. of **I** added at the start of catalysis. [b]Using **6** instead of **9**. [c]Using $D_3B{\cdot}NMe_3$ instead of $H_3B{\cdot}NMe_3$. [d]Using **8** instead of **9**.

| Entry | $[H_3B{\cdot}NMe_3]_0$ / M | $[TBE]_0$ / M | [9] / $10^{-4}$ M | Initial rate / $10^{-5}$ M $s^{-1}$ |
|---|---|---|---|---|
| 1 | 0.19 | 0.38 | 9.5 | 6.81 ± 0.12 |
| 2 | 0.19 | 0.19 | 9.5 | 3.64 ± 0.27 |
| 3 | 0.19 | 0.76 | 9.5 | 12.98 ± 0.38 |
| 4 | 0.19 | 0.38 | 19 | 13.25 ± 0.56 |
| 5 | 0.38 | 0.19 | 9.5 | 7.41 ± 0.53 |
| 6 | 0.76 | 0.19 | 9.5 | 6.33 ± 0.40 |
| 7[a] | 0.19 | 0.38 | 9.5 | 2.07 ± 0.11 |
| 8[b] | 0.19 | 0.38 | 9.5 (**6**) | 7.44 ± 0.64 |
| 9[c] | 0.19 | 0.38 | 9.5 | 5.09 ± 0.07 |
| 10[d] | 0.19 | 0.76 | 9.5 (**8**) | 3.05 ± 0.12 |

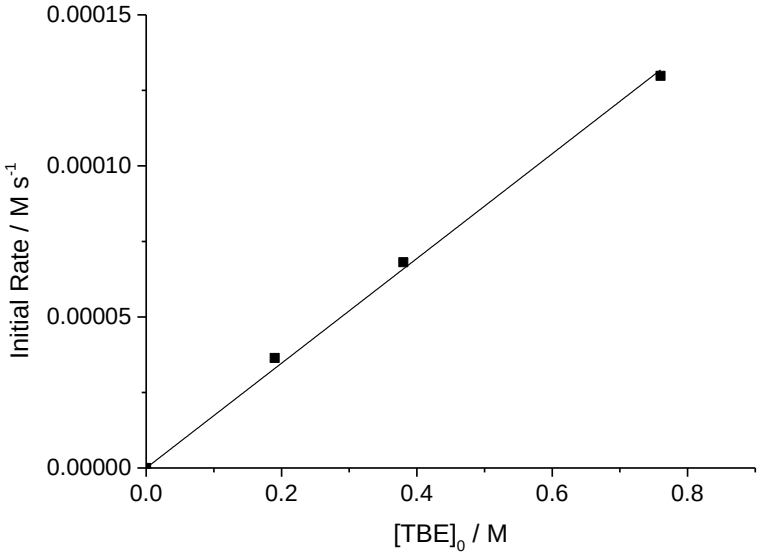



**Figure 3.6** Plot of initial rate *vs* $[TBE]_0$. $[H_3B{\cdot}NMe_3]_0$ = 0.19 M, [**9**] = 9.5 x $10^{-4}$ M. $R^2$ = 0.99879.

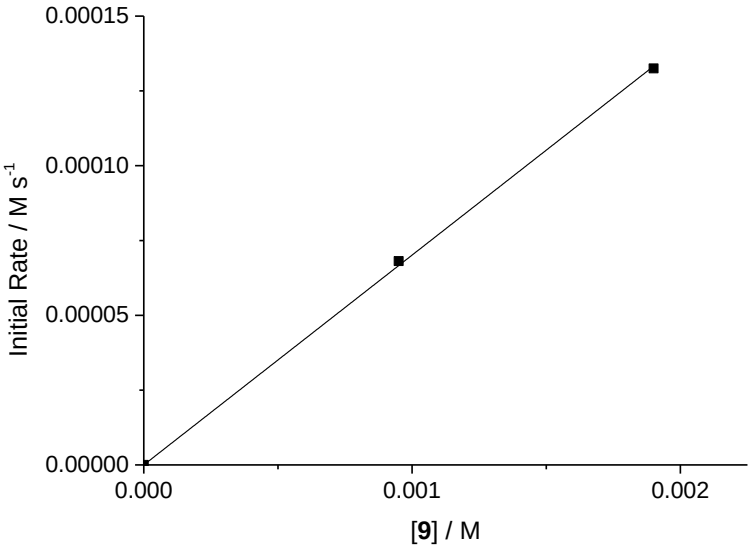



**Figure 3.7** Plot of initial rate *vs* [**9**]. $[H_3B{\cdot}NMe_3]_0$ = 0.19 M, $[TBE]_0$ = 0.38 M. $R^2$ = 0.99981.

On altering $[H_3B{\cdot}NMe_3]_0$ (Entries 2, 5 and 6, Table 3.1) while maintaining constant concentrations of TBE (0.19 M) and **9** ($9.5 \times 10^{-4}$ M), the initial rate doubled on doubling $[H_3B{\cdot}NMe_3]_0$ from 0.19 M to 0.38 M, implying a first order dependence on $[H_3B{\cdot}NMe_3]$. However, when $[H_3B{\cdot}NMe_3]_0$ = 0.76 M (*i.e.* a four-fold excess of $H_3B{\cdot}NMe_3$ relative to TBE) the initial rate was suppressed compared with the expected first order relationship (Figure 3.8). Under these conditions, it is presumed that the homocoupling reaction occurs to yield **8**, which is inactive in catalysis and so lowers turnover.

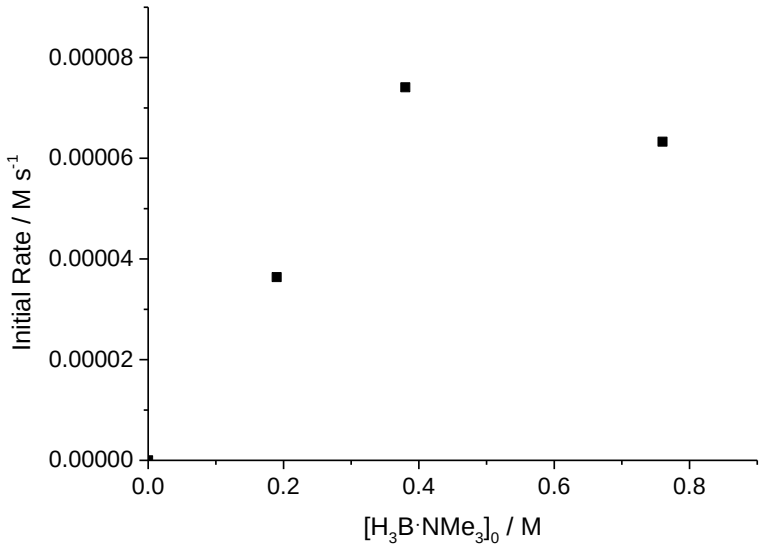



**Figure 3.8** Plot of initial rate *vs* $[H_3B{\cdot}NMe_3]_0$. $[TBE]_0$ = 0.19 M, [**9**] = 9.5 x $10^{-4}$ M.

### 3.5.2 Role of 8 in the hydroboration

To probe whether the formation of **8** may be responsible for slower catalysis with an excess of $H_3B{\cdot}NMe_3$, **9** (5 mol%) was used under conditions of a four-fold excess of $H_3B{\cdot}NMe_3$, relative to TBE ([**9**] = 0.0095 M, $[H_3B{\cdot}NMe_3]_0$ = 0.76 M, $[TBE]_0$ = 0.19 M) to enable monitoring of the metal species by NMR spectroscopy. After two minutes of reaction, the $^1$H NMR spectrum showed a mixture of **6** and **9,** and that the catalysis had reached approximately 70% consumption of TBE (measured by the disappearance of the alkene signals in the $^1$H NMR spectrum). After 10 minutes (~80% consumption of TBE), **8** was observable in the $^1$H NMR spectrum by its characteristic hydride shift at δ –8.26, confirming that **8** can be formed during hydroboration under conditions of excess $H_3B{\cdot}NMe_3$. Under these conditions, however, it appears that the formation of **8** is slow compared with the rate of hydroboration.

Upon starting catalysis with 0.5 mol% preformed **8** ($[H_3B{\cdot}NMe_3]_0$ = 0.76 M, $[TBE]_0$ = 0.19 M, Entry 10, Table 3.1), the initial rate is less than half that seen when starting

under the same conditions with **9** (Entry 6, Table 3.1). Thus, it is likely that formation of **8** is the reason for the suppressed rate on increasing [$H_3B{\cdot}NMe_3$], although it is noteworthy that hydroboration turnover still occurs (albeit more slowly) when using **8**.

### 3.5.3 Inhibition by I

In the [$Rh(P^iBu_2{}^tBu)_2$][$BAr^F{}_4$] system, it was found that the hydroboration was inhibited with excess **I**; the equilibrium between **i-77** and $H_3B{\cdot}NMe_3$ favoured the binding of **I** ($K_{298K}$ = 1.62),[34] consistent with work by Shimoi (see discussion in Chapter 2).[45] Experiments to determine the equilibrium constant for the reaction of **6** with $H_3B{\cdot}NMe_3$ could not be undertaken due to the formation of **8** under these conditions. However, starting catalysis with **9** in the presence of **I** (70 eq. relative to **9**) induced an approximately threefold suppression of the initial rate (compare Entries 1 and 7, Table 3.1). Thus, product inhibition strongly affects the rate of hydroboration in this system also. This is likely to be the reason that, with 0.5 mol% **9**, the hydroboration reaction only reaches 85% completion as, under such loadings, only a small amount of active species would be available late in the reaction.

## 3.6 Labelling studies

Undertaking catalysis with $D_3B{\cdot}NMe_3$ instead of $H_3B{\cdot}NMe_3$ (Entries 1 and 9, Table 3.1) enabled the determination of a kinetic isotope effect (KIE) of 1.34 ± 0.04 by initial rates methods. The magnitude of the KIE implies that irreversible B—H activation is not likely to be turnover-limiting as this value would be significantly higher. For example, a primary KIE of 6.7 ± 0.1 was observed in Crudden's borenium-catalysed reduction of ketimines with HBCat.[46] However, due to the multiple equilibria that

appear to be operating in this hydroboration system (*vide infra*), this value should be treated with caution.[47]

Examination of the $^{1}H$, $^{2}H$ and $^{11}B$ NMR spectra of the reaction mixture using $D_3B{\cdot}NMe_3$ as a substrate gave insight into the equilibria operating in the reaction in a similar manner to early studies using DBCat (Section 3.1.2).[20-24] After 1 hour (28% conversion to **I**), the $^{1}H$ and $^{2}H$ NMR spectra showed deuterium incorporation into **I** at the position β to the boron atom (approximately 60% D, measured by $^{1}H$ NMR spectroscopy), as expected for an anti-Markovnikov hydroboration. Deuterium was also incorporated into the internal alkene position of unreacted TBE (approximately 25% D).[48] Only minor (< 5% relative to the internal position) deuterium incorporation into the terminal alkene positions – and, consequently, the position α to the boron atom in **I** – was observed by $^{2}H$ NMR spectroscopy (Figure 3.9). The $^{11}B$ NMR spectrum of the free amine-borane showed increased B—H coupling as the reaction progressed, forming $(H/D)_3B{\cdot}NMe_3$ (Scheme 3.16).

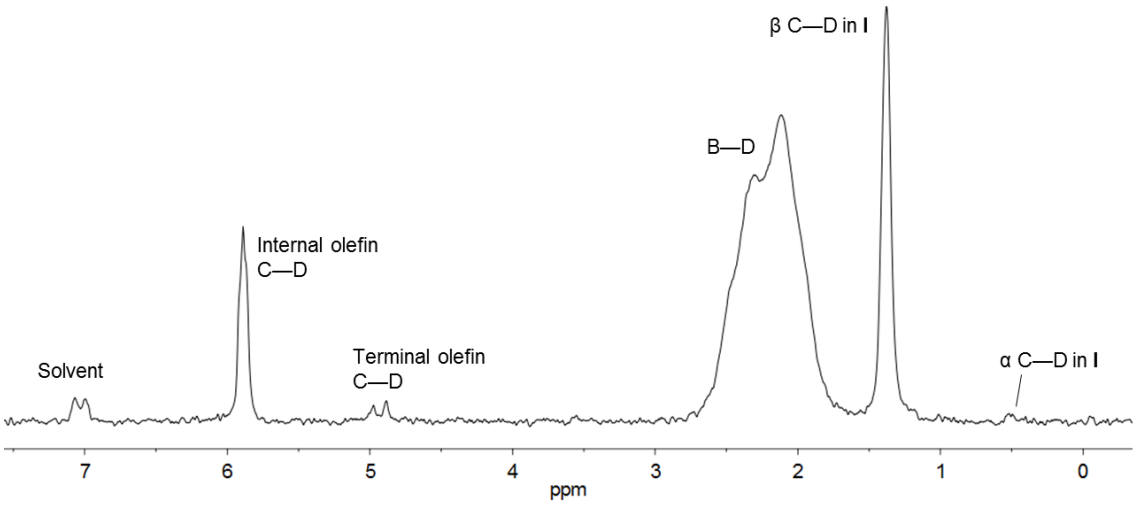
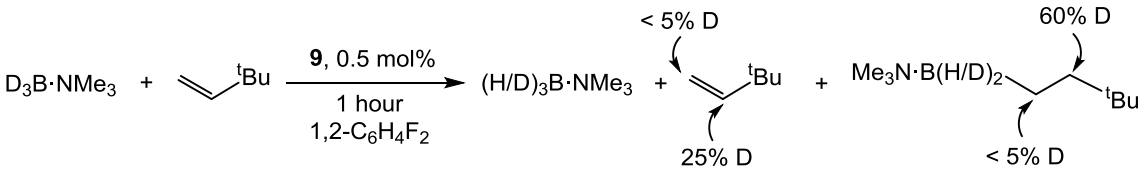



**Figure 3.9** $^{2}H$ NMR spectrum after 1 hour of the hydroboration reaction between $D_3B{\cdot}NMe_3$ (0.19 M), TBE (0.38 M) and **9** (0.5 mol%) in 1,2-$C_6H_4F_2$.

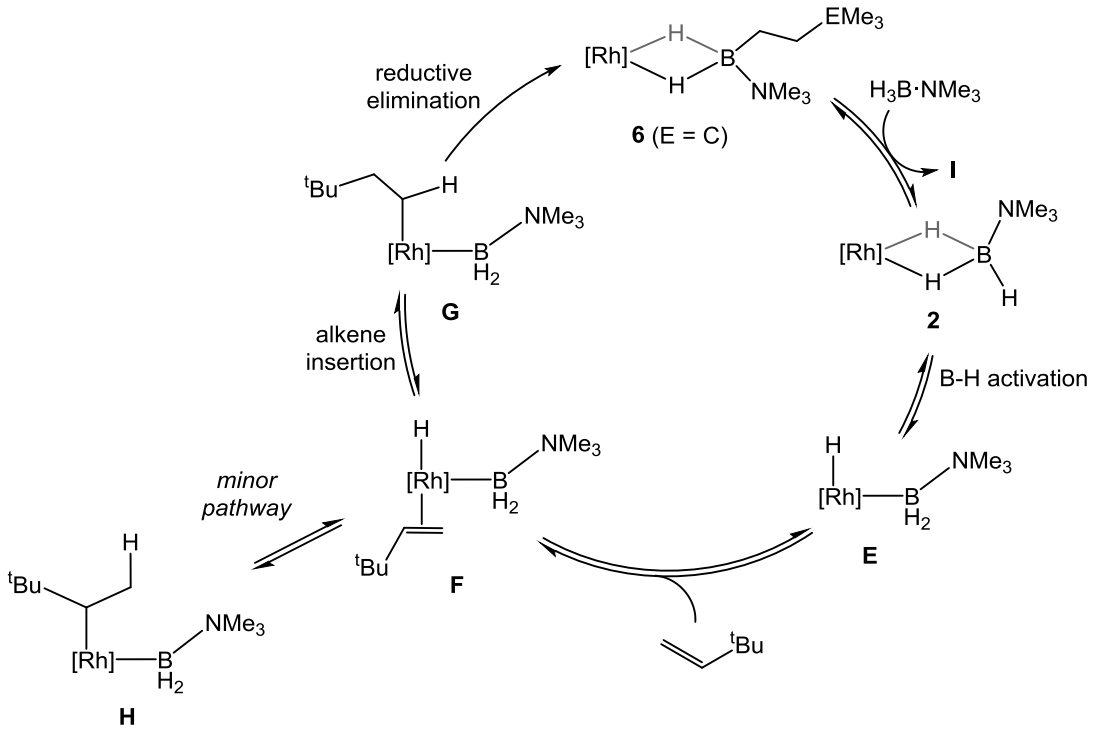



**Scheme 3.16** Products observed after 1 hour of the hydroboration reaction between $D_3B{\cdot}NMe_3$ (0.19 M), TBE (0.38 M) and **9** (0.5 mol%) in 1,2-$C_6H_4F_2$. The % of H in the B—(H/D) groups was not measured as the B—H signals for **I** and $H_3B{\cdot}NMe_3$ overlap.

These observations show that B—H activation of the amine-borane is reversible. Furthermore, alkene coordination to the metal and hydride insertion of the alkene are reversible. Small amounts of deuterium incorporation into the terminal alkene positions indicate that reversible hydride insertion to form the branched isomer is a minor pathway. No Markovnikov analogue of **I** was observed, suggesting that this branched isomer does not undergo reductive elimination.

## 3.7 Proposed mechanism

The kinetic data, labelling experiments and PSI ESI-MS investigations lead to the mechanism proposed in Scheme 3.17. From **6** (or **9**), $H_3B{\cdot}NMe_3$ displaces **I** to form **2**. B—H activation occurs to yield the $Rh^{III}$ boryl species **E**, which has a vacant site. TBE coordinates to the vacant site to form **F**, from which reversible alkene insertion/hydride migration occurs to yield the linear product **G**. Irreversible reductive elimination of **I** from **G** is turnover-limiting. On the basis of the deuterium labelling experiments, a minor pathway for reversible alkene insertion/hydride migration to form the branched product **H** is also proposed.




**Scheme 3.17** Proposed hydroboration pathway. [Rh] = {Rh(Xantphos)}$^+$. On starting with **9**, E = Si. E = C for subsequent turnovers (**6**) as shown.

## 3.8 Hydroboration with other alkenes

To explore the scope of the hydroboration, the propensity for hydroboration of other alkenes was tested.

### 3.8.1 Cyclohexene

As discussed in Chapter 2, addition of cyclohexene to a mixture of **6** and excess $H_3B{\cdot}NMe_3$ promotes complete formation of **8** by reducing **3** to **2**, which can homocouple further. Consistent with this, no hydroboration of cyclohexene was observed under the conditions of 5 mol% **9** ($[H_3B{\cdot}NMe_3]_0$ = 0.19 M, $[\text{cyclohexene}]_0$ = 0.38 M, 1,2-$C_6H_4F_2$), and **8** was formed as the sole metal-containing product, by NMR spectroscopy.

In light of the proposed hydroboration mechanism, however, the ability of cyclohexene to coordinate to the metal centre, but not couple with the amine-borane, was probed using $D_3B{\cdot}NMe_3$. After 90 minutes, the $^2H$ NMR spectrum (Figure 3.10) indicated that deuterium was present in all positions of the cyclohexene indicated by the chemical shifts of δ 5.67, δ 1.95 and δ 1.55 (assigned by comparison with literature values for cyclohexene).[48] A signal corresponding to deuterated cyclohexane was also observed at δ 1.41,[48] presumably due to the reduction of a deuterated analogue of **3** by (H/D)-cyclohexene. Rh—D—B signals for deuterated **8** were also observed.

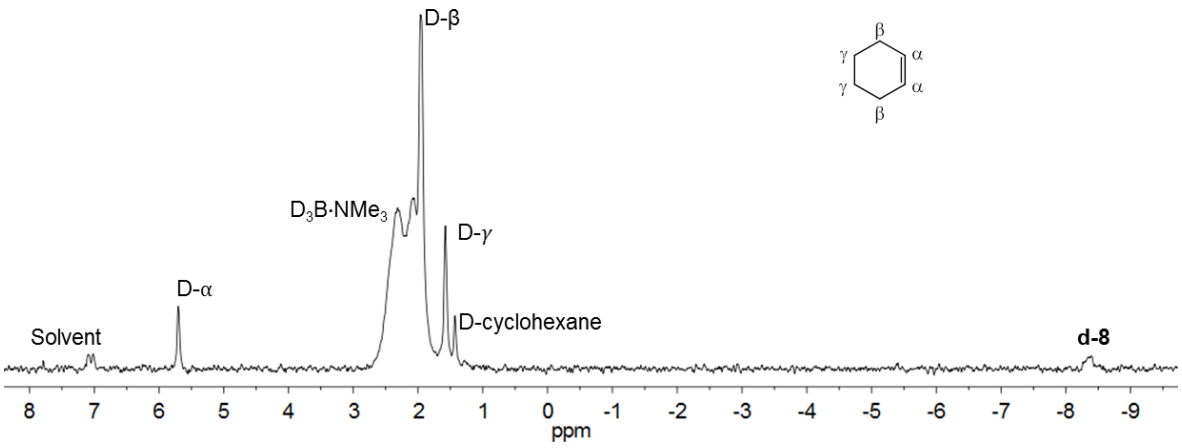
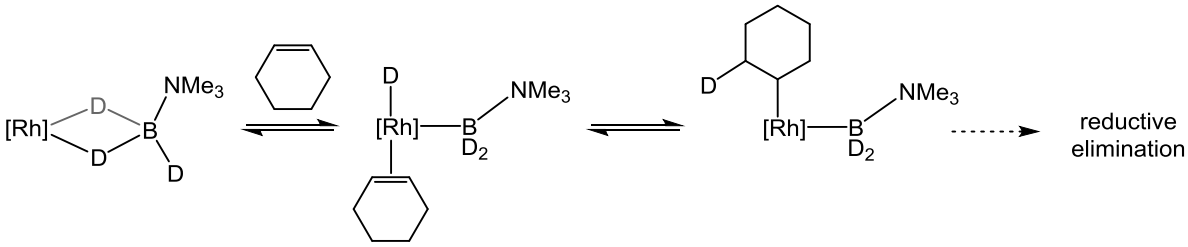



**Figure 3.10** $^2H$ NMR spectrum of the reaction between $D_3B{\cdot}NMe_3$, cyclohexene and **9** (5 mol%) after 90 minutes.

The $^{11}B$ NMR spectrum also showed evidence of B—H coupling in the signal for $D_3B{\cdot}NMe_3$, as seen in the hydroboration with TBE (Section 3.6). These results indicate that, with cyclohexene, reversible alkene coordination and hydride insertion occurs (Scheme 3.18).



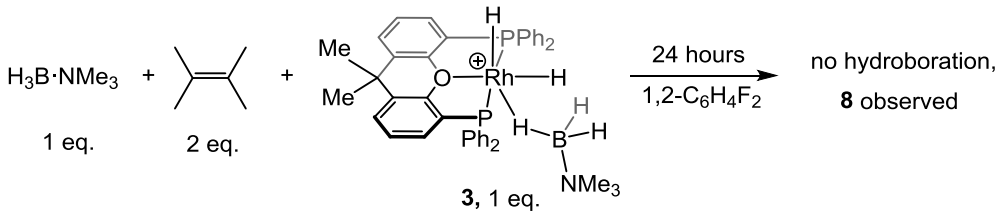

**Scheme 3.18** Proposed equilibria involved in cyclohexene H/D exchange. [Rh] = {Rh(Xantphos)}$^+$.

Although cyclohexene coordination and insertion occur, reductive elimination (the proposed turnover-limiting step with TBE, Section 3.7) to form the putative $H_2B$(cyclohexyl)·$NMe_3$ is apparently not favourable. Therefore, the slow B—B homocoupling becomes competitive, and hydroboration of cyclohexene is not observed. It is probable that the bulky cyclohexyl group requires greater reorganisation energy than the $CH_2CH_2{}^tBu$ group to align the $sp^3$ orbitals with those of $BH_2NMe_3$, and thus reductive elimination is not observed.[28,49] This high barrier to cyclohexyl reductive elimination may also reflect the lack of the branched hydroboration product observed in the reactions with TBE.

### 3.8.2 2,3-dimethyl-2-butene

The bulky alkene 2,3-dimethyl-2-butene showed no evidence of hydroboration on reaction with **3** and $H_3B{\cdot}NMe_3$ (Scheme 3.19). **3** remained the major organometallic species in solution after 1 hour, and, over 24 hours, slow B—B coupling occurred to yield a 2:1 mixture of **3** and **8.** No evidence for hydroboration was observed. Moreover, the reduction of **3** to form **8** was significantly slower with 2,3-dimethyl-2-butene than with cyclohexene. It is likely that the methyl groups hinder coordination to the metal. Similar steric effects have been noted previously. For example, catalytic hydrogenations of cyclohexene and 2,3-dimethyl-2-butene have been attempted with

both Wilkinson's catalyst and the cationic $[Rh(cod)(PPh_3)_2][BF_4]$ and, while catalytic hydrogenation of cyclohexene was observed with both catalysts (TOF = 70 $h^{-1}$ and 10 $h^{-1}$, respectively), no turnover with 2,3-dimethyl-2-butene was observed.[50-52] Interestingly, Crabtree's complex $[Ir(cod)(PCy_3)(py)][PF_6]$ was very active in the catalytic hydrogenation of both cyclohexene (TOF = 4500 $h^{-1}$) and 2,3-dimethyl-2-butene (TOF = 4000 $h^{-1}$).[52]

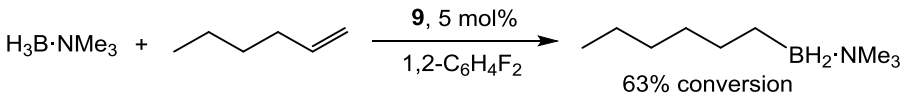



**Scheme 3.19** Reaction of $H_3B{\cdot}NMe_3$ (1 eq.), **3** (1 eq.) and 2,3-dimethyl-2-butene (2 eq.). $[BAr^F{}_4]^-$ anion not shown.

### 3.8.3 1-hexene

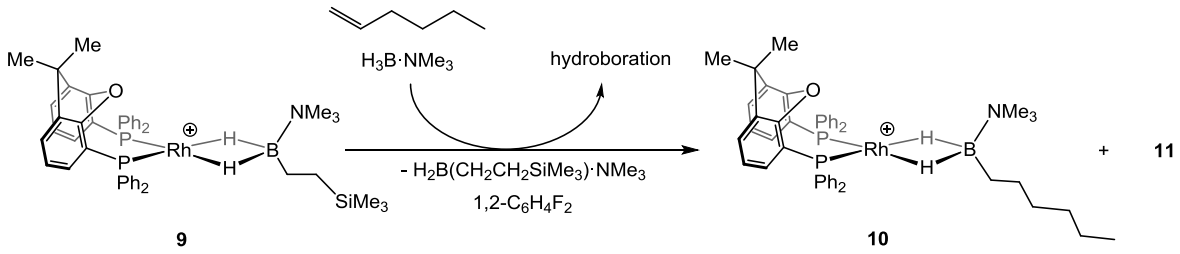
#### *3.8.3.1 Hydroboration catalysis*

The less bulky alkene 1-hexene was also screened in the hydroboration reaction. Reaction of $H_3B{\cdot}NMe_3$ (0.19 M), 1-hexene (0.38 M) and **9** (0.0095 M, *i.e.* 5 mol%), resulted in a new product being observed in the $^{11}B$ NMR spectrum at δ –1.4 (t, $^1J_{HB}$ = 91 Hz), consistent with $H_2B(hexyl){\cdot}NMe_3$ by comparison with **I** (Scheme 3.20). The product could not be isolated cleanly from the mixture and thus whether the product was linear or branched was not deduced. The reaction was sluggish compared with that of TBE, reaching a maximum conversion of 63% after 1 week. The control reaction between 1-hexene and $H_3B{\cdot}NMe_3$ in 1,2-$C_6H_4F_2$ in the absence of catalyst showed no evidence for hydroboration after 1 week.




**Scheme 3.20** Hydroboration reaction between 1-hexene and $H_3B{\cdot}NMe_3$ catalysed by **9** (5 mol%). Product depicted as the linear isomer, although linear:branched ratio unknown.

During this reaction, two new organometallic species were detected. One of these is assigned to the product [Rh($\kappa^2_{P,P}$-Xantphos)($\eta^2$-$H_2B$(hexyl)·$NMe_3$)][$BAr^F_4$] (**10**), alongside an unidentified species, **11** (Scheme 3.21). After 5 minutes, **10** was the major organometallic product (> 90%). After 30 minutes (38% conversion to $H_2B$(hexyl)·$NMe_3$), the ratio of **11**:**10** was 30:70. After several days, this ratio reached 65:35.




**Scheme 3.21** Formation of **10** and **11**. $[BAr^F_4]^-$ anions not shown.

### *3.8.3.2 Characterisation of **10***

NMR spectroscopic data for **10** are similar to those for **6** and **9**. The borane unit is sigma bound $\eta^2$ to the $Rh^I$ centre, evident by a broad resonance at δ –6.58 in the $^1H$ NMR spectrum that collapses to a virtual triplet upon $^{11}B$ decoupling ($^1J_{RhH}$ = 34 Hz, $^2J_{P\mathit{trans}H}$ = 34 Hz). The Xantphos methyl groups were observed as a singlet, relative integral 6H, at δ 1.72, suggesting that the Xantphos ligand inverts rapidly compared with the NMR timescale, rendering the methyl groups equivalent (*cf.* **8**, Chapter 2).[53] Due to overlapping peaks in the alkyl region, the regioselectivity of the hexyl chain could not be determined by $^1H$ NMR spectroscopy. The $^{11}B$ NMR spectrum shows a

broad resonance at δ 35.7. The $^{31}P\{^{1}H\}$ NMR spectrum shows a single $^{31}P$ environment at δ 26.9 ($^{1}J_{RhP}$ = 182 Hz), which is consistent with the formation of the anti-Markovnikov isomer; if the Markovnikov were formed, the phosphorus atoms would be inequivalent. ESI-MS is consistent with the formation of **10** (*m/z* = 838.31, calc. 838.30, expected isotopic pattern).

Recrystallisation of the reaction mixture formed dark green crystals (44% yield) of **10** from which a solid state structure could be determined (Figure 3.11). The structure exhibited considerable disorder in the borane fragment, $NMe_3$ group and $CF_3$ groups of the $[BAr^F_4]^-$ anion. The hydrides H11 and H12 were thus not located on the Fourier map and were placed in calculated positions. Nevertheless, the structure obtained confirms that the linear product of hydroboration is bound to the metal centre. No evidence for the branched product was apparent on the Fourier map. The Rh1—B1 distance of 2.183(10) Å is the same within error of those observed for **6** and **9**, implying $\eta^2$ coordination of the borane. The Xantphos ligand is bound in a $\kappa^2_{P,P}$ geometry, and, as with **6**, the alkyl chain of the borane is bound *syn* to the Xantphos backbone. The NMR spectra of the isolated crystals matched the NMR spectra of **10** observed *in situ*, corroborating the anti-Markovnikov regioselectivity.

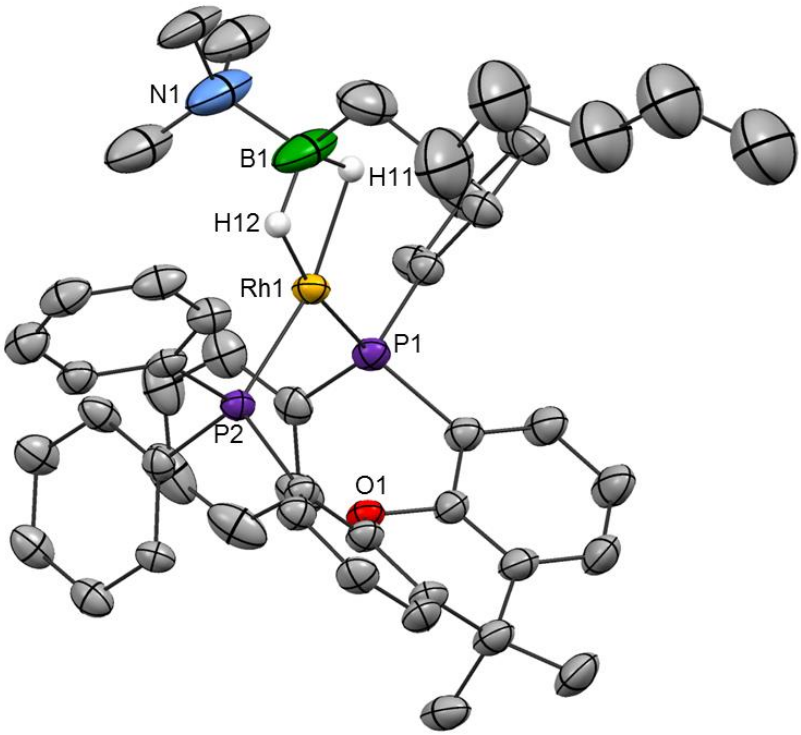



**Figure 3.11** Solid-state structure of the cationic portion of **10**. Displacement ellipsoids are drawn at the 30% probability level. $[BAr^{F}_{4}]^{-}$, residual disordered 1,2-$C_6H_4F_2$ solvent and all carbon-bound H atoms are omitted for clarity. H11 and H12 atoms placed in calculated positions. Only the major components of the disordered $NMe_3$ group and hexyl chain are shown. Selected bond lengths (Å) and angles (°): Rh1–P1, 2.284(2); Rh1–P2, 2.2572(18); Rh1–O1, 3.5059(53); Rh1–B1, 2.183(10); B1–N1, 1.621(4); P1–Rh1–P2, 101.04(7).

### *3.8.3.3 Tentative structure of **11***

The $^{31}P\{^{1}H\}$ NMR spectrum of the unidentified species **11** indicates a $Rh^{I}$ complex with two inequivalent mutually *cis* $^{31}P$ environments around a $Rh^{I}$ centre (δ 28.7, dd, $^{1}J_{RhP}$ = 184 Hz, $^{2}J_{PP}$ = 36 Hz; δ 13.2, dd, $^{1}J_{RhP}$ = 166 Hz, $^{2}J_{PP}$ = 36 Hz). In the $^{1}H$ NMR spectrum, a hydride signal is observed at δ –8.71 (br d, $^{2}J_{PH}$ = 63 Hz), which sharpens on decoupling to $^{11}B$ and collapses to a singlet on decoupling to $^{31}P$, suggesting a hydride *trans* to phosphorus.[54] Moreover, two broad multiplets at δ 4.63 and δ 4.23 are observed. The relative intensities of these three signals are 1:1:1. Unfortunately, **11** could not be formed independently of **10** and so further analysis is hindered by overlapping signals with **10**. Similarly, no clear signal for **11** in the $^{11}B$ NMR spectrum

was obtained; possibly it is broad, or overlapping with the signal for **10** at ~δ 36. ESI-MS indicated a monocation two mass units lower than **10** (*m/z* = 836.28, calc. 836.28), and the isotopic pattern showed that **11**$^+$ contains one boron atom. Despite repeated attempts, no crystalline material could be obtained for **11** and so the structure remains ambiguous. However, on the basis of the data available, a possible structure is shown in Figure 3.12.

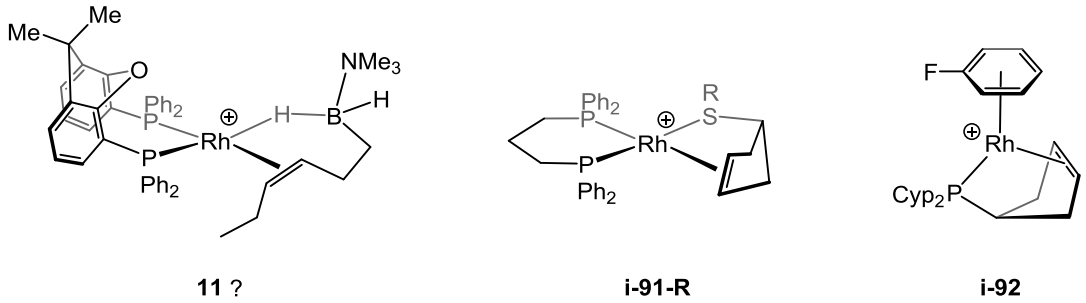



**Figure 3.12** Possible structure for **11**, and related complexes **i-91-R** and **i-92**. $[BAr^F_4]^-$ anions not shown. R = Ph, Cyp.

In this structure, the hexyl chain has undergone dehydrogenation and an internal alkene unit is bound to Rh, accounting for the resonances at δ 4.63 and δ 4.23 in the $^1$H NMR spectrum. The borane is bound η$^1$ through a B—H bond, *trans* to a phosphorus atom, and the chemical shift of δ –8.71 is similar to that of **8** (δ –8.47). The non-fluxional B—H hydride is 'locked' in place by the binding of the alkene group. The phosphorus atoms are *cis* disposed to each other in chemically inequivalent positions. The related complexes **i-91-R** (R = Ph, Cyp), in which a cyclic thioether has undergone dehydrogenation, show similar NMR data to **11.** For example, the $^{31}$P{$^1$H} NMR spectrum of **i-91-Cyp** also presents a doublet of doublets ($^1J_{RhP}$ = 150 Hz, $^2J_{PP}$ = 55 Hz and $^1J_{RhP}$ 152 Hz, $^2J_{PP}$ = 55 Hz) and, in the $^1$H NMR spectrum (200 K), the chemical shifts of the alkene resonances are at δ 4.69 and δ 4.34.[55] The fate of the lost hydrogen atoms from dehydrogenation of the hexyl chain was not explored. $H_2$ was

not observed in the $^{1}H$ NMR spectrum in the mixtures of **10** and **11** formed in *situ*. The excess of 1-hexene may facilitate the dehydrogenation, forming hexane.[56] The related intramolecular dehydrogenation of coordinated phosphines (*e.g.* **i-92**,[57] Figure 3.12),[55,58-60] ethers,[61] alkoxide ligands,[62] cyclopentadienyls[63] and NHCs[64] has also been reported.

#### *3.8.3.4 Comparison with the hydroboration of TBE*

The {Rh(Xantphos)}$^{+}$-catalysed hydroboration of 1-hexene by $H_3B{\cdot}NMe_3$ is slower than the analogous reaction with TBE (complete within 3 hours). Mechanistic studies were not conducted upon the 1-hexene system as the side formation of **11** would complicate kinetic analyses. However, if the turnover-limiting step is reductive elimination – as with TBE – hydroboration with the hexyl group is likely to be slower than that of the bulkier $CH_2CH_2{}^{t}Bu$ group owing to the lesser relief of steric strain around the metal centre upon reductive elimination.[28,65-67] The formation of **11** may also play a role in inhibiting turnover – presumably, the chelating ligand prevents $H_3B{\cdot}NMe_3$ from binding. As **10** and **6** exhibit very similar NMR spectra and Rh—B bond distances, $H_2B(hexyl){\cdot}NMe_3$ and **I** would be expected to have similar binding strengths, and so it is unlikely that stronger inhibition by $H_2B(hexyl){\cdot}NMe_3$ causes the striking difference in turnover.

## 3.9 Hydroboration of TBE with phosphine-boranes

### 3.9.1 Introduction

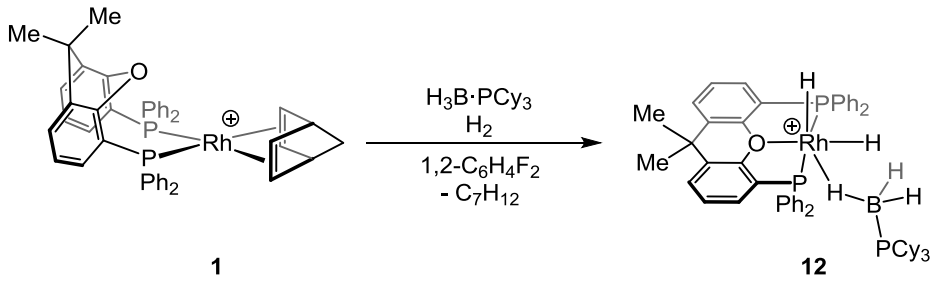
There are few examples of the hydroboration of alkenes using phosphine-boranes, and these use phosphine-boranes as a source of $BH_3$.[68-70] The dehydrocoupling chemistry of phosphine-boranes is also less developed than that of amine-boranes, but P—B based products resulting from the dehydrocoupling of phosphine-boranes

have potential applications as electron beam resists and precursors to boron phosphide.[71] Manners reported the first example of the dehydrocoupling of phosphine-boranes to form polymeric $[H_2BPPhH]_n$ ($M_w$ = 31 000 g $mol^{-1}$) using $[Rh(1,5\text{-cod})(\mu\text{-Cl})]_2$ as the catalyst.[72] More recent investigations by the Weller group have shed light upon the mechanistic details for the dehydrocoupling of phosphine-boranes and isolated $Rh^{I}$ and $Rh^{III}$ sigma complexes pertinent to the catalytic cycles.[54,73,74] To study the hydroboration of phosphine-boranes in this system, sigma complexes of the tertiary phosphine-borane $H_3B{\cdot}PCy_3$ with $\{Rh(Xantphos)\}^+$ were targeted first, followed by an investigation into the $\{Rh(Xantphos)\}^+$ mediated hydroboration of TBE by $H_3B{\cdot}PCy_3$. This work was carried out jointly with visiting student Laura Ortega (Instituto de Investigaciones Químicas (IIQ), Universidad de Sevilla).

### 3.9.2 Formation of $[Rh(\kappa^3_{P,O,P}\text{-Xantphos})(H)_2(\eta^1\text{-}H_3B{\cdot}PCy_3)][BAr^F_4]$

Addition of $H_2$ (4 atm) to **1** in the presence of one equivalent of $H_3B{\cdot}PCy_3$ in 1,2-$C_6H_4F_2$ formed $[Rh(\kappa^3_{P,O,P}\text{-Xantphos})(H)_2(\eta^1\text{-}H_3B{\cdot}PCy_3)][BAr^F_4]$ (**12**, Scheme 3.22) as a pale yellow solution. The conversion was quantitative by *in situ* NMR spectroscopy. **12** displays very similar NMR data to **3** and the related phosphine-borane complex $[Ru(Xantphos)(H)(PPh_2H)(\eta^1\text{-}H_3B{\cdot}PPh_2H)][BAr^F_4]$.[75] The *in situ* $^1H$ NMR spectrum shows three hydride environments, consistent with a fluxional $BH_3$ group (δ –1.42, br, relative integral 3H) and two mutually *cis* hydride environments, each relative integral 1H (δ –14.62, br dtd and δ –19.13, br dtd). The $^{31}P\{^1H\}$ NMR spectrum shows signals at δ 41.8 (d, $^1J_{RhP}$ = 114 Hz) and δ 20.1 (br, $PCy_3$). The $^{11}B$ NMR spectrum shows a broad signal at δ –43.5 corresponding to the bound borane unit. The chemical shift values for the bound $H_3B{\cdot}PCy_3$ are not significantly shifted from the

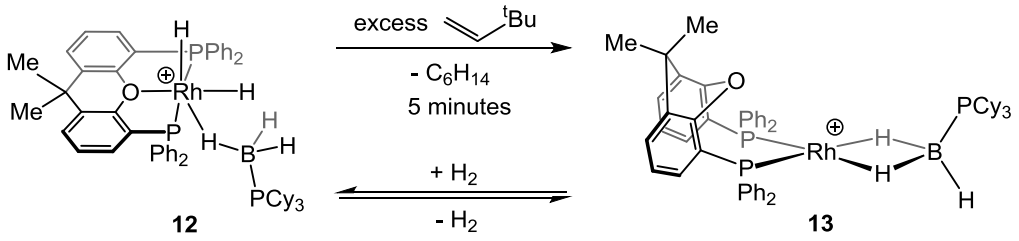
free values (δ(*11B*) –43.2, δ(*31P*) 28.4, 1,2-$C_6H_4F_2$), consistent with $\eta^1$ binding to the $Rh^{III}$ centre. Attempts to isolate **12** were unsuccessful, resulting in decomposition, but clean NMR spectra of **12** could be produced by hydrogenating pre-formed **13** (see Section 3.9.3) in $CD_2Cl_2$.




**Scheme 3.22** Formation of **12**. $[BAr^F_4]^-$ anions not shown.

### 3.9.3 Formation of [Rh(κ²P,P-Xantphos)(η²-H₃B·PCy₃)][BArF₄]

Addition of two equivalents of TBE to **12** resulted the clean formation of the complex [Rh(κ²P,P-Xantphos)(η²-$H_3B{\cdot}PCy_3$)][$BAr^F_4$] (**13**, Scheme 3.23) within five minutes. Removal of the volatiles enabled the isolation of **13** as a dark green solid. Although crystals suitable for X-ray diffraction could not be grown, despite repeated attempts, the NMR spectroscopic data are consistent with $\eta^2$ binding of $H_3B{\cdot}PCy_3$. In the $^1H$ NMR spectrum, a broad signal is observed at δ –2.38 (relative integral 3H, sharpens on $^{11}B$ decoupling) and the $^{11}B$ NMR spectrum shows a signal at δ –3.0, shifted 40.2 ppm downfield from free $H_3B{\cdot}PCy_3$. This is a similar chemical shift change to that seen with related $Rh^I$ $\eta^2$-bound amine-borane[38] and phosphine-borane[54,74] complexes. The $^{31}P\{^1H\}$ NMR spectrum shows two environments at δ 28.9 (d, $^1J_{RhP}$ = 190 Hz) and δ 17.3 (br, $PCy_3$), consistent with the phosphine-borane bound to a $Rh^I$ centre.[54]



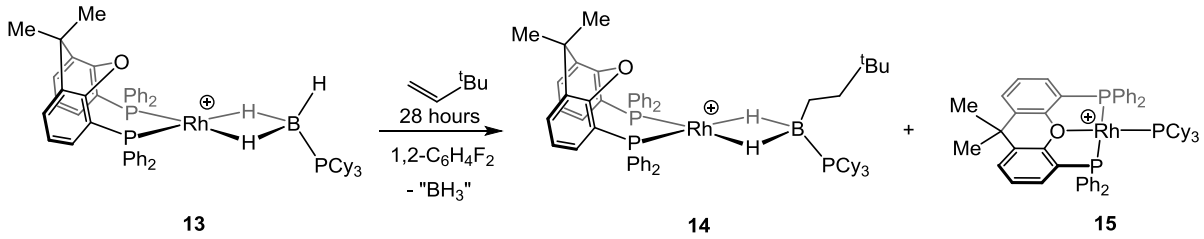

**Scheme 3.23** Formation of **13**. $[BAr^F_4]^-$ anions not shown.

Placing **13** under $H_2$ (4 atm) in $CD_2Cl_2$ resulted in complete conversion to **12**. Degassing the solution and leaving under a static vacuum for 4 hours resulted in an approximately 1:1 ratio of **12**:**13**, suggesting an equilibrium between the two species (Scheme 3.23).

### 3.9.4 Hydroboration of TBE by 13

Prolonging the exposure of **13** to excess TBE during its synthesis – or adding one equivalent of TBE to isolated **13** (Scheme 3.24) – resulted in the formation of a new species, $[Rh(\kappa^2_{P,P}\text{-Xantphos})(\eta^2\text{-}H_2B(CH_2CH_2{}^tBu)\cdot PCy_3)][BAr^F_4]$ (**14**), the metal-bound product of the hydroboration of TBE by $H_3B\cdot PCy_3$. **14** was first observed after approximately 45 minutes by a broad hydride signal at δ –5.58 in the $^1H$ NMR spectrum, which sharpens to a doublet of doublets (virtual triplet) on $^{11}B$ decoupling ($^1J_{RhH}$ = 33 Hz, $^2J_{P\mathit{trans}H}$ = 33 Hz), consistent with an $\eta^2$-$H_2BR\cdot L$ sigma interaction. The $^{11}B$ NMR spectrum shows a broad signal at δ 18.5. The $^{31}P\{^1H\}$ NMR spectrum is consistent with a $Rh^I$ species with signals at δ 29.5 (d, $^1J_{RhP}$ = 190 Hz) and δ 8.8 (br, $PCy_3$). The hydroboration reaction progressed slowly; after 16 hours, an approximately 5:1 ratio of **14**:**13** was established. However, around 5% of $[Rh(\kappa^3_{P,O,P}\text{-Xantphos})(PCy_3)][BAr^F_4]$ (**15**), a product of P—B cleavage of the phosphine-borane, was also detected in the reaction mixture by $^{31}P\{^1H\}$ NMR spectroscopy (δ 61.3, dt, $^1J_{RhP}$ = 192 Hz, $^2J_{PP}$ = 34 Hz; δ 37.8, dd, $^1J_{RhP}$ = 155 Hz, $^2J_{PP}$ = 34 Hz). P—B bond

cleavage has been previously observed in the metal-catalysed dehydrocoupling of phosphine-boranes.[73-75] After a further 12 hours, all of **13** was consumed, yielding a 2:1 mixture of **14**:**15**. The fate of the free borane that would result from P—B cleavage was not investigated.




**Scheme 3.24** Formation of **14** and **15** (2:1 ratio after 28 hours). $[BAr^F_4]^-$ anions not shown.

After several hours of reaction, crystallisation of the mixture from 1,2-$C_6H_4F_2$/pentane at −30 °C resulted in green crystals of **14** suitable for X-ray diffraction. The crystals diffracted weakly and so the data quality was poor, giving a high R-factor, but a ball and stick model could be refined to show the gross connectivity of **14** (Figure 3.13). The structure indicates that the anti-Markovnikov product of hydroboration is formed, and the Xantphos ligand adopts $\kappa^2_{P,P}$ geometry, as with **6**, **9** and **10**. The NMR spectra of these crystals indicated that some of **13** had co-crystallised and cyclohexyl peaks dominated the alkyl region of the $^1$H NMR spectrum, so more detailed NMR data for **14** was not obtained.

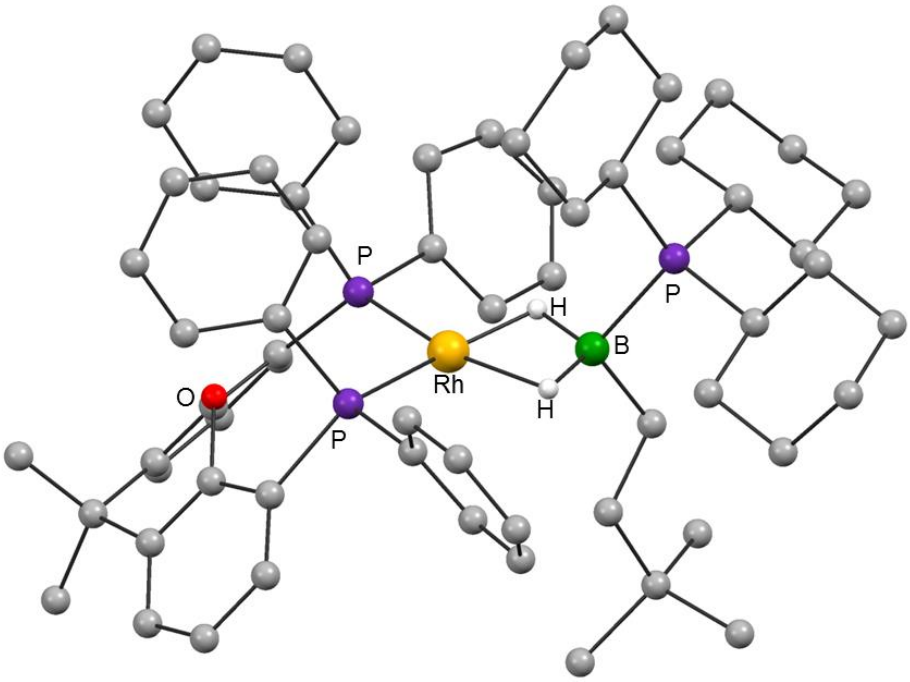



**Figure 3.13** Ball and stick representation of a partially refined structure of **14**. Hydrogen atoms placed in calculated positions. The $[BAr^{F}_{4}]^{-}$ anion and all carbon-bound H atoms omitted for clarity. The X-ray data is of poor quality so the structure is presented for connectivity purposes only. Selected crystallographic data: Triclinic, *P*-1, $a$ = 18.0544(7) Å, $b$ = 23.5573(10) Å, $c$ = 28.2957(12) Å, $\alpha$ = 100.4469(17)˚, $\beta$ = 90.0292(19)˚, $\gamma$ = 112.4783(19)˚, $V$ = 10903.5(8) Å$^3$.

Repeating the crystallisation attempt resulted in the formation of several orange crystals of **15**. The solid state structure (Figure 3.14) indicates a Rh$^{I}$ *pseudo*-square planar complex (sum of angles around Rh = 361.5°). The Xantphos bite angle of 159.70(3)° and Rh1—O1 distance of 2.2395(19) Å indicate *mer* $\kappa^3_{P,O,P}$ coordination of Xantphos, similar to the closely related complexes $[Rh(\kappa^3_{P,O,P}\text{-Xantphos})(CO)][BF_4]$[76] and $[Rh(\kappa^3_{P,O,P}\text{-Xantphos})(PCyp_3)][BAr^{F}_{4}]$[77] (Cyp = cyclopentyl) with bite angles of 164.42(4)° and 158.40(7)°, respectively. Presumably the wider bite angle of the CO complex reflects the lesser steric bulk of CO *vs* $PCy_3$ or $PCyp_3$.

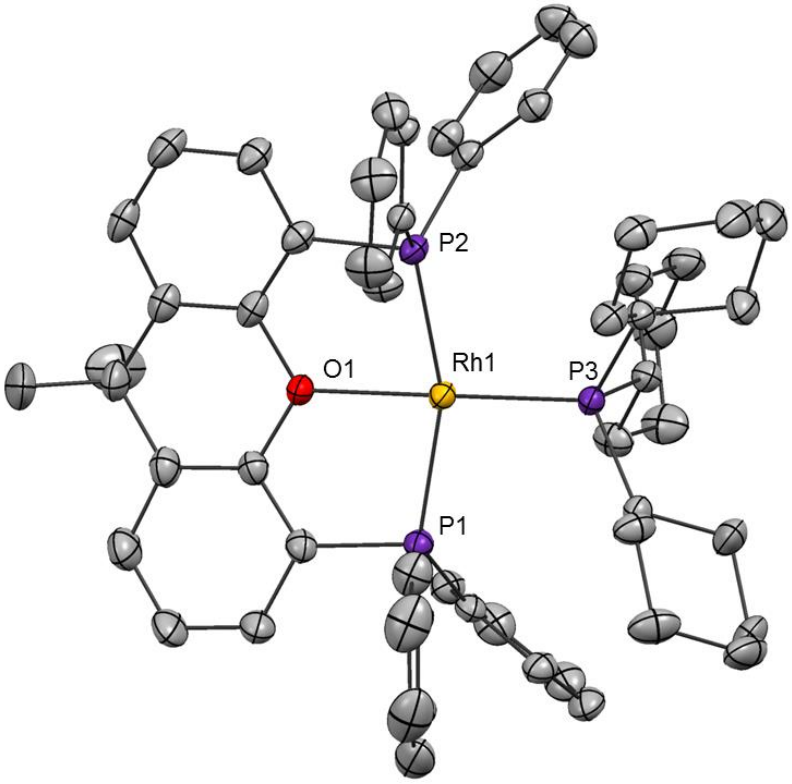
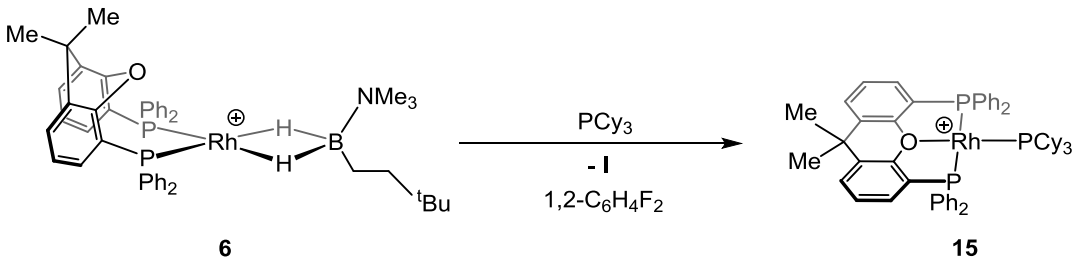



**Figure 3.14** Solid state structure of the cationic portion of **15**. $[BAr^{F}_{4}]^{-}$ anion and H atoms are omitted for clarity. Displacement ellipsoids are drawn at the 50% probability level. Selected bond lengths (Å) and angles (°): Rh1–P1, 2.2854(7); Rh1–P2, 2.2923(7); P3–Rh1, 2.2611(7); Rh1–O1, 2.2395(19); P2–Rh1–P1,159.70(3); P3–Rh1–O1, 170.44(6).

**15** could be independently synthesised cleanly by addition of one equivalent of $PCy_3$ to **6**, liberating **I** (Scheme 3.25). These spectroscopic data match those observed *in situ* in the hydroboration of **13** by TBE.




6 15

**Scheme 3.25** Independent synthesis of **15**. $[BAr^{F}_{4}]^{-}$ anions not shown.

Therefore, although $H_3B{\cdot}PCy_3$ can hydroborate TBE on the $\{Rh(Xantphos)\}^+$ fragment, the reaction is much slower than for $H_3B{\cdot}NMe_3$ and, on this timescale, P—B bond cleavage is competitive.

### 3.9.5 Attempted hydroboration using $H_3B{\cdot}PEt_3$

The less sterically hindered tertiary phosphine-borane $H_3B{\cdot}PEt_3$ was also screened for hydroboration to investigate whether the bulky $PCy_3$ group was responsible for the slow hydroboration. The complex $[Rh(\kappa^3_{P,O,P}\text{-Xantphos})(H)_2(\eta^1\text{-}H_3B{\cdot}PEt_3)][BAr^F{}_4]$ (**16**) was formed by hydrogenation of **1** in the presence of $H_3B{\cdot}PEt_3$ and showed very similar NMR data to **12** (see Chapter 7). However, **16** underwent P—B cleavage within minutes of addition of TBE to form $[Rh(\kappa^3_{P,O,P}\text{-Xantphos})(PEt_3)][BAr^F{}_4]$ (**17**) in > 90% yield *in situ*, as characterised by $^{31}P\{^1H\}$ NMR spectroscopy (δ 38.9, dt, $^1J_{RhP}$ = 189 Hz, $^2J_{PP}$ = 37 Hz; δ 35.4, dd, $^1J_{RhP}$ = 146 Hz, $^2J_{PP}$ = 37 Hz) by analogy with **15**. No evidence of hydroboration was observed.

## 3.10 Conclusions

This chapter presented a detailed study upon the catalytic hydroboration of TBE by $H_3B{\cdot}NMe_3$, catalysed by **9**, to produce the anti-Markovnikov product **I** selectively. This proved much faster than the related system with $[Rh(P^iBu_2{}^tBu)_2][BAr^F{}_4]$, reaching greater completion at lower catalyst loadings, but also suffered from product inhibition and deactivation with excess $H_3B{\cdot}NMe_3$. Nonetheless, a mechanism was proposed for the hydroboration on the basis of kinetics and observations by ESI-MS in which reductive elimination of **I** is the turnover-limiting step. The scope of the hydroboration was explored with an extension to other alkenes and phosphine-boranes. Hydroboration of cyclohexene was not observed, although deuteration

experiments indicated reversible coordination and insertion, suggesting that the reductive elimination step is not favourable in this system. While 1-hexene underwent hydroboration, conversion was lower than with TBE. The phosphine-boranes screened underwent P—B bond cleavage competitively with hydroboration.

## 3.11 References


(1) McMurry, J. *Organic Chemistry*; Brooks/Cole Publishing Company, 1996.
(2) Miyaura, N.; Suzuki, A. *Chem. Rev.* **1995**, *95*, 2457.
(3) Brown, H.; Rao, B. C. *J. Org. Chem.* **1957**, *22*, 1137.
(4) Hutchins, R. O.; Cistone, F. *Org. Prep. Proced. Int.* **1981**, *13*, 225.
(5) Kollonitsch, J. *J. Am. Chem. Soc.* **1961**, *83*, 1515.
(6) Adams, R. M.; Braun, L. M.; Braun, R. A.; Crissman, H. R.; Opprman, M. *J. Org. Chem.* **1971**, *36*, 2388.
(7) Staubitz, A.; Robertson, A. P. M.; Sloan, M. E.; Manners, I. *Chem. Rev.* **2010**, *110*, 4023.
(8) Hawthorne, M. F. *J. Am. Chem. Soc.* **1961**, *83*, 2541.
(9) Carboni, B.; Monnier, L. *Tetrahedron* **1999**, *55*, 1197.
(10) Brown, H. C.; Kanth, J. V. B.; Dalvi, P. V.; Zaidlewicz, M. *J. Org. Chem.* **2000**, *65*, 4655.
(11) Rotermund, G. W.; Köster, R. *Liebigs Ann.* **1965**, *686*, 153.
(12) Scheideman, M.; Shapland, P.; Vedejs, E. *J. Am. Chem. Soc.* **2003**, *125*, 10502.
(13) Scheideman, M.; Wang, G.; Vedejs, E. *J. Am. Chem. Soc.* **2008**, *130*, 8669.
(14) Sheeller, B.; Ingold, K. U. *J. Chem. Soc., Perkin Trans. 2* **2001**, 480.
(15) Carey, F. A.; Sundberg, R. J. *Advanced Organic Chemistry Part B: Reactions and Synthesis*; Springer, 2007.
(16) Tucker, C. E.; Davidson, J.; Knochel, P. *J. Org. Chem.* **1992**, *57*, 3482.
(17) Crudden, Cathleen M.; Edwards, D. *Eur. J. Org. Chem.* **2003**, *2003*, 4695.
(18) Männig, D.; Nöth, H. *Angew. Chem. Int. Ed. Engl.* **1985**, *24*, 878.
(19) Kono, H.; Ito, K.; Nagai, Y. *Chem. Lett.* **1975**, *4*, 1095.
(20) Brown, J. M.; Lloyd-Jones, G. C. *J. Am. Chem. Soc.* **1994**, *116*, 866.
(21) Burgess, K.; Van der Donk, W. A.; Kook, A. M. *J. Org. Chem.* **1991**, *56*, 2949.
(22) Evans, D. A.; Fu, G. C. *J. Org. Chem.* **1990**, *55*, 2280.
(23) Evans, D. A.; Fu, G. C.; Anderson, B. A. *J. Am. Chem. Soc.* **1992**, *114*, 6679.
(24) Burgess, K.; Van der Donk, W. A.; Westcott, S. A.; Marder, T. B.; Baker, R. T.; Calabrese, J. C. *J. Am. Chem. Soc.* **1992**, *114*, 9350.
(25) Caballero, A.; Sabo-Etienne, S. *Organometallics* **2007**, *26*, 1191.
(26) Gunanathan, C.; Hölscher, M.; Pan, F.; Leitner, W. *J. Am. Chem. Soc.* **2012**, *134*, 14349.
(27) Haberberger, M.; Enthaler, S. *Chem. Asian J.* **2013**, *8*, 50.
(28) Hartwig, J. F. *Organotransition Metal Chemistry*; University Science Books, 2010.
(29) Crudden, C. M.; Hleba, Y. B.; Chen, A. C. *J. Am. Chem. Soc.* **2004**, *126*, 9200.
(30) He, X.; Hartwig, J. F. *J. Am. Chem. Soc.* **1996**, *118*, 1696.
(31) Lata, C. J.; Crudden, C. M. *J. Am. Chem. Soc.* **2009**, *132*, 131.
(32) Evans, D. A.; Muci, A. R.; Stuermer, R. *J. Org. Chem.* **1993**, *58*, 5307.
(33) Wang, Q.; Motika, S. E.; Akhmedov, N. G.; Petersen, J. L.; Shi, X. *Angew. Chem. Int. Ed.* **2014**, *53*, 5418.
(34) Sewell, L. J.; Chaplin, A. B.; Weller, A. S. *Dalton Trans.* **2011**, *40*, 7499.
(35) Morrill, T. C.; D'Souza, C. A.; Yang, L.; Sampognaro, A. J. *J. Org. Chem.* **2002**, *67*, 2481.
(36) Espenson, J. H. *Chemical Kinetics and Reaction Mechanisms*; McGraw-Hill, Inc., 1995.
(37) Torry-Harris, R., Part II Thesis, University of Oxford, 2013.
(38) Dallanegra, R.; Robertson, A. P. M.; Chaplin, A. B.; Manners, I.; Weller, A. S. *Chem. Commun.* **2011**, *47*, 3763.
(39) Williams, G. L.; Parks, C. M.; Smith, C. R.; Adams, H.; Haynes, A.; Meijer, A. J. H. M.; Sunley, G. J.; Gaemers, S. *Organometallics* **2011**, *30*, 6166.

(40) Lubben, A. T.; McIndoe, J. S.; Weller, A. S. *Organometallics* **2008**, *27*, 3303.
(41) Vikse, K. L.; Woods, M. P.; McIndoe, J. S. *Organometallics* **2010**, *29*, 6615.
(42) Yunker, L. P. E.; Stoddard, R. L.; McIndoe, J. S. *J. Mass Spectrom.* **2014**, *49*, 1.
(43) Göttker-Schnetmann, I.; Brookhart, M. *J. Am. Chem. Soc.* **2004**, *126*, 9330.
(44) Pawley, R. J.; Moxham, G. L.; Dallanegra, R.; Chaplin, A. B.; Brayshaw, S. K.; Weller, A. S.; Willis, M. C. *Organometallics* **2010**, *29*, 1717.
(45) Kawano, Y.; Yamaguchi, K.; Miyake, S.-y.; Kakizawa, T.; Shimoi, M. *Chem. Eur. J.* **2007**, *13*, 6920.
(46) Eisenberger, P.; Bailey, A. M.; Crudden, C. M. *J. Am. Chem. Soc.* **2012**, *134*, 17384.
(47) Jones, W. D. *Acc. Chem. Res.* **2002**, *36*, 140.
(48) *SDBSWeb : http://sdbs.db.aist.go.jp (National Institute of Advanced Industrial Science and Technology, 08/01/2015)*.
(49) Ghosh, R.; Emge, T. J.; Krogh-Jespersen, K.; Goldman, A. S. *J. Am. Chem. Soc.* **2008**, *130*, 11317.
(50) Osborn, J. A.; Jardine, F. H.; Young, J. F.; Wilkinson, G. *J. Chem. Soc. A* **1966**, 1711.
(51) Crabtree, R. *Acc. Chem. Res.* **1979**, *12*, 331.
(52) Crabtree, R. H.; Felkin, H.; Morris, G. E. *J. Organomet. Chem.* **1977**, *141*, 205.
(53) Pontiggia, A. J.; Chaplin, A. B.; Weller, A. S. *J. Organomet. Chem.* **2011**, *696*, 2870.
(54) Huertos, M. A.; Weller, A. S. *Chemical Science* **2013**, *4*, 1881.
(55) Dallanegra, R.; Pilgrim, B. S.; Chaplin, A. B.; Donohoe, T. J.; Weller, A. S. *Dalton Trans.* **2011**, *40*, 6626.
(56) Brayshaw, S. K.; Ingleson, M. J.; Green, J. C.; McIndoe, J. S.; Raithby, P. R.; Kociok-Köhn, G.; Weller, A. S. *J. Am. Chem. Soc.* **2006**, *128*, 6247.
(57) Douglas, T. M.; Brayshaw, S. K.; Dallanegra, R.; Kociok-Köhn, G.; Macgregor, S. A.; Moxham, G. L.; Weller, A. S.; Wondimagegn, T.; Vadivelu, P. *Chem. Eur. J.* **2008**, *14*, 1004.
(58) Douglas, T. M.; Notre, J. L.; Brayshaw, S. K.; Frost, C. G.; Weller, A. S. *Chem. Commun.* **2006**, 3408.
(59) Baya, M.; Buil, M. L.; Esteruelas, M. A.; Oñate, E. *Organometallics* **2004**, *23*, 1416.
(60) Deblon, S.; Liesum, L.; Harmer, J.; Schönberg, H.; Schweiger, A.; Grützmacher, H. *Chem. Eur. J.* **2002**, *8*, 601.
(61) Holtcamp, M. W.; Henling, L. M.; Day, M. W.; Labinger, J. A.; Bercaw, J. E. *Inorg. Chim. Acta* **1998**, *270*, 467.
(62) Yu, J. S.; Fanwick, P. E.; Rothwell, I. P. *J. Am. Chem. Soc.* **1990**, *112*, 8171.
(63) Ma, Y.; Bergman, R. G. *Organometallics* **1994**, *13*, 2548.
(64) Prinz, M.; Grosche, M.; Herdtweck, E.; Herrmann, W. A. *Organometallics* **2000**, *19*, 1692.
(65) Frech, C. M.; Milstein, D. *J. Am. Chem. Soc.* **2006**, *128*, 12434.
(66) Roy, A. H.; Hartwig, J. F. *J. Am. Chem. Soc.* **2003**, *125*, 13944.
(67) Le, C. M.; Menzies, P. J. C.; Petrone, D. A.; Lautens, M. *Angew. Chem. Int. Ed.* **2014**, n/a.
(68) Bestmann, H. J.; Sühs, K.; Röder, T. *Angew. Chem.* **1981**, *93*, 1098.
(69) Pelter, A.; Rosser, R.; Mills, S. *J. Chem. Soc., Chem. Commun.* **1981**, 1014.
(70) Bestmann, H. J.; Röder, T.; Sühs, K. *Chem. Ber.* **1988**, *121*, 1509.
(71) Clark, T. J.; Lee, K.; Manners, I. *Chem. Eur. J.* **2006**, *12*, 8634.
(72) Dorn, H.; Singh, R. A.; Massey, J. A.; Lough, A. J.; Manners, I. *Angew. Chem. Int. Ed.* **1999**, *38*, 3321.
(73) Hooper, T. N.; Huertos, M. A.; Jurca, T.; Pike, S. D.; Weller, A. S.; Manners, I. *Inorg. Chem.* **2014**, *53*, 3716.
(74) Huertos, M. A.; Weller, A. S. *Chem. Commun.* **2012**, *48*, 7185.
(75) Ledger, A. E. W.; Ellul, C. E.; Mahon, M. F.; Williams, J. M. J.; Whittlesey, M. K. *Chem. Eur. J.* **2011**, *17*, 8704.
(76) Sandee, A. J.; van der Veen, L. A.; Reek, J. N. H.; Kamer, P. C. J.; Lutz, M.; Spek, A. L.; van Leeuwen, P. W. N. M. *Angew. Chem. Int. Ed.* **1999**, *38*, 3231.
(77) Dallanegra, R.; Chaplin, A. B.; Weller, A. S. *Organometallics* **2012**, *31*, 2720.

# 4 Exploring the mechanism of the dehydrocoupling of amine-boranes with {Rh(Xantphos)}$^+$

## 4.1 Introduction

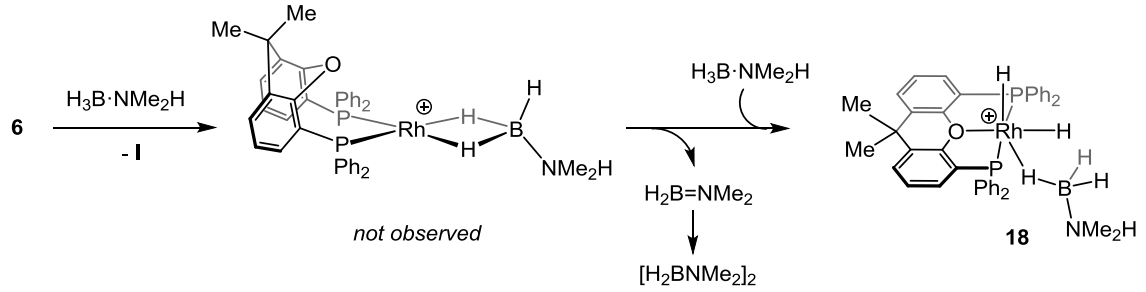
Following the exploration of the reactivity of the tertiary amine-borane $H_3B{\cdot}NMe_3$ with **6**, the reactivity of **6** with the secondary and primary amine-boranes $H_3B{\cdot}NMe_2H$ and $H_3B{\cdot}NMeH_2$, respectively, was next focused upon, with the goal of understanding the mechanism of polyaminoborane formation. The steps implicated in the dehydrogenative homocoupling of $H_3B{\cdot}NMe_3$ (two B—H activation steps and B—B coupling) resemble those required for dehydropolymerisation of $H_3B{\cdot}NMeH_2$ (B—H activation, N—H activation and B—N coupling), and thus it was speculated that **6** may be adept as a dehydropolymerisation catalyst. This chapter presents a study upon the dehydrocoupling of $H_3B{\cdot}NMeH_2$ and $H_3B{\cdot}NMe_2H$ using **6** and ultimately presents a postulated mechanism for these processes.

## 4.2 Stoichiometric reactivity of 6 with amine-boranes

### 4.2.1 Reactivity with $H_3B{\cdot}NMe_2H$

Prior to investigations into the catalytic dehydrocoupling activity of **6** with $H_3B{\cdot}NMe_2H$ and $H_3B{\cdot}NMeH_2$, stoichiometric investigations with these substrates were conducted to ascertain the likely metal complexes that may be involved in catalysis. Upon addition of a blue solution of **6** in $C_6H_5F$ to 2 equivalents of $H_3B{\cdot}NMe_2H$ in an NMR tube, the colour changed immediately to pale yellow. *In situ* monitoring by NMR spectroscopy indicated the formation of a new complex, [Rh($\kappa^3_{P,O,P}$-Xantphos)$(H)_2$($\eta^1$-$H_3B{\cdot}NMe_2H$)][$BAr^F_4$] (**18**, Scheme 4.1). **18** showed very similar NMR data to **3**. In

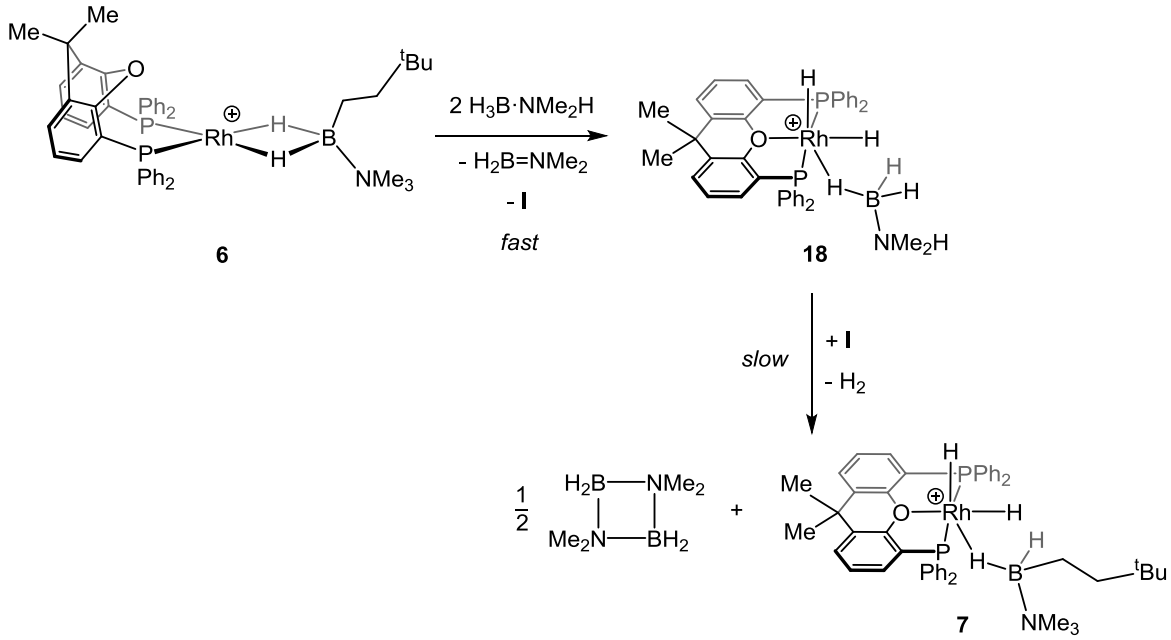
particular, the hydride region of the $^{1}H$ NMR spectrum showed three environments at δ –1.29 (br), δ –14.11 (br) and δ –19.05 (dtd, $^{2}J_{PH}$ = 15 Hz, $^{2}J_{HH}$ = 6 Hz, $^{1}J_{RhH}$ = 27 Hz) with relative integrals of 3H, 1H and 1H, respectively. These data, as with **3**, imply a Rh···$H_3B$ unit rapidly exchanging between terminal and bridging positions, and two mutually *cis* Rh—H groups. The $^{11}B$ NMR spectrum showed a broad signal at δ –12.0, barely shifted from that of free $H_3B{\cdot}NMe_2H$ at δ –12.9, consistent with $\eta^1$ binding of the amine-borane. These data are similar to previous reports of $H_3B{\cdot}NMe_2H$ bound $\eta^1$ to metal centres.[1-3] The $^{31}P\{^{1}H\}$ NMR spectrum indicated equivalent phosphorus environments coupled to a $Rh^{III}$ centre (δ 44.5, d, $J_{RhP}$ = 115 Hz).[4] Further NMR data for **18** could not be deduced due to various overlapping peaks in the aliphatic region.




**Scheme 4.1** Formation of **18** from **6**. $[BAr^{F}_4]^-$ anions not shown.

The formation of **18** may be similar to the formation of $[Rh(P^{i}Bu_3)_2(H)_2(\eta^2\text{-}H_3B{\cdot}NMe_2H)][BAr^{F}_4]$ from $[Rh(P^{i}Bu_3)_2(\eta^2\text{-}H_3B{\cdot}NMe_2H)][BAr^{F}_4]$, as previously calculated by Weller and Hall (Chapter 1).[5] A plausible pathway involves displacement of **I** by $H_3B{\cdot}NMe_2H$ to form $[Rh(\kappa^2_{P,P}\text{-Xantphos})(\eta^2\text{-}H_3B{\cdot}NMe_2H)][BAr^{F}_4]$ (not observed). Then, dehydrogenation of $H_3B{\cdot}NMe_2H$ forms $[Rh(Xantphos)(H)_2][BAr^{F}_4]$[6] (not observed) with concomitant loss of $H_2B{=}NMe_2$ that dimerises to form $[H_2BNMe_2]_2$. Both $H_2B{=}NMe_2$ and $[H_2BNMe_2]_2$ were observed in the $^{11}B$ NMR spectrum immediately after addition. $[Rh(Xantphos)(H)_2]^+$ coordinates the

excess $H_3B{\cdot}NMe_2H$ to form **18** (Scheme 4.1). Addition of excess MeCN to **18** formed **4**[4] with expulsion of $H_3B{\cdot}NMe_2H$, further supporting the proposed structure of **18**. **18** could not be isolated from the reaction mixture due to slow conversion to **7** (~5 hours). During the conversion, more $[H_2BNMe_2]_2$ was formed, indicating that slow dehydrocoupling of $H_3B{\cdot}NMe_2H$ occurs upon the $Rh^{III}$ centre. As $H_3B{\cdot}NMe_2H$ is consumed, **I** re-coordinates to the metal centre, forming **7** (Scheme 4.2).



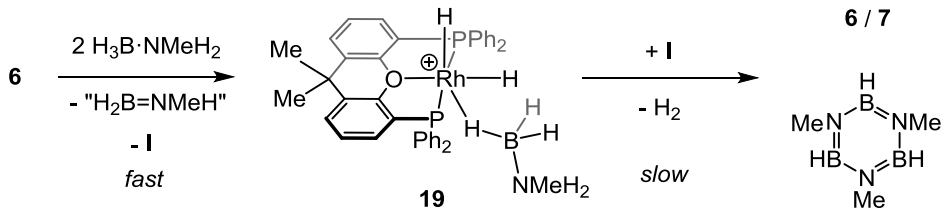

**Scheme 4.2** Reaction of **6** with 2 eq. $H_3B{\cdot}NMe_2H$ in $C_6H_5F$. $[BAr^F{}_4]^-$ anions not shown.

With addition of a single equivalent of $H_3B{\cdot}NMe_2H$ to **6**, a mixture of **6**, **18** and **7** was observed immediately after addition, and $[Rh(\kappa^2{}_{P,P}\text{-Xantphos})(\eta^2\text{-}H_3B{\cdot}NMe_2H)][BAr^F{}_4]$ was not observed by NMR spectroscopy.

### 4.2.2 Reactivity with $H_3B{\cdot}NMeH_2$

The reactivity between **6** and $H_3B{\cdot}NMeH_2$ was similar to that seen with $H_3B{\cdot}NMe_2H$. Again, a blue to yellow colour change was observed on addition of **6** in $C_6H_5F$ to 2 equivalents of $H_3B{\cdot}NMe_2H$. NMR spectroscopy indicated the formation of $[Rh(\kappa^3{}_{P,O,P}\text{-}$

Xantphos)(H)$_2$($\eta^1$-H$_3$B·NMeH$_2$)][BAr$^F_4$] (**19**, Scheme 4.3). **19** showed very similar spectroscopic data to **3** and **18**. The $^{11}$B NMR spectrum showed a broad resonance at δ –17.0. Upon addition of MeCN to **19**, **4** was formed, and free H$_3$B·NMeH$_2$ was observed in the $^{11}$B NMR spectrum at δ –17.3. As with **18**, slow formation of **7** was observed, although in this case conversion was complete after 2 hours yielding a mixture of **6** and **7**. To form **19** from **6**, dehydrogenation of one equivalent of H$_3$B·NMeH$_2$ is required. The putative aminoborane H$_2$B=NMeH was not seen in the $^{11}$B NMR spectrum (δ 37.1, dd, $J_{BH\ av.}$ = 130 Hz),[7] but the corresponding borazine, [HBNMe]$_3$, was observed at δ 33.3.[8]

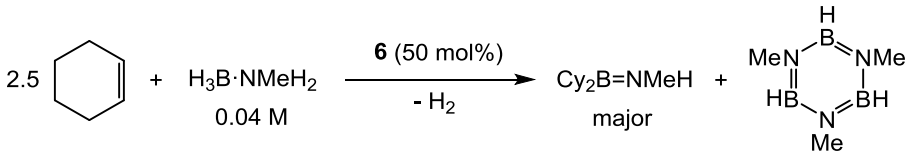



**Scheme 4.3** Reaction of **6** with 2 eq. H$_3$B·NMeH$_2$ in C$_6$H$_5$F. [BAr$^F_4$]$^-$ anion not shown.

As discussed in Chapter 1, H$_2$B=NMeH has recently been detected upon addition of 2,6-di-*tert*-butylpyridine to [H$_2$B(Et$_2$O)·NMeH$_2$][B(C$_6$F$_5$)$_4$], ultimately forming low molecular weight polyaminoborane, [H$_2$BNMeH]$_n$.[7] However, neither H$_2$B=NMeH nor H$_2$B=NH$_2$ have been directly observed in the metal catalysed dehydrocoupling of their respective amine-boranes, although they have been trapped using a metal fragment.[9] For example, a recent report showed that the dehydrocoupling of H$_3$B·NR$_2$H (R = Me, H) catalysed by OsH(SH)(CO)(P$^i$Pr$_3$)$_2$ formed OsH(CO){$\eta^2$-H(S)B=NR$_2$}(P$^i$Pr$_3$)$_2$ in later stages of catalysis by dehydrogenative trapping of free H$_2$B=NR$_2$.[10] Generally, however, borazines have been considered as a marker for free aminoboranes.[11-13] The primary aminoborane H$_2$B=N$^t$BuH was previously shown to undergo an 'off-metal'

hydrogen redistribution reaction to form the borazine $[HBN^tBu]_3$ and the parent amine-borane $H_3B{\cdot}N^tBuH_2$, and a similar pathway could operate here to form $H_3B{\cdot}NMeH_2$ (which can dehydrocouple) and $[HBNMe]_3$.[12] No evidence for an aminoborane complex was observed by NMR spectroscopy.

To further probe the involvement of $H_2B{=}NMeH$ in the formation of $[HBNMe]_3$ in this system, cyclohexene (2.5 eq. relative to $H_3B{\cdot}NMeH_2$) was added at the start of the reaction. The final product distribution, by $^{11}B$ NMR spectroscopy, indicated a mixture of $Cy_2B{=}NMeH$ (δ 45.7; lit. δ 44.9 in THF[14]) as the major product, with $[HBNMe]_3$ and a minor unidentified triplet at δ –1.1 ($^1J_{HB}$ = 98 Hz) also observed (Scheme 4.4). **6** was the major organometallic product observed, rather than **7**, suggesting that cyclohexene reduced **7** to **6**. As discussed in Chapters 2 and 3, cyclohexene reduces **3** to form **2**. Consistent with this, cyclohexane was observed in the $^1H$ NMR spectrum at δ 1.41.[15] Clear product ratio integrals could not be obtained as the signal for $[HBNMe]_3$ overlapped with that of **6** in the $^{11}B$ NMR spectrum. Nonetheless, the observation of $Cy_2B{=}NMeH$ implicates the involvement of liberated $H_2B{=}NMeH$ in this system.[11,13,14,16-18]




**Scheme 4.4** Addition of cyclohexene to the dehydrocoupling mixture.

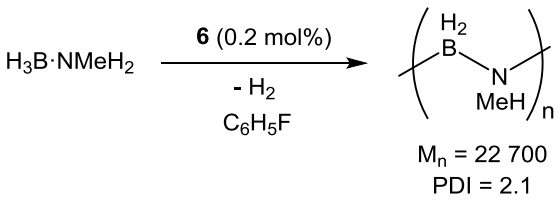
### 4.2.3 Conclusions on stoichiometric reactivity

Overall, these stoichiometric studies show that initial displacement of **I** by $H_3B{\cdot}NMeH_2$ or $H_3B{\cdot}NMe_2H$, and formation of **18** or **19**, respectively, are fast. Then,

slower dehydrogenation occurs upon the $Rh^{III}$ centre. This is similar to related monodentate rhodium phosphine systems, in which dehydrogenation of $H_3B{\cdot}NMe_2H$ by $[Rh(PR_3)_2][BAr^F{}_4]$ was faster than that by $[Rh(PR_3)_2(H)_2][BAr^F{}_4]$ (R = Cy[19] or $^i$Bu[5]). In the reaction with $H_3B{\cdot}NMeH_2$, the presence of free $H_2B{=}NMeH$ was inferred by the production of borazine and cyclohexene trapping experiments. The stoichiometric dehydrocoupling upon the $Rh^{III}$ centre in this system is slower than dehydrocoupling under catalytic conditions with much lower catalyst loadings (*vide infra*). This may imply that N—H···H—B dihydrogen bonding is key in promoting the dehydrocoupling, as has been suggested previously.[20,21]

## 4.3 Dehydropolymerisation of $H_3B{\cdot}NMeH_2$ with 6

Although the stoichiometric reaction of **6** with $H_3B{\cdot}NMeH_2$ produced $[HBNMe]_3$, the reaction was tried under similar catalytic conditions to those that formed $[H_2BNMeH]_n$ from $H_3B{\cdot}NMeH_2$ using $[Rh(Ph_2P(CH_2)_xPPh_2)(\eta^6\text{-}C_6H_5F)][BAr^F{}_4]$ (x = 3 – 5).[22] Using **6** (0.2 mol%), the catalytic dehydrocoupling of $H_3B{\cdot}NMeH_2$ (0.44 M) in $C_6H_5F$ solution under open conditions ($H_2$ released *via* a mercury bubbler) was complete within two hours to form $[H_2BNMeH]_n$ as the major product (Scheme 4.5). Upon addition of hexanes, $[H_2BNMeH]_n$ precipitated as a cream-coloured solid.




**Scheme 4.5** Dehydropolymerisation of $H_3B{\cdot}NMeH_2$ with **6**.

The $[H_2BNMeH]_n$ formed displayed a characteristic broad, symmetrical signal in the $^{11}B$ and $^{11}B\{^1H\}$ NMR spectra at δ −5.4 (FWHM = 720 Hz in the $^{11}B\{^1H\}$ NMR spectrum,

Figure 4.1a), indicative of multiple similar boron environments within a polymer chain.

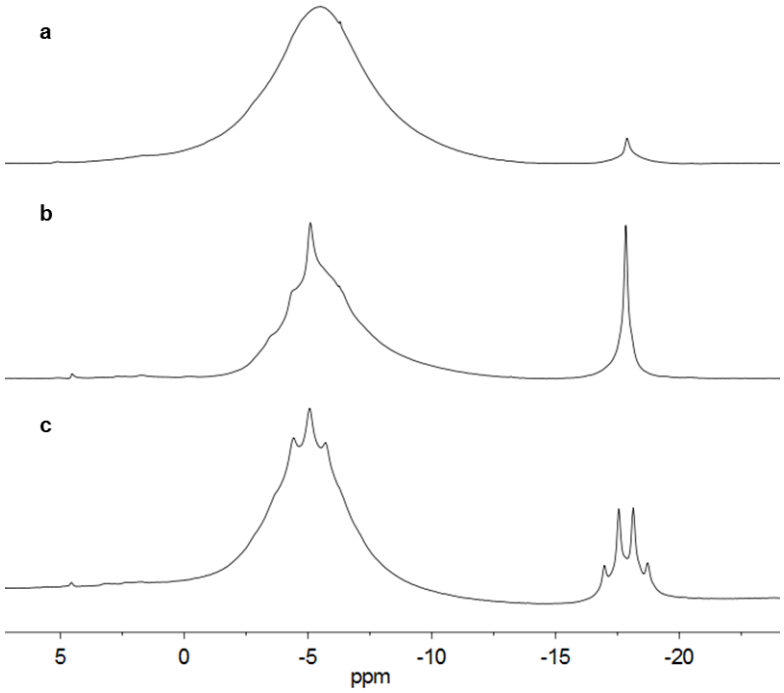
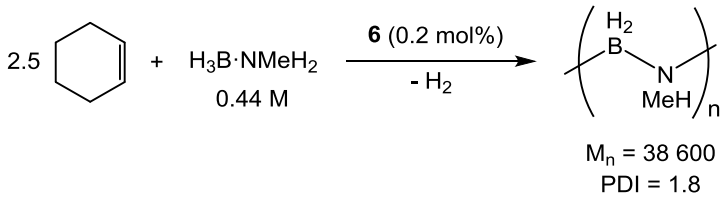



**Figure 4.1 (a)** $^{11}B\{^1H\}$ NMR spectrum of $[H_2BNMeH]_n$ produced under open conditions. The peak at δ –17.9 is entrained $H_3B{\cdot}NMeH_2$. **(b)** $^{11}B\{^1H\}$ NMR spectrum of $[H_2BNMeH]_n$ produced under closed conditions. **(c)** $^{11}B$ NMR spectrum of $[H_2BNMeH]_n$ produced under closed conditions. All spectra are in THF solvent and back-linear predicted.

These spectra are similar to those of $[H_2BNMeH]_n$ originally reported by Manners using the Ir($^t$BuPOCOP$^t$Bu)$(H)_2$ catalyst.[23] Analysis by gel permeation chromatography (GPC) relative to polystyrene standards was carried out by Dr George R. Whittell (Manners Group, University of Bristol), which confirmed the assignment of polymeric $[H_2BNMeH]_n$ and indicated a moderate molecular weight polymer ($M_w$ = 47 700 g mol$^{-1}$, $M_n$ = 22 700 g mol$^{-1}$, PDI = 2.1). The molecular weight is lower than those reported with the Ir($^t$BuPOCOP$^t$Bu)$(H)_2$ ($M_n$ = 55 000 g mol$^{-1}$, PDI = 2.9) and $[Rh(Ph_2P(CH_2)_4PPh_2)(\eta^6\text{-}C_6H_5F)][BAr^F{}_4]$ ($M_n$ = 138 500 g mol$^{-1}$, PDI = 1.3) systems.[22,23]

### 4.3.1 Role of $H_2B$=NMeH during dehydropolymerisation

Analysis by $^{11}B$ NMR spectroscopy of regular aliquots of the reaction mixture showed no evidence for the formation of $[HBNMe]_3$, contrasting the stoichiometric reactions (Section 4.2.2), nor was $H_2B$=NMeH observed. In the presence of cyclohexene (2.5 eq. relative to $H_3B{\cdot}NMeH_2$), $Cy_2B$=NMeH was not observed by $^{11}B$ NMR spectroscopy, and $[H_2BNMeH]_n$ was the major product formed (Scheme 4.6). This suggests that any $H_2B$=NMeH produced remains coordinated to the metal centre, or that polymerisation of free $H_2B$=NMeH is kinetically competitive with hydroboration under these conditions.[24] Interestingly, cyclohexane (~5% conversion) was observed in the $^1H$ NMR spectrum, and GPC analysis of the $[H_2BNMeH]_n$ indicated a higher molecular weight ($M_n$ = 38,600 g mol$^{-1}$, PDI = 1.8) than that prepared in the absence of cyclohexene. Possible reasons for this are discussed in Section 4.11.




**Scheme 4.6** Addition of cyclohexene to the dehydropolymerisation reaction.

These observations are consistent with previous reports in which cyclohexene trapping products were not formed under dehydropolymerisation conditions.[11,13,14,24,25] However, the presence of free $H_2B$=NMeH cannot be ruled out if polymerisation is kinetically competitive with hydroboration. Nevertheless, these observations indicate that the stoichiometric and catalytic dehydrocoupling pathways are different.

## 4.4 Polymer growth kinetics

### 4.4.1 Temporal profile for the dehydropolymerisation

Kinetic studies for the dehydropolymerisation of $H_3B{\cdot}NMeH_2$ are hampered due to the ill-defined oligomeric and polymeric species that may result from its dehydrocoupling. Additionally, $H_3B{\cdot}NMeH_2$ can lose over one equivalent of $H_2$, which may complicate kinetic analyses. In $C_6H_5F$ and 1,2-$C_6H_4F_2$, $H_3B{\cdot}NMeH_2$ has limited solubility, adding further complications. In spite of this, experiments were conducted to gain a qualitative overview of the dehydropolymerisation kinetics. Upon reaction of $H_3B{\cdot}NMeH_2$ (0.44 M) with 0.2 mol% **6** in $C_6H_5F$, the $H_2$ evolution was measured using a gas burette and the results of this are plotted in Figure 4.2 (blue points). Complementary data for the % conversion *vs* time were also plotted (red points). Each conversion point represents a separate experiment in which the $[H_2BNMeH]_n/H_3B{\cdot}NMeH_2$ mixture was precipitated with hexanes and dissolved in THF for analysis by $^{11}B\{^1H\}$ NMR spectroscopy. Direct sampling of the $C_6H_5F$ reaction mixture showed similar conversions but, owing to limited solubility of $H_3B{\cdot}NMeH_2$ in $C_6H_5F$, the conversions obtained by the precipitation method are plotted. The conversion and $H_2$ evolution plots track each other and show that there is an induction period of ~15 minutes. This is followed by a *pseudo*-zero order $H_2$ release regime until approximately 0.9 eq. $H_2$ are released. Complete conversion (by NMR spectroscopy) is achieved within approximately 7200 s, a TOF of 250 $h^{-1}$, by which point approximately 1.1 eq. of $H_2$ was released. This could imply some chain branching had occurred, but is consistent with an approximate empirical formula of $[H_2BNMeH]_n$.

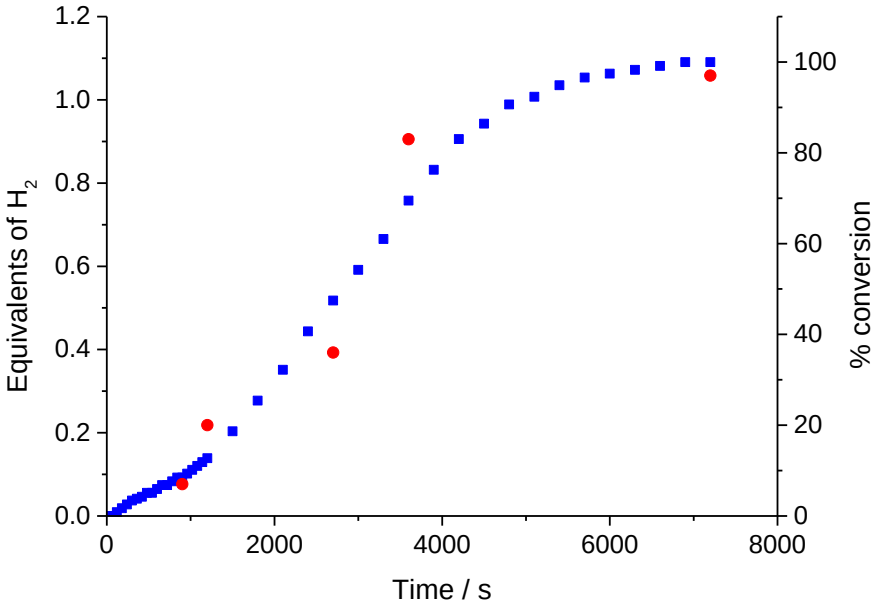



**Figure 4.2** Plot showing $H_2$ evolution *vs* time (■) and % conversion *vs* time (●). $H_2$ evolution determined by gas burette. Conversions determined by precipitation of the $C_6H_5F$ reaction mixture with hexanes, dissolution in THF and measuring by $^{11}B\{^1H\}$ NMR spectroscopy.

### 4.4.2 Molecular weight *vs* conversion

To determine the nature of the polymer growth in this system, molecular weight *vs* conversion experiments were conducted. The polymers isolated from each conversion point in Figure 4.2 were analysed by GPC and their molecular weights plotted *vs* the % conversions (Figure 4.3). The plot shows that, at low conversions, high molecular weight material is produced, indicative of a chain growth polymerisation in which the polymer chain grows through monomer insertion to the metal centre, until a chain transfer event occurs (*cf.* Ziegler-Natta olefin polymerisation[26]) and the process starts again.[27] Within error, similar molecular weights were observed across the range of conversions, typical of a classical chain growth mechanism. Chain growth polymerisation was proposed by Schneider and co-workers for the Ru-catalysed dehydropolymerisation of $H_3B{\cdot}NH_3$.[24] Baker and Gordon also suggested that a chain growth insertion pathway for $H_3B{\cdot}NH_3$

dehydropolymerisation using [Fe($Cy_2PCH_2CH_2PCy_2$)($PhNCH_2CH_2NPh$)] was more likely than an alternative end-chain propagation pathway.[25] Manners and co-workers suggested a modified chain growth mechanism for the Ir-catalysed dehydropolymerisation of $H_3B{\cdot}NMeH_2$, in which slow metal-catalysed formation of $H_2B{=}NMeH$ is followed by rapid metal-catalysed polymerisation of $H_2B{=}NMeH$.[28] This mechanism was proposed as high molecular weight polymer was observed at low conversions, but the molecular weight increased further at higher conversions.

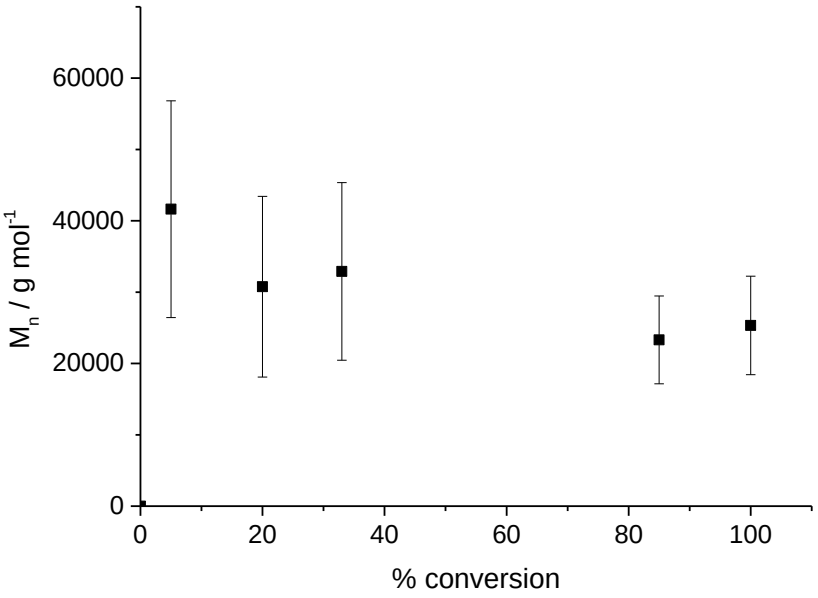



**Figure 4.3** $M_n$ *vs* % conversion graph. Mean values over three separate runs are plotted, with standard error. GPC performed by Dr G. Whittell, University of Bristol.

When using 1 mol% **6**, the molecular weight of the $[H_2BNMeH]_n$ produced was markedly lower ($M_n$ = 7 500 g $mol^{-1}$, PDI = 1.5) than that obtained using 0.2 mol%. This is also consistent with a single site chain growth mechanism as more initiating sites statistically result in shorter polymer chains.

The molecular weight distribution also implies that this is not a living polymerisation system. In a living polymerisation, there is no chain transfer step and so molecular

weight increases with increasing addition of substrate.[26] To explicitly test for living polymerisation, the reaction mixture after two hours was transferred to a new Schlenk flask containing 500 eq. of $H_3B{\cdot}NMeH_2$. After a further two hours, all $H_3B{\cdot}NMeH_2$ had been consumed to form $[H_2BNMeH]_n$ ($M_n$ = 17,900 g mol$^{-1}$, PDI = 1.8) with a similar molecular weight to that produced prior to the addition of fresh $H_3B{\cdot}NMeH_2$, implying that this polymerisation not a living polymerisation. This experiment also demonstrated recyclability of the catalyst.

## 4.5 Effect of solvent upon polymerisation

THF solvent was reported to cease dehydropolymerisation catalysis in the $[Rh(Ph_2P(CH_2)_xPPh_2)(\eta^6\text{-}C_6H_5F)][BAr^F{}_4]$ (x = 3 – 5) system, thought to be a result of THF blocking the catalytic sites.[22] By contrast, the neutral Ir($^t$BuPOCOP$^t$Bu)$(H)_2$ catalyst rapidly formed high molecular weight $[H_2BNMeH]_n$ in THF.[23] In Chapter 2, it was found that $H_3B{\cdot}NMe_3$ was competitive with the binding of THF to $\{Rh(Xantphos)(H)_2\}^+$, suggesting that dehydropolymerisation in THF may be feasible with **6**. In THF, the **6**-catalysed dehydropolymerisation of $H_3B{\cdot}NMeH_2$ did occur, but was slower than in $C_6H_5F$, taking 19 hours to reach 85% completion. However, the molecular weight was higher ($M_n$ = 52 500 g mol$^{-1}$, PDI = 1.4) than with $C_6H_5F$ solvent. This implies that, while slowing the polymerisation, THF also attenuates chain transfer. If THF coordinates to vacant site(s) in the active catalyst, this could impede incoming $H_3B{\cdot}NMeH_2$ and slow catalysis, yet also obstruct chain transfer pathways, resulting in higher molecular weights. THF may also better solvate the growing chains, which could result in longer polymer chains. Furthermore, THF has been demonstrated to play an active role in the mechanism for the dehydrocoupling of

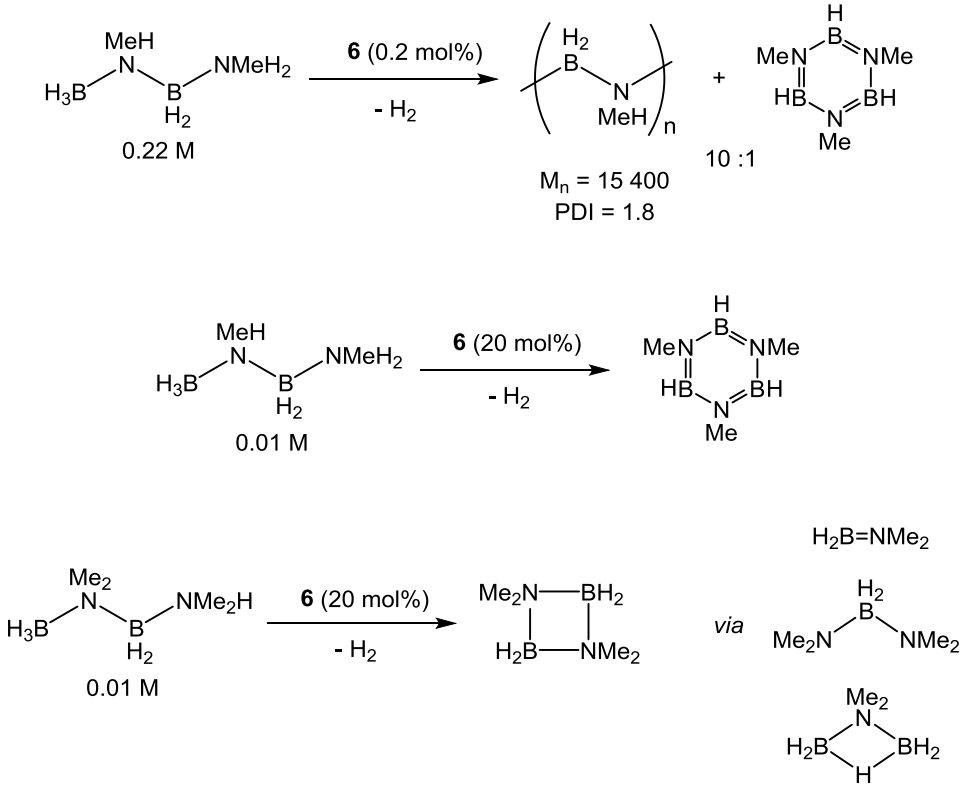
$H_3B{\cdot}NMe_2H$ using Pt catalysts (described in Chapter 1) *via* the formation of $[(THF)BH_2NMe_2H]^+$,[29] and a related pathway operating with **6** cannot be discounted.

## 4.6 Role of $H_3B{\cdot}NMeHBH_2{\cdot}NMeH_2$ in dehydropolymerisation

The role of the linear diborazane $H_3B{\cdot}NMeHBH_2{\cdot}NMeH_2$ as a potential intermediate in the dehydropolymerisation of $H_3B{\cdot}NMeH_2$ was explored. As discussed in Chapter 1, Manners concluded that $H_3B{\cdot}NMeHBH_2{\cdot}NMeH_2$ is cleaved by $Ir(^tBuPOCOP^tBu)(H)_2$ to form $H_3B{\cdot}NMeH_2$ and $H_2B{=}NMeH$, with the eventual Ir-catalysed formation of $[H_2BNMeH]_n$.[13,14] Similarly, reaction of $H_3B{\cdot}NMeHBH_2{\cdot}NMeH_2$ (0.22 M, 0.44 M "BN" units) with **6** (0.4 mol%, 0.2 mol% relative to "BN" units) in $C_6H_5F$ resulted in dehydropolymerisation to form $[H_2BNMeH]_n$ ($M_n$ = 15 400 g $mol^{-1}$, PDI = 1.8). $[HBNMe]_3$ (~10%) was also observed in the reaction mixture (Scheme 4.7). The observation of $[HBNMe]_3$ may imply B—N bond cleavage of $H_3B{\cdot}NMeHBH_2{\cdot}NMeH_2$ occurs to yield $H_2B{=}NMeH$ and $H_3B{\cdot}NMeH_2$, which then polymerise, as was proposed in Manners' system.

By contrast, addition of **6** (20 mol%) to a 0.01 M solution of $H_3B{\cdot}NMeHBH_2{\cdot}NMeH_2$ formed the borazine $[HBNMe]_3$ alongside unidentified metal-containing products (Scheme 4.7). This suggests that $H_3B{\cdot}NMeHBH_2{\cdot}NMeH_2$ undergoes B—N bond cleavage to form $H_3B{\cdot}NMeH_2$ and $H_2B{=}NMeH$, which results in the production of $[HBNMe]_3$, as in the stoichiometric reactions of **6** with $H_3B{\cdot}NMeH_2$. No evidence for the cyclic trimer $[H_2BNMeH]_3$,[30] a plausible intermediate in $[HBNMe]_3$ formation,[8,31] was observed. With $H_3B{\cdot}NMe_2BH_2{\cdot}NMe_2H$, $[H_2BNMe_2]_2$ was formed as the product of dehydrocoupling after 24 hours. Significant amounts of $H_2B{=}NMe_2$, $HB(NMe_2)_2$ and $(H_2B)_2(\mu\text{-}H)NMe_2$ were observed at 55% conversion (100 minutes), indicating **6**

mediates the B—N bond cleavage of $H_3B{\cdot}NMe_2BH_2{\cdot}NMe_2H$. $(H_2B)_2(\mu\text{-}H)NMe_2$ has been observed previously as an intermediate in the thermal redistribution of $H_3B{\cdot}NMe_2BH_2{\cdot}NMe_3$.[13] As both $H_3B{\cdot}NMeHBH_2{\cdot}NMeH_2$ and $H_3B{\cdot}NMe_2BH_2{\cdot}NMe_2H$ are cleaved by **6**, their formation during catalytic dehydrocoupling of $H_3B{\cdot}NMeH_2$ and $H_3B{\cdot}NMe_2H$ cannot be ruled out, despite not being observed directly (<1 % in the catalytic dehydrocoupling of $H_3B{\cdot}NMe_2H$, *vide infra*).




**Scheme 4.7** Reactions of linear diborazanes with **6**.

## 4.7 Dehydropolymerisation under closed conditions

The dehydropolymerisation of $H_3B{\cdot}NMeH_2$ with **6** was conducted also under sealed conditions to gauge the effect of $H_2$ build-up upon the catalysis. In a sealed Young's vessel (*ca.* 30 $cm^3$ volume, $[H_3B{\cdot}NMeH_2]_0$ = 0.44 M, 0.2 mol% **6**, $C_6H_5F$, *ca.* 2 atm $H_2$ generated), dehydropolymerisation reached completion in approximately 24 hours,

much longer than in an open system (within 2 hours). The material isolated from closed conditions had a waxier consistency than the powder isolated from analogous dehydropolymerisation under open conditions (Figure 4.4), suggesting the presence of shorter chain oligomers.[13]

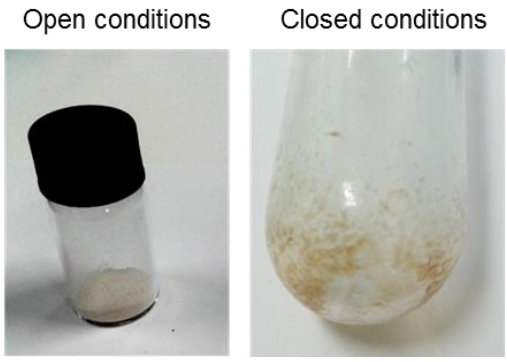



**Figure 4.4** Photographs of $[H_2BNMeH]_n$ produced under open and sealed conditions.

The $^{11}B\{^1H\}$ NMR spectrum of the material produced under these closed conditions also indicated the presence of shorter chain oligomers. A broad peak centred at δ –5 was observed with additional sharper resonances overlapping, suggesting several species with $BH_2$ groups (Figure 4.1b). In the $^{11}B$ NMR spectrum (Figure 4.1c), the region at δ –5 appears as a broad triplet overlaying broader resonances, suggesting multiple species with $BH_2$ groups are present. Furthermore, peaks in the region *ca.* δ –18, coincident with $H_3B{\cdot}NMeH_2$, were observed in the $^{11}B\{^1H\}$ NMR spectrum, indicating various $BH_3$ moieties. In the $^{11}B$ NMR spectrum, these peaks appear as overlapping quartets (Figure 4.1c). These data resemble those for $H_3B{\cdot}NMeHBH_2{\cdot}NMeH_2$, again consistent with the production of shorter chain oligomers as well as longer chain polymers.[31] Analysis of the material by GPC showed that lower molecular weight $[H_2BNMeH]_n$ ($M_n$ = 2 800 g mol$^{-1}$, PDI = 1.8) had indeed been produced under closed conditions. Therefore, $H_2$ appeared to be both inhibiting

catalysis and acting as a chain transfer agent. Comparably, $H_2$ has been used to control molecular weights by acting as a chain transfer agent *via* a sigma bond metathesis pathway in Ziegler-Natta olefin polymerisation.[26,32]

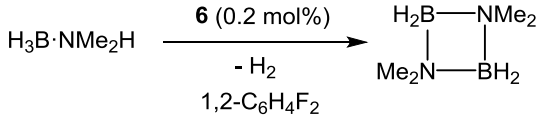
## 4.8 Catalytic dehydrocoupling of $H_3B{\cdot}NMe_2H$ with 6

In studying the mechanism of the dehydropolymerisation of $H_3B{\cdot}NMeH_2$, several features have been established: chain growth polymerisation, increased molecular weights using THF and decreased molecular weights under sealed conditions. For a more quantitative overview of the kinetics, the catalytic dehydrocoupling of $H_3B{\cdot}NMe_2H$ by **6** was examined. The dehydrocoupling of $H_3B{\cdot}NMe_2H$ is more easily studied than that of $H_3B{\cdot}NMeH_2$. $H_3B{\cdot}NMe_2H$, its final dehydrocoupling product $[H_2BNMe_2]_2$, and common intermediates, $H_2B{=}NMe_2$ and $H_3B{\cdot}NMe_2BH_2{\cdot}NMe_2H$, are well-defined species readily recognised by their characteristic chemical shifts in $^{11}B$ NMR spectra, and are soluble in $C_6H_5F$ and 1,2-$C_6H_4F_2$.

### 4.8.1 Open conditions

The prior results obtained in the dehydropolymerisation studies indicated that $H_2$ build-up can strongly affect the rate of dehydrocoupling with **6**. Therefore, catalysis was first conducted under open conditions enabling escape of $H_2$ through a mineral oil bubbler. The conditions chosen were analogous to those used for the dehydrocoupling of $H_3B{\cdot}NMe_2H$ with $[Rh(Ph_2P(CH_2)_xPPh_2)(\eta^6\text{-}C_6H_5F)][BAr^F{}_4]$ (x = 3 – 5): $H_3B{\cdot}NMe_2H$ (0.072 M) and 0.2 mol% **6** in 1,2-$C_6H_4F_2$. Upon addition of **6**, an immediate colour change from blue to pale yellow was observed. 0.1 mL aliquots of the reaction mixture were periodically removed *via* syringe, diluted with 0.25 mL 1,2-$C_6H_4F_2$ in high pressure NMR tubes, and the samples were frozen in liquid $N_2$

prior to analysis by $^{11}B$ NMR spectroscopy. The same method was used previously with the $[Rh(PCy_3)_2L_n][BAr^F{}_4]$ system.[19]




**Scheme 4.8** Overall catalytic dehydrocoupling of $H_3B{\cdot}NMe_2H$ (0.072 M) with **6** (0.2 mol%).

The $^{11}B$ NMR spectra showed the consumption of $H_3B{\cdot}NMe_2H$ and formation of the dehydrocoupling product, $[H_2BNMe_2]_2$ (Scheme 4.8). The intermediate $H_2B{=}NMe_2$ and small amounts (typically < 5%) of the diaminoborane $HB(NMe_2)_2$[33] were also observed. $HB(NMe_2)_2$ has been observed in various other dehydrocoupling systems[1,5,19,22,34-36] and may be a product of the decomposition of reactive $H_2B{=}NMe_2$ during sampling.[19] Less than 1% of the linear diborazane $H_3B{\cdot}NMe_2BH_2{\cdot}NMe_2H$ was observed. This distribution contrasts some rhodium-catalysed systems, *e.g.* $[Rh(PR_3)_2][BAr^F{}_4]$ (R = Cy[19] or $^i$Bu[5]), in which the linear diborazane is a significant intermediate, but is similar to the $[Rh(Ph_2P(CH_2)_xPPh_2)(\eta^6\text{-}C_6H_5F)][BAr^F{}_4]$ (x = 3 – 5) systems in which no linear diborazane was observed.[22] A plot of the concentration *vs* time for the major boron-containing species observed in the dehydrocoupling is shown in Figure 4.5. The plot shows an induction period of approximately 300 – 400 s, shorter than the induction period measured by $H_2$ evolution for the dehydropolymerisation of $H_3B{\cdot}NMeH_2$ (900 s). After this, catalysis is relatively fast (TOF ~1000 $h^{-1}$). This is quicker than the dehydropolymerisation of $H_3B{\cdot}NMeH_2$ (TOF ~250 $h^{-1}$), although this may be due to the differing solubilities of the amine-boranes. The decay of $[H_3B{\cdot}NMe_2H]$ during the productive period appears zero order at first (400 – 1200 s), and tends towards first order decay at lower $[H_3B{\cdot}NMe_2H]$. This

behaviour is explored in more depth in Section 4.8.5. The catalyst could be recycled – upon transferring the spent solution to a new Schlenk flask containing 500 eq. $H_3B{\cdot}NMe_2H$, catalysis continued at a similar rate with no observed induction period.

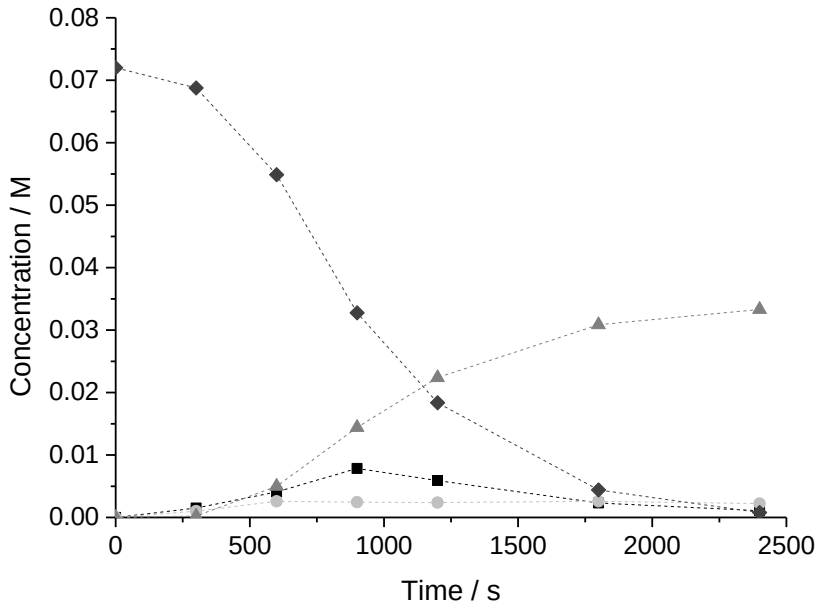



**Figure 4.5** Plot of concentration (by $^{11}B$ NMR spectroscopy) during the catalytic dehydrocoupling of $H_3B{\cdot}NMe_2H$ (initial concentration 0.072 M) with [**6**] = 1.44 x $10^{-4}$ M (0.2 mol%). Open conditions. ◆ = $H_3B{\cdot}NMe_2H$; ■ = $H_2B{=}NMe_2$; ● = $HB(NMe_2)_2$; ▲ = $[H_2BNMe_2]_2$.

The catalysis with **6** is similar to the $[Rh(Ph_2P(CH_2)_3PPh_2)(\eta^6\text{-}C_6H_5F)][BAr^F{}_4]$ system, which also had an induction period of ~300 s and a post-induction turnover frequency of 1250 $h^{-1}$.[22] Induction periods can indicate heterogeneous catalysis due to the formation of colloidal rhodium as the active catalyst.[37] During catalysis, the solution remained a clear pale yellow colour with no dark material that may signify the production of colloidal rhodium. Addition of Hg in large excess (~2400 eq. relative to **6**) after the induction period did not halt catalysis, as was observed in Manners' heterogeneous system with $[Rh(1,5\text{-cod})(\mu\text{-Cl})]_2$ upon the addition of 70 eq. mercury.[38,39] Overall turnover was reduced, however, reaching ~80% completion and

we suggest catalyst decomposition due to other factors. Upon passing the spent reaction mixture through a 0.2 μm filter, and addition to 500 eq. of $H_3B{\cdot}NMe_2H$ in a new reaction flask, catalysis continued with no observed induction period, as in the catalyst recycling experiment. These observations suggest homogeneous catalysis, and that the species generated during the induction period is still active, as was concluded for the closely related $[Rh(Ph_2P(CH_2)_3PPh_2)(\eta^6\text{-}C_6H_5F)][BAr^F{}_4]$ system.[22] Possible alternative explanations for the induction period are discussed in Section 4.9.

### 4.8.2 Catalysis in the presence of excess $[H_2BNMe_2]_2$

As discussed in Chapter 1, it was found that $[H_2BNMe_2]_2$ had an autocatalytic role in the dehydrocoupling of $H_3B{\cdot}NMe_2H$ by $[Rh(PCy_3)_2][BAr^F{}_4]$ by driving hydrogen loss from $\{Rh(PCy_3)_2(H)_2\}^+$ to form $\{Rh(PCy_3)_2\}^+$, which mediated a fast $Rh^I/Rh^{III}$ catalytic dehydrocoupling cycle.[19] To test whether $[H_2BNMe_2]_2$ had a similar role in catalysis with **6**, catalysis was conducted starting with $H_3B{\cdot}NMe_2H$ (0.072 M) and $[H_2BNMe_2]_2$ (0.036 M) with 0.2 mol% **6** (relative to $H_3B{\cdot}NMe_2H$) under open conditions. The consumption of $H_3B{\cdot}NMe_2H$ showed a very similar profile to that in the absence of excess $[H_2BNMe_2]_2$, implying that $[H_2BNMe_2]_2$ is innocent in this system.

### 4.8.3 Role of I in dehydrocoupling

As noted in Chapter 2, placing **6** under $H_2$ (4 atm) established an equilibrium between **6** and **7**. Therefore, whether **I** had a role in promoting $Rh^I$ formation from a $Rh^{III}$ species (*cf.* $[H_2BNMe_2]_2$, Section 4.8.2) was tested by addition of excess **I** at the start of catalysis. **I** was prepared through the hydroboration of TBE by $H_3B{\cdot}NMe_3$ by **6** (see Chapter 3), isolated and added to catalysis ($[H_3B{\cdot}NMe_2H]_0$ = 0.072 M, 0.2 mol% **6**, 1,2-$C_6H_4F_2$, open conditions, 70 eq. **I** relative to **6**). The reaction profile was very

similar to that observed in the absence of excess **I**, implying that **I** is a spectator during catalysis.

### 4.8.4 Effect of [6] upon dehydrocoupling

To probe the effect of the concentration of **6** upon catalysis, catalysis was conducted using 0.072 M $H_3B{\cdot}NMe_2H$ and varied catalyst loadings of 0.1, 0.2 and 0.4 mol% **6**. The plot at 0.2 mol% is shown in Figure 4.5 and those for 0.4 mol% and 0.1 mol% are shown in Figure 4.6a and Figure 4.6b, respectively. In the region of first order decay of [$H_3B{\cdot}NMe_2H$] (*vide infra*), a first order dependence upon [**6**] was observed. Additionally, the induction period decreased with increased catalyst loading, although the limited data density in this region precludes a detailed analysis.

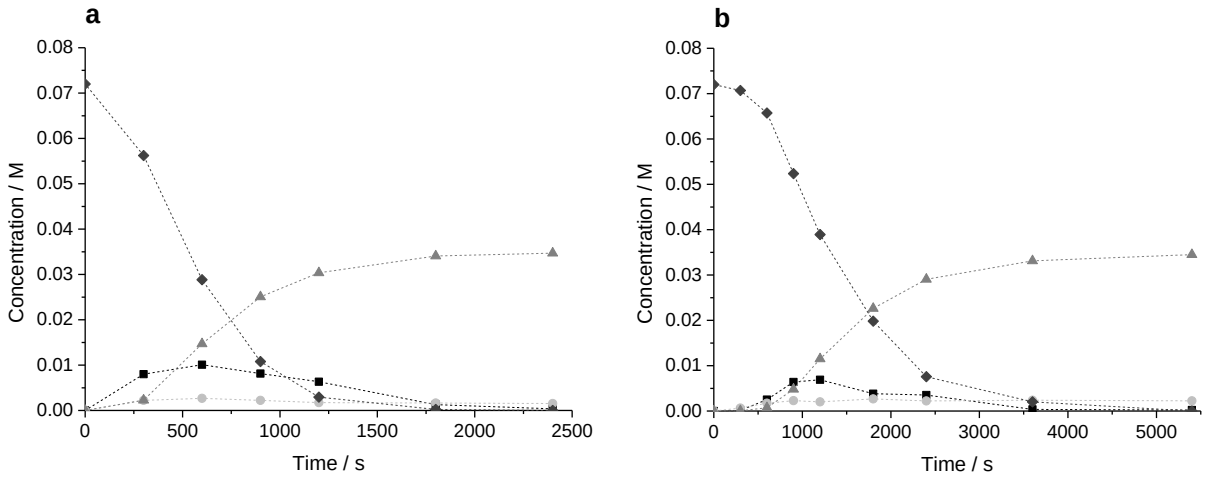



**Figure 4.6** Plots of concentration (by $^{11}B$ NMR spectroscopy) during the catalytic dehydrocoupling of $H_3B{\cdot}NMe_2H$ (0.072 M). ◆ = $H_3B{\cdot}NMe_2H$; ■ = $H_2B{=}NMe_2$; ● = $HB(NMe_2)_2$; ▲ = $[H_2BNMe_2]_2$. Open conditions. **(a)** [**6**] = 2.88 x $10^{-4}$ M (0.4 mol%). **(b)** [**6**] =0.72 x $10^{-4}$ M (0.1 mol%).

### 4.8.5 Effect of [$H_3B{\cdot}NMe_2H$] upon dehydrocoupling: saturation kinetics

The reaction profile for the dehydrocoupling of $H_3B{\cdot}NMe_2H$ (0.072 M) by **6** (0.2 mol%) in open conditions showed, following the induction period, decay of

[$H_3B{\cdot}NMe_2H$] that appeared zero order and tended towards first order at lower concentrations (Figure 4.5). To investigate this further, catalytic runs were conducted in which the starting concentrations of $H_3B{\cdot}NMe_2H$ were varied over a sixteen-fold range (0.018 M, 0.036 M, 0.072 M, 0.144 M and 0.288 M), maintaining a constant concentration of **6** ($1.44 \times 10^{-4}$ M). In the highest concentration regime (0.288 M $H_3B{\cdot}NMe_2H$), the *pseudo*-zero order decay of $H_3B{\cdot}NMe_2H$ was pronounced (Figure 4.7a). By contrast, the lowest concentration regime (0.018 M $H_3B{\cdot}NMe_2H$) showed a first order decay of [$H_3B{\cdot}NMe_2H$] post-induction period (Figure 4.7b).

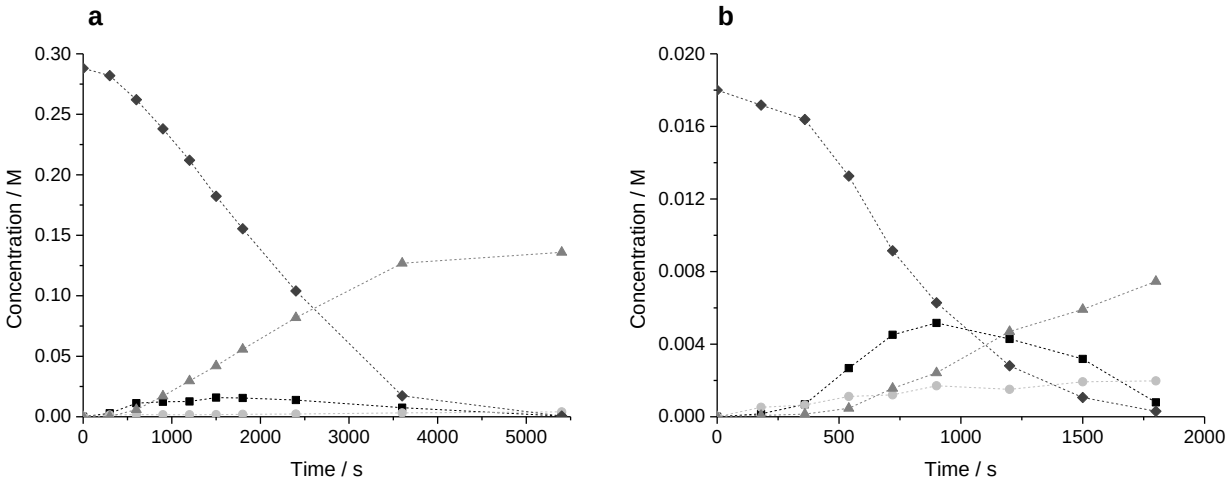



**Figure 4.7** Plots of concentration (by $^{11}B$ NMR spectroscopy) during the catalytic dehydrocoupling of $H_3B{\cdot}NMe_2H$ with [**6**] = $1.44 \times 10^{-4}$ M. ◆ = $H_3B{\cdot}NMe_2H$; ■ = $H_2B{=}NMe_2$; ● = $HB(NMe_2)_2$; ▲ = $[H_2BNMe_2]_2$. Open conditions. **(a)** $[H_3B{\cdot}NMe_2H]_0$ = 0.288 M. **(b)** $[H_3B{\cdot}NMe_2H]_0$ = 0.018 M.

The data from each run (excluding those corresponding to the induction period) were compiled and plotted as individual rates *vs* [$H_3B{\cdot}NMe_2H$] (Figure 4.8a). This plot confirms a *pseudo*-zero order regime at concentrations above ~0.1 M, in which the rate does not change with increasing [$H_3B{\cdot}NMe_2H$], and a *pseudo*-first order regime below ~0.05 M, with a linear dependence of the rate upon [$H_3B{\cdot}NMe_2H$].

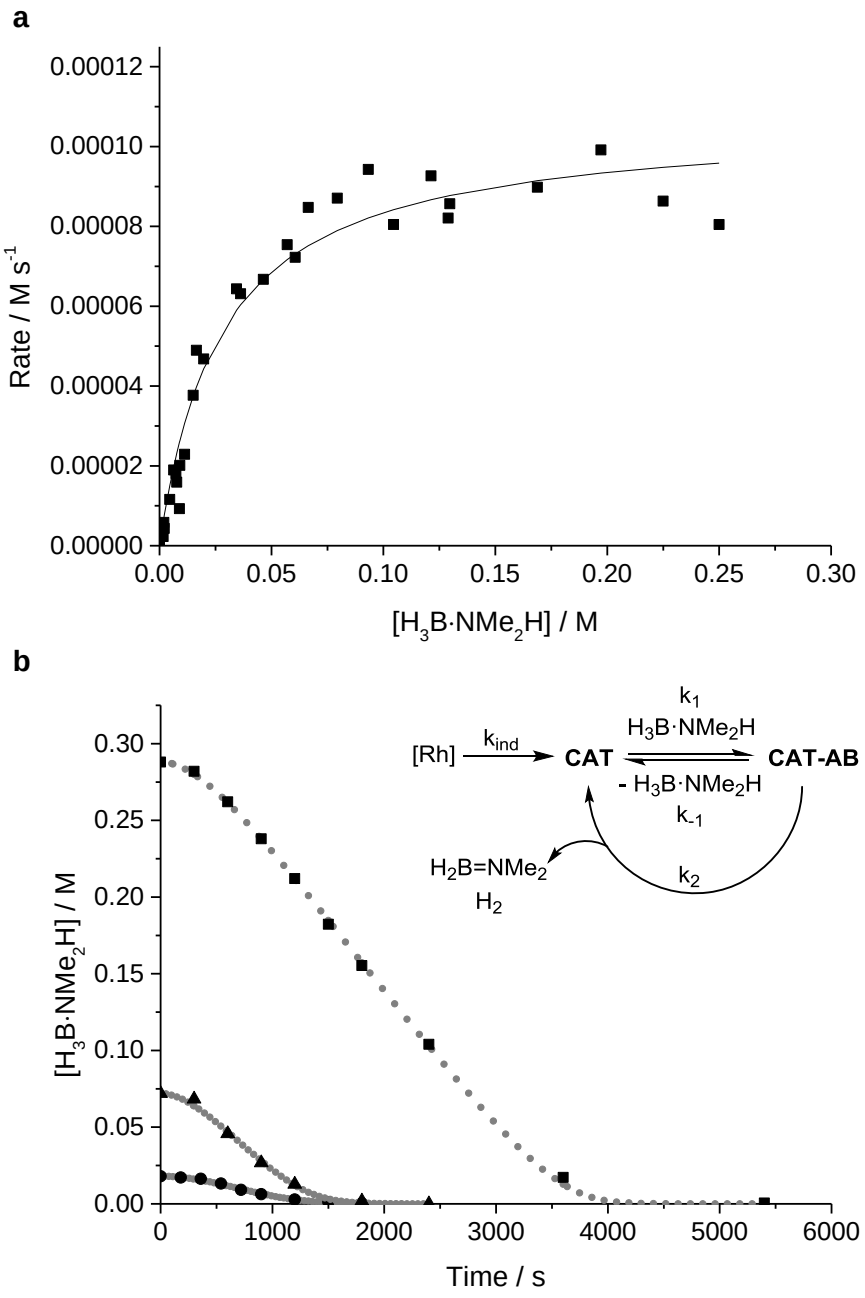



**Figure 4.8 (a)** Rate of $H_3B{\cdot}NMe_2H$ consumption *vs* $[H_3B{\cdot}NMe_2H]$. [**6**] = 1.44 x $10^{-4}$ M. Open system. The solid line is a Michaelis-Menten steady-state curve fitted by non-linear regression. $K_m$ = 0.03 M. $k_2$ = 0.74 $s^{-1}$. $k_{ind}$ varied between the runs in the range 0.8 – 2.8 x $10^{-3}$ $s^{-1}$. **(b)** Experimental concentration *vs* time data with $[H_3B{\cdot}NMe_2H]_0$ = 0.018 M (●), 0.072 M (▲) and 0.288 M (■). Dotted lines represent simulations. ($k_{-1}$ + $k_2$)/$k_1$ = $K_m$. Simulations performed by Professor Guy C. Lloyd-Jones (University of Edinburgh, UK).

Steady-state/saturation kinetics modelling was performed by Professor Guy C. Lloyd-Jones (University of Edinburgh), and the model agreed with the experimental results

(Figure 4.8). In the model, the induction period ($k_{ind}$, not further analysed) forms **CAT**. **CAT** can bind a molecule of $H_3B{\cdot}NMe_2H$ to form **CAT-AB**. We speculate that **CAT-AB** has two amine-borane (or related) moieties bound to the metal, but not necessarily in the same manner. *Bis*-amine-borane binding has been observed experimentally,[2] and calculated,[40] for a cationic rhodium system. Ligation of two amine-boranes at a single metal centre during dehydrocoupling catalysis has also been implicated computationally in the $[CpFe(CO)_2I]$,[41] $[Rh(Ph_2P(CH_2)_xPPh_2)(\eta^6\text{-}C_6H_5F)][BAr^F{}_4]$,[42] and $[Ir(PCy_3)_2(H)_2(\eta^2\text{-}H_2)_2][BAr^F{}_4]$[21] systems, and suggested by kinetic modelling upon the $[Cp_2Ti]$ system (see Chapter 1).[36] Coordination of two $H_3B{\cdot}NMe_3$ molecules to the $\{Rh(Xantphos)\}^+$ moiety were proposed in the calculated mechanism for the dehydrogenative homocoupling of $H_3B{\cdot}NMe_3$ (Chapter 2). From **CAT-AB**, the dehydrogenation step occurs, forming $H_2B{=}NMe_2$. At $[H_3B{\cdot}NMe_2H]$ above ~0.2 M, the rate-limiting step occurs after formation of **CAT-AB**, and, if present, the equilibrium between **CAT** and **CAT-AB** is strongly biased towards **CAT-AB**. Therefore, the rate is not altered with increasing $[H_3B{\cdot}NMe_2H]$, giving *pseudo*-zero order kinetics. At lower $[H_3B{\cdot}NMe_2H]$, the position of the equilibrium between **CAT** and **CAT-AB** is dependent upon $[H_3B{\cdot}NMe_2H]$, and so *pseudo*-first order kinetics are observed. Zero order decay of $[H_3B{\cdot}NH_3]$ was recently observed in the dehydrocoupling of $H_3B{\cdot}NH_3$ by an $[Fe(^iPrPOCOP^iPr)(H)(PMe_2Ph)_2]$ ($^iPrPOCOP^iPr$ = $\kappa^3{}_{P,C,P}$-1,3-$(OP^iPr_2)_2$-5-OMe-$C_6H_2$) precatalyst, thought to be due to the rate determining step being concerted N—H and B—H cleavage (aided by ligand cooperativity) from the sigma complex $[Fe(^iPrPOCOP^iPr)H(PMe_2Ph)(\eta^1\text{-}H_3B{\cdot}NH_3)]$; presumably the $H_3B{\cdot}NH_3$ binding is essentially irreversible under these conditions.[43] With Shvo's catalyst, Williams observed an induction period (corresponding to dissociation of Shvo's catalyst)

followed by zero order decay of [$H_3B{\cdot}NH_3$], attributed to the rate determining step being conversion of complex **i-49** to the dihydrogen complex **i-51** (see Chapter 1).[44]

### 4.8.6 Saturation kinetics in the dehydrocoupling of $H_3B{\cdot}NMeH_2$

Using the temporal hydrogen evolution data (Figure 4.2) for the **6**-catalysed dehydropolymerisation of $H_3B{\cdot}NMeH_2$, a plot of rate *vs* [$H_3B{\cdot}NMeH_2$] was obtained (Figure 4.9), excluding the induction period. The plot is reminiscent of saturation kinetics, similar to the $H_3B{\cdot}NMe_2H$ system, but kinetic modelling was not performed due to the limited solubility of $H_3B{\cdot}NMeH_2$ in $C_6H_5F$, which may result in artefacts in the data. Broadly, however, zero order behaviour occurs at [$H_3B{\cdot}NMeH_2$] above approximately 0.1 M, similar to the $H_3B{\cdot}NMe_2H$ system (Figure 4.8a).

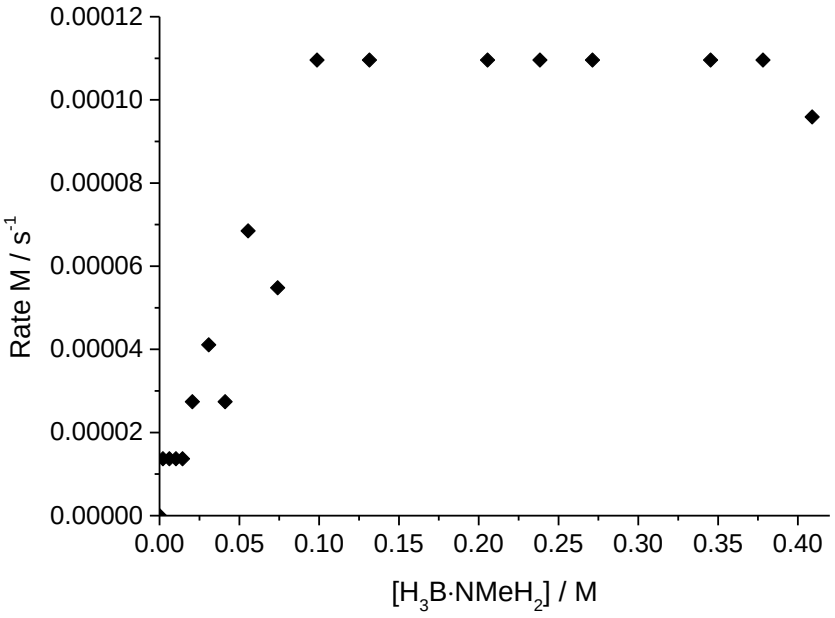



**Figure 4.9** Plot of rate *vs* [$H_3B{\cdot}NMeH_2$] as determined by $H_2$ evolution.

### 4.8.7 Kinetic isotope effects

The substrates $D_3B{\cdot}NMe_2H$, $H_3B{\cdot}NMe_2D$ and $D_3B{\cdot}NMe_2D$ were employed to deduce kinetic isotope effects (KIE = $k_H/k_D$, zero order region, $[\text{amine-borane}]_0$ = 0.072 M, 0.2

mol% **6**). Little change was observed on substituting B—H for B—D bonds (KIE = 0.9 ± 0.1). A KIE of 2.1 ± 0.2 was calculated on substituting N—H for N—D bonds. Consistent with both of these values, a KIE of 1.8 ± 0.2 was obtained using $D_3B{\cdot}NMe_2D$. These results imply that N—H bond cleavage is likely to be involved in, or in an equilibrium prior to, the rate-determining step. Large primary KIEs of 3.6 ± 0.3 and 5.3 ± 1.2 were observed for N—H/D substitution in systems for the dehydrocoupling of $H_3B{\cdot}NMe_2H$ catalysed by $[Cp_2Ti]$[36] and $Rh(PCy_3)_2(H)_2Cl$,[45] respectively, in which N—H activation was proposed to be turnover limiting. Similarly, in the dehydrocoupling of $H_3B{\cdot}NH_3$, Schneider's complex **55** (Chapter 1) showed a large KIE of 5.3 for N—H/D substitution.[24] However, Baker's Ni(NHC) system (Chapter 1) showed a similar KIE to that of **6** of 2.3 on N—H/D substitution with a KIE of 1.7 upon B—H/D substitution.[46] Various mechanistic pathways have been calculated for this system.[47-51] Hall and co-workers suggested a mechanism to account for the experimental KIEs involving, for the first equivalent of $H_2$ released, rate-limiting N—H activation by the carbene ligand.[48] For the second equivalent of $H_2$ lost, the calculated rate-limiting step was cleavage of a 3-centre-2-electron Ni—H—B interaction.[47] $[Fe(^iPrPOCOP^iPr)H(PMe_2Ph)_2]$ showed B—H/D and N—H/D KIEs of 1.7 and 2.0, respectively, consistent with postulated concerted rate-limiting B—H and N—H cleavage.[43]

The effect of N—D or B—D substitution upon the induction period in this system is discussed in Section 4.9.2.

### 4.8.8 Closed conditions

Given the significant effect of closed conditions upon $[H_2BNMeH]_n$ polymer chain length (Section 4.7), the dehydrocoupling of $H_3B{\cdot}NMe_2H$ with **6** was also explored in a

closed system. Experiments were conducted under analogous conditions but in a sealed high pressure NMR tube and monitored *in situ* by $^{11}B$ NMR spectroscopy. A typical plot of the concentration *vs* time of the boron-containing species is shown in Figure 4.10.

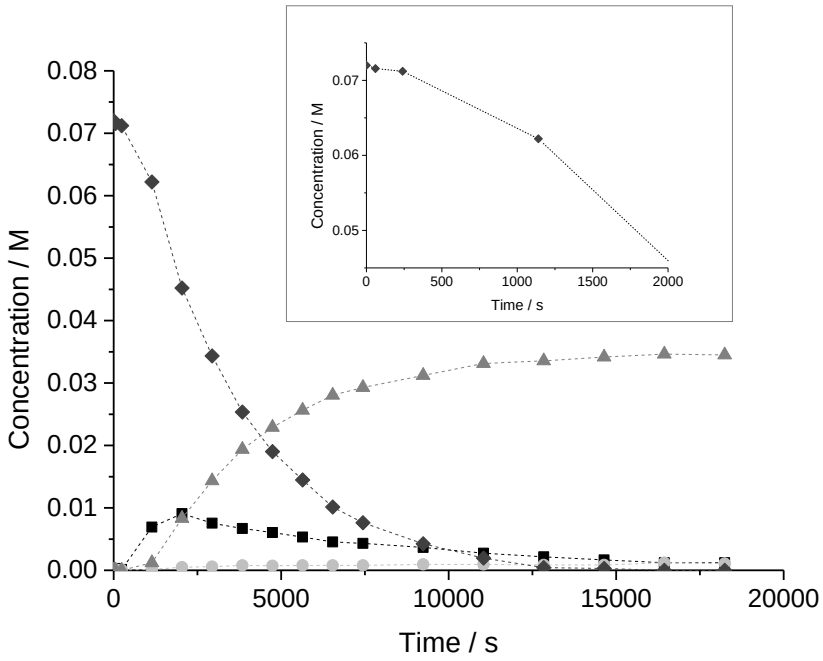



**Figure 4.10** Plot of concentration (by $^{11}B$ NMR spectroscopy) during the catalytic dehydrocoupling of $H_3B{\cdot}NMe_2H$ (initial concentration 0.072 M) with [**6**] = 1.44 x $10^{-4}$ M (0.2 mol%). Sealed conditions. ◆ = $H_3B{\cdot}NMe_2H$; ■ = $H_2B{=}NMe_2$; ● = $HB(NMe_2)_2$; ▲ = $[H_2BNMe_2]_2$. Inset shows the induction period.

As in the open conditions, $H_3B{\cdot}NMe_2H$ is dehydrocoupled to yield the cyclic dimer $[H_2BNMe_2]_2$, with $H_2B{=}NMe_2$ being the major intermediate observed. Again, less than 1% $H_3B{\cdot}NMe_2BH_2{\cdot}NMe_2H$ was observed. In the open system, up to 5% $HB(NMe_2)_2$ was observed, thought to be due to decomposition of $H_2B{=}NMe_2$ when sampling aliquots (Section 4.8.1). In the sealed system (not sampled), only ~1% $HB(NMe_2)_2$ was observed, supporting this hypothesis. A similar induction period (~500 s) is observed as in the open system (inset, Figure 4.10). However, the catalysis is

appreciably slower than in the open system, with an approximate turnover frequency of 140 $h^{-1}$ (*cf.* 1000 $h^{-1}$ in the open system). Unlike in the open system, the post-induction decay of [$H_3B{\cdot}NMe_2H$] is *pseudo*-first order across the whole concentration range. This was corroborated by a plot of ln[$H_3B{\cdot}NMe_2H$] *vs* time (Figure 4.11). From this plot, a first order rate constant, k, of (3.42 ± 0.05) x $10^{-4}$ $s^{-1}$ was determined.

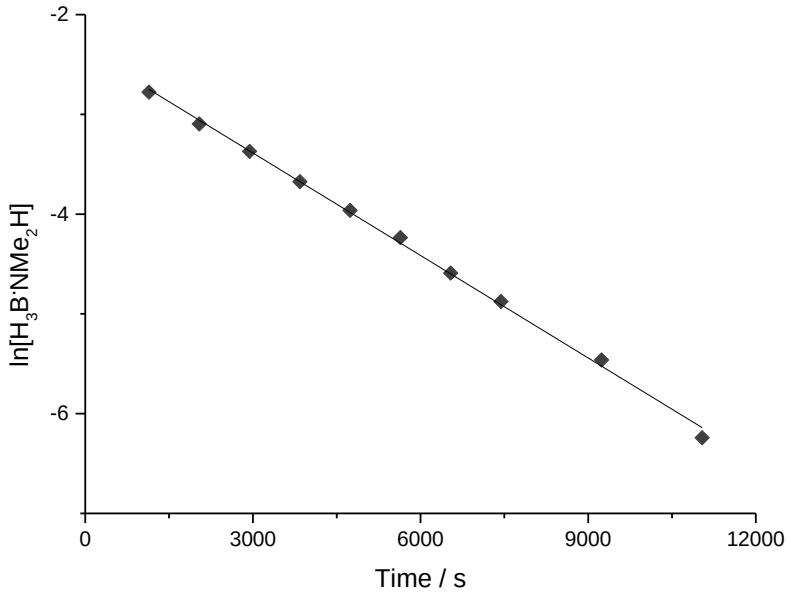



**Figure 4.11** Plot of ln[$H_3B{\cdot}NMe_2H$] *vs* time during productive catalysis. Linear fit depicted by trendline. From trendline, k = (3.42 ± 0.05) x $10^{-4}$ $s^{-1}$. $R^2$ = 0.99778.

These observations could suggest that $H_2$ reversibly binds to the active catalytic species, inhibiting turnover, or that an irreversible catalyst deactivation pathway, which follows a first order profile, occurs under $H_2$. To test this, catalysis was conducted under the usual sealed conditions but, at 1560 s (*ca.* 40% consumption of $H_3B{\cdot}NMe_2H$), the sample was frozen, degassed with two freeze-pump-thaw cycles and the headspace replaced with argon, then monitored again by *in situ* $^{11}B$ NMR spectroscopy. The plots of [$H_3B{\cdot}NMe_2H$] *vs* time (Figure 4.12a) and ln[$H_3B{\cdot}NMe_2H$] *vs* time (Figure 4.12b) indicate that *pseudo*-first order decay of [$H_3B{\cdot}NMe_2H$] is retained

upon degassing the reaction mixture, with no observed induction period. However, the rate constant after degassing is approximately twice that prior to degassing. This implies that irreversible catalyst deactivation is not occurring in this system, and a plausible reason for the inhibited rate in a sealed system may be reversible dihydrogen binding to the metal.[52] Moreover, if dihydrogen binding to **CAT** is competitive with the binding of $H_3B{\cdot}NMe_2H$ to form **CAT-AB** – as implicated in the saturation kinetics model – this would lead to a first order dependence upon $[H_3B{\cdot}NMe_2H]$. In Berke's Re-catalysed dehydrocoupling of $H_3B{\cdot}NMe_2H$, the observed resting state is a dihydrogen complex, in equilibrium with the active species that was proposed to contain a vacant site.[53] By contrast, Phillips found that flushing solvent with $H_2$ increased the rate of Ru-catalysed dehydrocoupling of $H_3B{\cdot}NMe_2H$ as $H_2$ was required to generate the proposed active catalyst.[54]

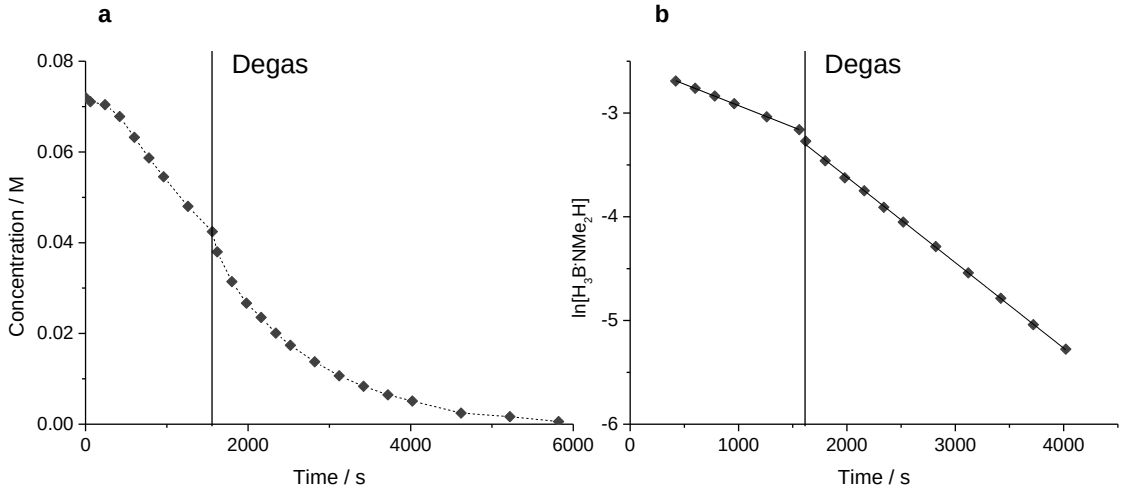


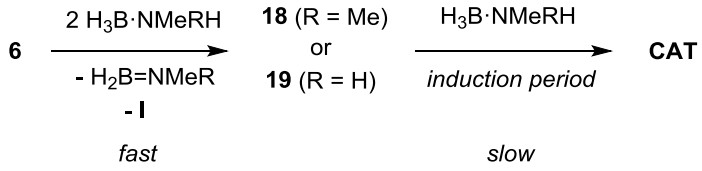

**Figure 4.12a** Plot of $[H_3B{\cdot}NMe_2H]$ *vs* time with degassing at 1560 s. **b** Plot of $\ln[H_3B{\cdot}NMe_2H]$ *vs* time with degassing at 1560 s. Before degassing, k = (4.13 ± 0.02) x $10^{-4}$ $s^{-1}$. $R^2$ = 0.99986. After degassing, k = (8.25 ± 0.06) x $10^{-4}$ $s^{-1}$. $R^2$ = 0.99951.

## 4.9 Exploring rationale for the induction period

Experiments were next conducted to attempt to explain the reason for the induction periods observed in **6**-catalysed dehydrocoupling of $H_3B{\cdot}NMe_2H$ and $H_3B{\cdot}NMeH_2$, with the aim of identifying the active species, **CAT**.

### 4.9.1 Testing complex 3 as a dehydrocoupling catalyst

It was speculated that the induction period may be due to slow formation of a $Rh^{III}$ complex, *e.g.* **18** or **19**, from initial reaction with **6**. This seemed unlikely in light of the rapid (time of mixing) formation of **18** or **19** upon addition of stoichiometric amounts of $H_3B{\cdot}NMe_2H$ or $H_3B{\cdot}NMeH_2$, respectively, to **6** (Section 4.2). Nevertheless, dehydrocoupling catalysis was undertaken using **3** (0.2 mol% **3**, formed *in situ*) as a source of $\{Rh(Xantphos)(H)_2\}^+$. With $H_3B{\cdot}NMe_2H$, a very similar reaction profile was obtained as when using **6**, including an induction period. With $H_3B{\cdot}NMeH_2$, $[H_2BNMeH]_n$ was produced similar to that obtained with **6** ($M_n$ = 24 800 g $mol^{-1}$, PDI = 1.9). Thus, although it appears likely that **6** does initially form **18** or **19** at the start of catalysis, this is not responsible for the induction period (Scheme 4.9).




**Scheme 4.9** Proposed early stages of catalysis with **6**.

That the active catalyst is not **18**/**19** is also consistent with the saturation kinetics model, in which **CAT** is proposed to require a vacant site to bind another amine-borane molecule.

### 4.9.2 Effect of using $D_3B{\cdot}NMe_2H$ and $H_3B{\cdot}NMe_2D$ upon the induction period

As well as providing information about KIEs, using $D_3B{\cdot}NMe_2H$ and $H_3B{\cdot}NMe_2D$ gave insight into the chemical transformation occurring during the induction period. With $D_3B{\cdot}NMe_2H$, the induction period was measured as being approximately the same as with $H_3B{\cdot}NMe_2H$ (Figure 4.13). With $H_3B{\cdot}NMe_2D$ and $D_3B{\cdot}NMe_2D$, however, the induction period was longer (~360 s *vs* ~600 s, respectively), although the limited data density in this region obtained with this sampling method impeded a more detailed analysis. This implies that N—H activation is likely to be involved in the rate-determining step that forms the active species **CAT**, whereas B—H activation, if occurring during formation of **CAT**, is not involved in the rate-determining step. That N—H activation is involved during the induction period may imply that **CAT** contains an amidoborane unit.

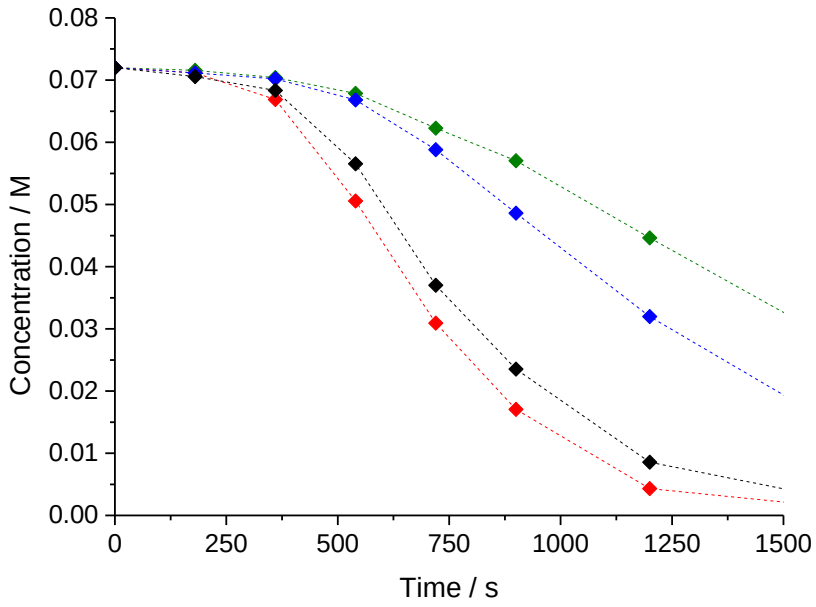
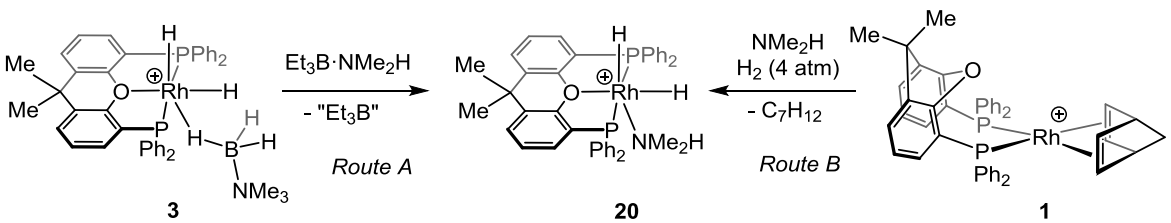



**Figure 4.13** Concentration of amine-borane *vs* time over the first 1500 s of reaction. ◆ = $H_3B{\cdot}NMe_2H$, ◆ = $D_3B{\cdot}NMe_2H$, ◆ = $H_3B{\cdot}NMe_2D$, ◆ = $D_3B{\cdot}NMe_2D$. $[amine\text{-}borane]_0$ = 0.072 M. [**6**] = 1.44 x $10^{-4}$ M. Open conditions.

### 4.9.3 Attempts to form a 'model' N—H activated complex

In an attempt to mimic the N—H activation process proposed to occur in the induction period, $Et_3B{\cdot}NMe_2H$ was reacted with **3**. $Et_3B{\cdot}NMe_2H$ has no B—H functionality, and it was speculated that this may enable the isolation of an amidoborane complex. A similar approach has recently been used by Schneider with $Et_3B{\cdot}NH_3$ that allowed the observation of small amounts (< 10%) of an Ru-amidoborane complex $[Ru(PNP^H)(H)(NH_2BH_3)(PMe_3)]$ ($PNP^H = HN(CH_2CH_2P^iPr_2)_2$) in equilibrium with the dihydride complex **i-73**.[24] Similarly, $Et_3B{\cdot}NH_3$ has been shown to react with the molybdenum complex [Mo(*para*-terphenyldiphosphine)$(H)_3$], suggesting that an amidoborane intermediate was likely in the dehydrocoupling of $H_3B{\cdot}NH_3$, although the resultant complexes were not described.[55] In Weller's $Rh(PCy_3)_2(H)_2Cl$ system, which implicated N—H activation as the rate determining step, no reaction was observed on addition of $Et_3B{\cdot}NMe_2H$ to $Rh(PCy_3)_2(H)_2Cl$, presumed due to the steric bulk of the $BEt_3$ group.[45] Addition of 5 eq. $Et_3B{\cdot}NMe_2H$ to **3** in 1,2-$C_6H_4F_2$ showed, by NMR spectroscopy, an approximately 1:1 mixture of **3** and a new species, assigned as $[Rh(\kappa^3_{P,O,P}\text{-Xantphos})(H)_2(NMe_2H)][BAr^F_4]$ (**20**), the product of B—N cleavage of $Et_3B{\cdot}NMe_2H$ (Scheme 4.10, Route A). After 90 minutes, the ratio was approximately 2:1 **20**:**3**. The fate of the resultant $BEt_3$ group was not investigated. No evidence for N—H activation was observed by NMR spectroscopy.

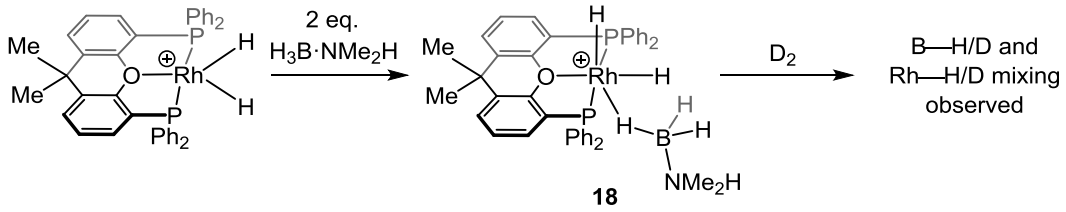



**Scheme 4.10** Formation of **20**. 1,2-$C_6H_4F_2$ solvent. $[BAr^F_4]^-$ anions not shown.

Complex **20** shows very similar NMR data to **4**. In particular, two hydride signals in the $^{1}$H NMR spectrum are observed at δ –15.71 (br dtd, $^{1}J_{RhH}$ ~28 Hz, $^{2}J_{PH}$ ~15 Hz, $J_{HH}$ unresolved) and δ –20.19 (dtd, $^{1}J_{RhH}$ = 32 Hz, $^{2}J_{PH}$ = 15 Hz, $^{2}J_{HH}$ = 10 Hz), and a doublet in the $^{31}$P{$^{1}$H} NMR spectrum at δ 44.3 ($^{1}J_{RhP}$ = 118 Hz), which together suggest *mer*-$\kappa^{3}_{P,O,P}$-Xantphos with two mutually *cis* inequivalent hydrides. **20** could also be formed quantitatively by the hydrogenation of **1** in the presence of $NMe_2H$ (2.0 M solution in THF) in 1,2-$C_6H_4F_2$, forming a complex that exhibited identical spectral data to that formed from $Et_3B{\cdot}NMe_2H$ (Scheme 4.10, Route B). **20** was further characterised by ESI-MS and elemental microanalysis. It is likely that the B—N bond cleavage occurs as $Et_3B{\cdot}NMe_2H$ is more sterically crowded than $H_3B{\cdot}NMe_2H$. No evidence for **20** as the active catalyst was observed by $^{1}$H or $^{31}$P{$^{1}$H} NMR spectroscopies in resting state experiments with $H_3B{\cdot}NMe_2H$ and 5 mol% **6** (*vide infra*).

### 4.9.4 Probing H/D exchange in 18

Since the experiment with $Et_3B{\cdot}NMe_2H$ was inconclusive in investigating N—H activation, **18** was formed *in situ* by addition of $H_3B{\cdot}NMe_2H$ (2 eq.) to [Rh($\kappa^{3}_{P,O,P}$-Xantphos)$(H)_2$][$BAr^{F}_4$][6] in $CH_2Cl_2$ and placed under an atmosphere of $D_2$ to probe the relative ease of B—H *vs* N—H activation through H/D exchange (Scheme 4.11). Under these conditions (or, alternatively, under $H_2$), **18** is stable for approximately 24 hours before decomposition is observed by NMR spectroscopy, whereas **18** was consumed after 5 hours under argon in the stoichiometric reactions described in Section 4.2.1.



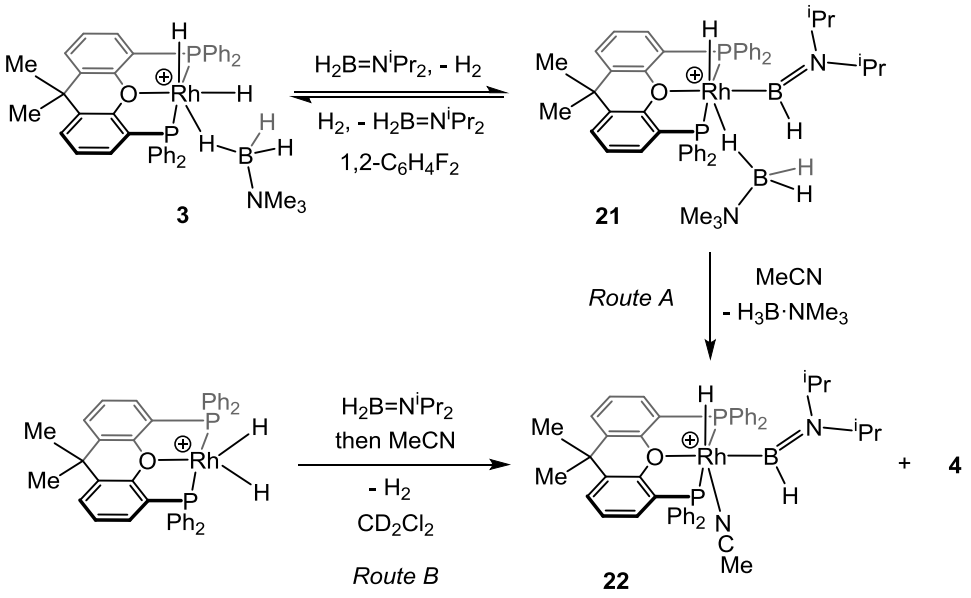

**Scheme 4.11** Formation of **18** in $CH_2Cl_2$ and placing under $D_2$. $[BAr^F{}_4]^-$ anions not shown.

As expected on the basis of experiments with **3** (Chapter 2), B—H and Rh—H activation were fast. In the $^1$H NMR spectrum after two minutes, the signals for **8** at δ –1.37 (Rh···$(H/D)_3$B group), δ –14.24 (Rh—H) and δ –19.04 (Rh—H) had relative integrals of 2.4H, 0.8H and 0.8H, respectively, showing deuterium incorporation. Consistent with this, the $^2$H NMR spectrum showed three signals consistent with the Rh···$(H/D)_3$B group and two Rh—D groups. A signal was also observed at δ 1.42 corresponding to free B—D groups from excess $(H/D)_3B{\cdot}NMe_2H$. The $^{11}$B NMR spectrum showed the excess $H_3B{\cdot}NMe_2H$, but with decreased resolution of B-H coupling, indicating deuterium incorporation into the $H_3B$ group. No evidence for N—D substitution was observed in the $^2$H NMR spectrum (δ(*$^1$H*) 3.67 for the N—H group of $H_3B{\cdot}NMe_2H$ in $CH_2Cl_2$). This indicates that N—H activation is slow compared with B—H activation in this system, as was previously concluded from a similar experiment upon the $Rh(PCy_3)_2(H)_2Cl$ system.[45] Moreover, N—H activation to form the active species **CAT** may require an excess of $H_3B{\cdot}NMe_2H$, possibly to provide stabilising B—H···H—N interactions,[20] as has been noted as a requirement for dehydrogenation in other systems.[21,31]

### 4.9.5 Aminoboryl complexes as the active catalyst

#### 4.9.5.1 *B—H activation of $H_2B{=}N^iPr_2$*

Another possibility for the identity of **CAT** was an aminoboryl complex, formed through B—H activation of an aminoborane.[10,56,57] To probe the viability of this pathway, an excess (10 eq.) of $H_2B{=}N^iPr_2$, a stable monomeric aminoborane,[8] was added to **3** in 1,2-$C_6H_4F_2$. NMR spectroscopy revealed the formation of a new complex (~80%) with the remaining 20% being **3**. The new complex was formulated as [Rh(κ$^3_{P,O,P}$-Xantphos)(H){B(H)N$^i$Pr$_2$}(η$^1$-$H_3B{\cdot}NMe_3$)][BAr$^F_4$] (**21**) (Scheme 4.12). The $^{11}$B NMR spectrum showed a broad signal at δ 49, characteristic of an aminoboryl unit,[56,57] and at δ –8, corresponding to η$^1$-bound $H_3B{\cdot}NMe_3$, as in **3**. The $^1$H NMR spectrum showed a broad hydride signal at δ –14.15, which resolved to a doublet ($^1J_{RhH}$ = 33 Hz) upon $^{31}$P decoupling. A very broad signal at δ –0.06 was also observed (FWHM = 204 Hz) that sharpened upon $^{11}$B decoupling (FWHM = 159 Hz), likely corresponding to bound $H_3B{\cdot}NMe_3$. The $^{31}$P{$^1$H} NMR spectrum showed a single environment at δ 39.6 (d, $^1J_{RhP}$ = 126 Hz). No further signals for **21** could be determined in the mixture. We suggest an equilibrium between **3** and **21**; addition of 5 eq. $H_2B{=}N^iPr_2$ to **3** resulted in a mixture of approximately equal amounts of **3** and **21**. Moreover, addition of $H_2$ (4 atm) to this mixture led to a 10:1 ratio of **3**:**21**.




**Scheme 4.12** Formation of **21**, and two routes to the formation of **22**. Route A resulted in 12% **4** formed alongside **22**. Route B resulted in 5% **4** alongside **22**. $[BAr^F{}_4]^-$ anions not shown.

Despite repeated attempts, **21** could not be isolated and readily underwent decomposition to unidentified species. However, the aminoboryl complex could be trapped by addition of MeCN to the mixture, forming [Rh($\kappa^3$P,O,P-Xantphos)(H){B(H)N$^i$Pr$_2$}(NCMe)][$BAr^F{}_4$] (**22**) (88%) and **4** (12%) (Route A, Scheme 4.12). $H_3B{\cdot}NMe_3$ was displaced from the metal centre by MeCN, evident by the disappearance of the signal at δ –0.06 in the $^1$H NMR spectrum and the sharpening of the $H_3B{\cdot}NMe_3$ signal to a quartet (δ –7.6, $^1J_{HB}$ = 96 Hz) in the $^{11}$B NMR spectrum. An alternative route to **22** was developed (Route B, Scheme 4.12) that facilitated the crystallisation of **22**. Hydrogenation of **1** in $CD_2Cl_2$ formed [Rh($\kappa^3$P,O,P-Xantphos)(H)$_2$][$BAr^F{}_4$] *in situ*,[6] and addition of $H_2B{=}N^iPr_2$ followed by MeCN resulted in ~95% **22** (~5% **4**). From this mixture, crystals of **22** were obtained by layering the solution with pentane at 5 °C, although the NMR spectra of the crystals indicated that ~10% **4** had co-crystallised. Full NMR data for **22** were obtained in spite of this, and matched those of **22** obtained *via* addition of MeCN to **21**. Similar to **21**, the $^1$H NMR

spectrum showed a single hydride signal at δ –14.44 (dt, $^{1}J_{RhH}$ = 24 Hz, $^{2}J_{PH}$ = 14 Hz) that became a doublet on $^{31}P$ decoupling, implying a single hydride disposed *cis* to two equivalent phosphorus atoms. Separate environments were observed for the two $^{i}Pr$ groups, consistent with one $^{i}Pr$ group *E* and one *Z* to the B—H group. The B—H signal was observed as a broad resonance at δ 6.75 and sharpened upon $^{11}B$ decoupling. The $^{11}B$ NMR spectrum is also consistent with the aminoboryl unit remaining intact, showing a broad signal at δ 48. The $^{31}P\{^{1}H\}$ spectrum of **22** (δ 39.6, d, $^{1}J_{RhP}$ = 125 Hz) is very similar to that of **21**.

Some crystals of **22** were suitable for single crystal X-ray diffraction. The solid state structure of **22** is shown in Figure 4.14, and is consistent with the solution NMR data. The Xantphos bite angle of 163.02(2)° and Rh—O distance of 2.2842(17) Å support *mer*-$\kappa^{3}_{P,O,P}$ geometry. The hydrides were located and indicate a single Rh—H group, and a B—H environment where the H atom does not bridge the Rh—B bond, as implied by NMR spectroscopy. The hydride and borane are *cis* disposed, consistent with the oxidative addition of $H_2B{=}N^{i}Pr_2$, and this has been observed for related HBCat systems.[58,59] The Rh—B bond length of 2.034(3) Å is consistent with a direct Rh—B bond and markedly shorter than in the sigma complexes **3** ($\eta^1$ coordination, Rh—B distance = 2.759(6) Å) and **6** ($\eta^2$ coordination, Rh—B distance = 2.162(5) Å). The Rh—B and B—N (1.378(4) Å) distances in **22** are similar to the M—B and B—N distances in Aldridge's related boryl complexes $[Rh(IMes)_2(H)\{B(H)NMe_2\}][BArF_4]$ (1.960(9) Å and 1.393(15) Å, respectively)[57] and $[Ir(PMe_3)_3(H)Cl\{B(H)NCy_2\}]$ (2.074(4) and 1.401(5) Å, respectively).[56] These M—B distances are also similar to that in the related complex $[Rh(P^{i}Pr_3)_2(H)Cl(BCat)]$ (1.9812(15) Å).[60] The B—N distance in **22** is the same within error as in the aminoborane complex

$[Rh(PCy_3)_2(H)_2(\eta^2\text{-}H_2B{=}N^iPr_2)][BAr^F{}_4]$ (1.357(13) Å); this complex has a shorter B—N bond than in the valence isoelectronic cationic Ir and neutral Ru analogues due to poor π back-donation into the B=N π* orbital from the cationic Rh centre.[61] Sabo-Etienne has commented upon the B—H activation continuum between $\eta^2$-bound aminoborane complexes and hydridoboryl complexes.[62]

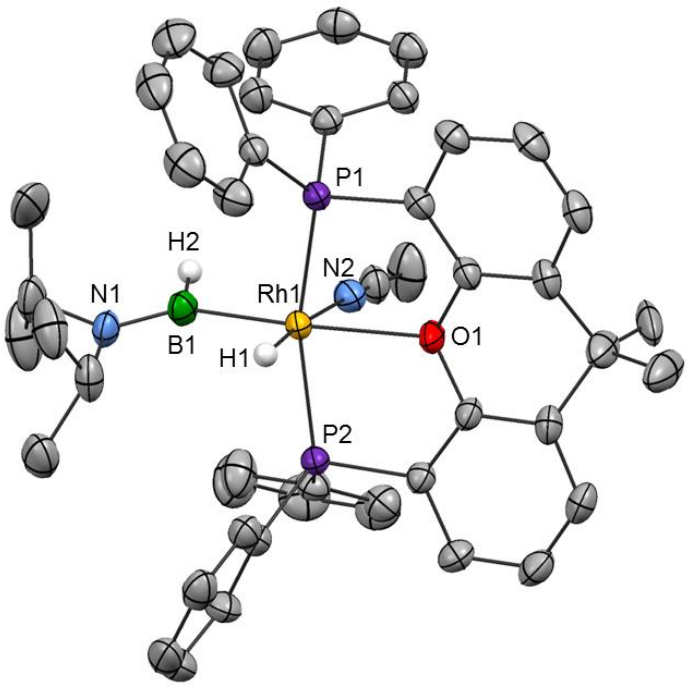
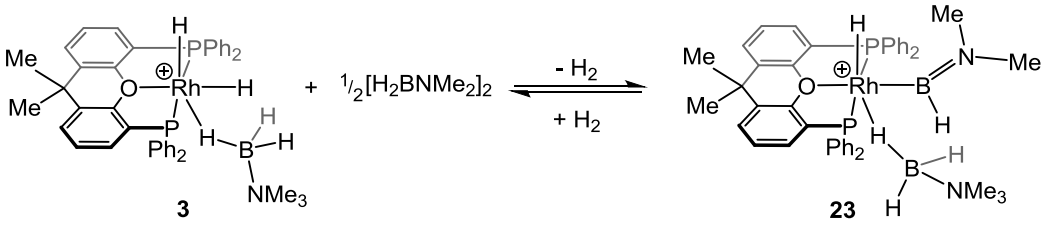



**Figure 4.14** Solid state structure of the cationic portion of **22**. Displacement ellipsoids are drawn at the 50% probability level. All carbon-bound H atoms omitted for clarity. Selected bond lengths (Å) and angles (°): Rh1–B1, 2.034(3); Rh1–P1, 2.2681(7); Rh1–P2, 2.2684(7); Rh1–O1, 2.2842(17); Rh1–N2, 2.135(2); B1–N1, 1.378(4); B1–Rh1–O, 175.53(11); B1–Rh1–P1, 96.53(10); B1–Rh1–P2, 100.17(10); N1–B1–Rh1, 133.9(2), P1–Rh1–P2, 163.02(2).

### 4.9.5.2 *B—H activation of $H_2B{=}NMe_2$*

With **21** and **22** in hand, the methodology was extended to form the analogous complex that would result from the B—H activation of $H_2B{=}NMe_2$, $[Rh(\kappa^3_{P,O,P}\text{-}Xantphos)(H)\{B(H)N^iPr_2\}(\eta^2\text{-}H_3B{\cdot}NMe_3)][BAr^F{}_4]$ (**23**), a model for an aminoboryl complex that could be plausibly formed in the induction period of $H_3B{\cdot}NMe_2H$

dehydrocoupling catalysis. $[H_2BNMe_2]_2$ was used as a source of $H_2B{=}NMe_2$. $[H_2BNMe_2]_2$ and $H_2B{=}NMe_2$ exist in equilibrium in solution and the gas phase, heavily biased towards the dimer.[63,64] However, metal fragments have been used previously to trap $H_2B{=}NMe_2$, their formation driving the retrodimerisation of $[H_2BNMe_2]_2$.[65] This strategy was employed to target **23**. A solution of **3** (as a model for **18**) was formed *in situ*, degassed to remove excess $H_2$, and 15 eq. $[H_2BNMe_2]_2$ were added. Over 2 hours, no change was evident by NMR spectroscopy, contrasting the $[Rh(PCy_3)_2(H)_2][BAr^F{}_4]$ system that formed the $Rh^I$ complex $[Rh(PCy_3)_2(\eta^2\text{-}(H_2BNMe_2)_2)][BAr^F{}_4]$ on addition of $[H_2BNMe_2]_2$ (see Chapter 1 and Section 4.8.2).[19] However, over 12 hours, evidence for a roughly 50:50 ratio of **3** and **23** was observed by NMR spectroscopy (Scheme 4.13).




**Scheme 4.13** Formation of **23**. Approximately 50:50 ratio of **3**:**23** after 12 hours. $[BAr^F{}_4]^-$ anions not shown.

The longer timescale than for the formation of **21** presumably reflects the slow dissociation of $[H_2BNMe_2]_2$. The ratio did not change appreciably over a further 12 hours, suggesting an equilibrium between **3** and **23**. **23** was characterised by analogy with **21** and **22**. The $^1H$ NMR spectrum showed a hydride signal at δ –14.22 (dt, $^1J_{RhH}$ = 33 Hz, $^2J_{PH}$ = 14 Hz), which collapsed to a doublet upon $^{31}P$ decoupling. A very broad signal at δ –0.23 corresponding to bound $H_3B{\cdot}NMe_3$ was also observed. The $^{11}B$ NMR spectrum showed broad resonances at δ 52 (boryl) and δ –8 ($H_3B{\cdot}NMe_3$), as well as the excess $[H_2BNMe_2]_2$ and small (~1%) amounts of $H_2B{=}NMe_2$, $BH(NMe_2)_2$ and an

unidentified triplet at δ 1.80 ($^1J_{BH}$ = 119 Hz). The $^{31}P\{^1H\}$ NMR spectrum was also consistent with the formation of **23**, with a doublet at δ 39.5 ($^1J_{RhP}$ = 123 Hz).

#### 4.9.5.3 *Role of **23** in dehydrocoupling catalysis*

This mixture of **3** and **23** was used in the catalytic dehydrocoupling of $H_3B{\cdot}NMe_2H$ (0.2 mol% total [Rh], 0.072 M $H_3B{\cdot}NMe_2H$, open system). The reaction profile (induction period, overall timescale) was very similar to that when using **6** (or **3**). Therefore, although aminoboryl complexes are formed by reaction of aminoboranes with **3**, and so may be present during catalysis, the formation of these complexes is not likely to be responsible for the induction period.

### 4.9.6 Induction period: conclusions

Stoichiometric and catalytic investigations into the nature of the induction period have ruled out various scenarios that may induce an induction period. The formation of **18** or **19** from **6** was shown to be fast, and the model **3** as a precatalyst also exhibited an induction period. B—H activation in **3** and **18** is also fast. Isotope labelling experiments suggest that N—H activation is rate-limiting in the formation of the catalytically active species. Attempts to trap this N—H activation with $Et_3B{\cdot}NMe_2H$ instead led to B—N bond cleavage. Deuterium exchange experiments with **18** indicated that N—H activation was slow compared with B—H activation. The fast B—H activation of aminoboranes upon the $Rh^{III}$ centre to form aminoboryl complexes – and the induction period observed upon trialling **23** as a dehydrocoupling catalyst – further support the hypothesis that N—H activation is required to form **CAT**.

## 4.10 Resting state experiments

At 0.2 mol% loading of **6**, the concentration of the precatalyst is too low to detect resting states by NMR spectroscopy. Aliquots of the catalytic reaction mixture were sampled for analysis by ESI-MS instead, but, other than signals for **18**$^+$ at *m/z* = 742.19 (calc. 742.20), no plausible molecular ions could be deciphered. Therefore, the loading of **6** was raised to 5 mol% and the evolution of the metal-containing species was monitored in a sealed NMR tube by $^1$H, $^{31}$P{$^1$H} and $^{11}$B NMR spectroscopies during catalysis. As in the 0.2 mol% systems, the major dehydrocoupling product was $[H_2BNMe_2]_2$, with intermediate $H_2B{=}NMe_2$ also observed. Initially, **18** was formed, as expected from the stoichiometric reactivity (Section 4.2). Over time, new species were observed to form, evident by the $^1$H and $^{31}$P{$^1$H} NMR spectra. The hydride region of a representative $^1$H NMR spectrum is shown in Figure 4.15. At this point in catalysis, 65% $H_3B{\cdot}NMe_2H$ had been consumed (measured by $^{11}$B NMR spectroscopy) forming mostly $[H_2BNMe_2]_2$, with $H_2B{=}NMe_2$ (4%) and $(H_2B)_2(\mu\text{-}H)NMe_2$ (1%) also observed.

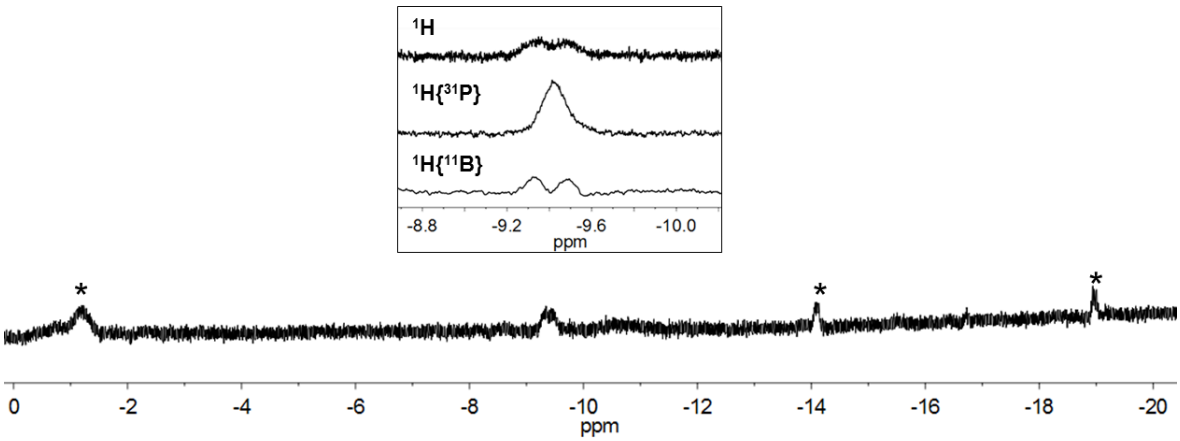



**Figure 4.15** Hydride region of the $^1$H NMR spectrum taken during dehydrocoupling catalysis of $H_3B{\cdot}NMe_2H$ with **6** in a sealed NMR tube. 65% consumption of $H_3B{\cdot}NMe_2H$ (by $^{11}$B NMR spectroscopy). * = **18**. Inset shows the $^1$H, $^1$H{$^{31}$P} and $^1$H{$^{11}$B} NMR spectra of the peak at δ –9.4.

The new species showed a broad doublet at δ –9.4 in the $^{1}$H NMR spectrum, which became a broad singlet upon $^{31}$P decoupling, and sharpened upon $^{11}$B decoupling to reveal a $J_{PH}$ coupling constant of 84 Hz. This is consistent with a B—H···Rh group *trans* to a phosphine,[66] which could arise from N—H activation to yield an amidoborane species with a B—H agostic is bound to the metal centre and may suggest a formulation for **CAT-L** as [Rh(κ$^{2}_{P,P}$-Xantphos)(H)(NMe$_2$·BH$_3$)(L)][BAr$^{F}_4$]. In these sealed conditions, it is likely that L = $H_2$, as depicted in Figure 4.16a. Clear signals for neither the suggested dihydrogen nor hydride ligands could be observed, which could suggest hydride/dihydrogen exchange,[67] although broad regions at δ –1, overlapping with signals for **18**, and δ –10.5 could also correspond to fluxional hydrides. The $^{31}$P{$^{1}$H} NMR spectrum shows two poorly resolved $^{31}$P environments at δ 23 ($^{1}J_{RhP}$ ~160 Hz) and δ 4 ($^{1}J_{RhP}$ ~120 Hz). In support of this assignment, the phosphidoborane complex [Rh(Ph$_2$P(CH$_2$)$_3$PPh$_2$)(H)(PPh$_2$·BH$_3$)(η$^{1}$-H$_3$B·PPh$_2$H)][BAr$^{F}_4$] (Figure 4.16b) was identified as an intermediate during the catalytic dehydrocoupling of H$_3$B·PPh$_2$H by [Rh(Ph$_2$P(CH$_2$)$_3$PPh$_2$)(η$^{6}$-C$_6$H$_5$F)][BAr$^{F}_4$].[66] The NMR data of the complex are similar to that for **CAT-H$_2$**, particularly the non-fluxional agostic B—H group in the phosphidoborane (δ –6.9, br d, $^{2}J_{P\mathit{trans}H}$ = 77 Hz).[66]

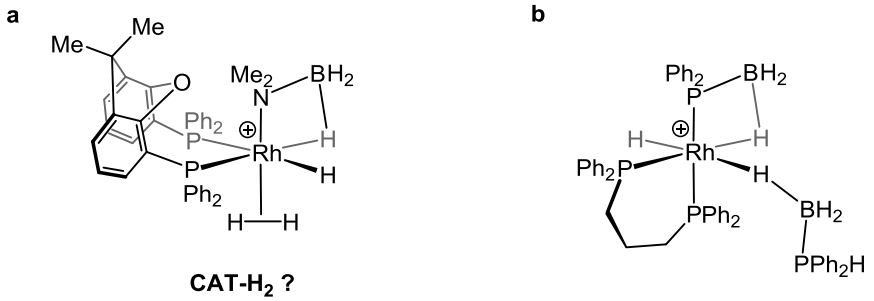



**Figure 4.16 (a)** Tentative structure for **CAT-H$_2$**. **(b)** Structure of [Rh(κ$^{2}_{P,P}$-Ph$_2$P(CH$_2$)$_3$PPh$_2$)(H)(PPh$_2$·BH$_3$)(η$^{1}$-H$_3$B·PPh$_2$H)][BAr$^{F}_4$]. [BAr$^{F}_4$]$^{-}$ anions not shown.

An alternative formulation of **CAT** to that suggested in Figure 4.16 would be a base-stabilised boryl[68] such as [Rh($\kappa^2_{P,P}$-Xantphos)(H)($BH_2$·$NMe_2H$)(L)][$BAr^F_4$]. This is unlikely owing to the rapid B—H activation observed in **18**, and the difference observed in the induction period between using $H_3B$·$NMe_2H$ and $H_3B$·$NMe_2D$, but not $D_3B$·$NMe_2H$. However, the identity of **CAT** as a dimer or a neutral complex cannot be discounted on the basis of the available data. Dimers based upon the {Rh(Xantphos)}$^+$ motif are investigated in Chapter 5.

The resting state during the dehydrocoupling of $H_3B$·$NMeH_2$ was investigated in a similar manner (5 mol% **6**, sealed NMR tube). The hydride region of the $^1$H NMR spectrum showed initial formation of **19**, the signals for which quickly disappeared with the formation of multiple very broad signals between δ −8 and −10. Broad signals were observed in the $^{31}$P{$^1$H} NMR spectrum. However this may be consistent with species containing growing polymer chains, leading to multiple environments. The $^{11}$B NMR spectrum of the mixture after two hours showed broad overlapping peaks at δ −5.0 (apparent broad triplet) and overlapping quartets at δ −18.0. These spectra resemble those of $[H_2BNMeH]_n$ produced under closed conditions (Section 4.7), and suggest that oligomers or short chain polymers are produced under these sealed conditions.

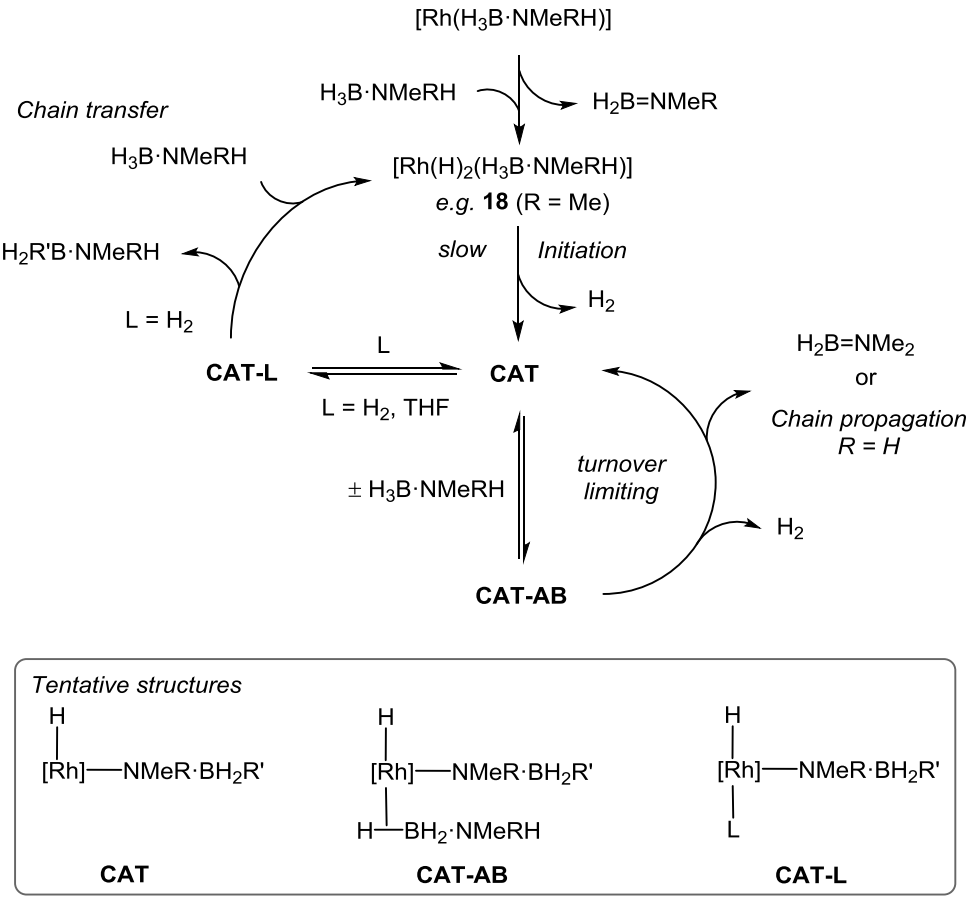
## 4.11 Proposed dehydrocoupling mechanism

The key points garnered from the stoichiometric and catalytic studies that aid with the development of a mechanism for dehydropolymerisation/dehydrocoupling using {Rh(Xantphos)}$^+$ are:

- Induction period, thought to involve N—H activation

- Catalysis appears to operate in a $Rh^{III}$ oxidation state
- Chain growth polymerisation
- Saturation kinetics operate during productive catalysis (open systems)
- $H_2$ induces a first order decay of [$H_3B{\cdot}NMe_2H$] (closed system)
- $H_2$ induces chain transfer in the dehydropolymerisation (closed system)
- THF impedes dehydropolymerisation, but results in higher molecular weight polymer
- Addition of cyclohexene results in higher molecular weight polymer, with no evidence for trapped aminoborane $Cy_2B{=}NMeH$
- Catalytic activity is retained immediately at the end of catalysis with both $H_3B{\cdot}NMe_2H$ and $H_3B{\cdot}NMeH_2$ with no apparent induction period (measured for $H_3B{\cdot}NMe_2H$)

Since $H_3B{\cdot}NMe_2H$ and $H_3B{\cdot}NMeH_2$ exhibit similar dehydrocoupling kinetic profiles, stoichiometric behaviour and inhibition under $H_2$, it is reasonable to speculate that they can be considered to operate *via* related catalytic cycles. The major differences between these cycles is that with $H_3B{\cdot}NMe_2H$, $H_2B{=}NMe_2$ is released (forming $[H_2BNMe_2]_2$), whereas $H_3B{\cdot}NMeH_2$ undergoes dehydrogenation to form $H_2B{=}NMeH$ (or a related species) that undergoes propagation to form $[H_2BNMeH]_n$ at high [$H_3B{\cdot}NMeH_2$]. The overall suggested cycle is depicted in Scheme 4.14.

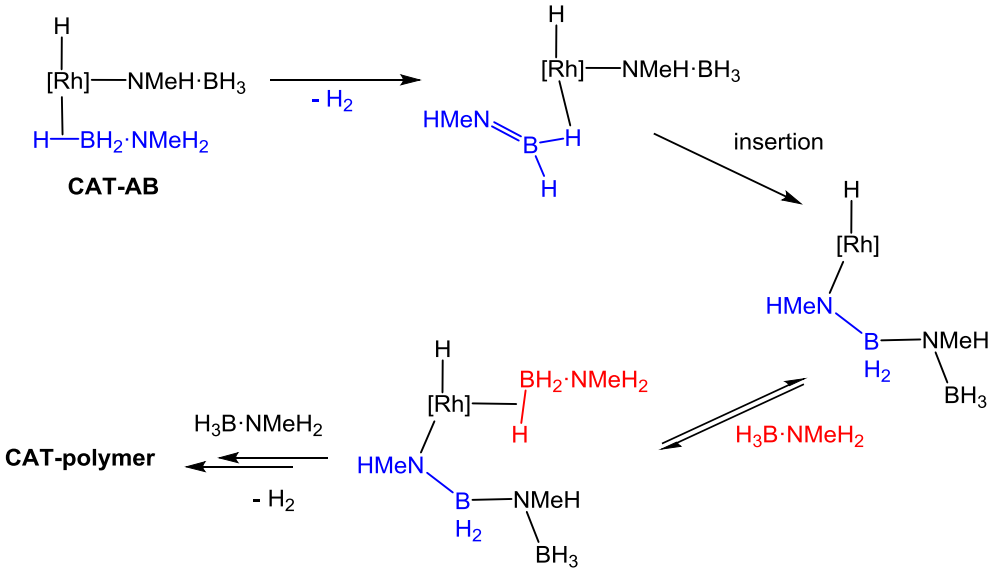



**Scheme 4.14** Overall proposed mechanism for the dehydrocoupling of $H_3B{\cdot}NMe_2H$ (R' = H, R = Me) and dehydropolymerisation of $H_3B{\cdot}NMeH_2$ (R' = H or growing polymer chain, R = H). [Rh] = {Rh(Xantphos)}$^+$.

The first step is presumed to be displacement of **I** from **6** to form the putative $[Rh(\kappa^2_{P,P}\text{-Xantphos})(\eta^2\text{-}H_3B{\cdot}NMeRH)][BAr^F{}_4]$ (R = Me or H) complexes, which rapidly form **18** or **19** with loss of $H_2B{=}NMeR$ (which undergoes dimerization or dehydrogenative trimerisation, forming $[H_2BNMe_2]_2$ or $[HBNMe]_3$, respectively), as suggested by the stoichiometric reactivity (Section 4.2). Such small amounts of $[HBNMe]_3$ produced under catalytic conditions would not be observed within the detection limit of $^{11}B$ NMR spectroscopy.

From **18** or **19**, an induction period prior to fast catalysis is observed. B—H activation of amine-boranes and aminoboranes is fast at the $Rh^{III}$ centre, but N—H activation is

slower, suggesting that N—H activation is key in the formation of the active catalytic species, **CAT**. On the basis of *in situ* NMR data, **CAT** is very tentatively assigned as an amidoborane complex, but other structures cannot be discounted. **CAT** could be formed from **18** or **19** by N—H transfer to a hydride, similar to a mechanism suggested for N—H activation of $H_3B{\cdot}NH_3$ by (PSiP)RuN($SiMe_3$)$_2$ (PSiP = (2-$Cy_2PC_6H_4$)$_2$SiMe).[69] Amidoborane complexes have been proposed in various catalytic cycles based upon Mg,[34] Ti,[36] bimetallic Zr/Ru,[70] Fe[25], Mo[55] and Rh catalysts.[45] This induction period can be thought to represent the initiation period in dehydropolymerisation. **CAT** has a vacant site, which can reversibly bind another equivalent of amine-borane to form **CAT-AB**, as implied by the experimentally observed and kinetically modelled saturation kinetics. From **CAT-AB**, a dehydrogenation step occurs, in which N—H activation is involved in, or in an equilibrium prior to, the rate determining step, as suggested by the KIE values. With $H_3B{\cdot}NMe_2H$, $H_2B{=}NMe_2$ is formed and dimerises to form $[H_2BNMe_2]_2$. It is likely that on-metal B—N coupling to form the linear diborazane $H_3B{\cdot}NMe_2BH_2{\cdot}NMe_2H$ is not occurring as only very low amounts (< 1%) of $H_3B{\cdot}NMe_2BH_2{\cdot}NMe_2H$ were observed during catalysis. This contrasts various dehydrocoupling systems in which $H_3B{\cdot}NMe_2BH_2{\cdot}NMe_2H$ is observed,[5,19,36,71] although the closely related [Rh($Ph_2P(CH_2)_3PPh_2$)($\eta^6$-$C_6H_5F$)][$BAr^F_4$] system also catalyses the dehydropolymerisation of $H_3B{\cdot}NMeH_2$ while apparently not forming $H_3B{\cdot}NMe_2BH_2{\cdot}NMe_2H$ from $H_3B{\cdot}NMe_2H$.[22] However, if B—N bond cleavage of $H_3B{\cdot}NMe_2BH_2{\cdot}NMe_2H$ is fast compared with its formation under these conditions, it would not be observed. With $H_3B{\cdot}NMeH_2$, dehydrogenative B—N insertion to form a growing polymer chain instead occurs. A proposed mechanism for this process is shown in Scheme 4.15.

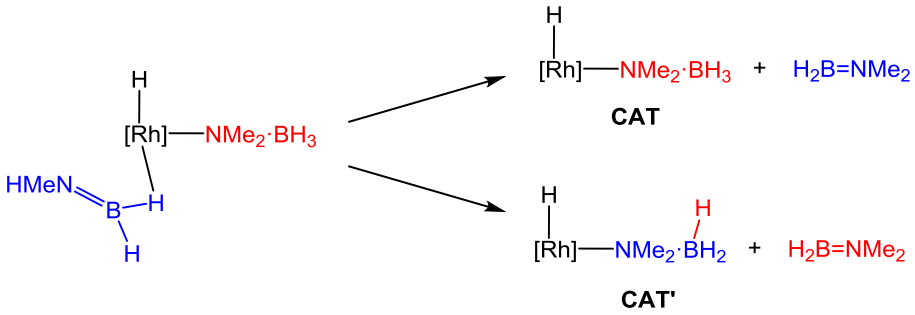



**Scheme 4.15** Proposed pathway for the B—N coupling in the dehydropolymerisation of $H_3B{\cdot}NMeH_2$ using **6**. [Rh] = $\{Rh(Xantphos)\}^+$.

The mechanism consists of on-metal dehydrogenation of the $H_3B{\cdot}NMeH_2$ to form a weakly bound aminoborane complex.[72,73] The aminoborane then inserts into the Rh—N amido bond. Hill has demonstrated the insertion of aminoboranes into M—N bonds to form $[L_nM(NR_2BH_2NR'_2)]$ (M = group II metal).[74] This mechanism fits with the chain growth observed by the polymer growth kinetics, and is not dissimilar to the chain growth mechanisms proposed for Ziegler-Natta catalysis.[26] Neither $H_2B{=}NMeH$ nor $[HBNMe]_3$ were observed by $^{11}B$ NMR spectroscopy upon sampling the dehydropolymerisation reaction mixture, and no $Cy_2B{=}NMeH$ was observed upon addition of exogenous cyclohexene, so it is unlikely that a reservoir of $H_2B{=}NMeH$ is produced prior to insertion.

It is likely that steric reasons prevent the analogous formation of oligomers based upon $H_3B{\cdot}NMe_2H$. Recently, this was demonstrated explicitly in the $\{Ir(PCy_3)_2(H)_2\}^+$ system, where B—N oligomers were formed on-metal for $H_3B{\cdot}NH_3$[21] and $H_3B{\cdot}NMeH_2$ (one oligomerisation),[31] but only the bound aminoborane was formed with

$H_3B{\cdot}NMe_2H$.[65] Two possible pathways for the release of $H_2B{=}NMe_2$ from the $\{Rh(Xantphos)\}^+$ system are shown in Scheme 4.16. These either involve direct loss of weakly bound $H_2B{=}NMe_2$, or H atom transfer enabling interchange between the amidoborane unit and free $H_2B{=}NMe_2$. These pathways cannot be distinguished with the available data. Owing to the variety of Xantphos coordination modes, the ligand geometry has not been speculated upon.[75]




**Scheme 4.16** Possible pathways for the formation of $H_2B{=}NMe_2$ from **CAT-AB** in the dehydrocoupling of $H_3B{\cdot}NMe_2H$ using **6**. [Rh] = $\{Rh(Xantphos)\}^+$. Pathways based upon B—N bond formation not shown.

The proposed general mechanism (Scheme 4.14) shows that dihydrogen acts as a chain transfer agent, *via* the formation of **CAT-H$_2$**. In a closed system, the dehydropolymerisation of $H_3B{\cdot}NMeH_2$ is significantly slower and shorter polymer chains are formed, with evidence for oligomeric material, *e.g.* $H_3B{\cdot}NMeHBH_2{\cdot}NMeH_2$, also observed. The dehydrocoupling of $H_3B{\cdot}NMe_2H$ is also significantly slower in a closed system and follows *pseudo*-first order kinetics (post-induction period). This was justified by proposing that $H_2$ can bind competitively with amine-boranes to **CAT**, slowing down propagation/dehydrogenation. As a result, under these conditions, the rate of dehydrocoupling $H_3B{\cdot}NMe_2H$ is dependent upon $[H_3B{\cdot}NMe_2H]$, resulting in the *pseudo*-first order decay. With $H_3B{\cdot}NMeH_2$, **CAT-H$_2$** provides a chain transfer pathway to eliminate the polymer with formation of a dihydride species, *e.g.* **19**, through

heterolytic cleavage of $H_2$.[76] With THF, **CAT-THF** is formed competitively with **CAT-AB** and **CAT-$H_2$**,[77] attenuating this chain transfer pathway, resulting in higher molecular weight polymer. Addition of cyclohexene to the reaction mixture formed $[H_2BNMeH]_n$ of a higher molecular weight. This could be attributed to the reduction of the $Rh^{III}$ species, *e.g.* **19**, meaning that less **CAT** is formed and so the chain length increases. Cyclohexene could also be competitive with $H_2$, inhibiting chain termination. This mechanism also accounts for the difference between the catalytic and stoichiometric pathways. Under the conditions of lower $[H_3B{\cdot}NMeH_2]$, slow B—H/N—H transfer from **19**, or β-H elimination from **CAT**, would expel $H_2B{=}NMeH$, with dehydrogenative trimerisation to form $[HBNMe]_3$. No evidence for an amidoborane complex was observed in the stoichiometric regime, suggesting that a slow dehydrogenation upon $[Rh(H)_2(Xantphos)]^+$ is more likely.

## 4.12 Conclusions and future work

This Chapter has described a thorough mechanistic investigation into the dehydrocoupling of $H_3B{\cdot}NMe_2H$ and dehydropolymerisation of $H_3B{\cdot}NMeH_2$ using **6**. Similar mechanisms appear to operate in each system, proposed to contain an amidoborane complex as the active catalyst. Although the molecular weight of the $[H_2BNMeH]_n$ obtained was lower than that for previously reported systems, this work offered mechanistic insight and a means of controlling molecular weights by addition of $H_2$ or using THF. Further work could exploit these principles; by extension, forming $[H_2BNMeH]_n$ in the presence of substrates that may inhibit the chain transfer pathway, or in a flask pre-pressurised with $H_2$, may enable the formation of longer and shorter chain polymers, respectively. An ultimate goal in the field is to develop a means of characterising and controlling the tacticity of $[H_2BNMeH]_n$, analogous to the

progression of technologically ubiquitous polyolefins, and these insights may help guide future progress in the area.

## 4.13 References


(1) Kawano, Y.; Uruichi, M.; Shimoi, M.; Taki, S.; Kawaguchi, T.; Kakizawa, T.; Ogino, H. *J. Am. Chem. Soc.* **2009**, *131*, 14946.
(2) Dallanegra, R.; Chaplin, A. B.; Weller, A. S. *Angew. Chem. Int. Ed.* **2009**, *48*, 6875.
(3) Ledger, A. E. W.; Ellul, C. E.; Mahon, M. F.; Williams, J. M. J.; Whittlesey, M. K. *Chem. Eur. J.* **2011**, *17*, 8704.
(4) Pawley, R. J.; Moxham, G. L.; Dallanegra, R.; Chaplin, A. B.; Brayshaw, S. K.; Weller, A. S.; Willis, M. C. *Organometallics* **2010**, *29*, 1717.
(5) Douglas, T. M.; Chaplin, A. B.; Weller, A. S.; Yang, X. Z.; Hall, M. B. *J. Am. Chem. Soc.* **2009**, *131*, 15440.
(6) Pawley, R. J., DPhil Thesis, University of Oxford, 2012.
(7) Metters, O. J.; Chapman, A. M.; Robertson, A. P. M.; Woodall, C. H.; Gates, P. J.; Wass, D. F.; Manners, I. *Chem. Commun.* **2014**, *50*, 12146.
(8) Jaska, C. A.; Temple, K.; Lough, A. J.; Manners, I. *J. Am. Chem. Soc.* **2003**, *125*, 9424.
(9) Alcaraz, G.; Vendier, L.; Clot, E.; Sabo-Etienne, S. *Angew. Chem. Int. Ed.* **2010**, *49*, 918.
(10) Esteruelas, M. A.; Fernández, I.; López, A. M.; Mora, M.; Oñate, E. *Organometallics* **2014**, *33*, 1104.
(11) Pons, V.; Baker, R. T.; Szymczak, N. K.; Heldebrant, D. J.; Linehan, J. C.; Matus, M. H.; Grant, D. J.; Dixon, D. A. *Chem. Commun.* **2008**, 6597.
(12) Johnson, H. C.; Weller, A. S. *J. Organomet. Chem.* **2012**, *721*, 17.
(13) Robertson, A. P. M.; Leitao, E. M.; Jurca, T.; Haddow, M. F.; Helten, H.; Lloyd-Jones, G. C.; Manners, I. *J. Am. Chem. Soc.* **2013**, *135*, 12670.
(14) Robertson, A. P. M.; Leitao, E. M.; Manners, I. *J. Am. Chem. Soc.* **2011**, *133*, 19322.
(15) *SDBSWeb : http://sdbs.db.aist.go.jp (National Institute of Advanced Industrial Science and Technology, 08/01/2015)*.
(16) Kalviri, H. A.; Gartner, F.; Ye, G.; Korobkov, I.; Baker, R. T. *Chem. Sci.* **2015**, *6*, 618.
(17) Chapman, A. M.; Haddow, M. F.; Wass, D. F. *J. Am. Chem. Soc.* **2011**, *133*, 8826.
(18) Shrestha, R. P.; Diyabalanage, H. V. K.; Semelsberger, T. A.; Ott, K. C.; Burrell, A. K. *Int. J. Hydrogen Energy* **2009**, *34*, 2616.
(19) Sewell, L. J.; Lloyd-Jones, G. C.; Weller, A. S. *J. Am. Chem. Soc.* **2012**, *134*, 3598.
(20) Chen, X.; Zhao, J.-C.; Shore, S. G. *Acc. Chem. Res.* **2013**, *46*, 2666.
(21) Kumar, A.; Johnson, H. C.; Hooper, T. N.; Weller, A. S.; Algarra, A. G.; Macgregor, S. A. *Chem. Sci.* **2014**, *5*, 2546.
(22) Dallanegra, R.; Robertson, A. P. M.; Chaplin, A. B.; Manners, I.; Weller, A. S. *Chem. Commun.* **2011**, *47*, 3763.
(23) Staubitz, A.; Soto, A. P.; Manners, I. *Angew. Chem. Int. Ed.* **2008**, *47*, 6212.
(24) Marziale, A. N.; Friedrich, A.; Klopsch, I.; Drees, M.; Celinski, V. R.; Guenne, J.; Schneider, S. *J. Am. Chem. Soc.* **2013**, *135*, 13342.
(25) Baker, R. T.; Gordon, J. C.; Hamilton, C. W.; Henson, N. J.; Lin, P. H.; Maguire, S.; Murugesu, M.; Scott, B. L.; Smythe, N. C. *J. Am. Chem. Soc.* **2012**, *134*, 5598.
(26) Hartwig, J. *Organotransition Metal Chemistry From Bonding to Catalysis*; University Science Books, 2010.
(27) Elias, H. *An Introduction to Polymer Science*; VCH Publishers, Inc., 1997.
(28) Staubitz, A.; Sloan, M. E.; Robertson, A. P. M.; Friedrich, A.; Schneider, S.; Gates, P. J.; Gunne, J.; Manners, I. *J. Am. Chem. Soc.* **2010**, *132*, 13332.
(29) Rosello-Merino, M.; Lopez-Serrano, J.; Conejero, S. *J. Am. Chem. Soc.* **2013**, *135*, 10910.
(30) Narula, C. K.; Janik, J. F.; Duesler, E. N.; Paine, R. T.; Schaeffer, R. *Inorg. Chem.* **1986**, *25*, 3346.
(31) Johnson, H. C.; Robertson, A. P. M.; Chaplin, A. B.; Sewell, L. J.; Thompson, A. L.; Haddow, M. F.; Manners, I.; Weller, A. S. *J. Am. Chem. Soc.* **2011**, *133*, 11076.
(32) Alt, H. G.; Köppl, A. *Chem. Rev.* **2000**, *100*, 1205.
(33) Paetzold, P. *Adv. Inorg. Chem.* **1987**, *31*, 123.

(34) Liptrot, D. J.; Hill, M. S.; Mahon, M. F.; MacDougall, D. J. *Chem. Eur. J.* **2010**, *16*, 8508.
(35) Cowley, H. J.; Holt, M. S.; Melen, R. L.; Rawson, J. M.; Wright, D. S. *Chem. Commun.* **2011**, *47*, 2682.
(36) Sloan, M. E.; Staubitz, A.; Clark, T. J.; Russell, C. A.; Lloyd-Jones, G. C.; Manners, I. *J. Am. Chem. Soc.* **2010**, *132*, 3831.
(37) Widegren, J. A.; Finke, R. G. *J. Mol. Catal. A: Chem.* **2003**, *198*, 317.
(38) Jaska, C. A.; Manners, I. *J. Am. Chem. Soc.* **2004**, *126*, 9776.
(39) Jaska, C. A.; Manners, I. *J. Am. Chem. Soc.* **2004**, *126*, 1334.
(40) Butera, V.; Russo, N.; Sicilia, E. *Chem. Eur. J.* **2011**, *17*, 14586.
(41) Vance, J. R.; Schafer, A.; Robertson, A. P. M.; Lee, K.; Turner, J.; Whittell, G. R.; Manners, I. *J. Am. Chem. Soc.* **2014**, *136*, 3048.
(42) Butera, V.; Russo, N.; Sicilia, E. *ACS Catal.* **2014**, *4*, 1104.
(43) Bhattacharya, P.; Krause, J. A.; Guan, H. *J. Am. Chem. Soc.* **2014**, *136*, 11153.
(44) Conley, B. L.; Williams, T. J. *Chem. Commun.* **2010**, *46*, 4815.
(45) Sewell, L. J.; Huertos, M. A.; Dickinson, M. E.; Weller, A. S.; Lloyd-Jones, G. C. *Inorg. Chem.* **2013**, *52*, 4509.
(46) Keaton, R. J.; Blacquiere, J. M.; Baker, R. T. *J. Am. Chem. Soc.* **2007**, *129*, 1844.
(47) Yang, X.; Hall, M. B. *J. Organomet. Chem.* **2009**, *694*, 2831.
(48) Yang, X.; Hall, M. B. *J. Am. Chem. Soc.* **2008**, *130*, 1798.
(49) Zimmerman, P. M.; Paul, A.; Musgrave, C. B. *Inorg. Chem.* **2009**, *48*, 5418.
(50) Zimmerman, P. M.; Paul, A.; Zhang, Z.; Musgrave, C. B. *Angew. Chem. Int. Ed.* **2009**, *48*, 2201.
(51) Ai, D.; Guo, Y.; Liu, W.; Wang, Y. *J. Phys. Org. Chem.* **2014**, *27*, 597.
(52) Jessop, P. G.; Morris, R. H. *Coord. Chem. Rev.* **1992**, *121*, 155.
(53) Jiang, Y. F.; Blacque, O.; Fox, T.; Frech, C. M.; Berke, H. *Organometallics* **2009**, *28*, 5493.
(54) Schreiber, D. F.; O'Connor, C.; Grave, C.; Ortin, Y.; Muller-Bunz, H.; Phillips, A. D. *ACS Catal.* **2012**, *2*, 2505.
(55) Buss, J. A.; Edouard, G. A.; Cheng, C.; Shi, J.; Agapie, T. *J. Am. Chem. Soc.* **2014**, *136*, 11272.
(56) O'Neill, M.; Addy, D. A.; Riddlestone, I.; Kelly, M.; Phillips, N.; Aldridge, S. *J. Am. Chem. Soc.* **2011**, *133*, 11500.
(57) Tang, C. Y.; Phillips, N.; Bates, J. I.; Thompson, A. L.; Gutmann, M. J.; Aldridge, S. *Chem. Commun.* **2012**, *48*, 8096.
(58) Knorr, J. R.; Merola, J. S. *Organometallics* **1990**, *9*, 3008.
(59) Souza, F. E. S.; Nguyen, P.; Marder, T. B.; Scott, A. J.; Clegg, W. *Inorg. Chim. Acta* **2005**, *358*, 1501.
(60) Lam, W. H.; Shimada, S.; Batsanov, A. S.; Lin, Z.; Marder, T. B.; Cowan, J. A.; Howard, J. A. K.; Mason, S. A.; McIntyre, G. J. *Organometallics* **2003**, *22*, 4557.
(61) Alcaraz, G.; Chaplin, A. B.; Stevens, C. J.; Clot, E.; Vendier, L.; Weller, A. S.; Sabo-Etienne, S. *Organometallics* **2010**, *29*, 5591.
(62) Bénac-Lestrille, G.; Helmstedt, U.; Vendier, L.; Alcaraz, G.; Clot, E.; Sabo-Etienne, S. *Inorg. Chem.* **2011**, *50*, 11039.
(63) Nöth, H.; Vahrenkamp, H. *Chem. Ber.* **1967**, *100*, 3353.
(64) Burg, A. B.; Randolph, C. L. *J. Am. Chem. Soc.* **1951**, *73*, 953.
(65) Stevens, C. J.; Dallanegra, R.; Chaplin, A. B.; Weller, A. S.; Macgregor, S. A.; Ward, B.; McKay, D.; Alcaraz, G.; Sabo-Etienne, S. *Chem. Eur. J.* **2011**, *17*, 3011.
(66) Huertos, M. A.; Weller, A. S. *Chem. Sci.* **2013**, *4*, 1881.
(67) Douglas, T. M.; Brayshaw, S. K.; Dallanegra, R.; Kociok-Köhn, G.; Macgregor, S. A.; Moxham, G. L.; Weller, A. S.; Wondimagegn, T.; Vadivelu, P. *Chem. Eur. J.* **2008**, *14*, 1004.
(68) Chaplin, A. B.; Weller, A. S. *Angew. Chem. Int. Ed.* **2010**, *49*, 581.
(69) MacInnis, M. C.; McDonald, R.; Ferguson, M. J.; Tobisch, S.; Turculet, L. *J. Am. Chem. Soc.* **2011**, *133*, 13622.
(70) Miyazaki, T.; Tanabe, Y.; Yuki, M.; Miyake, Y.; Nishibayashi, Y. *Organometallics* **2011**, *30*, 2394.
(71) Friedrich, A.; Drees, M.; Schneider, S. *Chem. Eur. J.* **2009**, *15*, 10339.
(72) Vidovic, D.; Addy, D. A.; Krämer, T.; McGrady, J.; Aldridge, S. *J. Am. Chem. Soc.* **2011**, *133*, 8494.
(73) Addy, D. A.; Bates, J. I.; Kelly, M. J.; Riddlestone, I. M.; Aldridge, S. *Organometallics* **2013**, *32*, 1583.
(74) Bellham, P.; Hill, M. S.; Kociok-Kohn, G.; Liptrot, D. J. *Chem. Commun.* **2013**, *49*, 1960.
(75) Williams, G. L.; Parks, C. M.; Smith, C. R.; Adams, H.; Haynes, A.; Meijer, A. J. H. M.; Sunley, G. J.; Gaemers, S. *Organometallics* **2011**, *30*, 6166.
(76) Kubas, G. J. *J. Organomet. Chem.* **2014**, *751*, 33.

(77) Ingleson, M. J.; Brayshaw, S. K.; Mahon, M. F.; Ruggiero, G. D.; Weller, A. S. *Inorg. Chem.* **2005**, *44*, 3162.

# 5 Synthesis and dehydrocoupling activity of P—C activated Rh Xantphos dimers

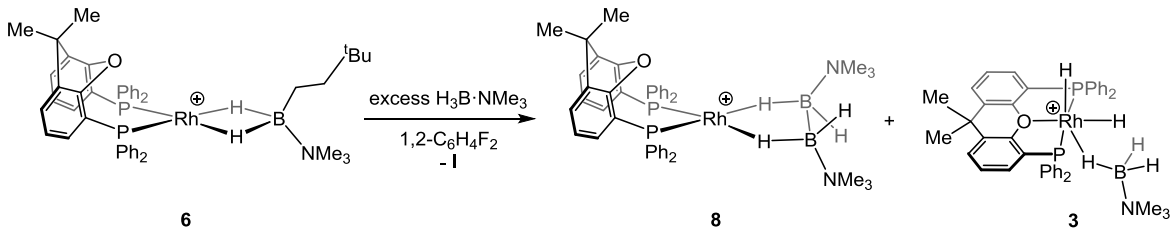
## 5.1 Introduction

This chapter presents new Rh-Xantphos-based dimers obtained through the products of dehydrogenative homocoupling (described in Chapter 2) and, separately, the dehydrocoupling of $H_3B{\cdot}NMe_2H$ with **6**. The synthesis, structure and reactivity of these new complexes – including their role in catalytic dehydrocoupling – is explored.

## 5.2 Formation of a P—C activated dimeric complex

### 5.2.1 Synthesis and characterisation

As **6** proved an active precatalyst for the dehydrocoupling of $H_3B{\cdot}NMe_2H$ and $H_3B{\cdot}NMeH_2$, it was speculated that the dehydrogenative homocoupling of $H_3B{\cdot}NMe_3$ discussed in Chapter 2 (Scheme 5.1) may proceed catalytically if the strongly bound diborane(4) could be dissociated from the metal centre in the product complex **8**.

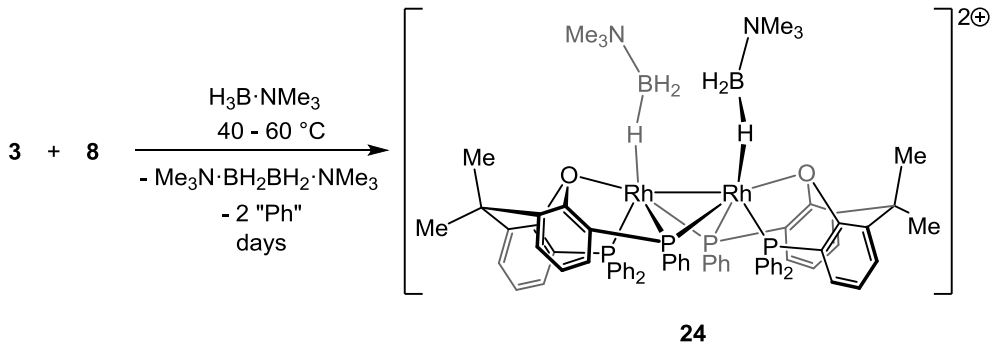



**Scheme 5.1** Formation of **8** and **3** from **6**. $[BAr^F{}_4]^-$ anions not shown.

In an attempt to drive the loss of $B_2H_4{\cdot}2NMe_3$ from **8** in the presence of excess (20 eq.) $H_3B{\cdot}NMe_3$, the 50:50 reaction mixture of **3** and **8** was heated to 40 °C in 1,2-$C_6H_4F_2$. No evidence for catalytic dehydrogenative homocoupling was observed in this mixture, but a new species (**24**) was observed to form by $^1H$ and $^{31}P\{^1H\}$ NMR

spectroscopy over several days, reaching completion after 6 days at 40 °C. Over this time, the colour of the solution changed from orange to dark red. At 60 °C, the transformation took 2 – 3 days to reach completion as measured by NMR spectroscopy.

Complex **24** was characterised by X-ray crystallography and NMR spectroscopy, which were consistent in showing it to be a dicationic dimer (Scheme 5.2). Each Xantphos ligand has undergone a P—C activation, with loss of a phenyl group, to form [4-phenylphosphido-5-diphenylphosphino-9,9-dimethylxanthene]$^{-}$; this anionic ligand shall be referred to henceforth as Xantphos*. The phosphido unit of each Xantphos* ligand bridges the two formally $Rh^{II}$ centres. Each rhodium centre engages in a sigma bond with a molecule of $H_3B{\cdot}NMe_3$.




**24**

**Scheme 5.2** Formation of **24** from a 1,2-$C_6H_4F_2$ solution of **3**, **8** and 20 eq. $H_3B{\cdot}NMe_3$. $[BAr^F{}_4]^-$ anions not shown.

The solid state structure of **24** (Figure 5.1) indicates *fac*-$\kappa^3{}_{P,O,P}$ coordination of Xantphos*, evident by the P2—Rh1—P1 bite angle of 119.72(3)° and Rh1—O1 distance of 2.288(2) Å. The Rh—Rh distance of 2.7965(5) Å is consistent with a single Rh—Rh bond with bridging phosphido groups; the distance is the same within error as the Rh—Rh distance of 2.7952(4) Å in Werner's formally $Rh^{II}$-$Rh^{II}$ dimer

[(Cp*Rh)$_2$(μ-PPh$_2$)(μ-PMe$_2$)] (**i-93**, Figure 5.2),[1] and longer than in the related complexes [Rh$_2$H(μ-PPh$_2$)$_2$(PPh$_3$)$_3$][K(2,2,2-crypt)] (2.7533(4) Å)[2] and [Rh$_2$(μ-PPh$_2$)$_2$(PEt$_3$)$_2$(1,5-cod)] (2.752 Å).[3] In **24**, there is a crystallographically imposed $C_2$ axis through the Rh—Rh bond, consistent with the equivalent environments suggested by the solution NMR data (*vide infra*).

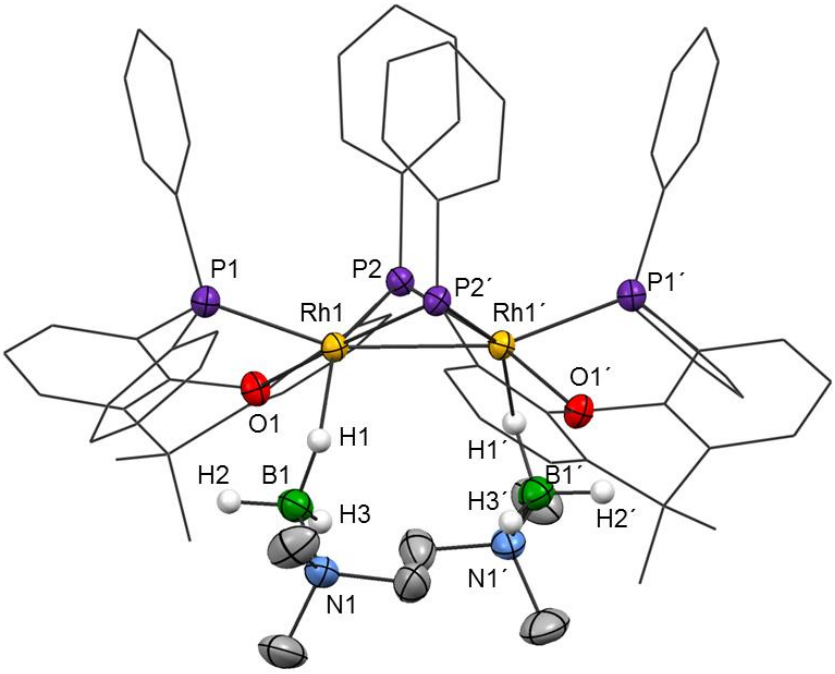
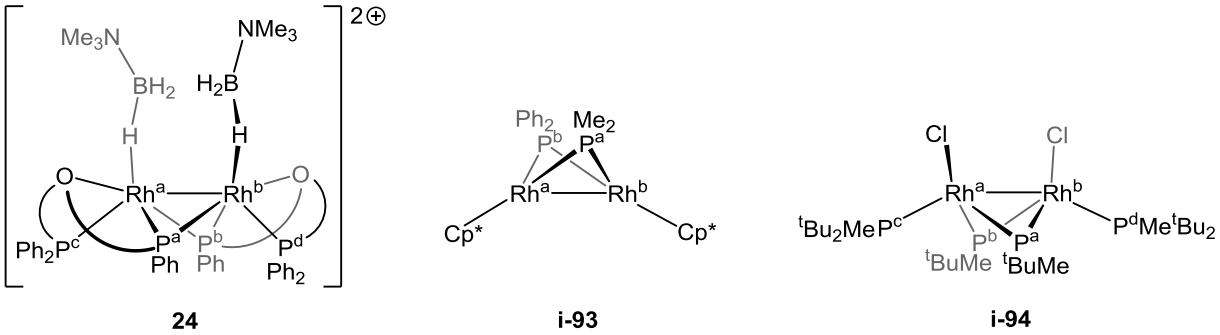



**Figure 5.1** Solid state structure of the cationic portion of **24**. Displacement ellipsoids are drawn at the 50% probability level. For clarity, all carbon-bound H atoms omitted, and the carbon atoms in the chelating ligand backbone are depicted as a wireframe. Selected bond lengths (Å) and angles (°): Rh1-Rh1´, 2.7965(5); Rh1-P2´, 2.1940(9); Rh1-P2, 2.2192(8); Rh1-P1, 2.3344(9); Rh1-O1, 2.288(2); Rh1-B1, 2.722(4); N1-B1, 1.594(5); P2-Rh1-P1, 119.72(3); Rh1-P2-Rh1´, 78.64(3); Rh1´-Rh1-P2´, 51.08(2); Rh1´-Rh1-P2, 50.28(2).

The hydrogen atoms were located upon the Fourier map and indicate $\eta^1$ binding of each H$_3$B·NMe$_3$ molecule to a Rh centre. Moreover, the Rh1—B1 distance of 2.722(4) Å is similar to the Rh—B distance of 2.759(6) Å in complex **3**.




**24** **i-93** **i-94**

**Figure 5.2** Complexes **24**, **i-93** and **i-94**. For clarity, $Ph_2P$-O-PPh = Xantphos*. $[BAr^F{}_4]^-$ anions not shown.

The $Rh_2(\mu\text{-}P)_2$ core of **24** exhibits a 'butterfly' geometry, as was observed for **i-93** and Goldman's complex $[(PMe^tBu_2)ClRh(\mu\text{-}PMe^tBu)]_2$ (**i-94**, Figure 5.2).[4] The structural parameters for each complex are summarised in Table 5.1 and show that, despite the complexes having different ligand sets and electron counts at Rh (18 for **24** and **i-93**, 16 for **i-94**), the geometries are very similar.

**Table 5.1** Comparison of selected bond lengths (Å) and angles (°) for **i-94**, **i-93** and **24**. Labelling is as shown in Figure 5.2. Table adapted from reference 4. *As calculated by Goldman and co-workers.[4]

| | **i-94** | **i-93** | **24** |
|---|---|---|---|
| **$Rh^a$-$Rh^b$** | 2.7310(7) | 2.7952(4) | 2.7965(5) |
| **$Rh^a$-$P^a$** | 2.202(2) | 2.230(1) | 2.2192(8) |
| **$Rh^a$-$P^b$** | 2.232(2) | 2.240(1) | 2.1940(9) |
| **$Rh^a$-$P^a$-$Rh^b$** | 75.98(5) | 77.81(4) | 78.64(3) |
| **$P^a$-$Rh^a$-$P^b$** | 78.40(6) | 80.01(5) | 81.95(4) |
| **$P^b$-$Rh^a$-$Rh^b$** | 51.46(4) | 51.13* | 50.28(2) |
| **$P^a$-$Rh^a$-$Rh^b$-$P^b$** | 106.6 | 111.5 | 115.9 |
| **$P^c$-$Rh^a$-$Rh^b$-$P^d$** | 12.1 | - | 16.7 |

The solution NMR data for **24** is consistent with the solid state structure. The $^{31}P\{^1H\}$ NMR spectrum in $CD_2Cl_2$ shows environments at δ 135.1 (triplet of triplets, phosphido groups) and δ 19.2 (doublet of doublet of triplets, phosphino groups)

showing second order effects. The downfield chemical shift of δ 135.1 is consistent with a phosphido ligand bridging a metal-metal bond,[5] and is similar to related complexes with phosphido group(s) bridging a Rh—Rh bond.[6,7] In the absence of a metal-metal interaction, the chemical shift is expected to be at higher field.[8,9] The $^{31}P\{^{1}H\}$ NMR spectrum of **24** was simulated using the program gNMR (Figure 5.3).[10] The small estimated $^{2}J_{PP}$ coupling constants of 10 Hz imply that the phosphine/phosphido groups are mutually *cis*. The $^{2}J_{RhP}$ and $^{1}J_{RhRh}$ values of 56 Hz and 4 Hz, respectively, are consistent with literature values.[11-13]

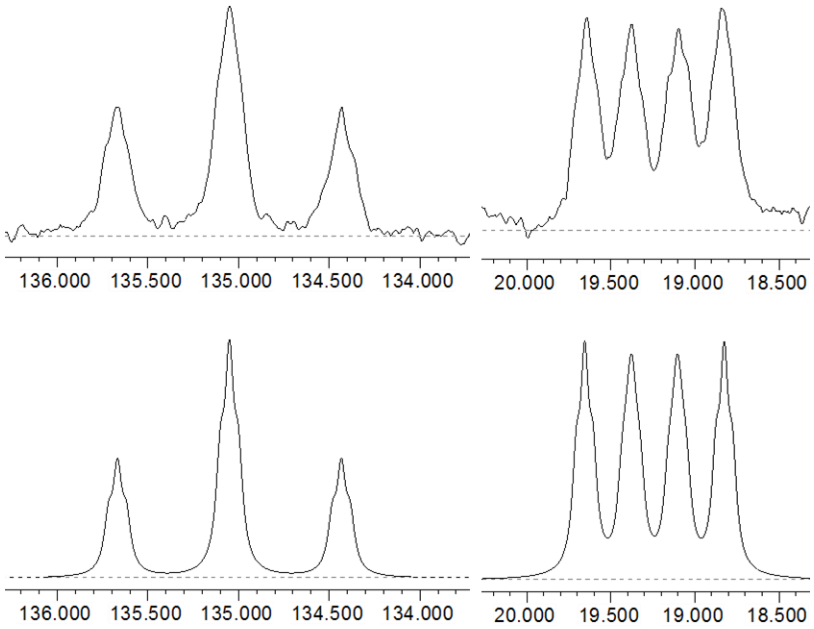



**Figure 5.3** Experimental (top) and simulated (bottom) $^{31}P\{^{1}H\}$ NMR signals for **24**. Scale is in ppm. Simulations performed using gNMR. Estimated coupling constants (Hz): $J(P_aP_c)$ = 10, $J(P_bP_c)$ = 10, $J(P_aP_d)$ = 10, $J(P_bP_d)$ = 10, $J(Rh_aP_a)$ = 125, $J(Rh_aP_b)$ = 125, $J(Rh_aP_c)$ = 112, $J(Rh_aP_d)$ = 56, $J(Rh_bP_a)$ = 125, $J(Rh_bP_b)$ = 125, $J(Rh_bP_c)$ = 56, $J(Rh_bP_d)$ = 112, $J(Rh_aRh_b)$ = 4. Labelling is as shown in Figure 5.2.

The $^{1}H$ NMR spectrum shows a broad signal, relative integral 6H, at δ –0.39 (FWHM = 92 Hz) that sharpens upon $^{11}B$ decoupling (FWHM = 30 Hz), corresponding to the two $H_3B$—Rh interactions. A signal is observed for the two $NMe_3$ groups at δ 1.66 of relative integral 18H, and two signals are observed at δ 1.96 and δ 1.48, each relative

integral 6H, corresponding to two sets of two Xantphos methyl groups, presumably those pointing towards the $H_3B{\cdot}NMe_3$ groups and those pointing away from $H_3B{\cdot}NMe_3$ (*cf.* the solid state structure). Upon cooling the $CD_2Cl_2$ solution to 200 K, no splitting of the $BH_3$ signals was observed, suggesting site exchange is rapid; by contrast, the $H_3B{\cdot}NMe_3$ fluxionality in **3** ceased (relative to the NMR timescale) upon cooling to 218 K (Chapter 2). The $^{11}B$ NMR spectrum shows a broad signal at δ –7.8, barely shifted from that of free $H_3B{\cdot}NMe_3$, consistent with $\eta^1$ binding.

### 5.2.2 Exploring the formation of 24

Bridging phosphido complexes were first synthesised by Hayter by addition of $P_2R_4$ compounds to Fe,[14] Ni,[15] Mo,[15] W[15] and Co[16] precursors, and many examples of phosphido ligands bridging Rh centres have since been reported for dimeric[1-4,6] and multimetallic structures.[17-19] No analogous complexes to **24** *via* the P—C activation of Xantphos have been reported, to our knowledge. However, the complex **i-95** (Figure 5.4) has been reported to form from a standing solution of [Pd($\kappa^3_{P,O,P}$-Xantphos)(*closo*-$SnB_{11}H_{11}$)] in DMF,[20] speculated to arise from B—H and P—C activation to eliminate benzene (observed by $^1H$ NMR spectroscopy). Interestingly, phosphido ligands bridging Pt/Pd centres have been reported to undergo reductive coupling with aryl ligands to form phosphines.[21,22]

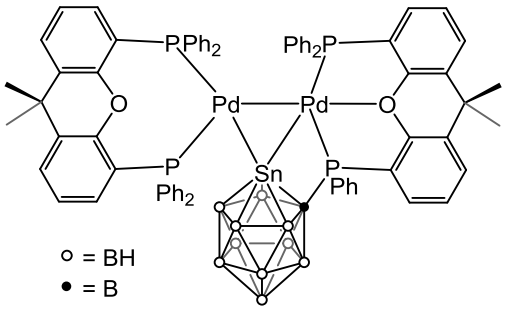
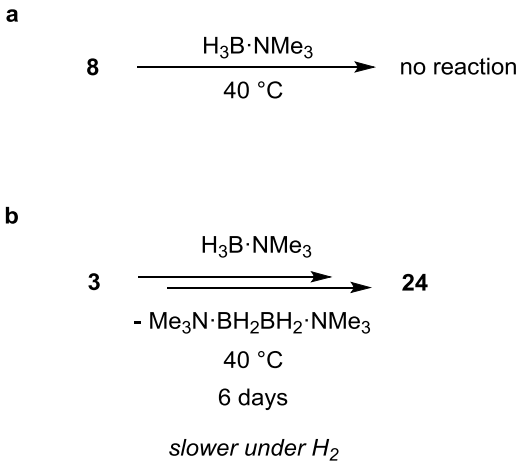



**Figure 5.4** Complex **i-95**.

During the formation of **24**, no organometallic intermediates were observed by NMR spectroscopy, and **3** and **8** were consumed at approximately similar rates. Free $Me_3N{\cdot}BH_2BH_2{\cdot}NMe_3$ was observed, assigned by comparison of the NMR data [$\delta(^{11}B)$: 3.8 (t, $^1J_{HB}$ = 123 Hz); $\delta(^1H)$: 3.75 (s, $NMe_3$), ~1.6 (br, obscured by **24** alkyl signals, $BH_2$)] with the literature values originally reported by Kodama.[23] In 1,2-$C_6H_4F_2$ solution, the fate of the lost phenyl groups could not be determined by NMR spectroscopy. However, analysis of the reaction mixture by GC-MS indicated the presence of benzene and biphenyl in a 3:1 ratio, respectively. Analysis of the blank 1,2-$C_6H_4F_2$ solvent by GC-MS indicated that neither benzene nor biphenyl were present as trace impurities.

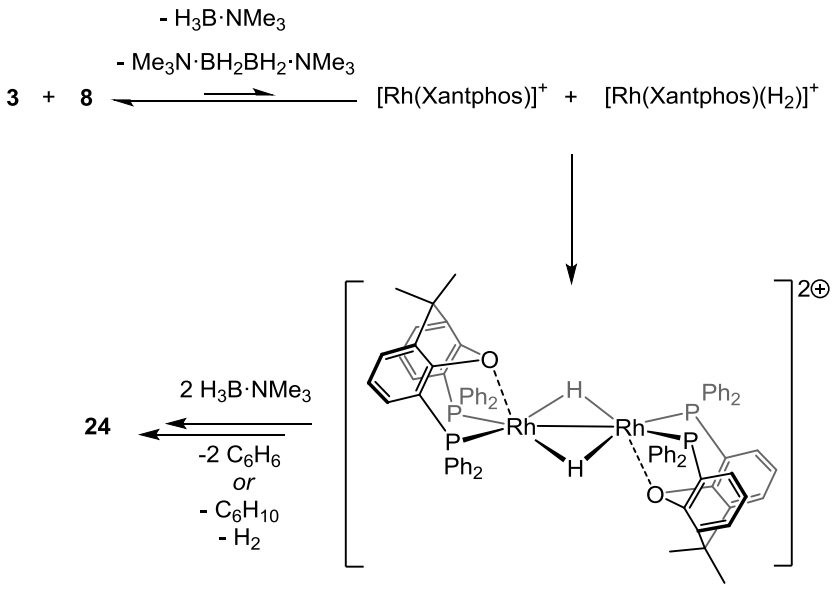
The roles of **8** and **3** in the formation of **24** were further investigated. Addition of 20 eq. of $H_3B{\cdot}NMe_3$ to pre-formed **8** in 1,2-$C_6H_4F_2$ showed no reaction (by NMR spectroscopy) upon heating to 40 °C for several days (Scheme 5.3a). By contrast, when **3** was formed in the presence of 20 eq. $H_3B{\cdot}NMe_3$, degassed to remove excess $H_2$, the headspace replaced with argon, and heated to 40 °C, **24** was formed quantitatively *in situ* (40% after 1 day, 80% after 4 days, complete within 6 days, measured by $^{31}P\{^1H\}$ NMR spectroscopy, Scheme 5.3b). Minor amounts of **8** were observed by NMR spectroscopy during the reaction, as well as signals for $Me_3N{\cdot}BH_2BH_2{\cdot}NMe_3$ that grew upon greater conversion to **24**. Overall, the amount of $Me_3N{\cdot}BH_2BH_2{\cdot}NMe_3$ produced by each route was roughly similar (measured by $^1H$ NMR spectroscopy). Conversion to **24** was markedly slower (33% in 6 days) if **3** and $H_3B{\cdot}NMe_3$ were heated under $H_2$ (4 atm).




**Scheme 5.3 (a)** Reaction of **8** with excess $H_3B{\cdot}NMe_3$ at 40 °C. **(b)** Reaction of **3** with excess $H_3B{\cdot}NMe_3$ at 40 °C.

These observations indicate that **3** is required in the formation of **24**. While **8** alone does not form **24**, **8** appears to be formed and consumed during the formation of **24** by **3**. Moreover, the reaction inhibition under $H_2$ implies that a $Rh^I$ complex is required for **24** to be formed. A possible pathway for formation of **24** is shown in Scheme 5.4. This involves the loss of the amine-boranes from **3** and **8** to form $[Rh(Xantphos)(H)_2]^+$ and $[Rh(Xantphos)]^+$ fragments. These could dimerise to form a complex with two bridging hydrides, *e.g.* $[Rh(Xantphos)(\mu\text{-}H)]_2[BAr^F{}_4]_2$. This complex was not observed, but the related complexes $[Rh(dippe)(\mu\text{-}H)]_2$[24] and $[Ir(\kappa^3{}_{P,O,P}\text{-}Xantphos)(H)(\mu\text{-}H)]_2[BAr^F{}_4]_2$[25] have been structurally characterised. From $[Rh(Xantphos)(\mu\text{-}H)]_2[BAr^F{}_4]_2$, parallel pathways could lead to **24** with either the loss of benzene (major pathway, by GC-MS), or biphenyl and $H_2$ (minor pathway, by GC-MS). Dissolved $H_2$ was not observed in the reaction mixture during formation of **24**, although this could reflect the small amounts produced and presumed low solubility in 1,2-$C_6H_4F_2$.[26] P—C activations of Xantphos to form phenyl ligands – possibly bridging the metal centres[27,28] – could be followed by reductive elimination of P—X (X

= H or Ph) to form the products observed by GC-MS. However, detailed mechanistic insight could not be gleaned from the data available.



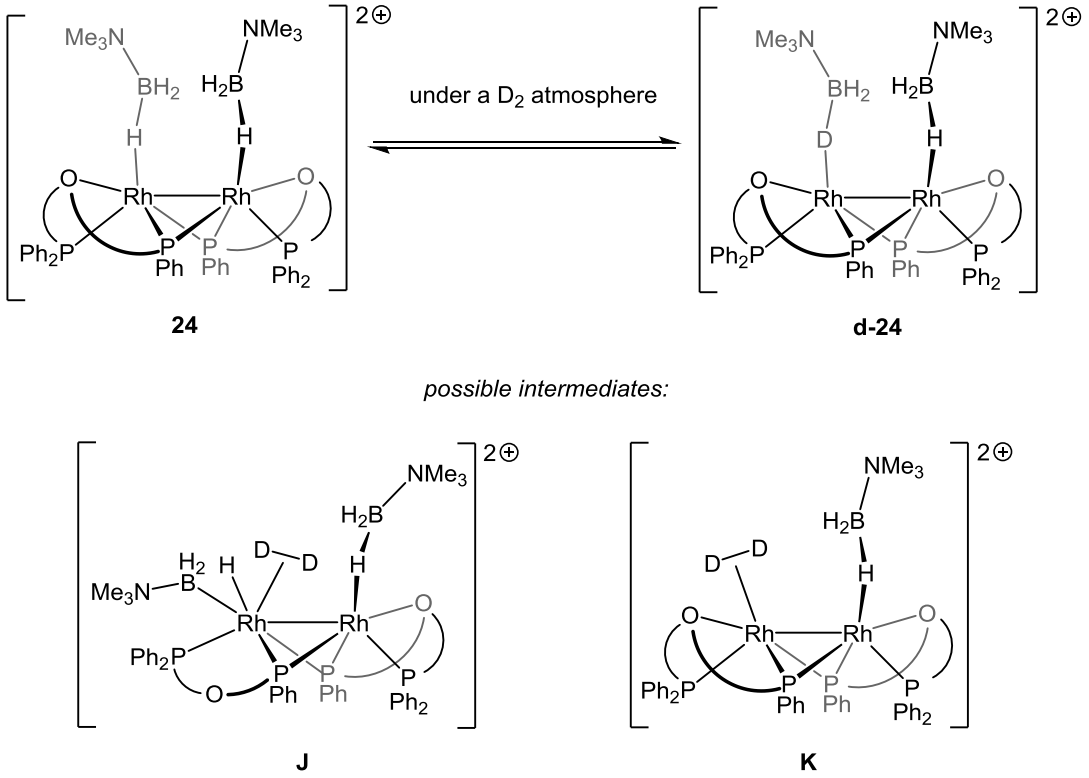

**Scheme 5.4** Possible pathway for the formation of **24** from **3** and **8**. $[BAr^F{}_4]^-$ anions not shown.

P—C activation of phosphines has been observed in a variety of systems, often upon heating the precursor complexes.[29-38] For example, the complex Cp*Ru(μ-H)$_3$IrCp* underwent P—C cleavage upon heating with $PPh_3$ to 120 °C to form Cp*Ru(μ-$PPh_2$)(μ-H)(μ-η$^1$:η$^2$-$C_6H_5$)IrCp* with loss of $H_2$, thought to occur *via* initial coordination of $PPh_3$ to Ru.[38]

### 5.2.3 Reaction of 24 with $H_2$ and $D_2$

Some metal-metal bonds with bridging phosphido groups have been reported to be cleaved under $H_2$,[39,40] although others have remained intact.[39-41] Placing **24** under $H_2$ (4 atm) in 1,2-$C_6H_4F_2$ solution resulted in no apparent change (by NMR spectroscopy) after 2 days. Under $D_2$, however, fast (minutes) mixing into the $BH_3$ group of the η$^1$

bound $H_3B{\cdot}NMe_3$ was observed by $^1H$ and $^2H$ NMR spectroscopy (Scheme 5.5). HD was observed also in the $^1H$ and $^2H$ NMR spectra.




**Scheme 5.5** Mixing of $D_2$ into the Rh···$H_3B$ groups of **24** and two possible intermediates. $Ph_2P$-O-PPh = Xantphos*. Not all H/D combinations shown. $[BAr^F{}_4]^-$ anions not shown.

The $^1H$ NMR spectra of the Rh···$(H/D)_3B$ region after 2 and 20 minutes under $D_2$ are shown in Figure 5.5. Increasing incorporation of $D_2$ leads to a more upfield chemical shift of the Rh···$(H/D)_3B$ resonances in the $^1H$ NMR spectrum. This is due to isotopic perturbation of equilibrium;[42] there is a preference for the heavier D atoms to be in the terminal B—D positions rather than the bridging Rh—D—B positions, leading to more upfield shifts in the $^1H$ NMR spectrum upon greater D incorporation (for **24**, both $\Delta\delta$ = 0.2 ppm). Similar effects have been noted upon placing the complexes $[M(PCy_3)_2(H)_2(\eta^2\text{-}H_3B{\cdot}NMe_3)][BAr^F{}_4]$ (M = Ir, Rh) under $D_2$;[43] when M = Ir, $\Delta\delta$ = 0.4

and 0.5 ppm, and this larger change in shift likely reflects a stronger Ir···$(H/D)_3B$ interaction than in **24**.

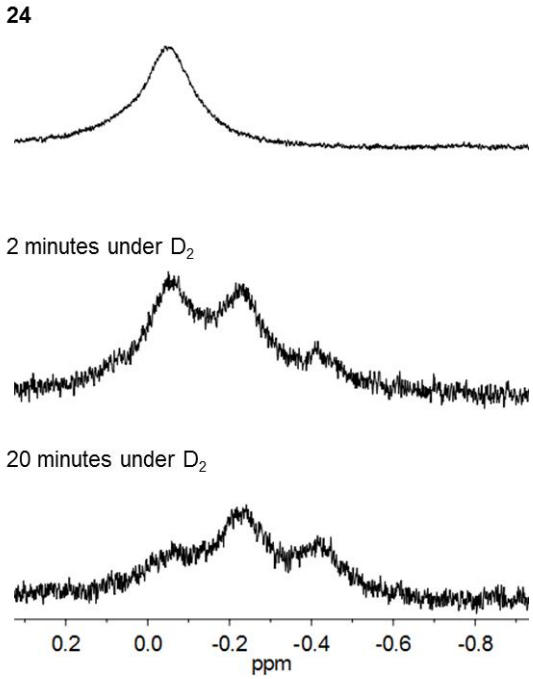



**Figure 5.5** The Rh···$(H/D)_3B$ region of the $^1H$ NMR spectrum of **24** (upper) and after 2 (middle) and 20 (lower) minutes under an atmosphere of $D_2$ in 1,2-$C_6H_4F_2$.

Possible intermediates for the exchange are shown in Scheme 5.5. For example, B—H activation of $H_3B{\cdot}NMe_3$ and coordination of $D_2$ could form the base-stabilised boryl compound **J**. To form **J**, the hemilabile oxygen atom is displaced from the metal centre (a $\kappa^2_{P,P}$-Xantphos* complex is discussed in Section 5.3) to retain an 18 electron configuration. A rearrangement could form a HD complex, from which HD is lost and **d-24** is formed. We suggest a σ-CAM[44] type process, as was calculated for B—H/M—H exchange in $[M(PCy_3)_2(H)_2(\eta^2\text{-}H_3B{\cdot}NMe_2R)][BAr^F_4]$ systems (M = Ir, R = Me, H; M = Rh, R = Me).[43,45] Although the formation of **J** invokes displacement of the hemilabile oxygen atoms in Xantphos*, these are not displaced by addition of excess MeCN or dpp2 to **24** (*vide infra*), possibly due to sterics. Alternatively, therefore, $D_2$ could displace one of the $H_3B{\cdot}NMe_3$ ligands in **24**, forming **K**, in which the oxygen

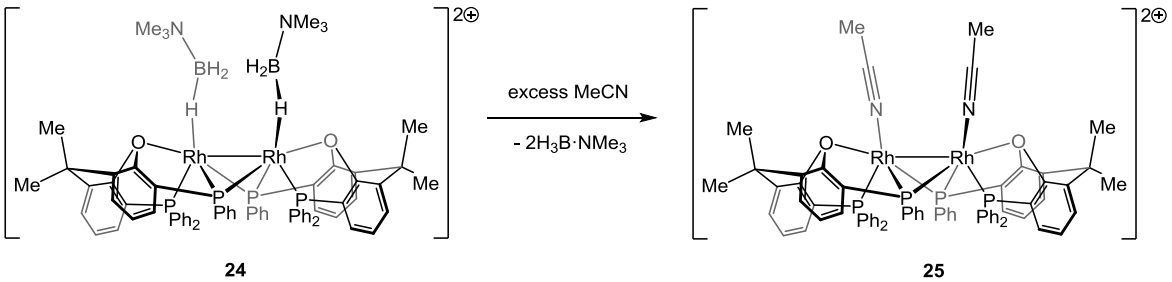
atom remains coordinated to the metal centre. B—H activation of the other, coordinated, $H_3B{\cdot}NMe_3$ and a bimetallic σ-CAM-type pathway forms an HD complex, which then forms **d-24** upon re-coordination of $H_3B{\cdot}NMe_3$ by displacing HD. No evidence for intermediates, *e.g.* **J** or **K**, was observed by NMR spectroscopy.

### 5.2.4 Reactivity of 24 with electrophiles

Bridging phosphido complexes have been reported to act as nucleophiles.[46-48] To explore its nucleophilicity, **24** was reacted with MeI, HCl and PhBr. Reactions with MeI or HCl (2.0 M in $Et_2O$) led to mixtures from which the products could not be determined by NMR spectroscopy or ESI-MS. PhBr lead to no reaction at room temperature, although decomposition occurred upon heating at 40 °C for 24 hours. Thus, although **24** does react with these substrates, the products could not be characterised.

### 5.2.5 Addition of MeCN to 24

Addition of MeCN to **24** resulted in the fast (< 2 minutes) displacement of $H_3B{\cdot}NMe_3$ to form the dimer $[Rh_2(\mu\text{-Xantphos*})_2(NCMe)_2][BAr^F{}_4]_2$ (**25**), quantitatively by NMR spectroscopy (Scheme 5.6).

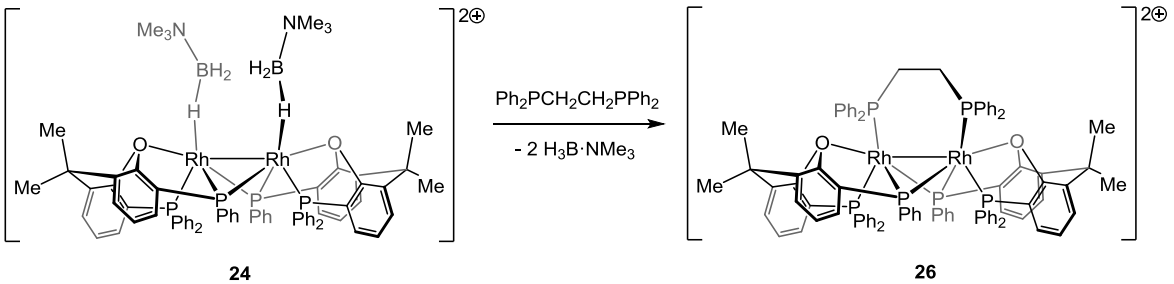



**Scheme 5.6** Formation of **25** from **24**. 1,2-$C_6H_4F_2$ or $CD_2Cl_2$ solvent. $[BAr^F{}_4]^-$ anions not shown.

Attempts to isolate **25** resulted only in an orange 'oily solid', from which no solid state structure could be obtained. However, NMR spectroscopy of the material in $CD_2Cl_2$ solution indicated clean formation of **25**. The $^{31}P\{^1H\}$ NMR spectrum was very similar to that of **24**, with 1:1 signals at δ 130.2 (tt) and δ 20.7 (ddt) (see Chapter 7). The $^1H$ NMR spectrum showed, as with **24**, two environments for the Xantphos* methyl groups at δ 1.93 and δ 1.45, each relative integral 6H, and one signal at δ 1.06 of relative integral 6H, corresponding to two molecules of MeCN bound, a similar chemical shift to that of coordinated MeCN in **4**.[49] ESI-MS showed molecular ions consistent with $[Rh_2(Xantphos^*)_2]^{2+}$ (major), $[Rh_2(Xantphos^*)_2(NCMe)]^{2+}$ and $[Rh_2(Xantphos^*)_2(NCMe)_2]^{2+}$ (minor), indicating loss of MeCN in the high vacuum conditions.

### 5.2.6 Addition of $Ph_2PCH_2CH_2PPh_2$ to 24

Addition of 1 or 2 eq. of $Ph_2PCH_2CH_2PPh_2$ (dpp2) to **24** in 1,2-$C_6H_4F_2$ formed $[Rh_2(\mu\text{-}Xantphos^*)_2(Ph_2PCH_2CH_2PPh_2)][BAr^F{}_4]_2$ (**26**) rapidly (< 2 minutes) with concomitant displacement of $H_3B{\cdot}NMe_3$ (Scheme 5.7), measured by NMR spectroscopy.




**Scheme 5.7** Formation of **26** from **24** in 1,2-$C_6H_4F_2$. $[BAr^F{}_4]^-$ anions not shown.

Layering the reaction mixture with pentane at 5 °C formed red crystals of **26** suitable for single crystal X-ray diffraction. The solid-state structure (Figure 5.6) indicates that

the $Rh_2$ unit remained intact upon addition of dpp2, and that dpp2 bridges the two metal centres.

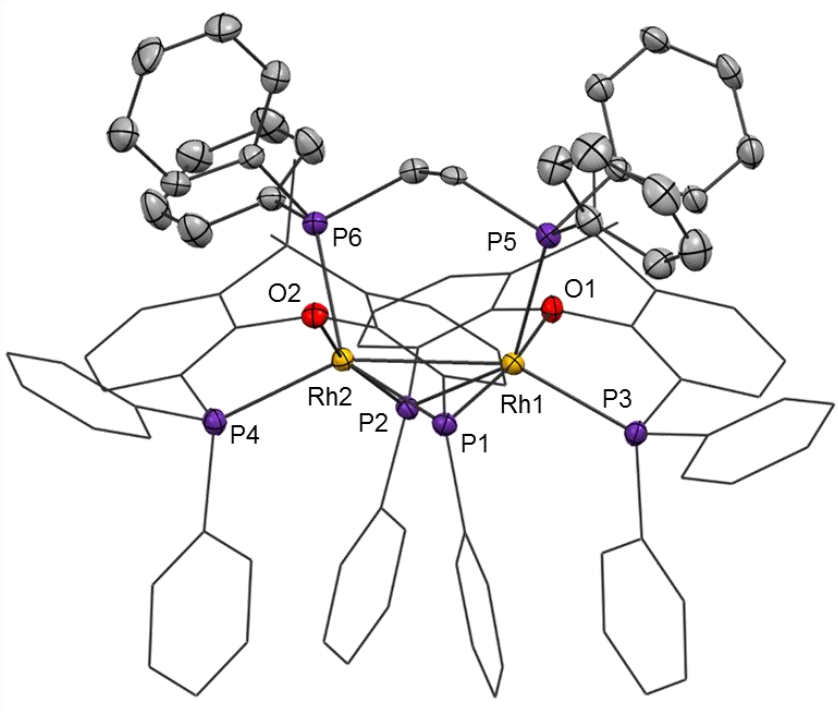



**Figure 5.6** Solid state structure of the cationic portion of **26**. Displacement ellipsoids are drawn at the 50% probability level. For clarity, H atoms are omitted, and the carbon atoms in Xantphos* ligands are depicted as a wireframe. Selected bond lengths (Å) and angles (°): Rh1-Rh2, 2.8362(5); Rh1-P1, 2.2134(12); Rh1-P2, 2.2464(12); Rh1-P3, 2.3360(12); Rh1-P5, 2.4352(12); Rh1-O1, 2.309(3); Rh2-P1, 2.2571(12); Rh2-P2, 2.2194(12); Rh2-P4, 2.3565(12); Rh2-P6, 2.4165(12); Rh2-O2, 2.285(3); P2-Rh1-P3, 114.58(4); P1-Rh2-P4, 111.92(4); P6-Rh2-P4, 106.74(4); P6-Rh2-P1, 137.67(4); P6-Rh2-P2, 97.28(4); P5-Rh1-P3, 106.67(4); P5-Rh1-P1, 99.56(4); P5-Rh1-P2, 135.08(4).

The Rh—Rh distance of 2.8362(5) Å is longer than that in **24** (2.7965(5) Å), possibly due to the steric demands of the dpp2 ligand. The Xantphos* ligands coordinate to Rh with a *fac*-$\kappa^3_{P,O,P}$ geometry, evident by the bite angles around Rh2 and Rh1 of 111.92(4)° and 114.58(4)°, respectively, and the Rh2—O2 and Rh1—O1 distances of 2.285(3) Å and 2.309(3) Å, respectively. The $Rh_2P_2$ 'butterfly' core shows similar structural parameters to **24**, with a P1-Rh2-Rh1-P2 torsion of 117.9° (*cf.* 115.9° in **24**). However, the P4-Rh2-Rh1-P3 dihedral angle of 1.7° is narrower in **26** than that

in **24** and the related **i-94**[4] (16.7° and 12.1°, respectively), possibly due to the bulky dpp2 ligand constraining the angle.

The solution NMR data for **26** is also consistent with the solid structure. The $^{1}$H NMR spectrum of **26** in $CD_2Cl_2$ solution shows two singlets at δ 1.73 and δ 0.70, each relative integral 6H, representing the Xantphos methyl groups. The upfield shift of δ 0.70 (*cf.* δ 1.45 in **25** and δ 1.48 in **24**) may arise from through-space shielding from the aromatic ring current of the neighbouring dpp2 ligand. In the solid state, a methyl C—H group sits 2.802 Å over the centroid of a dpp2 phenyl ring, and, if the structure is retained in solution, this is consistent with the slight upfield shift.[50,51] The protons on the dpp2 backbone are observed as two multiplets (each relative integral 2H) that sharpen to doublets ($^{2}J_{HH}$ = 12 Hz) upon $^{31}$P decoupling. The $^{31}$P{$^{1}$H} NMR spectrum consists of three relative integral 1:1:1 environments at δ 134.1, δ 19.2 and δ 3.9. Each shows complicated second order coupling patterns and, unfortunately, we were unable to simulate this satisfactorily. A $^{1}$H-$^{31}$P HMBC experiment showed a correlation between the $^{31}$P signal at δ 3.9 and the dpp2 chain protons, showing that this signal corresponds to the dpp2 ligand (P5 and P6). On the basis of the chemical shift, the signal at δ 134.1 was assigned to the bridging phosphido groups (P1 and P2), and the signal at δ 19.2 was assigned to P3 and P4. A $^{31}$P-$^{31}$P COSY experiment indicated the strongest coupling between P5/P6 and P1/P2, with weaker coupling between P5/P6 and P3/P4, and P3/4 and P1/P2 (Figure 5.7). ESI-MS was also consistent with the formation of **26**, with a molecular ion shown at *m/z* = 803.63 (calc. 803.63) with the correct isotopic pattern.

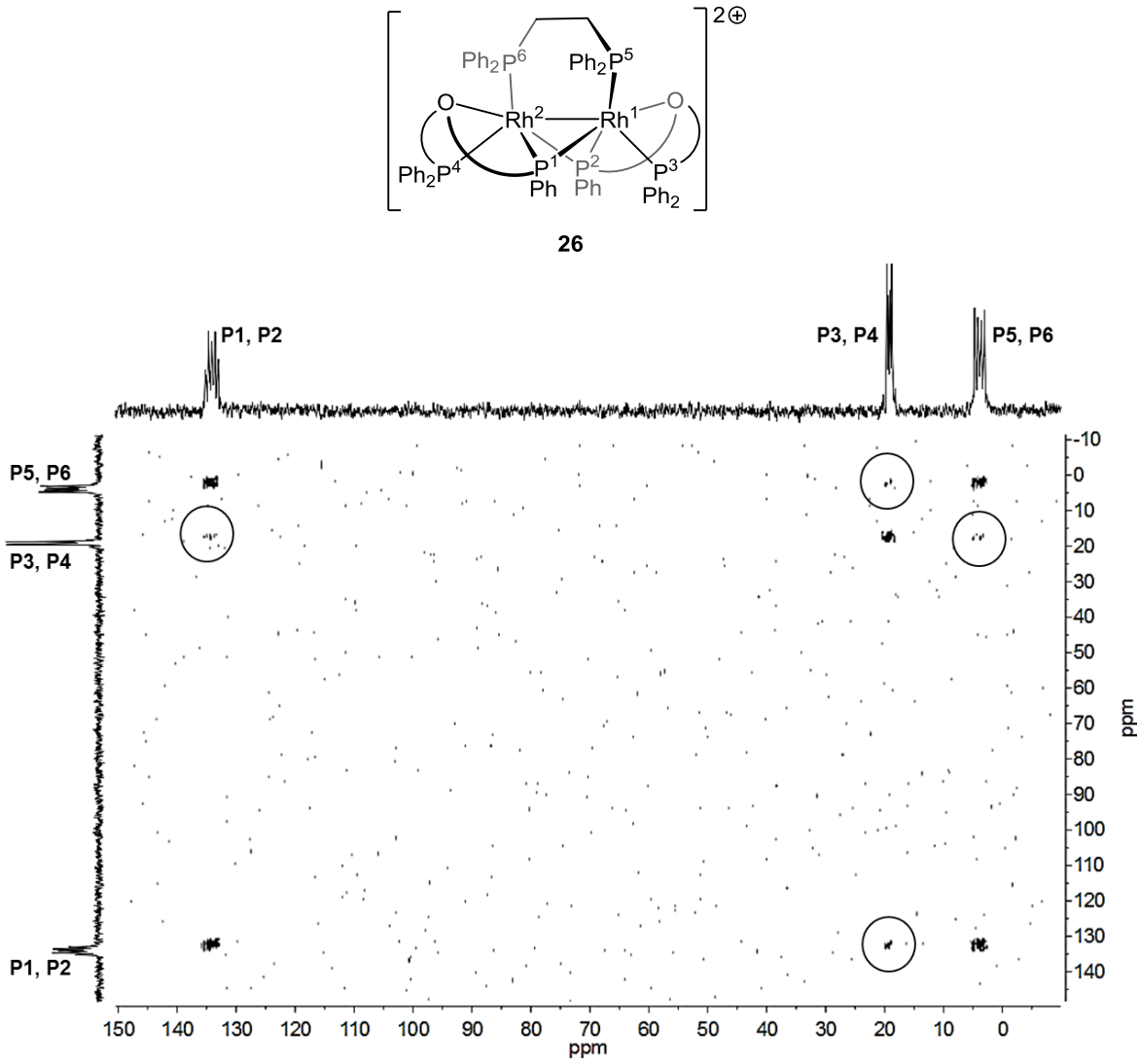
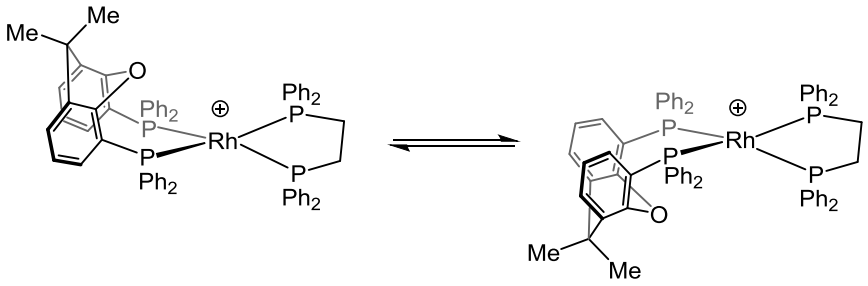



**Figure 5.7** Simplified representation of **26**, and $^{31}$P-$^{31}$P COSY NMR spectrum of **26**. Circles are drawn to highlight the weaker cross peaks. For clarity, $Ph_2$P-O-PPh = Xantphos*.

### 5.2.6.1 *Reaction between **6** and dpp2*

To test whether **26** could be alternatively formed by direct addition of dpp2 to **6**, one equivalent of dpp2 was reacted with **6**. The solution turned a dark reddish brown, and NMR spectroscopy and ESI-MS indicated that a new compound, [Rh($\kappa^2_{P,P}$-Xantphos)(dpp2)][$BAr^F_4$] (**27**) had been formed as the major product, with ~5% of [Rh(dpp2)$_2$][$BAr^F_4$][52] also observed, presumably due to a slight excess of dpp2 added. The $^1$H NMR spectrum showed a broad, relative integral 6H, environment for the

Xantphos methyl groups at δ 1.82, and a broad, relative integral 4H, multiplet at δ 2.21 that collapsed to a singlet upon $^{31}P$ decoupling, corresponding to the dpp2 backbone. The $^{31}P\{^{1}H\}$ NMR spectrum showed two environments at δ 50.9 (broad) and δ 21.0 (dt, $^{1}J_{RhP}$ = 145 Hz, $^{2}J_{PP}$ = 104 Hz). A $^{31}P$-$^{1}H$ HMBC experiment showed a correlation between the $^{1}H$ signal at δ 2.21 and the $^{31}P$ signal at δ 50.9, indicating that this signal corresponds to the dpp2 ligand. A structure for **27** as shown in Scheme 5.8 would render the each of the dpp2 and Xantphos $^{31}P$ environments magnetically equivalent to give a doublet of triplets, and the Xantphos methyl groups equivalent, if the Xantphos ligand inverts faster than the NMR timescale.[25] The $^{2}J_{PP}$ coupling constant of 104 Hz implies an angle of approximately 120° between the Xantphos and dpp2 atoms, being similar to those found in trigonal bipyramidal Rh(diphoshine)($PR_3$)(H)(CO) complexes reported by van Leeuwen in which the phosphines occupy equatorial sites ($^{2}J_{PP}$ = 123 – 126 Hz).[53,54]




**Scheme 5.8** Proposed solution equilibria operating in **27**. $[BAr^{F}_{4}]^{-}$ anions not shown.

At 190 K, the $^{31}P\{^{1}H\}$ NMR spectrum of **27** in $CD_2Cl_2$ solution showed separate broad environments for the dpp2 groups at δ 53.3 and δ 49.3. The Xantphos signal appeared as a broad multiplet at δ 22.7, from which individual couplings could not be resolved. In the $^{1}H$ NMR spectrum at 190 K, separate, relative integral 3H, singlets were observed at δ 1.94 and δ 1.72, corresponding to inequivalent Xantphos methyl

groups. The dpp2 $CH_2$ groups appeared broad and poorly resolved at this temperature. These data suggest that, at 190 K, the Xantphos inversion has ceased (on the NMR timescale). This results in inequivalent environments for the dpp2 phosphorus atoms, dpp2 $CH_2$ groups and Xantphos methyl groups, consistent with the proposed structure.

An alternative rigorously *pseudo* square planar structure, as proposed for the complexes [Rh(dpp2)(dpp3)][$BAr^F_4$][52] (dpp3 = $Ph_2P(CH_2)_3PPh_2$) and [Pt(dpp2)(dpp3)]$Cl_2$,[55] would render the each of the dpp2 and Xantphos phosphorus environments magnetically inequivalent, and be expected to produce complicated multiplets in the $^{31}P\{^1H\}$ NMR spectrum with large (*ca.* 200 – 400 Hz) *trans*-$^2J_{PP}$ coupling constants.[56,57] The magnitude of the $^2J_{PP}$ coupling constant in **27** also suggests that a trigonal bipyramidal [Rh(*mer*-$\kappa^3_{P,O,P}$-Xantphos)(dpp2)][$BAr^F_4$] structure is unlikely as smaller *cis*-$^2J_{PP}$ coupling constants (*e.g.* 34 Hz in **15**, Chapter 3) would be expected. It is likely that the bulk and rigidity of Xantphos compared with dpp3 (calculated natural bite angles of 111.7° and 90.7°, respectively)[54,58] disfavours *pseudo* square planar coordination in **27**.

Layering a dark reddish brown 1,2-$C_6H_4F_2$ solution of **27** with hexanes at 5 °C produced pale orange crystals suitable for analysis by single crystal X-ray diffraction. The solid state structure of **27** (Figure 5.8) indicates a distorted square planar geometry, different to that implied by the solution NMR data, with an angle between the P1-Rh1-P2 and P3-Rh1-P4 planes of 20.8°, likely to relieve the steric strain of the two bulky ligands. The Xantphos is coordinated $\kappa^2_{P,P}$ to the metal with a bite angle of 96.44(3)°. This bite angle is very narrow for Xantphos, whose typical $\kappa^2_{P,P}$ bite angles are of the range *ca.* 99° to 120°,[59] although calculations have implicated a flexibility

range of 97° to 135°.[54] The dpp2 bite angle of 81.41(3)° lies within its calculated flexibility range of 76° to 89°.[58]

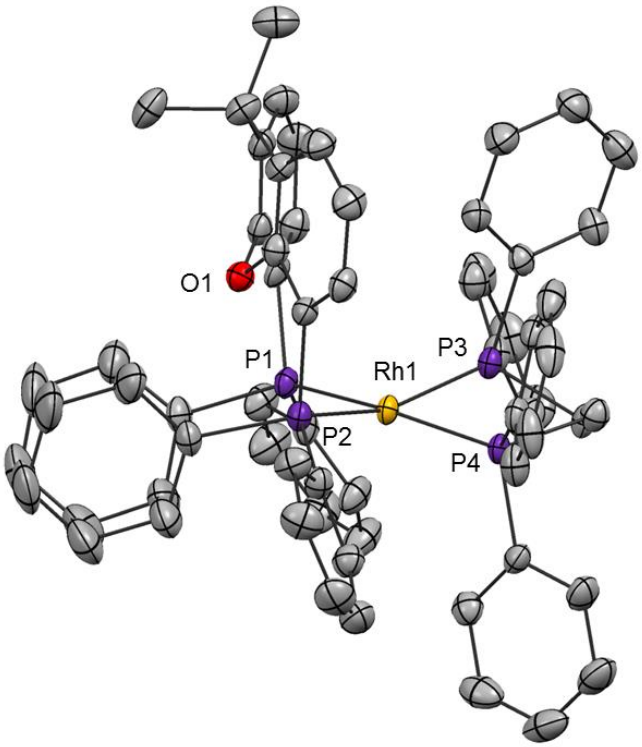



**Figure 5.8** Solid state structure of the cationic portion of **27**. Displacement ellipsoids are drawn at the 50% probability level. Only one of three independent cations in the unit cell shown. The other independent cations show similar structural metrics. H atoms omitted for clarity. Selected bond lengths (Å) and angles (°): Rh1-P1, 2.3546(8); Rh1-P2, 2.3594(9); Rh1-P3, 2.3157(9); Rh1-P4, 2.3054(8); Rh1-O1, 3.2902(39); P1-Rh1-P2, 96.44(3); P3-Rh1-P4, 81.41(3); P1-Rh1-P3, 91.93(3); P2-Rh1-P4, 92.55(3); P1-Rh1-P4, 169.46(3); P2-Rh1-P3, 159.34(3).

If this solid state structure were retained in solution, large *trans* coupling constants would be expected between P1 and P4, and to a lesser extent P2 and P3. Additionally, P3/P4, and P1/P2, are suggested to be magnetically equivalent on the timescale of NMR spectroscopy, but are not in the solid state structure. Dissolving the pale orange crystals in $CD_2Cl_2$ resulted in a dark reddish brown solution and identical NMR spectra to those obtained prior to crystallisation. It is likely that the tight Xantphos bite angle encourages the solution fluxionality. Heating a 1,2-$C_6H_4F_2$ solution of **27** at

40 °C for a week did not lead to any observable decomposition, and **26** was not formed.

### 5.2.7 Summary of the reactivity of 24

The formation of **24** appears to require both $Rh^{I}$ and $Rh^{III}$ fragments, of which **3** and **8** are suitable sources. Once formed, the dimeric unit appears stable, remaining intact upon the addition of strong σ donors such as MeCN and dpp2. However, the reactivity with sources of electrophiles, *e.g.* HCl and MeI, requires further exploration. The reactivity of **24** with amine-boranes is discussed in Section 5.3.2.2.

## 5.3 Formation of a Rh(Xantphos*) dimer *via* dehydrocoupling reactions

### 5.3.1 Final product of 6-catalysed dehydrocoupling of $H_3B{\cdot}NMe_2H$

As described in Chapter 4, addition of 5 mol% **6** to a 1,2-$C_6H_4F_2$ solution of $H_3B{\cdot}NMe_2H$ in a sealed NMR tube resulted in dehydrocoupling to form $[H_2BNMe_2]_2$ and enabled the observation of the metal-containing species by NMR spectroscopy. As discussed, the spectra obtained at 65% consumption of $H_3B{\cdot}NMe_2H$ were consistent – tentatively – with the formation of an amidoborane complex during catalysis, although alternative formulations could not be discounted.

However, towards the end of catalysis (> 90% consumption of $H_3B{\cdot}NMe_2H$), a new species $[Rh_2(\mu\text{-Xantphos*})_2(\mu\text{-}\eta^2{:}\eta^2\text{-}H_3B{\cdot}NMe_2{\cdot}BH_3)][BAr^F{}_4]$ (**28**) was observed to form in the mixture, evident by two broad signals at δ –2.38 and δ –3.24 in the $^1H$ NMR spectrum, and was the major species after 24 hours (Figure 5.9).

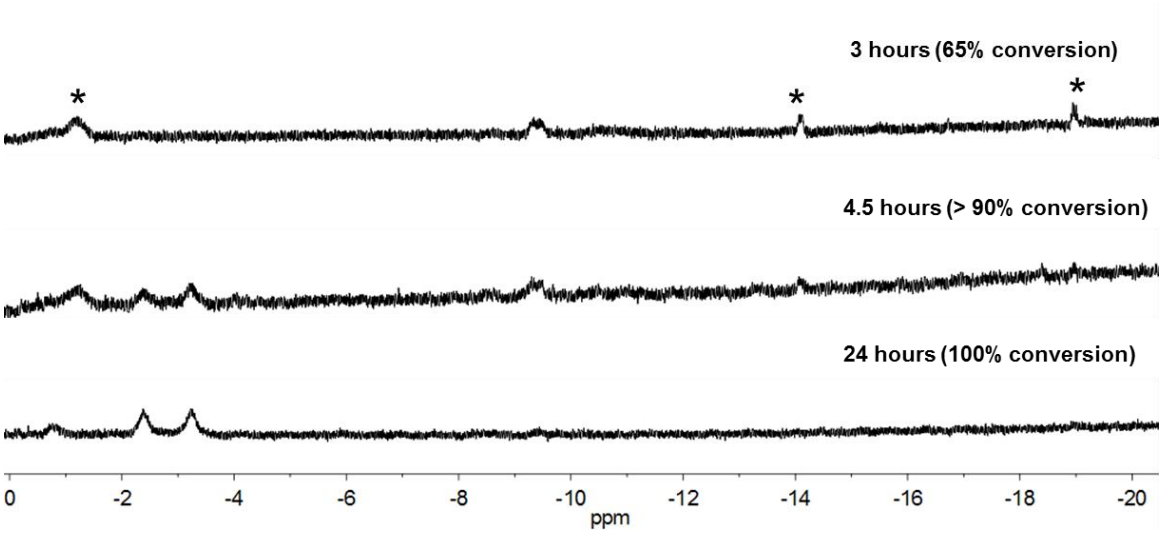
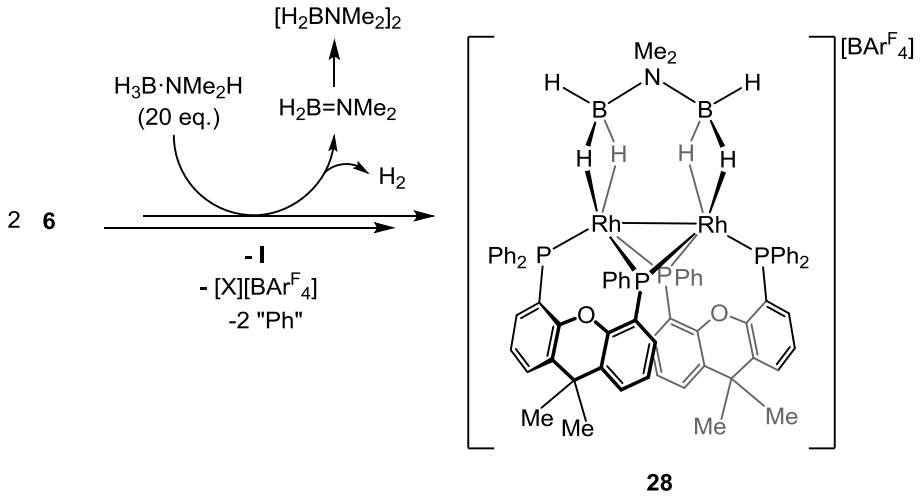



**Figure 5.9** Hydride region of the $^{1}H$ NMR spectra of the reaction between $H_3B{\cdot}NMe_2H$ and **6** (5 mol%) in a sealed NMR tube in 1,2-$C_6H_4F_2$. Conversions reflect the consumption of $H_3B{\cdot}NMe_2H$, measured by $^{11}B$ NMR spectroscopy. * = **18**.

The dimer **28** results from the P—C activation of the Xantphos ligands, as was observed in the formation of **24**, and contains a $[H_3B{\cdot}NMe_2{\cdot}BH_3]^-$ ligand bridging the two Rh centres.




**28**

**Scheme 5.9** Formation of **28** from reaction of **6** with 20 eq. $H_3B{\cdot}NMe_2H$ in 1,2-$C_6H_4F_2$.

Recrystallisation of the 1,2-$C_6H_4F_2$ mixture with pentane at 5 °C formed several orange crystals of **28** suitable for X-ray diffraction, and the solid state structure is shown in Figure 5.10. Brown oil was formed alongside the crystals which, by NMR

spectroscopy, contained some **28**, but appeared to consist mostly of unidentified decomposition products.

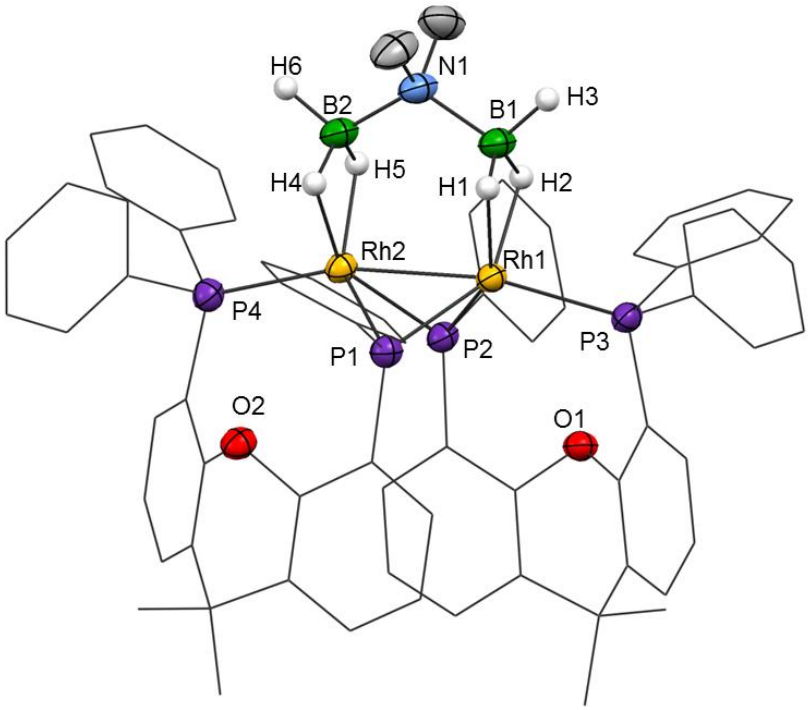
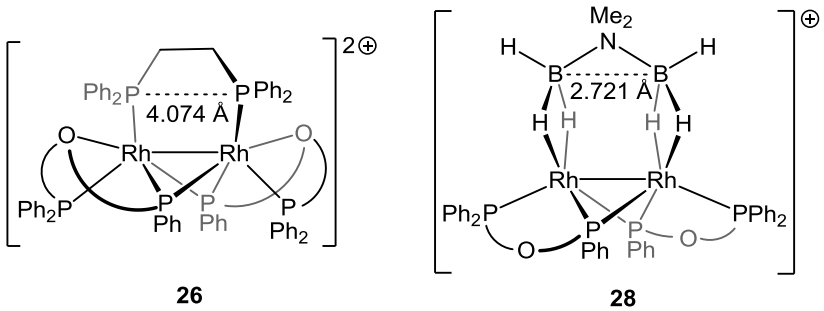



**Figure 5.10** Solid state structure of the cationic portion of **28**. Displacement ellipsoids are drawn at the 50% probability level. For clarity, carbon-bound H atoms are omitted, and the carbon atoms in the Xantphos* ligands are depicted as a wireframe. Selected bond lengths (Å) and angles (°): Rh1-Rh2, 2.5929(4); Rh1-P1, 2.2452(11); Rh1-P2, 2.2504(11); Rh1-P3, 2.3429(11); Rh2-P1, 2.2460(11); Rh2-P2, 2.2667(11); Rh2-P4, 2.3330(11); Rh1-B1, 2.232(5); Rh2-B2, 2.230(5); Rh1-O1, 3.393(4); Rh2-O2, 3.413(4); B1-N1, 1.603(6); N1-B2, 1.581(7); P1-Rh2-P4, 114.63(4); P2-Rh1-P3, 110.88(4); B1-N1-B2, 117.4(3).

The solid state structure of **28** indicates that the phosphido arms of the Xantphos* ligands bridge the metal centres, and the Rh—P bond lengths are very similar to those in **24** and **26**. However, in **28**, the Xantphos* is now coordinated in a *cis*-$\kappa^2_{P,P}$ fashion to the metal centre, indicated by the Rh—O distances (3.413(4) Å and 3.393(4) Å) and the bite angles of the Xantphos* ligands (114.63(4)° and 110.88(4)°). The hydrogen atoms in the structure were located and show that a $[H_3B{\cdot}NMe_2{\cdot}BH_3]^-$ unit bridges the two metal centres with each $BH_3$ group binding $\eta^2$ to a Rh centre, as also implied by the Rh—B distances of 2.232(5) Å and 2.230(5) Å. These distances are

the same within error, indicating symmetrical distribution over the Rh—Rh unit. Overall, the complex is a monocation with one $[BAr^F{}_4]^-$ counterion and, like **24** and **26**, is formally a $Rh^{II}$-$Rh^{II}$ dimer. The Rh—Rh distance of 2.5929(4) Å is shorter than those in **24** and **26** of 2.7965(5) Å and 2.8362(5) Å, respectively, and is similar to the distances that have been considered within the range for double bonds in related complexes containing a bridging phosphido group (*cf.* $[Rh(\mu\text{-}P^tBu_2)(CO)(PMe_3)]_2$, 2.550(1) Å,[60] and $[Rh(\mu\text{-}P^tBuH)(PMe_3)_2]_2$, 2.552(2) Å).[61] If **28** contained a Rh—Rh double bond, however, the valence electron count for each Rh atom would be 19. Therefore, it is suggested that **24**, **26** and **28** contain single Rh—Rh bonds, but that the $Rh_2P_2$ unit is relatively adaptable, depending upon the coordinated ligands. The B···B distance in **28** is 2.721 Å, whereas the P···P distance in the dpp2 ligand in **26** is 4.074 Å (Figure 5.11), suggesting that the differing steric requirements of the chelating ligands impacts the Rh—Rh bond distance. Moreover, the B-Rh-Rh-B torsion angle in **28** is 0.54°, whereas the P5-Rh-Rh-P6 torsion angle in **26** is 52.58°, indicating that the bulky dpp2 ligand induces a twist across the Rh—Rh bond, whereas the smaller $[H_3B{\cdot}NMe_2{\cdot}BH_3]^-$ ligand is not twisted across the Rh—Rh bond.




**26** **28**

**Figure 5.11** Diagram depicting the distances between the dpp2 P atoms and B atoms in **26** and **28**, respectively. For clarity, $Ph_2P$-O-PPh = Xantphos*, and $[BAr^F{}_4]^-$ anions are not shown.

The NMR data of **28** ($CD_2Cl_2$) are consistent with the solid state structure. The $^{31}P\{^1H\}$ NMR spectrum shows two signals at δ 108.5 (triplet of triplets, phosphido group) and δ 13.3 (doublet of doublet of triplets, phosphine groups). Simulations using gNMR[10] (Figure 5.12) produced estimated coupling constants similar to those for **24** (see Chapter 7).

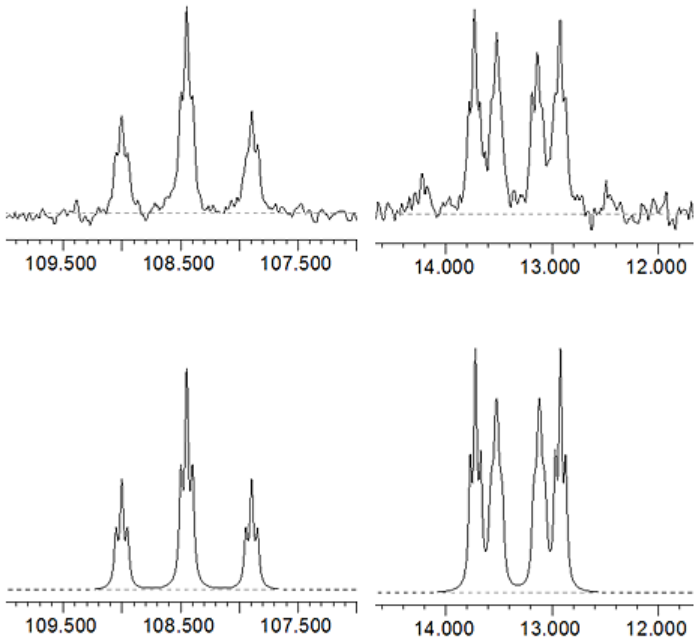



**Figure 5.12** Experimental (top) and simulated (bottom) $^{31}P\{^1H\}$ NMR signals for **28** in $CD_2Cl_2$. Scale is in ppm. Simulations performed using gNMR.

In the $^1H$ NMR spectrum, two Xantphos methyl environments, each relative integral 6H, are observed at δ 1.79 and δ 1.24. The $NMe_2$ region appears as a singlet at δ 2.47 with relative integral 6H. The Rh—H—B groups appear as two broad signals, each relative integral 2H, at δ –2.67 and δ –3.53, presumably reflecting that one B—H in each Rh—$H_2$B group is closer through space to a Xantphos* oxygen atom, as seen in the solid state structure. The free B—H groups were observed at δ 4.14. Each of the signals assigned to B—H resonances sharpened upon $^{11}B$ decoupling. These data indicate that there is no site exchange between free and bound B—H groups. The $^{11}B$

NMR spectrum shows a broad peak at δ 16.2 corresponding to the bound $BH_3$ groups. This is shifted *ca.* 29 ppm downfield from the chemical shift of the complex $Na[H_3B{\cdot}NMe_2{\cdot}BH_3]$ (δ(*11B*) –12.5, q, $^1J_{HB}$ = 91 Hz, in THF),[62] suggestive of covalent $\eta^2$ interactions in **28**. $[H_3B{\cdot}NMe_2{\cdot}BH_3]^-$ has been used by Girolami and coworkers in the formation of group II complexes $M(H_3B{\cdot}NMe_2{\cdot}BH_3)_2$ that may be useful as chemical vapour deposition precursors.[63-65] The $^{11}B$ chemical shifts of these complexes range between *ca.* δ –8 and δ –13 and consist of quartets, suggesting primarily electrostatic interactions, contrasting **28**. ESI-MS of **28** showed a molecular ion at *m/z* = 1280.23 (calc. 1280.24) with the expected isotopic pattern.

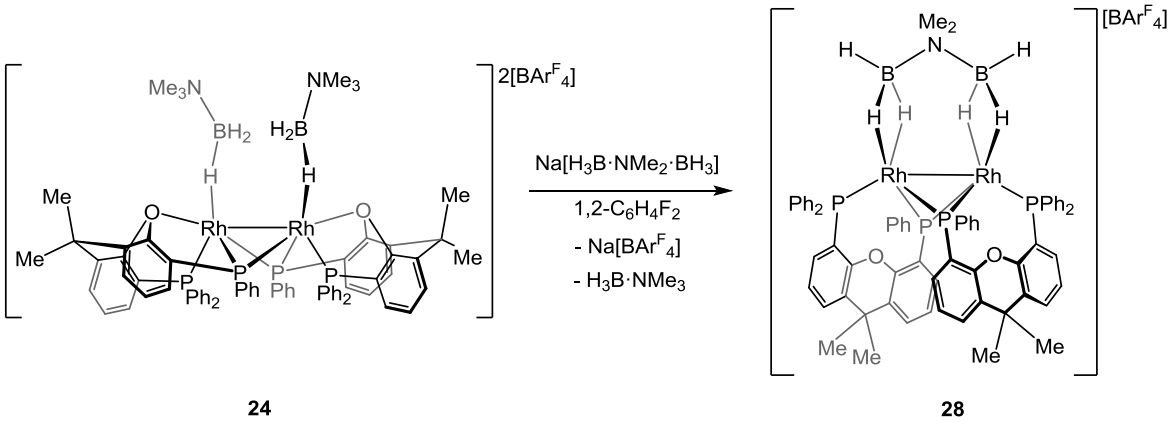
As the structure of **CAT** remains unresolved, we cannot speculate upon the mechanism for the ultimate formation of **28** from **6**, *via* **CAT**, and the fate of the lost phenyl groups in this system has not been investigated. Moreover, the identity of the species $[X][BAr^F{}_4]$ (that is required to balance the charges, Scheme 5.9) has not been identified. A reasonable candidate would be $[BH_2(NMe_2H)_2][BAr^F{}_4]$, which has been found recently to play a role in Pt-catalysed dehydrocoupling of $H_3B{\cdot}NMe_2H$ (see Chapter 1),[66] but no evidence for this complex was observed by NMR spectroscopy.

### 5.3.2 Formation of 28 from 24

#### 5.3.2.1 *Addition of $Na[H_3B{\cdot}NMe_2{\cdot}BH_3]$ to **24***

Given the structural similarities between **24** and **28**, whether **28** could be formed *via* **24** was examined. Upon addition of $Na[H_3B{\cdot}NMe_2{\cdot}BH_3]$ (~1.5 eq.) to **24**, slight bubbling was observed and $^{11}B$ NMR spectroscopy showed some $(H_2B)_2(\mu\text{-}H)NMe_2$ had formed. Dissolved $H_2$ was observed in the reaction mixture, presumably arising from the formation of $(H_2B)_2(\mu\text{-}H)NMe_2$. $^1H$ and $^{31}P\{^1H\}$ NMR spectroscopies showed the consumption of **24** and the formation of intermediates with complicated

overlapping signals in the $^{31}P\{^{1}H\}$ NMR spectrum (*ca.* δ 104 and δ 13), and in the $^{1}H$ NMR spectrum, broad signals at δ –1 (overlapping) and δ –3. Within 24 hours, however, **28** had formed as the major (90%) product (Scheme 5.10).




**24** **28**

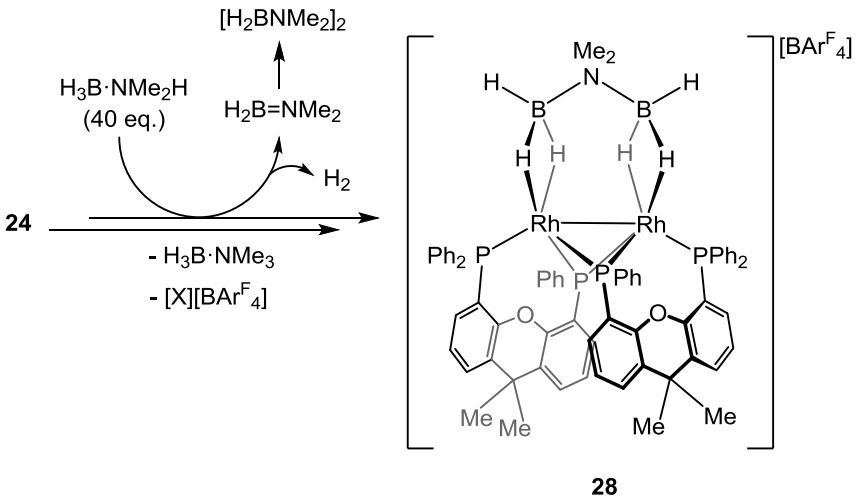
**Scheme 5.10** Overall scheme for the formation of **28** from **24** by the addition of $Na[H_3B{\cdot}NMe_2{\cdot}BH_3]$.

Filtration and crystallisation of the mixture with 1,2-$C_6H_4F_2$ and pentane formed some crystalline material. However, NMR spectroscopy indicated that Na[BAr$^F_4$] (~1 eq.) had co-crystallised with **28** and so material suitable for microanalysis was not obtained.

### 5.3.2.2 *Dehydrocoupling of $H_3B{\cdot}NMe_2H$*

Next, the possible formation of **28** through the dehydrocoupling of $H_3B{\cdot}NMe_2H$ by **24** was explored. Analogous conditions were used as that in the system with **6**: 2.5 mol% **24** (5 mol% [Rh]), sealed NMR tube, 1,2-$C_6H_4F_2$ solvent. Under these conditions, **24** dehydrocoupled $H_3B{\cdot}NMe_2H$ rapidly, reaching > 90% consumption of $H_3B{\cdot}NMe_2H$ by the time an $^{11}B$ NMR spectrum was taken (*ca.* 1 – 2 minutes after mixing). $H_2B{=}NMe_2$ and $[H_2BNMe_2]_2$ were the major species present, but $H_3B{\cdot}NMe_2BH_2{\cdot}NMe_2H$ (~2%), $HB(NMe_2)_2$ (~1%) and $(H_2B)_2(\mu\text{-}H)NMe_2$ (~4%) were also observed in the reaction

mixture. The $^{31}P\{^{1}H\}$ NMR spectrum showed several broad regions at δ 180 and δ –8, and sharper complicated multiplet(s) at δ 34.2. The broad region at δ 180 may correspond to a bridging phosphido group, but whether the dimeric unit of **24** had remained intact or been wholly/partially cleaved during catalysis could not be deduced. The $^{1}H$ NMR spectrum showed several broad signals in the hydride region (δ –1.34, δ –10.19 and δ –18.20) that appeared to be composed of overlapping species. Within 22 hours, however, **28** had formed as the sole organometallic product (Scheme 5.11). As with the formation of **28** *via* the dehydrocoupling of $H_3B{\cdot}NMe_2H$ by **6**, $[X][BAr^F{}_4]$ was not identified.




**28**

**Scheme 5.11** Formation of **28** *via* the dehydrocoupling of $H_3B{\cdot}NMe_2H$ by **24**. **28** formed within 22 hours.

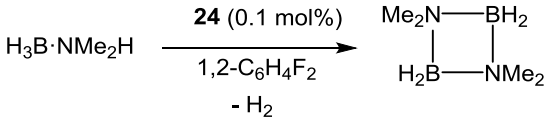
P—C activation of phosphines during catalysis to form phosphido-bridged species has been considered a decomposition pathway, with the stable bridged structures giving reduced catalytic activity in, for example, hydroformylation.[32,67,68] However, the fast activity of **24** (2.5 mol%, sealed NMR tube) as a dehydrocoupling catalyst compared with the analogous **6**-catalysed system contrasts this. That both **6** and **24** produce **28** as the end product of catalysis could suggest also that both systems operate through

similar intermediates, and may imply that the $\{Rh_2(Xantphos^*)_2\}^{2+}$ fragment is **CAT**. Thus, lower catalyst loadings of **24** were next investigated to provide a comparison with the kinetics of the dehydrocoupling of $H_3B{\cdot}NMe_2H$ with **6**.

## 5.4 Kinetic studies upon 24-catalysed dehydrocoupling

### 5.4.1 Catalytic dehydrocoupling of $H_3B{\cdot}NMe_2H$ by 24

Under conditions analogous to those described in Chapter 4 using **6**, **24** (0.1 mol%, 0.2 mol% [Rh]) in 1,2-$C_6H_4F_2$ in an open system catalysed the dehydrocoupling of $H_3B{\cdot}NMe_2H$ (0.072 M) to form $[H_2BNMe_2]_2$ (Scheme 5.12).




**Scheme 5.12** Catalytic dehydrocoupling of $H_3B{\cdot}NMe_2H$ by **24**.

The reaction profile for the dehydrocoupling of $H_3B{\cdot}NMe_2H$ with **24** (Figure 5.13) was very similar to those seen with **6**. $H_2B{=}NMe_2$ was observed as the major intermediate, with < 5% $HB(NMe_2)_2$ and < 1% $H_3B{\cdot}NMe_2BH_2{\cdot}NMe_2H$ observed. Significantly, an induction period (~300 s) was observed with **24**, suggesting that $\{Rh_2(Xantphos^*)_2\}^{2+}$ is not the active form of **CAT**. Post-induction period, a TOF of ~2300 $h^{-1}$ (1150 $h^{-1}$ relative to [Rh]) was observed, similar to that of **6** (TOF ~1000 $h^{-1}$).

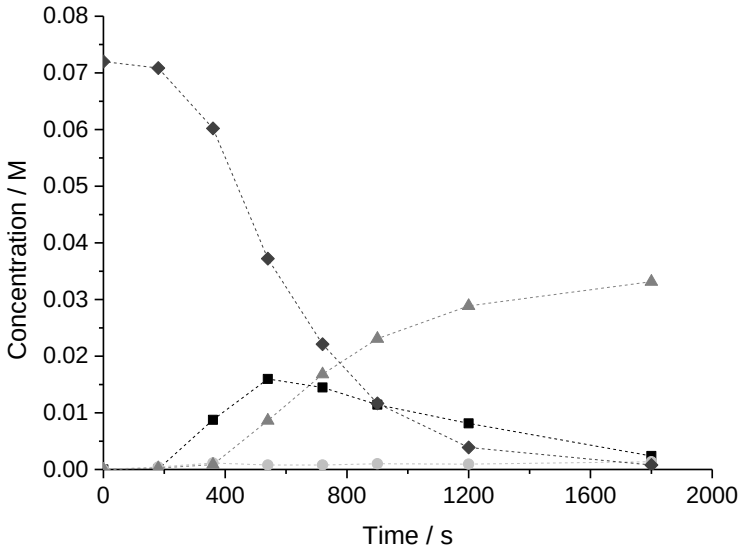



**Figure 5.13** Plot of concentration (by $^{11}B$ NMR spectroscopy) during the catalytic dehydrocoupling of $H_3B{\cdot}NMe_2H$ with $[H_3B{\cdot}NMe_2H]_0$ = 0.072 M and [**24**] = 7.2 x $10^{-5}$ M. ◆ = $H_3B{\cdot}NMe_2H$; ■ = $H_2B{=}NMe_2$; ● = $HB(NMe_2)_2$; ▲ = $[H_2BNMe_2]_2$.

### 5.4.2 Saturation kinetics

Given the similar reaction profiles between **6** and **24** at 0.072 M $H_3B{\cdot}NMe_2H$, runs were conducted with initial $H_3B{\cdot}NMe_2H$ concentrations of 0.288 M, 0.144 M and 0.018 M. When $[H_3B{\cdot}NMe_2H]_0$ = 0.018 M, *pseudo*-first order decay of $[H_3B{\cdot}NMe_2H]$ was observed (Figure 5.14a), whereas *pseudo*-zero order decay of $[H_3B{\cdot}NMe_2H]$ was seen when $[H_3B{\cdot}NMe_2H]_0$ = 0.288 M (Figure 5.14b).

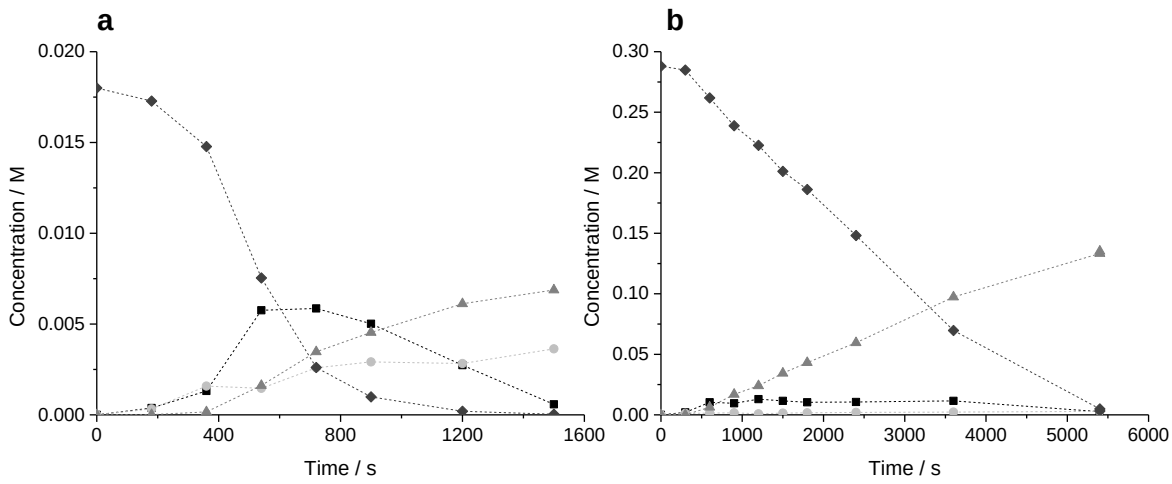



**Figure 5.14** Plots of concentration (by $^{11}B$ NMR spectroscopy) during the catalytic dehydrocoupling of $H_3B{\cdot}NMe_2H$ with [**24**] = 7.2 x $10^{-5}$ M. ◆ = $H_3B{\cdot}NMe_2H$; ■ = $H_2B{=}NMe_2$; ● = $HB(NMe_2)_2$; ▲ = $[H_2BNMe_2]_2$. Open conditions. **(a)** $[H_3B{\cdot}NMe_2H]_0$ = 0.018 M. **(b)** $[H_3B{\cdot}NMe_2H]_0$ = 0.288 M.

The rates *vs* $[H_3B{\cdot}NMe_2H]$ across these runs were calculated (post-induction period) and plotted in Figure 5.15. The plot shows a curve reminiscent of saturation kinetics; approximate *pseudo* zero order behaviour is observed at $H_3B{\cdot}NMe_2H$ concentrations above *ca.* 0.1 M, with approximate *pseudo* first order consumption of $H_3B{\cdot}NMe_2H$ observed at lower concentrations. This, and the observation of an induction period, suggests that similar mechanisms may be operating with **6** and **24** that involve the coordination of a second equivalent of amine-borane to the catalytically active species (**CAT**, for **6**-catalysed dehydrocoupling). Doubling the concentration of **24** from 7.2 x $10^{-5}$ M to 1.44 x $10^{-4}$ M approximately doubled the rate constant obtained from the zero order regions (0.144 M run) from (0.79 ± 0.01) x $10^{-4}$ M $s^{-1}$ to (1.84 ± 0.04) x $10^{-4}$ M $s^{-1}$, suggesting kinetics first order in [Rh].

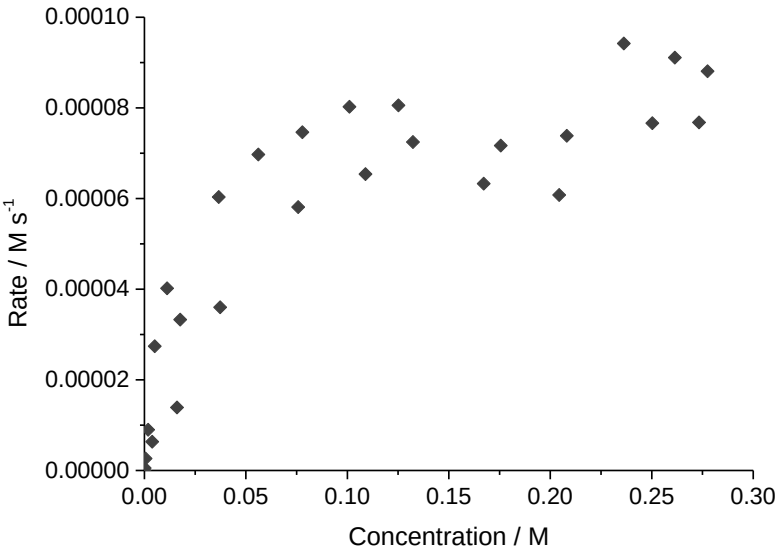



**Figure 5.15** Rate of $H_3B{\cdot}NMe_2H$ consumption *vs* $[H_3B{\cdot}NMe_2H]$. [**24**] = 7.2 x $10^{-5}$ M.

### 5.4.3 Kinetic isotope effects

$D_3B{\cdot}NMe_2H$ and $H_3B{\cdot}NMe_2D$ were used to ascertain kinetic isotope effects for this system. In the zero order regime, the KIEs determined were 1.1 ± 0.2 for B—H/D substitution, and 2.0 ± 0.3 for N—H/D substitution ($[amine\text{-}borane]_0$ = 0.288 M, [**24**] = 7.2 x $10^{-5}$ M, 1,2-$C_6H_4F_2$ solvent, open conditions). These values are similar to those obtained using **6** as a precatalyst and imply that N—H activation may be involved in, or in an equilibrium prior to, the rate determining step (see discussion in Chapter 4). Moreover, the induction period approximately doubled from ~300 s with $H_3B{\cdot}NMe_2H$ and $D_3B{\cdot}NMe_2H$ to ~600 s when using $H_3B{\cdot}NMe_2D$, again similar to the **6**-catalysed system, and suggests again that N—H activation may be involved in the rate-limiting process for the formation of the active catalyst.

### 5.4.4 Dehydrocoupling of $H_3B{\cdot}NMe_2H$ under sealed conditions

Given the similarities between the **24** and **6** systems under open conditions, the catalytic dehydrocoupling of $H_3B{\cdot}NMe_2H$ was conducted under sealed conditions in

an analogous manner to that of **6** ([$H_3B{\cdot}NMe_2H]_0$ = 0.072 M, [**24**] = 7.2 x $10^{-5}$ M, sealed NMR tube). As with catalytic dehydrocoupling using **6**, and **24**-catalysed dehydrocoupling under open conditions, $[H_2BNMe_2]_2$ was the product of dehydrocoupling, the major intermediate was $H_2B{=}NMe_2$, and < 1% $H_3B{\cdot}NMe_2BH_2{\cdot}NMe_2H$ was observed. A plot of concentrations *vs* time is shown in Figure 5.16a. Following an induction period of approximately 200 s, the reaction proceeded with *pseudo*-first order decay of [$H_3B{\cdot}NMe_2H$] with a first order rate constant of (4.37 ± 0.07) x $10^{-4}$ $s^{-1}$ (calculated from a plot of ln[$H_3B{\cdot}NMe_2H$] *vs* time, Figure 5.16b). This is a similar value to those obtained in the closed systems with **6** (*ca.* 4 x $10^{-4}$ $s^{-1}$, Chapter 4). The dehydrocoupling reached completion in approximately 8000 s, slower than in the analogous open system (~1500 s, Figure 5.13).

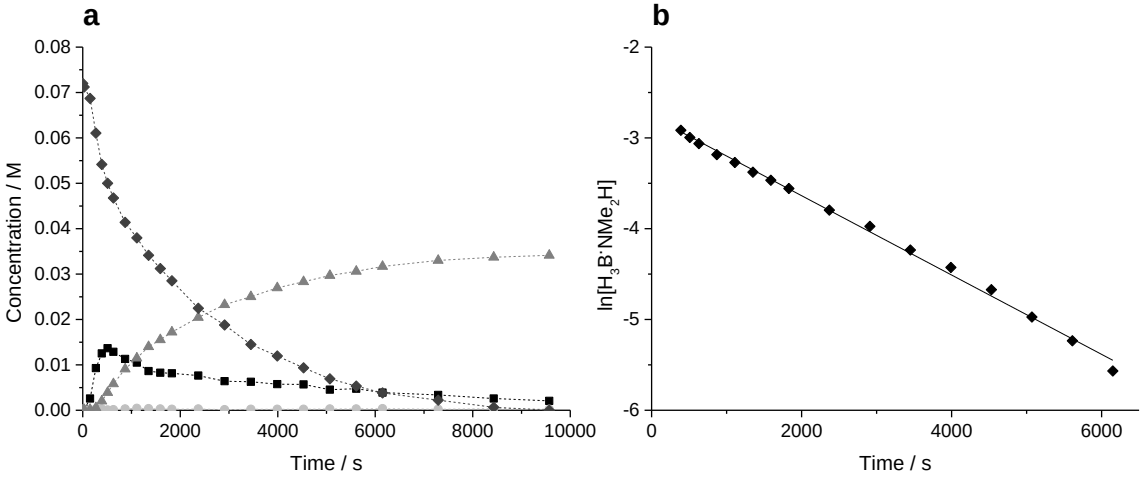


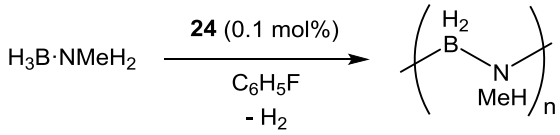

**Figure 5.16 (a)** Plot of concentration (by $^{11}B$ NMR spectroscopy) during the catalytic dehydrocoupling of $H_3B{\cdot}NMe_2H$ (initial concentration 0.072 M) with [**24**] = 7.2 x $10^{-5}$ M. ◆ = $H_3B{\cdot}NMe_2H$; ■ = $H_2B{=}NMe_2$; ● = $HB(NMe_2)_2$; ▲ = $[H_2BNMe_2]_2$. Sealed conditions. **(b)** Plot of ln[$H_3B{\cdot}NMe_2H$] *vs* time during productive catalysis. Linear fit depicted by trendline. From trendline, k = (4.37 ± 0.07) x $10^{-4}$ $s^{-1}$. $R^2$ = 0.99656.

These data show that catalysis by **24**, like **6**, is slower under sealed conditions and that $H_2$ build-up induces a first order decay of [$H_3B{\cdot}NMe_2H$]. This is consistent with

the reversible coordination of $H_2$ to the metal, binding competitively with $H_3B{\cdot}NMe_2H$, as was discussed in Chapter 4.

### 5.4.5 Dehydropolymerisation of $H_3B{\cdot}NMeH_2$ by 24

The ability of **24** to act as a catalyst for dehydropolymerisation of $H_3B{\cdot}NMeH_2$ was also probed. 0.1 mol% of **24** catalysed the dehydropolymerisation of $H_3B{\cdot}NMeH_2$ to form $[H_2BNMeH]_n$ (Scheme 5.13) under analogous conditions to those used with **6** ($[H_3B{\cdot}NMeH_2]_0$ = 0.44 M, $C_6H_5F$ solvent, open system). The dehydropolymerisation was slower than that with **6**, reaching 80% completion within 2 hours.




**Scheme 5.13** Dehydropolymerisation of $H_3B{\cdot}NMeH_2$ by **24**.

The $^{11}B\{^1H\}$ NMR spectrum of the $[H_2BNMeH]_n$ produced consisted of a broad (FWHM = 700 Hz) peak at δ –5.4 (Figure 5.17), similar to that produced by **6** under open conditions. GPC analysis performed by Dr G. Whittell, University of Bristol, indicated $[H_2BNMeH]_n$ with $M_n$ = 28 700 g mol$^{-1}$ and PDI = 1.7, similar to that formed using **6** ($M_n$ = 22 700 g mol$^{-1}$, PDI = 2.1, Chapter 4).

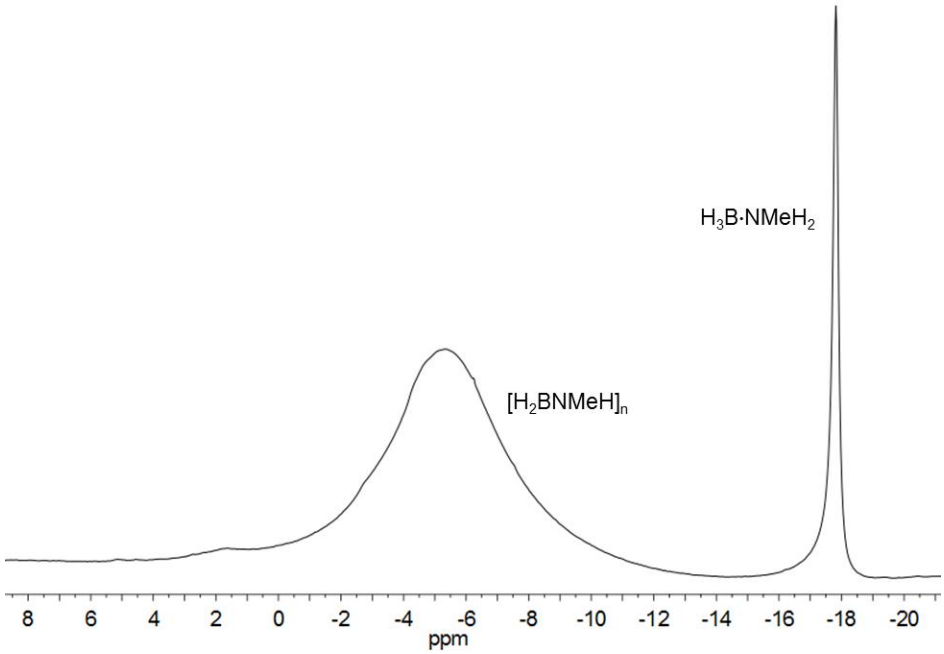



**Figure 5.17** Back-linear corrected $^{11}B\{^1H\}$ NMR spectrum (THF solvent) of the $[H_2BNMeH]_n$ produced from the dehydrocoupling of $H_3B{\cdot}NMeH_2$ with **24**.

### 5.4.6 Comparison of 24 and 6 as dehydrocoupling catalysts

Under catalytic conditions, the temporal evolution of the dehydrocoupling of $H_3B{\cdot}NMe_2H$ with **24** is similar to that observed with dehydrocoupling by **6.** Each precatalyst shows an induction period of ~300 s upon reaction of 0.2 mol% [Rh] with $H_3B{\cdot}NMe_2H$, suggesting that formation of the $\{Rh_2(Xantphos^*)_2\}^{2+}$ motif is not responsible for the induction period, but whether catalysis occurs *via* a monomeric or dimeric species has not been established. Previous work upon the $Rh(PCy_3)_2(H)_2Cl$ system for the dehydrocoupling of $H_3B{\cdot}NMe_2H$ showed that the active catalyst was in equilibrium with an off-cycle dimer, $[Rh(PCy_3)_2(H)_2Cl]_2$, on the basis of half order kinetics in [Rh].[69] Williams reported that Shvo's dimeric catalyst for the dehydrocoupling of $H_3B{\cdot}NH_3$ formed a monomeric active species during the fast regime,[70] and the mechanism is discussed in Chapter 1, although an off-cycle dimer was implicated in the slower regime.[71] The longer induction period observed in each

system when using $H_3B{\cdot}NMe_2D$, and the fast B—H activation demonstrated in both **24** and [Rh($\kappa^3_{P,O,P}$-Xantphos)$(H)_2(\eta^1$-$H_3B{\cdot}NMe_2H)$][$BAr^F_4$] (**18**, Chapter 4), suggests that each system involves formation of the active species *via* N—H activation. Moreover, the kinetic profiles for each system suggest saturation kinetics operate, and KIE values are comparable. Both precatalysts also show *pseudo* first order behaviour under sealed conditions. Moreover, they each produce similar $[H_2BNMeH]_n$ upon dehydrocoupling $H_3B{\cdot}NMeH_2$. These similarities between the two systems suggest that the active catalytic species may be closely related.

One possibility is that both precatalysts **6** and **24** produce the same $\{Rh_2(Xantphos^*)_2\}^{2+}$-based active catalyst. Given that, under catalytic conditions, the length of induction period is similar for each system, the formation of $\{Rh_2(Xantphos^*)_2\}^{2+}$ from **6** would have to be fast, followed by slower production of the active catalyst (involving N—H activation). No evidence for the $\{Rh_2(Xantphos^*)_2\}^{2+}$ motif was observed during stoichiometric reactions with **6** and $H_3B{\cdot}NMe_2H$ or $H_3B{\cdot}NMeH_2$ (Chapter 4), which may imply that a large excess of amine-borane would be required for this transformation.

Alternatively, precatalysts **6** and **24** could produce similar active catalysts based upon $\{Rh(Xantphos)\}^+$. For the formation of Xantphos from Xantphos*, P—phenyl bond formation is required. As no aryl reagents are added to the catalysis mixture, and **24** is stable for over 24 h in 1,2-$C_6H_4F_2$ solution, this scenario is unlikely. However, reaction of the phosphido groups with the protic H—N groups in $H_3B{\cdot}NMe_2H$ or $H_3B{\cdot}NMeH_2$ could produce Xantphos*H ligands, which could behave similarly to Xantphos. **24** was shown to react with HCl, for example, although the product(s) of this reaction were unable to be identified.

Finally, precatalysts **6** and **24** could produce different active species (by N—H activation), that both happen to show similar kinetic profiles for dehydrocoupling. However, upon reaction of $H_3B{\cdot}NMe_2H$ with 5 mol% loading of [Rh], that both **6** and **24** ultimately lead to **28** as the decomposition product may suggest that a similar active catalyst is a more likely scenario. We have been unable to produce enough clean material to test **28**, another possible identity for **CAT**, as the active catalyst. However, as suggested by saturation kinetics, the active species **CAT** requires a vacant site. The 18 valence electron count of **28**, and its observation only towards the end of the 5 mol% [Rh] reactions, both suggest that **28** is not **CAT**.

## 5.5 Conclusions and future work

The P—C activation of Xantphos has been reported and several new complexes based upon $\{Rh_2(Xantphos^*)_2\}^{2+}$ have been described. The formation of **24** has been demonstrated to require $\{Rh(Xantphos)\}^+$ and $\{Rh(Xantphos)(H)_2\}^+$ fragments. The role of **24** as a precatalyst for the dehydrocoupling of $H_3B{\cdot}NMeH_2$ has been explored, and shows many similarities with the **6** system described in depth in Chapter 4, including the formation of **28**. These studies may imply that the active catalyst is a dimer, although the induction period observed with **24** suggests that $\{Rh_2(Xantphos^*)_2\}^{2+}$ itself is not the active species. Future work could address the prevalence of this P—C activation of Xantphos. As Xantphos is widely used as a ligand in many catalytic applications including hydroformylation[54,72] and cross couplings,[73] it would be intriguing to explore whether P—C activation occurs in these systems, and if so, the effect upon catalytic activity.

## 5.6 References


(1) Werner, H.; Klingert, B.; Rheingold, A. L. *Organometallics* **1988**, *7*, 911.
(2) Downing, D. O.; Zavalij, P.; Eichhorn, B. W. *Inorg. Chim. Acta* **2011**, *375*, 329.
(3) Kreter, P. E.; Meek, D. W. *Inorg. Chem.* **1983**, *22*, 319.
(4) Wang, K.; Emge, T. J.; Goldman, A. S. *Inorg. Chim. Acta* **1997**, *255*, 395.
(5) Garrou, P. E. *Chem. Rev.* **1981**, *81*, 229.
(6) Meek, D. W.; Kreter, P. E.; Christoph, G. G. *J. Organomet. Chem.* **1982**, *231*, C53.
(7) Douglas, S.; Lowe, J. P.; Mahon, M. F.; Warren, J. E.; Whittlesey, M. K. *J. Organomet. Chem.* **2005**, *690*, 5027.
(8) Arif, A. M.; Jones, R. A.; Seeberger, M. H.; Whittlesey, B. R.; Wright, T. C. *Inorg. Chem.* **1986**, *25*, 3943.
(9) Stradiotto, M.; Fujdala, K. L.; D. Tilley, T. *Helv. Chim. Acta* **2001**, *84*, 2958.
(10) gNMR 5.1, Budzelaar, P. H. M., marketed by Adept Scientific until May 2005.
(11) Chisholm, M. H.; Huffman, J. C.; Iyer, S. S. *J. Chem. Soc., Dalton Trans.* **2000**, 1483.
(12) Telser, J.; Drago, R. S. *Inorg. Chem.* **1986**, *25*, 2989.
(13) Buchard, A.; Payet, E.; Auffrant, A.; Goff, X. L.; Floch, P. L. *New J. Chem.* **2010**, *34*, 2943.
(14) Hayter, R. G. *J. Am. Chem. Soc.* **1963**, *85*, 3120.
(15) Hayter, R. G. *Inorg. Chem.* **1963**, *2*, 1031.
(16) Hayter, R. G.; Williams, L. F. *J. Inorg. Nucl. Chem.* **1964**, *26*, 1977.
(17) Crowte, R. J.; Evans, J. *J. Chem. Soc., Chem. Commun.* **1984**, 1332.
(18) Haines, R. J.; Steen, N. D. C. T.; English, R. B. *J. Chem. Soc., Dalton Trans.* **1984**, 515.
(19) Kreter Jr, P. E.; Meek, D. W.; Christoph, G. G. *J. Organomet. Chem.* **1980**, *188*, C27.
(20) Dimmer, J.-A.; Hornung, M.; Wütz, T.; Wesemann, L. *Organometallics* **2012**, *31*, 7044.
(21) Ara, I.; Chaouche, N.; Forniés, J.; Fortuño, C.; Kribii, A.; Tsipis, A. C. *Organometallics* **2006**, *25*, 1084.
(22) Arias, A.; Forniés, J.; Fortuño, C.; Martín, A.; Latronico, M.; Mastrorilli, P.; Todisco, S.; Gallo, V. *Inorg. Chem.* **2012**, *51*, 12682.
(23) DePoy, R.; Kodama, G. *Inorg. Chem.* **1985**, *24*, 2871.
(24) Fryzuk, M. D.; Piers, W. E.; Einstein, F. W. B.; Jones, T. *Can. J. Chem.* **1989**, *67*, 883.
(25) Pontiggia, A. J.; Chaplin, A. B.; Weller, A. S. *J. Organomet. Chem.* **2011**, *696*, 2870.
(26) Brunner, E. *J. Chem. Eng. Data* **1985**, *30*, 269.
(27) Ara, I.; Falvello, L. R.; Forniés, J.; Lalinde, E.; Martín, A.; Martínez, F.; Moreno, M. T. *Organometallics* **1997**, *16*, 5392.
(28) Adams, R. D.; Rassolov, V.; Zhang, Q. *Organometallics* **2012**, *31*, 2961.
(29) Kourkine, I. V.; Sargent, M. D.; Glueck, D. S. *Organometallics* **1998**, *17*, 125.
(30) Waterman, S. M.; Tolhurst, V.-A.; Humphrey, M. G.; Skelton, B. W.; White, A. H. *J. Organomet. Chem.* **1996**, *515*, 89.
(31) Uddin, M. N.; Mottalib, M. A.; Begum, N.; Ghosh, S.; Raha, A. K.; Haworth, D. T.; Lindeman, S. V.; Siddiquee, T. A.; Bennett, D. W.; Hogarth, G.; Nordlander, E.; Kabir, S. E. *Organometallics* **2009**, *28*, 1514.
(32) Macgregor, S. A.; Wondimagegn, T. *Organometallics* **2007**, *26*, 1143.
(33) Kabir, S. E.; Ahmed, F.; Ghosh, S.; Hassan, M. R.; Islam, M. S.; Sharmin, A.; Tocher, D. A.; Haworth, D. T.; Lindeman, S. V.; Siddiquee, T. A.; Bennett, D. W.; Hardcastle, K. I. *J. Organomet. Chem.* **2008**, *693*, 2657.
(34) Rahman, M. A.; Begum, N.; Ghosh, S.; Hossain, M. K.; Hogarth, G.; Tocher, D. A.; Nordlander, E.; Kabir, S. E. *J. Organomet. Chem.* **2011**, *696*, 607.
(35) Knox, S. A. R.; Lloyd, B. R.; Orpen, A. G.; Vinas, J. M.; Weber, M. *J. Chem. Soc., Chem. Commun.* **1987**, 1498.
(36) Lorenzini, F.; Patrick, B. O.; James, B. R. *Inorg. Chem.* **2007**, *46*, 8998.
(37) Shaw, B. K.; Patrick, B. O.; Fryzuk, M. D. *Organometallics* **2012**, *31*, 783.
(38) Shima, T.; Suzuki, H. *Organometallics* **2005**, *24*, 1703.
(39) Arif, A. M.; Chandler, D. J.; Jones, R. A. *Inorg. Chem.* **1987**, *26*, 1780.
(40) Roberts, D. A.; Steinmetz, G. R.; Breen, M. J.; Shulman, P. M.; Morrison, E. D.; Duttera, M. R.; DeBrosse, C. W.; Whittle, R. R.; Geoffroy, G. L. *Organometallics* **1983**, *2*, 846.
(41) Breen, M. J.; Geoffroy, G. L.; Rheingold, A. L.; Fultz, W. C. *J. Am. Chem. Soc.* **1983**, *105*, 1069.
(42) Calvert, R. B.; Shapley, J. R. *J. Am. Chem. Soc.* **1978**, *100*, 7726.
(43) Algarra, A. G.; Sewell, L. J.; Johnson, H. C.; Macgregor, S. A.; Weller, A. S. *Dalton Trans.* **2014**, *43*, 11118.

(44) Perutz, R. N.; Sabo-Etienne, S. *Angew. Chem. Int. Ed.* **2007**, *46*, 2578.
(45) Stevens, C. J.; Dallanegra, R.; Chaplin, A. B.; Weller, A. S.; Macgregor, S. A.; Ward, B.; McKay, D.; Alcaraz, G.; Sabo-Etienne, S. *Chem. Eur. J.* **2011**, *17*, 3011.
(46) Crabtree, R. H. *The Organometallic Chemistry of the Transition Metals*; Wiley-Interscience, 2005.
(47) Mealli, C.; Ienco, A.; Galindo, A.; Carreño, E. P. *Inorg. Chem.* **1999**, *38*, 4620.
(48) Klingert, B.; Rheingold, A. L.; Werner, H. *Inorg. Chem.* **1988**, *27*, 1354.
(49) Pawley, R. J.; Moxham, G. L.; Dallanegra, R.; Chaplin, A. B.; Brayshaw, S. K.; Weller, A. S.; Willis, M. C. *Organometallics* **2010**, *29*, 1717.
(50) Vernet, R. D.; Boekelheide, V. *Proc. Natl. Acad. Sci. U.S.A.* **1974**, *71*, 2961.
(51) Martin, N. H.; Allen Iii, N. W.; Moore, J. C. *J. Mol. Graphics Modell.* **2000**, *18*, 242.
(52) Huertos, M. A.; Weller, A. S. *Chem. Sci.* **2013**, *4*, 1881.
(53) van der Veen, L. A.; Boele, M. D. K.; Bregman, F. R.; Kamer, P. C. J.; van Leeuwen, P. W. N. M.; Goubitz, K.; Fraanje, J.; Schenk, H.; Bo, C. *J. Am. Chem. Soc.* **1998**, *120*, 11616.
(54) Kranenburg, M.; van der Burgt, Y. E. M.; Kamer, P. C. J.; van Leeuwen, P. W. N. M.; Goubitz, K.; Fraanje, J. *Organometallics* **1995**, *14*, 3081.
(55) Irişli, S.; Sarikahya, F.; Sarikahya, Y. *Synth. React. Inorg. Met.-Org. Chem.* **1997**, *27*, 431.
(56) Pregosin, P. S. *NMR in Organometallic Chemistry*; Wiley-VCH, 2012.
(57) Chaplin, A. B.; Hooper, J. F.; Weller, A. S.; Willis, M. C. *J. Am. Chem. Soc.* **2012**, *134*, 4885.
(58) Achord, P. D.; Kiprof, P.; Barker, B. *J. Mol. Struct-THEOCHEM* **2008**, *849*, 103.
(59) Williams, G. L.; Parks, C. M.; Smith, C. R.; Adams, H.; Haynes, A.; Meijer, A. J. H. M.; Sunley, G. J.; Gaemers, S. *Organometallics* **2011**, *30*, 6166.
(60) Jones, R. A.; Wright, T. C. *Organometallics* **1983**, *2*, 1842.
(61) Jones, R. A.; Norman, N. C.; Seeberger, M. H.; Atwood, J. L.; Hunter, W. E. *Organometallics* **1983**, *2*, 1629.
(62) Nöth, H.; Thomas, S. *Eur. J. Inorg. Chem.* **1999**, *1999*, 1373.
(63) Dunbar, A. C.; Girolami, G. S. *Inorg. Chem.* **2013**, *53*, 888.
(64) Kim, D. Y.; Girolami, G. S. *Inorg. Chem.* **2010**, *49*, 4942.
(65) Daly, S. R.; Bellott, B. J.; Nesbit, M. A.; Girolami, G. S. *Inorg. Chem.* **2012**, *51*, 6449.
(66) Rosello-Merino, M.; Lopez-Serrano, J.; Conejero, S. *J. Am. Chem. Soc.* **2013**, *135*, 10910.
(67) van Leeuwen, P. W. N. M. *Appl. Catal., A* **2001**, *212*, 61.
(68) Garrou, P. E. *Chem. Rev.* **1985**, *85*, 171.
(69) Sewell, L. J.; Huertos, M. A.; Dickinson, M. E.; Weller, A. S.; Lloyd-Jones, G. C. *Inorg. Chem.* **2013**, *52*, 4509.
(70) Conley, B. L.; Williams, T. J. *Chem. Commun.* **2010**, *46*, 4815.
(71) Lu, Z.; Conley, B. L.; Williams, T. J. *Organometallics* **2012**, *31*, 6705.
(72) Kamer, P. C. J.; van Leeuwen, P. W. N. M.; Reek, J. N. H. *Acc. Chem. Res.* **2001**, *34*, 895.
(73) Birkholz, M.-N.; Freixa, Z.; van Leeuwen, P. W. N. M. *Chem. Soc. Rev.* **2009**, *38*, 1099.

# 6 Summary and future outlook

This thesis explored the reactivity of the {Rh(Xantphos)}$^+$ fragment with amine-boranes, with the ultimate goal of understanding the mechanism of the dehydropolymerisation of $H_3B{\cdot}NMeH_2$ to form polymeric $[H_2BNMeH]_n$. In the course of the investigations, the B—B homocoupling of $H_3B{\cdot}NMe_3$ was reported, and an investigation into hydroboration by the {Rh(Xantphos)}$^+$ fragment was conducted. The proposed dehydropolymerisation mechanism involves the slow formation of the catalytically active species, thought to involve N—H activation of the amine-borane. The isolation of related dimeric complexes may hint that a dimer is the active catalyst. The rate of polymerisation and the chain length were found to be affected by $H_2$ or using THF solvent, forming shorter and longer polymer chains, respectively.

A future extension to this work would be to further explore the factors that control polymer molecular weight, with the aim of producing tailored polyaminoboranes. Ultimately, a means of controlling the tacticity of the polymer chains would be useful, possibly using a chiral catalyst, that may enable the development of amine-boranes for a specific purpose, as has been demonstrated with isoelectronic polyolefins. Whether the results discussed in this thesis are more generally applicable to other dehydrocoupling systems would also be worthy of exploration.

Finally, exploration of whether the dehydrogenative homocoupling of $H_3B{\cdot}NMe_3$ could proceed catalytically warrants attention. By varying the Xantphos-based ligand and the tertiary amine-borane substrate, it may be possible to induce catalytic homocoupling to access synthetically useful diborane species.

# 7 Experimental

## 7.1 Experimental techniques

All manipulations, unless otherwise stated, were performed under an atmosphere of argon using standard Schlenk and glovebox techniques. Glassware was oven dried at 130 °C overnight and flamed under vacuum prior to use. $CH_2Cl_2$, THF, MeCN, $Et_2O$, pentane and hexane were dried using a Grubbs-type solvent purification system (MBraun SPS-800) and degassed by successive freeze-pump-thaw cycles. 1,2-$C_6H_4F_2$ (pretreated with alumina), $C_6H_5F$ and $CD_2Cl_2$ were dried over $CaH_2$, vacuum distilled and stored over 3 Å molecular sieves.

### 7.1.1 Nuclear Magnetic Resonance Spectroscopy

NMR spectra were recorded on Varian Unity 500 MHz, Bruker AVIII500, Bruker DPX250 or Bruker AVIII400 spectrometers at room temperature, unless otherwise stated. Residual protio solvent was used as a reference for $^1H$ NMR spectra in deuterated solvent samples. In 1,2-$C_6H_4F_2$ or $C_6H_5F$, the spectrometer was pre-locked and shimmed to a sample containing 25% $C_6D_6$ and 75% 1,2-$C_6H_4F_2$ and referenced to the centre of the downfield solvent multiplet (δ 7.07 or 7.11, respectively). $^{31}P\{^1H\}$ and $^{11}B$ NMR spectra were referenced externally against 85% $H_3PO_4$ and $BF_3{\cdot}OEt_2$, respectively. Chemical shifts are quoted in ppm. Coupling constants are quoted in Hz.

### 7.1.2 Mass spectrometry

Most electrospray ionisation mass spectrometry (ESI-MS) samples were recorded in Oxford using a Bruker MicrOTOF instrument directly connected to a modified Innovative Technology glovebox. The mass spectrometer was calibrated in positive ion mode using a 10 ng/mL mixture of tetraalkylammonium bromide salts

$[N(C_nH_{2n+1})_4]Br$ (n = 2 – 8, 12, 16, 18) in $CH_2Cl_2$. Typical acquisition parameters were: sample flow rate, 4 μL/min; nebuliser gas pressure, 0.4 bar; drying gas (argon) at 60 °C flowing at 4L/min; capillary voltage, 4.5 kV; funnel voltage, 200Vpp. The solvents used were 1,2-$C_6H_4F_2$ or $C_6H_5F$. Samples were diluted to a concentration of approximately 1 x $10^{-6}$ M before running.

Experiments using the pressurised sample infusion (PSI) ESI-MS technique were conducted at the University of Victoria, BC, Canada, under the supervision of Dr J. Scott McIndoe. A short length of PEEK tubing was connected from the reaction vessel to the Micromass Q-Tof mass spectrometer, and the sample infused using 1.5 psi 99.998% purity argon gas. The mass spectrometer was in positive ion mode using pneumatically assisted electrospray ionisation. Typical acquisition parameters were: capillary voltage, 2900 V; sample cone voltage, 15 V; extraction voltage, 0.5 V; source temperature, 92 °C; desolvation temperature, 192 °C; cone gas flow, 100 L $h^{-1}$; desolvation gas flow, 200 L $h^{-1}$; collision voltage, 2 V; MCP voltage, 2400 V. No smoothing of the data was performed.

GC-MS experiments were performed by Colin Sparrow (University of Oxford).

### 7.1.3 Gel permeation chromatography (GPC)

Gel permeation chromatography (GPC) was performed by Dr. George R. Whittell (University of Bristol, UK) on a Viscotek RImax chromatograph, equipped with an automatic sampler, a pump, an injector and inline degasser. The columns were contained within an oven (35°C) and consisted of styrene/divinyl benzene gels with pore sizes ranging from 500 Å to 100,000 Å. THF containing 0.1% w/w $[^nBu_4N]Br$ was used as the eluent at a flow rate of 1.0 mL $min^{-1}$. Samples were dissolved in the eluent

(2 mg $mL^{-1}$, unless otherwise stated), stirred for 1 hr at room temperature and filtered with a Ministart SRP 15 filter (polytetrafluoroethylene membrane of 0.45 μm pore size) before analysis. The calibration was conducted using a series of monodisperse polystyrene standards obtained from Aldrich.

### 7.1.4 Elemental microanalysis

Elemental microanalyses were performed by Elemental Microanalysis Ltd or Stephen Boyer at London Metropolitan University (UK).

### 7.1.5 X-ray crystallography

Structure determinations were carried out by Dr. Sebastian D. Pike (**6**, **3** and **8**) or myself, and relevant crystallographic data can be found in Tables in the Appendix. Data for **22**, **26**, **27** and **28** were collected on an Agilent Supernova diffractometer using graphite monochromated Cu Kα radiation (λ = 1.54180 Å) and a low temperature device; reduction and cell refinement was performed using CrysAlisPro.[1] Data for **6**, **3**, **8**, **9**, **10**, **14**, **15** and **24** were collected on a Enraf Nonious Kappa CCD difractometer using graphite monochromated Mo Kα radiation (λ = 0.71073 Å) and a low temperature device;[2] data were collected using COLLECT, reduction and cell refinement was performed using DENZO/SCALEPACK.[3] All structures were solved using Sir92[4] or Superflip.[5] All were refined using CRYSTALS.[6]

### 7.1.6 General procedure for hydrogenation

The sample was freeze-pump-thaw degassed twice, and backfilled with $H_2$ at 77 K (flask immersed in liquid $N_2$). The internal $H_2$ pressure on warming was *ca.* 4 atm.

## 7.2 Synthesis and characterisation

### 7.2.1 Starting materials

The starting materials $H_3B{\cdot}NMeH_2$,[7] $[H_2BNMe_2]_2$,[8] $H_3B{\cdot}NMe_2D$,[9] $D_3B{\cdot}NMe_2H$,[9] $D_3B{\cdot}NMe_2D$,[9] $D_3B{\cdot}NMe_3$,[9] $Na[BH_3NMe_2BH_3]$,[10] $H_3B{\cdot}NMe_2BH_2{\cdot}NMe_2H$,[8] $H_3B{\cdot}NMeHBH_2{\cdot}NMeH_2$[11] and $[Rh(\kappa^2_{P,P}\text{-Xantphos})(nbd)][BAr^F_4]$ (**1**)[12] were prepared by literature methods or variations thereof. $H_3B{\cdot}PCy_3$ and $H_3B{\cdot}PEt_3$ were prepared by Dr Miguel Huertos. $H_2B{=}N^iPr_2$ was prepared by a modification of the literature method,[8] instead using **6** (1 mol% loading) to produce $H_2B{=}N^iPr_2$ quantitatively in 24 hours. *Tert*-butylethylene (TBE), cyclohexene and 1-hexene were dried over sodium, vacuum distilled and stored over 3 Å molecular sieves. $H_3B{\cdot}NMe_3$ and $H_3B{\cdot}NMe_2H$ were purchased from Aldrich and sublimed once and twice prior to use ($5 \times 10^{-2}$ mbar, 298 K), respectively.

### 7.2.2 Synthesis of new complexes

**$[Rh(\kappa^3_{P,O,P}\text{-Xantphos})(H)_2(\eta^1\text{-}H_3B{\cdot}NMe_3)][BAr^F_4]$ (3)**

To a Young's crystallisation flask containing **1** (50 mg, 0.03 mmol) and $H_3B{\cdot}NMe_3$ (2.2 mg, 0.03 mmol) was added $C_6H_5F$ (1 mL), and the mixture immediately frozen in liquid $N_2$. The argon headspace was removed *in vacuo* and replaced with 4 atm $H_2$. On warming to room temperature, the mixture was shaken, yielding a pale orange solution. *In situ* NMR spectroscopy confirmed complete conversion to **3**. Pale yellow crystals suitable for X-ray diffraction (alongside some brown oil) were obtained by layering the solution with pentane under $H_2$ at 5 °C. After crystallisation, the supernatant solution was decanted, the solid/oil washed three times with pentane and dried *in vacuo* (< 2 minutes to avoid decomposition). The solid was redissolved in $C_6H_5F$ or $CD_2Cl_2$, transferred to a high pressure NMR tube and immediately placed

under 4 atm $H_2$, yielding the NMR data given below. In the $^1H$ NMR data reported, pentane and $H_2$ are also present (in $CD_2Cl_2$, pentane: δ 0.89, t and δ 1.30, m; $H_2$: δ 4.60, s). Pure solid material could not be isolated due to the instability of **3** upon removal of the $H_2$ atmosphere.

**$^1$H NMR (500 MHz, $C_6H_5F$):** δ 8.35 (br, 8H, $[BAr^F_4]^-$), 7.64 (br, 4H, $[BAr^F_4]^-$), 1.65 (s, 3H, Xantphos $CH_3$), 1.35 (s, 3H, Xantphos $CH_3$), 1.30 (br s, 9H, $NMe_3$), –0.97 (br, 3H, $BH_3$), –14.55 (br m, 1H, RhH), –19.00 (dtd, 1H, RhH). The aryl signals from the Xantphos ligand were obscured by the solvent.

**$^1$H{$^1$H @ δ –14.55} NMR (500 MHz, $C_6H_5F$, selected data):** δ –0.97 (br, 3H, $BH_3$), –19.00 (dt, $^2J_{PH}$ = 14, $^1J_{RhH}$ = 27, 1H, RhH).

**$^1$H{$^{31}$P @ δ 44.7} NMR (500 MHz, $C_6H_5F$, selected data):** δ –0.97 (br, 3H, $BH_3$), –14.55 (dd, $^2J_{HH}$ = 6, $^1J_{RhH}$ = 27, 1H, RhH), –19.00 (dt, $^2J_{HH}$ = 7, $^1J_{RhH}$ = 27, 1H, RhH).

**$^1$H NMR (500 MHz, $CD_2Cl_2$):** δ 7.90–7.07 (m, 26H, aryl groups from Xantphos), 7.74 (br, 8H, $[BAr^F_4]^-$), 7.56 (br, 4H, $[BAr^F_4]^-$), 1.93 (s, 3H, Xantphos $CH_3$), 1.55 (br s, 9H, $NMe_3$), 1.49 (s, 3H, Xantphos $CH_3$), –0.97 (br, 3H, $BH_3$), –14.69 (br m, 1H, RhH), –19.11 (br m, 1H, RhH). The signal at δ –0.97 sharpened considerably on $^{11}$B decoupling.

**$^1$H NMR (500 MHz, $CD_2Cl_2$, 218 K):** δ 7.84–7.04 (m, 26H, aryl groups from Xantphos), 7.74 (br, 8H, $[BAr^F_4]^-$), 7.52 (br, 4H, $[BAr^F_4]^-$), 1.81 (s, 3H, Xantphos $CH_3$), 1.35 (s, 3H, Xantphos $CH_3$), 1.32 (br s, 9H, $NMe_3$), –6.23 (v br, 1H, Rh-*H*-B), –14.35 (br m, 1H, RhH), –19.19 (br m, 1H, RhH). A peak for the unbound B-H groups was not observed, presumably as it is broad and obscured by the aliphatic signals.

**$^{31}$P{$^1$H} NMR (202 MHz, $C_6H_5F$):** δ 44.7 (d, $^1J_{RhP}$ = 118).

**$^{31}$P{$^1$H} NMR (202 MHz, $CD_2Cl_2$):** δ 43.6 (d, $^1J_{RhP}$ = 115).

**$^{31}$P{$^1$H} NMR (202 MHz, $CD_2Cl_2$, 218 K):** δ 44.2 (d, $^1J_{RhP}$ = 115).

**$^{11}$B NMR (160 MHz, $C_6H_5F$):** δ –6.0 (s, $[BAr^F_4]^-$), –8.7 (br, $BH_3$).

**$^{11}$B NMR (160 MHz, $CD_2Cl_2$):** δ –6.6 (s, $[BAr^F{}_4]^-$), –8.7 (br, $BH_3$).

ESI-MS was attempted but not obtained due to decomposition to unidentified species.

**[Rh(κ$^3$$_{P,O,P}$-Xantphos)$(H)_2$(THF)][$BAr^F{}_4$] (5)**

In a Young's crystallisation tube, **1** (40 mg, 0.02 mmol) was dissolved in THF (~ 1 mL) and hydrogenated to 4 atm. The colour changed from orange to pale yellow and *in situ* NMR spectroscopy showed the quantitative formation of **5**. Upon layering with pentane and storing at 5 ˚C, some solid material coated in oil was formed. $^1$H and $^{31}$P{$^1$H} NMR spectra of the material revealed **5** as the only organometallic product, with some excess THF (δ 3.75 and 1.78) and pentane (δ 1.32 and 0.93) also present.

**$^1$H NMR (500 MHz, 1,2-$C_6H_4F_2$):** δ 8.32 (br, 8H, $[BAr^F{}_4]^-$), 7.68 (br, 4H, $[BAr^F{}_4]^-$), 2.90 (br, 4H, bound THF $CH_2$ groups at the 3 and 4 positions), 1.92 (s, 3H, Xantphos $CH_3$), 1.49 (s, 3H, Xantphos $CH_3$), 0.84 (br, 4H, THF $CH_2$ groups at the 2 and 5 positions), –19.01 (1H, br dtd, $^2J_{PH}$ ~13, RhH), –19.88 (1H, br dtd, $^2J_{PH}$ ~13, RhH). The Xantphos aryl signals were obscured by the solvent.

**$^1$H{$^{31}$P} NMR (500 MHz, 1,2-$C_6H_4F_2$, selected data):** δ –19.00 (1H, dd, $^1J_{RhH}$ = 31, $^2J_{HH}$ = 8), –19.87 (1H, dd, $^1J_{RhH}$ = 29, $^2J_{HH}$ = 8).

**$^{31}$P{$^1$H} NMR (202 MHz, 1,2-$C_6H_4F_2$):** δ 43.8 (d, $^1J_{RhP}$ = 118)

**ESI-MS (1,2-$C_6H_4F_2$, 60 ˚C, 4.5 kV):** *m/z* [**5**]$^+$ 755.18 (calc. 755.17), minor peak, displays the expected isotopic pattern. Major peak observed has *m/z* 683.12 and corresponds to $[Rh(Xantphos)(H)_2]^+$ (calc. 683.12).

**[Rh(κ$^2_{P,P}$-Xantphos)(η$^2$-$H_2B(CH_2CH_2{}^tBu)\cdot NMe_3$)][$BAr^F{}_4$] (6)**

**3** was formed *in situ* in a Young's flask under 4 atm $H_2$ (**1**: 300 mg, 0.18 mmol; $H_3B\cdot NMe_3$: 13.2 mg, 0.18 mmol) in $C_6H_5F$ (3 mL). The solution was rapidly degassed with three successive freeze-pump-thaw cycles and placed under an atmosphere of argon. TBE (75 μL, 0.57 mmol) was injected *via* a gastight syringe and the reaction shaken. Within 1 minute, the colour changed from pale orange to dark blue. After 10 minutes, the solution was added to stirring pentane (30 mL) and precipitated as a blue solid. The solid was washed with pentane (3 x 5 mL) and dried *in vacuo* for several hours. Yield: 248 mg (79 %). Crystals suitable for X-ray diffraction were obtained by recrystallisation from 1,2-$C_6H_4F_2$/pentane at –30 ˚C.

**$^1$H NMR (500 MHz, $CD_2Cl_2$):** δ 7.73 (br, 8H, [$BAr^F{}_4$]$^-$), 7.62–6.52 (m, 26H, Xantphos aryl groups) 7.56 (br, 4H, [$BAr^F{}_4$]$^-$), 2.47 (s, 9H, $NMe_3$), 1.78 (s, 3H, Xantphos $CH_3$), 1.67 (s, 3H, Xantphos $CH_3$), 1.59 (m, 2H, $CH_2C\underline{H_2}{}^tBu$), 0.82 (br, 9H, $^t$Bu), 0.50 (br m, 2H, $C\underline{H_2}CH_2{}^tBu$), –6.91 (br, 2H, $BH_2$).

**$^1$H{$^{11}$B} NMR (500 MHz, $CD_2Cl_2$, selected data):** δ 1.59 (m, 2H, $CH_2C\underline{H_2}{}^tBu$), 0.82 (br, 9H, $^t$Bu), 0.50 (br m, 2H, $C\underline{H_2}CH_2{}^tBu$), –6.89 (virtual triplet, $^2J_{PH}$ ~ 36, $^1J_{RhH}$ ~ 36, 2H, $BH_2$). The signal at δ 0.50 sharpens slightly on $^{11}$B decoupling.

**$^{31}$P{$^1$H} NMR (202 MHz, $CD_2Cl_2$):** δ 26.8 (d, $^1J_{RhP}$ = 182).

**$^{11}$B NMR (160 MHz, $CD_2Cl_2$):** δ 36 (v br, $BH_2$), –6.6 (s, [$BAr^F{}_4$]$^-$).

**ESI-MS ($C_6H_5F$, 60 ˚C, 4.5 kV):** *m/z* [**6**]$^+$ 838.31 (calc. 838.30). Peak displays the expected isotopic pattern.

**Elemental Microanalysis:** Calc. $C_{80}H_{68}B_2F_{24}NOP_2Rh$ (1701.84 g mol$^{-1}$): C, 56.46; H, 4.03; N, 0.82. Found: C, 56.32; H, 3.95; N, 0.93.

**[Rh(κ$^3_{P,O,P}$-Xantphos)(H)$_2$(H$_2$B(CH$_2$CH$_2$$^t$Bu)·NMe$_3$)][BAr$^F_4$] (7)**

Hydrogenation (4 atm) of **6** in a high pressure NMR tube in 1,2-$C_6H_4F_2$ yielded an approximately 10:1 mixture of **7**:**6** (by $^1$H NMR spectroscopy). **7** could not be isolated, instead losing $H_2$ over the timescale of crystallisation, yielding **6**. The *in situ* NMR data of **7** are presented below. Peaks due to **6** and dissolved $H_2$ were also present.

**$^1$H NMR (500 MHz, 1,2-$C_6H_4F_2$):** δ 8.33 (br, 8H, [BAr$^F_4$]$^-$), 7.69 (br, 4H, [BAr$^F_4$]$^-$), 1.82 (s, 9H, NMe$_3$), 1.87 (s, 3H, Xantphos CH$_3$), 1.60 (s, 3H, Xantphos CH$_3$), 0.96 (m, 2H, CH$_2$<u>CH$_2$</u>$^t$Bu), 0.73 (s, 9H, $^t$Bu), –0.16 (m, 2H, <u>CH$_2$</u>CH$_2$$^t$Bu), –1.82 (br, 2H, H$_2$B), –15.13 (br, 1H, RhH), –19.70 (br, 1H, RhH). The Xantphos aryl signals were obscured by the solvent. The signal at -1.82 sharpens upon $^{11}$B decoupling.

**$^1$H{$^{31}$P} NMR (500 MHz, 1,2-$C_6H_4F_2$, selected data):** δ –1.82 (br, 2H, H$_2$B), –15.13 (br dd, $^1J_{RhH}$ = 26, $^2J_{HH}$ unresolved, 1H, RhH), –19.70 (br dd, $^1J_{RhH}$ = 29, $^2J_{HH}$ ~ 5, 1H, RhH).

**$^{31}$P{$^1$H} NMR (202 MHz, 1,2-$C_6H_4F_2$):** δ 41.8 (d, $^1J_{RhP}$ = 116).

**$^{11}$B NMR (160 MHz, 1,2-$C_6H_4F_2$):** δ –1.0 (br, BH$_2$), –6.2 (s, [BAr$^F_4$]$^-$).

**[Rh(κ$^2_{P,P}$-Xantphos)(NMe$_3$·H$_2$B-BH$_2$·NMe$_3$)][BAr$^F_4$] (8)**

$C_6H_5F$ (1.5 mL) was added to a Young's flask containing **6** (75 mg, 0.04 mmol) and H$_3$B·NMe$_3$ (60 mg, 0.82 mmol). The reaction mixture was sealed under argon for 3 h, during which time the colour changed from blue to orange. *In situ* NMR spectroscopy showed an approximately 50:50 mixture of **3** and **8**. To drive the reaction towards complete conversion to **8**, cyclohexene (75 μL, 0.74 mmol) was added and the solution turned immediately green. After 2 hours, a red/orange solution resulted. The solution was filtered into a Schlenk, the volume of $C_6H_5F$ reduced to ~ 1 mL, and

layered with pentane at room temperature, yielding red crystals overnight. The solid was washed with pentane with sonication (3 x 2 mL) and dried *in vacuo* for several hours. Yield: 50 mg (67 %). Crystals suitable for X-ray diffraction were obtained by layering the mixture of **3** and **8** with pentane at 5 ˚C, producing red crystals of **8** alongside brown oil, presumably decomposed **3**.

**$^{1}$H NMR (500 MHz, $CD_2Cl_2$):** δ 7.73 (br, 8H, $[BAr^F_4]^-$), 7.57 (br, 4H, $[BAr^F_4]^-$), 7.64 – 6.81 (m, 26H, aryl groups from Xantphos), 2.24 (s, 18H, $NMe_3$), 1.74 (s, 6H, Xantphos $CH_3$), 1.51 (v br, 2H, unbound BH), −8.47 (br, 2H, bound BH). The signals at δ 1.51 and −8.47 sharpen upon $^{11}$B decoupling.

**$^{1}$H NMR (500 MHz, $CD_2Cl_2$, 218 K):** δ 7.74 (br, 8H, $[BAr^F_4]^-$), 7.53 (br, 4H, $[BAr^F_4]^-$), 7.51 – 6.59 (m, 26H, aryl groups from Xantphos), 2.40 (s, 9H, $NMe_3$), 1.77 (s, 3H, Xantphos $CH_3$), 1.67 (s, 9H, $NMe_3$), 1.51 (s, 3H, Xantphos $CH_3$), −8.01 (br d, $^{2}J_{PH}$ = 42, 1H, bound BH), −8.54 (br d, $^{2}J_{PH}$ = 41, 1H, bound BH). The two free B-H signals were not observed, presumably broad and obscured by the aliphatic signals. Upon $^{31}$P decoupling, the signals at δ −8.01 and −8.54 collapse to broad apparent singlets.

**$^{31}$P{$^{1}$H} NMR (202 MHz, $CD_2Cl_2$):** δ 26.2 (d, $^{1}J_{RhP}$ = 172).

**$^{31}$P{$^{1}$H} NMR (202 MHz, $CD_2Cl_2$, 218 K):** δ 29.0 (dd, $^{1}J_{RhP}$ = 164, $^{2}J_{PP}$ = 35), 28.2 (dd, $^{1}J_{RhP}$ = 168, $^{2}J_{PP}$ = 35).

**$^{11}$B NMR (160 MHz, $CD_2Cl_2$):** δ -6.6 (s, $[BAr^F_4]^-$), -11.3 (br, $BH_2$).

**ESI-MS ($C_6H_5F$, 60 ˚C, 4.5 kV):** *m/z* [**8**]$^+$ 825.30 (calc. 825.30). Peak displays the expected isotopic pattern.

**Elemental Microanalysis:** Calc. $C_{77}H_{66}B_3F_{24}N_2OP_2Rh$ (1688.61 g mol$^{-1}$): C, 54.77; H, 3.94; N, 1.66. Found: C, 54.64; H, 3.87; N, 1.66.

**[Rh(κ$^2_{P,P}$-Xantphos)(η$^2$-$H_2B(CH_2CH_2SiMe_3)\cdot NMe_3$)][$BAr^F_4$] (9)**

Compound **9** was prepared by Part II student R. Torry-Harris.[13] **3** was formed in a Young's flask from the hydrogenation (4 atm) of **1** (100 mg, 0.06 mmol) and $H_3B\cdot NMe_3$ (4.4 mg, 0.06 mmol) in 1,2-$C_6H_4F_2$. The flask was degassed (3 freeze–pump–thaw cycles), opened to an argon atmosphere, and trimethylvinylsilane (40 μL, 0.272 mmol) was added. The solution turned from pale yellow to dark green. After 10 minutes, the volatiles were removed *in vacuo*, and the solid was washed with pentane (2 × 5 mL) with sonication. The solid was dried *in vacuo*, affording a blue/green powder, mass 86 mg (82% yield). Crystals suitable for X-ray diffraction were grown from recrystallisation from 1,2-$C_6H_4F_2$ and pentane at −30 °C.

**$^1$H NMR (500 MHz, 1,2-$C_6H_4F_2$):** δ 8.33 (br, 8H $[BAr^F_4]^-$), 7.69 (br, 4H, $[BAr^F_4]^-$), 2.61 (s, 9H, $NMe_3$), 1.73 (s, 3H, Xantphos $CH_3$), 1.67 (s, 3H, Xantphos $CH_3$), 1.17 (m, 2H, $\underline{CH_2}SiMe_3$), 0.78 (br m, 2H, $\underline{CH_2}BH_2NMe_3$), 0.06 (s, 9H, $SiMe_3$), −6.54 (br, 2H, $BH_2$). The peak at δ −6.54 sharpens into an overlapping doublet of doublets (virtual triplet) upon decoupling to $^{11}$B ($^1J_{RhH}$ = 36 and $^2J_{P\mathit{trans}H}$ = 36). Signals from the Xantphos aryl ligand were not observed, presumably obscured by the solvent.

**$^{29}$Si-$^1$H HMBC NMR (500 MHz, 1,2-$C_6H_4F_2$):** correlation observed between silicon at δ 2.1 and protons at δ 1.17 and 0.06.

**$^{31}$P{$^1$H} NMR (202 MHz, 1,2-$C_6H_4F_2$):** δ 26.7 (d, $^1J_{RhP}$ = 182).

**$^{11}$B NMR (160 MHz, 1,2-$C_6H_4F_2$):** δ 37 (br, $BH_2$), −6.2 (s, $[BAr^F_4]^-$).

**ESI-MS (1,2-$C_6H_4F_2$, 60 °C, 4.5 kV):** *m/z* 854.28 [**9**]$^+$ (calc. 854.28). Peak displays the expected isotopic pattern.

**Elemental Microanalysis:** Calc. $RhP_2OC_{79}H_{68}B_2F_{24}NSi$ (1717.94 g mol$^{-1}$): C, 55.23; H, 3.99; N, 0.82. Found: C, 55.16; H, 4.03; N, 0.88.

**[Rh(κ$^2$-$_{P,P}$-Xantphos)(η$^2$-H$_2$B(hexyl)·NMe$_3$)][BAr$^F{}_4$] (10)**

In a Young's crystallisation tube, a solution of 1-hexene (75 μL, 0.60 mmol) in 1,2-$C_6H_4F_2$ (2 mL) was added to **6** (25 mg, 0.02 mmol) and $H_3B{\cdot}NMe_3$ (20 mg, 0.27 mmol). After 24 hours, the mixture was dark brown. The volume was reduced to *ca.* 1 mL, layered with hexanes and stored at 5 °C, forming dark orange oil-coated crystals of **10** suitable for X-ray diffraction (11 mg), although NMR spectroscopy of the crystals indicated ~20% **11** was also present, presumably the oil.

**$^1$H NMR (500 MHz, 1,2-$C_6H_4F_2$):** δ 8.34 (br, 8H, [BAr$^F{}_4$]$^-$), 7.69 (br, 4H, [BAr$^F{}_4$]$^-$), 2.61 (s, 9H, $NMe_3$), 1.72 (s, 6H, Xantphos $CH_3$ groups), 1.86–0.74 (m, 13H, hexyl chain), −6.58 (br, 2H, $BH_2$). Upon decoupling to $^{11}$B, the signal at δ −6.58 collapsed to an overlapping doublet of doublets (virtual triplet) ($^1J_{RhH}$ = 34, $^2J_{P\mathit{trans}H}$ = 34). The Xantphos aryl signals were obscured by the solvent.

**$^{31}$P{$^1$H} NMR (202 MHz, 1,2-$C_6H_4F_2$):** δ 35.7 (d, $^1J_{RhP}$ = 182).

**$^{11}$B NMR (160 M Hz, 1,2-$C_6H_4F_2$):** δ 35.7 (br, $BH_2$), −6.2 (s, [BAr$^F{}_4$]$^-$).

**ESI-MS (1,2-$C_6H_4F_2$, 60 °C, 4.5 kV):** *m/z* 838.31 [**10**]$^+$ (calc. 838.30). Peak displays the expected isotopic pattern.

**[Rh(κ$^3{}_{P,O,P}$-Xantphos)(H)$_2$(η$^1$-H$_3$B·PCy$_3$)][BAr$^F{}_4$] (12)**

**12** was prepared *in situ* in an analogous manner to **3** using **1** (20 mg, 0.01 mmol) and $H_3B{\cdot}PCy_3$ (2.5 mg, 0.01 mmol). **12** could not be isolated due to loss of dihydrogen upon removal from the $H_2$ atmosphere. Attempts to recrystallise under $H_2$ resulted in impure oil, as measured by NMR spectroscopy. However, the following NMR spectroscopic data were obtained from the hydrogenation of preformed **13**.

**$^{1}$H NMR (500 MHz, $CD_2Cl_2$):** δ 8.10–7.27 (br, 26H, Xantphos aryl signals), 7.73 (br, 8H, $[BAr^F_4]^-$), 7.56 (s, 4H, $[BAr^F_4]^-$), 2.05–0.81 (m, 39H, overlapping Cy and Xantphos $CH_3$ signals), −1.63 (br, 3H, $BH_3$), −14.80 (br, 1H, RhH), −19.40 (br, 1H, RhH).

**$^{31}$P{$^{1}$H} NMR (202 MHz, $CD_2Cl_2$):** δ 41.8 (d, $^{1}J_{RhP}$ = 116), 20.2 (br, $PCy_3$).

**$^{11}$B NMR (160 MHz, $CD_2Cl_2$):** δ −6.6 (s, $[BAr^F_4]^-$), −43.5 (br, $BH_3$).

**[Rh(κ$^2_{P,P}$-Xantphos)(η$^2$-$H_3B$·$PCy_3$)][$BAr^F_4$] (13)**

**12** (starting from 55 mg **1**) was formed *in situ* under $H_2$ (4 atm) in a Young's crystallisation flask. The flask was degassed (3 freeze–pump–thaw cycles), opened to an argon atmosphere, and TBE (8 μL, 0.06 mmol) was added. The solution turned from pale yellow to dark green. After 5 minutes, the volatiles were removed *in vacuo* to prevent onward reactivity, and washed twice with pentane (3 mL) with sonication. The resulting oily solid was redissolved in 1,2-$C_6H_4F_2$ and layered with pentane, affording green needle-like crystals (not suitable for X-ray diffraction) at −30 °C. Mass 40 mg (73% yield).

**$^{1}$H NMR (500 MHz, $CD_2Cl_2$):** δ 7.73 (br, 8H, $[BAr^F_4]^-$), 7.56 (br, 4H, $[BAr^F_4]^-$), 7.64 – 6.40 (m, 26H, Xantphos aryl signals), 1.86–1.08 (m, 39H, $PCy_3$ and Xantphos $CH_3$ signals), −2.38 (br, 3H, $BH_3$). Upon decoupling to $^{11}$B, the signal at −2.38 sharpened.

**$^{31}$P{$^{1}$H} NMR (202 MHz, $CD_2Cl_2$):** δ 28.9 (d, $^{1}J_{RhP}$ = 190), 17.3 (br, $PCy_3$).

**$^{11}$B NMR (160 M Hz, $CD_2Cl_2$):** δ −3.0 (br, $BH_3$), −6.6 (s, $[BAr^F_4]^-$).

ESI-MS (1,2-$C_6H_4F_2$, 60 °C, 4.5 kV) was attempted but decomposition resulted under these conditions.

**Elemental Microanalysis:** Calc. $RhP_3OC_{89}H_{80}B_2F_{24}$ (1839.03 g mol$^{-1}$): C, 58.13; H, 4.38. Found: C, 57.43; H, 4.59.

**[Rh(κ$^2_{P,P}$-Xantphos)(η$^2$-H$_2$B(CH$_2$CH$_2$$^t$Bu)·PCy$_3$)][BAr$^F_4$] (14)**

The procedure for forming **13** was followed, by addition of TBE to **12** (0.02 mmol). Upon leaving the mixture for 45 minutes, a mixture of **13** and **14** was present. Standing for 12 hours resulted in a decreased amount of **13**, but **15** was observed (see below for an independent synthesis of **15**). Due to this mixture, attempts to isolate pure **14** were unsuccessful. A small number of green single crystals suitable for diffraction were obtained by leaving the reaction mixture for several, layering the solution with pentane and storing at −30 °C. Analysis by NMR spectroscopy of these crystals dissolved in $CD_2Cl_2$ indicated a mixture of **13** and **14**. Due to the mixture, only selected NMR data for **14** are available as the alkyl and aryl regions are obscured by **13** signals. Upon repeating the reaction, several orange crystals of **15** formed, which could be mechanically separated from green **13** and **14**, whose spectroscopic data match that from independently synthesised **15** (see below).

**$^1$H NMR (500 MHz, $CD_2Cl_2$):** δ −5.92 (br, Rh–$H_2$B). The signal sharpened to an overlapping doublet of doublets (virtual triplet) upon decoupling to $^{11}$B ($^1J_{RhH}$ = 33 and $^2J_{PtransH}$ = 33).

**$^{31}$P{$^1$H} NMR (202 MHz, $CD_2Cl_2$)**: δ 29.5 (d, $^1J_{RhP}$ = 190), 8.8 (br, $PCy_3$).

**$^{11}$B NMR (160 MHz, $CD_2Cl_2$):** δ 18.5 (br, $BH_3$), −6.6 (s, [BAr$^F_4$]$^-$).

ESI-MS (1,2-$C_6H_4F_2$, 60 °C, 4.5 kV) was attempted but decomposition resulted under these conditions.

**[Rh(κ$^3_{P,O,P}$-Xantphos)(PCy$_3$)][BAr$^F_4$] (15)**

1,2-$C_6H_4F_2$ (0.4 mL) was added to **6** (17 mg, 0.010 mmol) and $PCy_3$ (0.011 mmol) in a small Schlenk flask. The colour changed from blue to orange immediately on mixing. The solvent was removed *in vacuo*, and the remaining orange oil was washed three

times with pentane (2 mL) with sonication. Stirring under vacuum afforded an orange powder. Yield: 13 mg (71%).

**$^{1}$H NMR (500 MHz, $CD_2Cl_2$):** δ 7.72 (br, 8H, $[BAr^F_4]^-$), 8.05–7.71 (m, 30H, Xantphos aryl signals and second $[BAr^F_4]^-$ peak), 1.66 (s, 6H, Xantphos methyl signals), 1.84–0.50 (m, 33H, $PCy_3$).

**$^{31}$P{1H} NMR (202 MHz, $CD_2Cl_2$):** δ 55.4 (dt, $^1J_{RhP}$ = 192, $^2J_{PP}$ = 34, $PCy_3$), 31.6 (dd, $^1J_{RhP}$ = 155, $^2J_{PP}$ = 34, Xantphos).

**ESI-MS (1,2-$C_6H_4F_2$, 60 °C, 4.5 kV):** *m/z* 961.33 [**15**]$^+$ (calc. 961.33). Peak displays the expected isotopic pattern.

**[Rh(κ$^3$$_{P,O,P}$-Xantphos)(H)$_2$(η$^1$-$H_3B{\cdot}PEt_3$)][$BAr^F_4$] (16)**

**16** was prepared *in situ* in an analogous manner to **12** using **1** (20 mg, 0.01 mmol) and $H_3B{\cdot}PEt_3$ (1.6 mg, 0.01 mmol) in 1,2-$C_6H_4F_2$. Isolation attempts resulted in decomposition. Therefore, only selected NMR data are available:

**$^{1}$H NMR (500 MHz, 1,2-$C_6H_4F_2$):** δ 8.33 (br, 8H, $[BAr^F_4]^-$), 7.69 (br, 4H, $[BAr^F_4]^-$), −1.72 (br, 3H, $BH_3$), −13.96 (br, 1H, RhH), −18.89 (dtd, $^1J_{RhH}$ = 27, $^2J_{PH}$ = 14, $^2J_{HH}$ = 7, 1H, RhH).

**$^{31}$P{$^{1}$H} NMR (202 MHz, 1,2-$C_6H_4F_2$)**: δ 43.4 (d, $^1J_{RhP}$ = 115), 13.5 (br, $PCy_3$).

**$^{11}$B NMR (160 MHz, 1,2-$C_6H_4F_2$):** δ −6.6 (s, $[BAr^F_4]^-$), −41.5 ($BH_3$; overlapping with signal for free $H_3B{\cdot}PEt_3$ at −41.9).

**[Rh(κ$^3$$_{P,O,P}$-Xantphos)(H)$_2$(η$^1$-$H_3B{\cdot}NMe_2H$)][$BAr^F_4$] (18)**

**6** (20 mg, 0.012 mmol) was added to a high pressure NMR tube and dissolved in 0.4 mL $C_6H_5F$. The solution was added to 2 eq. $H_3B{\cdot}NMe_2H$ (1.4 mg, 0.024 mmol) and an immediate colour change to yellow was observed. The sample was frozen and

monitored by NMR spectroscopy, which showed the formation of **18**. **18** could not be isolated under these conditions as, during the course of the dehydrocoupling to yield $[H_2BNMe_2]_2$, **7** is formed slowly (around 25% **7** after 1 hour of reaction). Selected NMR data for **18**:

**$^1$H NMR (250 MHz, $C_6H_5F$):** δ –1.29 (br, 3H, $BH_3$); –14.11 (br, 1H, RhH); –19.05 (dtd, $^2J_{PH}$ = 15, $^2J_{HH}$ = 6, $^1J_{RhH}$ = 27, 1H, RhH).

**$^{31}$P{$^1$H} NMR (101 MHz, $C_6H_5F$):** δ 44.5 (d, $^1J_{RhP}$ = 115).

**$^{11}$B NMR (80 MHz, $C_6H_5F$)**: δ –12, v br.

**[Rh(κ$^3_{P,O,P}$-Xantphos)(H)$_2$(η$^1$-H$_3$B·NMeH$_2$)][BAr$^F_4$] (19)**

An identical procedure to forming **18** was used, instead with $H_3B{\cdot}NMeH_2$ (1.1 mg, 0.025 mmol). Immediately, the colour changed to yellow, and **19** was observed with **7** by NMR spectroscopy (~ 5:1 **19**:**7**). Over 2 hours, **7**, **6** and **19** are present (~ 5:1:2 ratio, respectively) and the product of dehydrocoupling, $[HBNMe]_3$, was observed in the $^{11}$B NMR spectrum. Selected NMR data for **19**:

**$^1$H NMR (250 MHz, $C_6H_5F$):** δ –1.27 (br, 3H, $BH_3$); –14.10 (br, 1H, RhH); –19.06 (dtd, $^2J_{PH}$ = 14, $^2J_{HH}$ = 6, $^1J_{RhH}$ = 28, 1H, RhH).

**$^{31}$P{$^1$H} NMR (101 MHz, $C_6H_5F$):** δ 44.3 (d, $^1J_{RhP}$ = 114).

**$^{11}$B NMR (80 MHz, $C_6H_5F$)**: δ –17, v br.

**[Rh(κ$^3_{P,O,P}$-Xantphos)(H)$_2$(NMe$_2$H)][BAr$^F_4$] (20)**

$NMe_2H$ (2.0 M in THF solution, 60 μL, 0.12 mmol) was added to a solution of **1** (33 mg, 0.02 mmol) in 1 mL 1,2-$C_6H_4F_2$ in a Young's crystallisation tube. The sample was frozen in liquid $N_2$, and the argon headspace replaced with hydrogen (4 atm) to yield a pale yellow solution on warming. The solution was layered with pentane at 5 ˚C.

Pale yellow crystals (unsuitable for X-ray diffraction) were obtained, washed with pentane with sonication (3 x 3 mL), and dried *in vacuo*. Yield: 22 mg (69%).

**$^{1}$H NMR (500 MHz, 1,2-$C_6H_4F_2$):** δ 8.33 (br, 8H, $[BAr^F{}_4]^-$), 7.69 (br, 4H, $[BAr^F{}_4]^-$), 1.93 (s, 3H, Xantphos $CH_3$), 1.80 (d, $^3J_{HH}$ = 5, 6H, $NMe_2$), 1.77 (br, 1H, NH), 1.45 (s, 3H, Xantphos $CH_3$), –15.71 (br overlapping dtd, $^1J_{RhH}$ ~28, $^2J_{PH}$ ~ 15, $^2J_{HH}$ unresolved, RhH), –20.19 (dtd, $^1J_{RhH}$ = 32, $^2J_{PH}$ = 15, $^2J_{HH}$ = 10, 1H, RhH). The Xantphos aryl signals were obscured by the solvent.

**$^{1}$H{$^{31}$P} NMR (500 MHz, 1,2-$C_6H_4F_2$, selected data):** δ –15.71 (dd, $^1J_{RhH}$ ~ 18, $^2J_{HH}$ ~ 10, RhH), –20.19 (dd, $^1J_{RhH}$ = 32, $^2J_{HH}$ = 10, 1H, RhH).

**$^{31}$P{$^{1}$H} NMR (202 MHz, 1,2-$C_6H_4F_2$):** δ 44.3 (d, $^1J_{RhP}$ = 118).

**ESI-MS (1,2-$C_6H_4F_2$, 60 °C, 4.5 kV):** *m/z* [**20**]$^+$ 728.17 (calc. 728.17). Peak displays the expected isotopic pattern.

**Elemental Microanalysis:** Calc. $RhP_2OC_{73}H_{53}BF_{24}N$ (1591.86 g mol$^{-1}$): C, 55.08; H, 3.36; N, 0.88. Found: C, 55.24; H, 3.42; N, 0.97.

**[Rh(κ$^3$$_{P,O,P}$-Xantphos)(H){B(H)N$^i$Pr$_2$}(η$^1$-$H_3B$·$NMe_3$)][$BAr^F{}_4$] (21)**

**3** was formed *in situ* in a high pressure NMR tube (4 atm $H_2$) in 1,2-$C_6H_4F_2$ and added to 10 eq. $H_2B{=}N^iPr_2$. **21** was formed as the major product (80%) and 20% **3** remained. Isolation attempts resulted in decomposition. Selected NMR data for **21**:

**$^{1}$H NMR (500 MHz, 1,2-$C_6H_4F_2$):** δ –14.15 (br). A broad peak at δ –0.06 is also observed and presumed to be coordinated $H_3B{\cdot}NMe_3$, but this could not be integrated due to overlap with the BH signal of **3** and residual grease signals. Upon decoupling to $^{31}$P, the peak at δ –14.15 resolved into a doublet ($^1J_{RhH}$ = 33). Upon decoupling to $^{11}$B, the peak at δ –0.06 sharpened.

**$^{31}$P{$^{1}$H} NMR (202 MHz, 1,2-$C_6H_4F_2$):** δ 39.6 (d, $^1J_{RhP}$ = 126).

**$^{11}$B NMR (160 MHz, 1,2-$C_6H_4F_2$):** δ 49 (v br, boryl), δ –8 (br, $H_3B{\cdot}NMe_3$).

**[Rh(κ$^3$$_{P,O,P}$-Xantphos)(H){B(H)N$^i$Pr$_2$}(NCMe)][BAr$^F$$_4$] (22)**

*Method 1*: Excess MeCN was added to *in situ* formed **21**, forming **22** (88%) and **4** (12%).

*Method 2*: **1** (15 mg, 0.009 mmol) was hydrogenated (4 atm) in $CD_2Cl_2$ to form [Rh(Xantphos)$(H)_2$][BAr$^F_4$].[14] To this, addition of $H_2B{=}N^iPr_2$ (10 μL, ~0.07 mmol) followed by excess MeCN formed 95% **22** and 5% **4**. Layering the mixture with pentane at 5 °C formed crystals of **22** suitable for X-ray diffraction. NMR spectroscopy of the crystals indicated the co-crystallisation of **4** (10%).

**$^1$H NMR (500 MHz, $CD_2Cl_2$):** δ 7.73 – 7.15 (m, 26H, Xantphos aryl groups), 7.72 (br, 8H, [BAr$^F_4$]$^-$), 7.48 (br, 4H, [BAr$^F_4$]$^-$), 6.75 (v br, 1H, BH), 4.17 (sept, $^3J_{HH}$ = 7, 1H, $^i$Pr CH), 3.08 (sept, $^3J_{HH}$ = 7, 1H, $^i$Pr CH), 1.91 (s, 3H, Xantphos $CH_3$), 1.52 (s, 3H, Xantphos $CH_3$), 1.16 (s, 3H, $NCCH_3$), 1.10 (d, $^3J_{HH}$ = 7, 6H, $^i$Pr $CH_3$), 0.30 (d, $^3J_{HH}$ = 7, 6H, $^i$Pr $CH_3$), –14.44 (dt, $^1J_{RhH}$ = 24, $^2J_{PH}$ = 14, 1H, RhH). Upon $^{11}$B decoupling, the signal at δ 6.75 sharpened. Upon $^{31}$P decoupling, the signal at δ –14.44 collapsed to a doublet ($^1J_{RhH}$ = 24).

**$^{31}$P{$^1$H} NMR (202 MHz, $CD_2Cl_2$):** δ 39.6 (d, $^1J_{RhP}$ = 125).

**$^{11}$B NMR (160 MHz, $CD_2Cl_2$):** δ 48 (v br, boryl), –6.61 (s, [BAr$^F_4$]$^-$).

ESI-MS was attempted but the main peaks observed were for [**4**]$^+$, [Rh(Xantphos)$(H)_2$]$^+$ (calc. 683.11; observed 683.12) and [Rh(Xantphos)(HB(OH)N$^i$Pr$_2$)]$^+$ (calc. 810.23; observed 810.23), showing decomposition under the conditions of ESI-MS. All peaks showed the expected isotopic pattern.

**[Rh(κ$^3$$_{P,O,P}$-Xantphos)(H){B(H)NMe$_2$}(η$^1$-H$_3$B·NMe$_3$)][BAr$^F$$_4$] (23)**

**3** (0.012 mmol) was formed *in situ* in 1,2-$C_6H_4F_2$ (0.4 mL), degassed twice (freeze-pump-thaw cycles), and added to a high pressure NMR tube containing $[H_2BNMe_2]_2$ (20 mg, 0.18 mmol). The reaction was monitored by NMR spectroscopy, which showed no change over 2 hours. Upon leaving the reaction overnight, however **23** was observed alongside **3** (~50:50 ratio). Selected NMR data for **23**:

**$^1$H NMR (500 MHz, 1,2-$C_6H_4F_2$):** δ –14.22 (dt, $^1J_{RhH}$ = 33, $^2J_{PH}$= 14). Broad signal at δ –0.23 is consistent with bound $H_3B{\cdot}NMe_3$, but could not be integrated due to overlap with the $BH_3$ signal from **3** and a grease peak at δ 0.34.

**$^1$H{$^{31}$P} NMR (500 MHz, 1,2-$C_6H_4F_2$):** δ –14.22 (d, $^1J_{RhH}$ = 33).

**$^{31}$P{$^1$H} NMR (202 MHz, 1,2-$C_6H_4F_2$):** δ 39.5 (d, $^1J_{RhP}$ = 123).

**$^{11}$B NMR (160 MHz, 1,2-$C_6H_4F_2$):** δ 52 (v br, boryl), –7.8 (br, $H_3B{\cdot}NMe_3$). Small (~ 1%) amounts of $H_2B{=}NMe_2$, $BH(NMe_2)_2$ and an unidentified triplet at δ 1.80 ($^1J_{BH}$ = 119) were also observed.

**[Rh(Xantphos*)(H$_3$B·NMe$_3$)]$_2$[BAr$^F$$_4$]$_2$ (24)**

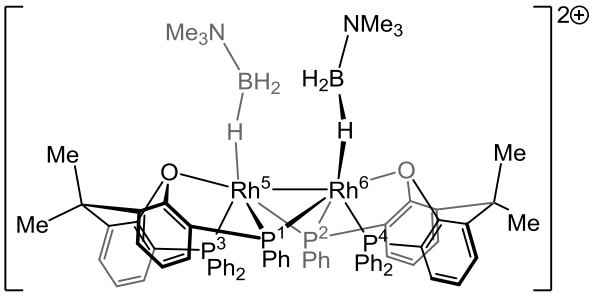



**Figure 7.1** Complex **24**. $[BAr^F_4]^-$ anions not shown.

To a Young's flask containing **6** (100 mg, 0.059 mmol) and $H_3B{\cdot}NMe_3$ (85 mg, 1.17 mmol), 1,2-$C_6H_4F_2$ was added (~ 3 mL). The flask was sealed and heated to 55 °C. Periodic sampling of the reaction mixture for $^{31}$P{$^1$H} NMR spectroscopy indicated

complete conversion to **24** within 48 hours, during which a dark red solution was formed (note: prolonged heating causes decomposition to unidentified materials). The volatiles were removed *in vacuo*, yielding dark red oil, which was washed and sonicated with pentane to form a dark red/orange solid. This was recrystallized from 1,2-$C_6H_4F_2$/pentane at 5 °C, affording crystals suitable for X-ray diffraction. Yield: 61 mg (67%).

**$^1$H NMR (500 MHz, $CD_2Cl_2$):** δ 7.75 – 6.53 (m, 42H, Xantphos aryl groups), 7.72 (br, 16H, $[BAr^F{}_4]^-$), 7.55 (br, 8H, $[BAr^F{}_4]^-$), 1.96 (s, 6H, Xantphos $CH_3$), 1.66 (s, 18H, $NMe_3$), 1.48 (s, 6H, Xantphos $CH_3$), –0.39 (br, 6H, $H_3B$). The signal at δ –0.39 sharpened upon $^{11}$B decoupling.

**$^{31}$P{$^1$H} NMR (202 MHz, $CD_2Cl_2$):** δ 135.1 (tt, phosphido groups), 19.2 (ddt, phosphino groups). Estimated coupling constants by gNMR simulations:[15] $J_{13}$ = 10, $J_{23}$ = 10, $J_{14}$ = 10, $J_{24}$ = 10, $J_{51}$ = 125, $J_{52}$ = 125, $J_{53}$ = 112, $J_{54}$ = 56, $J_{61}$ = 125, $J_{62}$ = 125, $J_{63}$ = 56, $J_{64}$ = 112, $J_{56}$ = 4 (numbering is as shown in Figure 7.1).

**$^{11}$B NMR (160 MHz, $CD_2Cl_2$)**: δ –6.6 (s, $[BAr^F{}_4]^-$), –7.8 (br, $BH_3$).

ESI-MS was attempted but decomposition to unidentified species resulted.

**Elemental Microanalysis:** Calc. $Rh_2P_4O_2N_2B_4F_{48}C_{136}H_{102}$ (3081.19 g mol$^{-1}$): C, 53.02; H, 3.34; N, 0.91. Found: C, 52.91; H, 3.44; N, 1.00.

**[Rh(Xantphos*)(NCMe)]$_2$[BAr$^F{}_4$]$_2$ (25)**

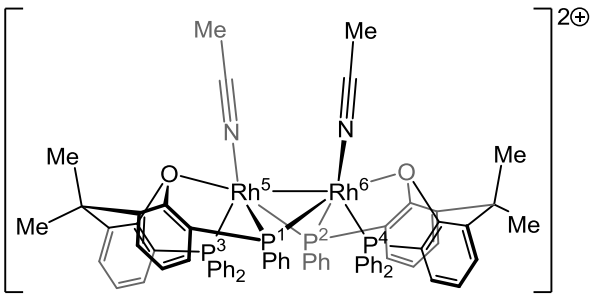



**Figure 7.2** Complex **25**. [BAr$^F{}_4$]$^-$ anions not shown.

Addition of MeCN to **24** in 1,2-$C_6H_4F_2$ or $CD_2Cl_2$ formed **25** immediately *in situ* (NMR spectroscopy). Attempts to recrystallize **25** resulted in the formation of orange oil.

**$^1$H NMR (500 MHz, $CD_2Cl_2$):** δ 7.71 (br, 16H, [BAr$^F{}_4$]$^-$), 7.65 – 6.71 (m, 42H, Xantphos aryl groups), 7.54 (br, 8H, [BAr$^F{}_4$]$^-$), 1.93 (s, 6H, Xantphos $CH_3$), 1.45 (s, 6H, Xantphos $CH_3$), 1.06 (s, 6H, MeCN).

**$^{31}$P{$^1$H} NMR (202 MHz, $CD_2Cl_2$):** δ 130.1 (tt, phosphido groups), 20.7 (ddt, phosphino groups). Estimated coupling constants by gNMR simulations:[15] $J_{13}$ = 10, $J_{23}$ = 10, $J_{14}$ = 10, $J_{24}$ = 10, $J_{51}$ = 122, $J_{52}$ = 122, $J_{53}$ = 104, $J_{54}$ = 53, $J_{61}$ = 122, $J_{62}$ = 122, $J_{63}$ = 53, $J_{64}$ = 104, $J_{56}$ = 5 (numbering is as in Figure 7.2).

**ESI-MS (1,2-$C_6H_4F_2$, 60 ˚C, 4.5 kV):** Molecular ions observed at 604.06 ([Rh(Xantphos*)]$_2^{2+}$, calc. 604.06, major), 624.57 ([{Rh(Xantphos*)}$_2$(NCMe)]$^{2+}$, calc. 624.57, mid), 645.09 ([**25**]$^{2+}$, calc. 645.09, minor).

**[Rh$_2$(Xantphos*)$_2$(Ph$_2$PCH$_2$CH$_2$PPh$_2$)][BAr$^F{}_4$]$_2$ (26)**

To a mixture of **24** (15 mg, 0.005 mmol) and dpp2 (2 mg, 0.005 mmol), 1,2-$C_6H_4F_2$ was added, forming a red solution. Upon layering the solution with pentane at 5 °C, red crystals of **26** formed. Yield: 10 mg (62%).

**$^1$H NMR (500 MHz, $CD_2Cl_2$):** δ 7.79 – 5.83 (multiple, 62H, ligand aryl groups), 7.72 (br, 16H, $[BAr^F{}_4]^-$), 7.55 (br, 8H, $[BAr^F{}_4]^-$), 3.38 (m, 2H, 2 x CH, $CH_2$ chain), 2.19 (m, 2H, 2 x CH, $CH_2$ chain), 1.73 (s, 6H, Xantphos $CH_3$), 0.70 (s, 6H, Xantphos $CH_3$).

Upon $^{31}$P decoupling, the signals at δ 3.38 and 2.19 collapsed to doublets ($^2J_{HH}$ = 12).

**$^{31}$P{$^1$H} NMR (202 MHz, $CD_2Cl_2$):** δ 134.1 (m, Xantphos* phosphido groups), 19.2 (m, Xantphos* phosphino groups), 3.9 (m, dpp2).

**ESI-MS (1,2-$C_6H_4F_2$, 60 ˚C, 4.5 kV):** *m/z* [**26**]$^{2+}$ 803.63 (calc. 803.63). Peak displays the expected isotopic pattern.

**Elemental Microanalysis:** Calc. $Rh_2P_6O_2B_2F_{48}C_{156}H_{102}$ (3333.73 g mol$^{-1}$): C, 56.20; H, 3.08. Found: C, 56.07; H, 3.16.

**[Rh(κ$^2_{P,P}$-Xantphos)(dpp2)][$BAr^F{}_4$] (27)**

1,2-$C_6H_4F_2$ (1 mL) was added to a mixture of **6** (39 mg, 0.023 mmol) and dpp2 (9 mg, 0.023 mmol) in a crystallisation tube. The colour changed immediately to a dark red/brown. *In situ* NMR spectroscopy indicated formation of **27**, with ~ 5% $[Rh(dpp2)_2][BAr^F{}_4]$[16] also observed. Layering the solution with hexanes at 5 °C resulted in pale orange crystals of **27** suitable for X-ray diffraction. Yield: 30 mg (67%).

**$^1$H NMR (500 MHz, $CD_2Cl_2$):** δ 7.72 (m, 8H, $[BAr^F{}_4]^-$), 7.69 – 6.56 (m, 46H, Xantphos and dpp2 aryl groups), 7.56 (br, 4H, $[BAr^F{}_4]^-$), 2.21 (m, 4H, dpp2 $CH_2$ groups), 1.82 (br, 6H, Xantphos $CH_3$). Upon $^{31}$P decoupling, the signal at δ 2.21 collapses to a singlet.

**$^1$H NMR (500 MHz, $CD_2Cl_2$, 190 K, selected data):** δ 2.20 (m, 2H, dpp2), 1.73 (m, 2H, dpp2) 1.94 (s, 3H, Xantphos $CH_3$), 1.72 (s, 3H, Xantphos $CH_3$).

**$^{31}P\{^{1}H\}$ NMR (202 MHz, $CD_2Cl_2$):** δ 50.9 (br, dpp2), 21.0 (dt, $^{1}J_{RhP}$ = 145, $^{2}J_{PP}$ = 104, Xantphos).

**$^{31}P\{^{1}H\}$ NMR (202 MHz, $CD_2Cl_2$, 190 K):** δ 53.3 (br, dpp2), 49.3 (br, dpp2), 22.7 (br m, Xantphos).

**$^{31}P$-$^{1}H$ HMBC NMR (500 MHz, $CD_2Cl_2$):** correlation observed between $^{31}P$ at δ 50.9 and protons at δ 2.21.

**$^{31}P$-$^{31}P$ COSY (202 MHz, $CD_2Cl_2$):** correlation observed between the two $^{31}P$ signals.

**ESI-MS (1,2-$C_6H_4F_2$, 60 ˚C, 4.5 kV):** *m/z* [**27**]$^{+}$ 1079.23 (calc. 1079.23). Peak displays the expected isotopic pattern.

**Elemental analysis:** $RhP_4OBF_{24}C_{97}H_{68}$ Calc: C, 59.96; H, 3.53. Found: C, 59.86; H, 3.46.

**[$Rh_2$(Xantphos*)$_2$(μ-η$^2$:η$^2$-$H_3B{\cdot}NMe_2{\cdot}BH_3$)][$BAr^F_4$] (28)**

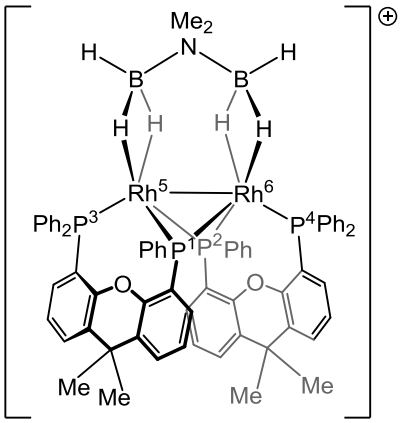



**Figure 7.3** Complex **28**. $[BAr^F_4]^-$ anion not shown.

To a Young's flask containing **24** (30 mg, 0.01 mmol) dissolved in 1 mL 1,2-$C_6H_4F_2$, $H_3B{\cdot}NMe_2H$ (23 mg, 0.390 mmol) dissolved in 1 mL 1,2-$C_6H_4F_2$ was added. Bubbling was observed immediately upon addition and the flask was sealed. After 12 hours, $^{1}H$, $^{31}P\{^{1}H\}$ and $^{11}B$ NMR spectroscopies indicated that **28** was the major metal-containing product, and complete consumption of $H_3B{\cdot}NMe_2H$ had occurred to yield

$[H_2BNMe_2]_2$ as the major product of dehydrocoupling. The total volume of solution was reduced to ~ 0.5 mL *in vacuo* and pentane (10 mL) was added with stirring, resulting in a cloudy brown solution. On cooling to –78 °C, a brown solid precipitated. The yellow supernatant solution was decanted and the solid washed twice with pentane (2 x 3 mL), each time with sonication. The remaining brown solid was recrystallized from 1,2-$C_6H_4F_2$ and pentane at 5 °C, from which orange crystals suitable for X-ray diffraction had grown, alongside brown oil. Some crystals could be manually separated from the oil, yield: 8 mg (38 %). These were nevertheless coated finely with oil and so were unsuitable for microanalysis.

**$^1$H NMR (500 MHz, $CD_2Cl_2$):** δ 7.72 (br, 8H, $[BAr^F{}_4]^-$), 7.69 – 5.50 (m, 42H, Xantphos aryl groups), 7.55 (br, 4H, $[BAr^F{}_4]^-$), 4.14 (br, 2H, free HB), 2.47 (s, 6H, $NMe_2$), 1.79 (s, 6H, Xantphos $CH_3$), 1.24 (s, 6H, Xantphos $CH_3$), –2.68 (br, 2H, coordinated HB), –3.52 (br, 2H, coordinated HB). The signals at δ 4.14, –2.65 and –3.50 sharpen upon $^{11}$B decoupling.

**$^{31}$P{$^1$H} NMR (202 MHz, $CD_2Cl_2$):** δ 108.5 (tt, phosphido groups), 13.3 (ddt, phosphino groups). Estimated coupling constants by gNMR simulations: $J_{13}$ = 10, $J_{23}$ = 10, $J_{14}$ = 10, $J_{24}$ = 10, $J_{51}$ = 112, $J_{52}$ = 112, $J_{53}$ = 122, $J_{54}$ = 40, $J_{61}$ = 112, $J_{62}$ = 112, $J_{63}$ = 40, $J_{64}$ = 122, $J_{56}$ = 4 (numbering is as shown in Figure 7.3).

**$^{11}$B NMR (160 MHz, $CD_2Cl_2$)**: δ 16.6 (br, $BH_3$), –6.6 (s, $[BAr^F{}_4]^-$).

**ESI-MS (1,2-$C_6H_4F_2$, 60 ˚C, 4.5 kV):** *m/z* [**28**]$^+$ 1280.23 (calc. 1280.24). Peak displays the expected isotopic pattern.

## 7.3 Catalytic procedures

### 7.3.1 General procedure for catalytic hydroboration

The alkene and 1,2-$C_6H_4F_2$ (0.6 mL) were mixed in a Young's NMR tube and transferred to a new Young's NMR tube containing the catalyst and $H_3B{\cdot}NMe_3$. The samples were immediately frozen in liquid $N_2$, and monitored *in situ* by $^{11}B$ NMR spectroscopy on warming.

### 7.3.2 General procedure for the dehydropolymerisation of $H_3B{\cdot}NMeH_2$

To a Schlenk flask containing $H_3B{\cdot}NMeH_2$ (100 mg, 2.22 mmol) and a stirrer bar, 4.5 mL $C_6H_5F$ was added. To a Young's NMR tube containing the required amount of catalyst, 0.5 mL $C_6H_5F$ was added, the catalyst was fully dissolved and transferred by cannula to the stirring solution of $H_3B{\cdot}NMeH_2$. The mixture was stirred under argon, open to a mercury bubbler for the allotted time period, then quenched by addition of hexanes (35 mL). Following addition of hexanes, the $[H_2BNMeH]_n/H_3B{\cdot}NMeH_2$ mixture precipitated as an off-white solid at –78 ˚C. The yellow supernatant solution was filtered off, and the solid was dried for 2 minutes *in vacuo* to remove residual $C_6H_5F$. THF (2.5 mL) was added, dissolving the $[H_2BNMeH]_n/H_3B{\cdot}NMeH_2$ mixture, and this was filtered into a new Schlenk. Hexanes (40 mL) were added to the solution and cooled immediately to –78 ˚C, allowing the product to precipitate. The supernatant solution was removed by filtration, and the resulting solid was dried *in vacuo* for at least 12 hours before GPC analysis. Isolated yields of $[H_2BNMeH]_n$ varied from 60% to 25%.

For experiments under closed conditions, the same procedure was followed but the reactions were conducted in a sealed (*ca.* 30 $cm^3$ volume) Young's flask.

### 7.3.3 General procedure for the dehydrocoupling of $H_3B{\cdot}NMe_2H$ – open conditions

In a typical experiment (*e.g.* 0.072 M $H_3B{\cdot}NMe_2H$, 0.2 mol% **6**), $H_3B{\cdot}NMe_2H$ (21.2 mg, 0.36 mmol) in 4.75 mL 1,2-$C_6H_4F_2$ was added to a 3-necked Schlenk flask with a magnetic stirrer bar. Under a flow of argon, an external mineral oil bubbler was connected and the argon flow adjusted to bubble at a rate of approximately 1.5 bubbles per second. In a separate flask, the required catalyst (*e.g.* **6**, 4.8 mg, 0.003 mmol) was dissolved in 1 mL of 1,2-$C_6H_4F_2$. 0.25 mL of this precatalyst solution was injected *via* syringe into the 3-necked Schlenk flask. Catalysis was monitored by analysing regular aliquots of the reaction solution (0.1 mL samples, diluted with 0.25 mL 1,2-$C_6H_4F_2$ under argon, frozen in liquid $N_2$) by $^{11}B$ NMR spectroscopy.

### 7.3.4 General procedure for the dehydrocoupling of $H_3B{\cdot}NMe_2H$ – closed conditions

To $H_3B{\cdot}NMe_2H$ (5.6 mg, 0.095 mmol), 1 mL of 1,2-$C_6H_4F_2$ was added. 0.3 mL was sampled and added to a high pressure NMR tube. To the catalyst (*e.g.* **6**, 2.0 mg, 0.001 mmol), 2 mL 1,2-$C_6H_4F_2$ was added. 0.1 mL was sampled and added to the high pressure NMR tube, resulting in a 0.072 M $H_3B{\cdot}NMe_2H$ solution with 0.2 mol% **6** in this case. The reaction was followed *in situ* by $^{11}B$ NMR spectroscopy at 298 K.

## 7.4 Computational details

Computational work (Chapter 2) was carried out by Professor S. A. Macgregor and Dr C. L. McMullin (Heriot-Watt University). Structures were fully optimised in Gaussian (G03) with the standard BP86 density functional. Rh and P were described using the Stuttgart-Dresden RECPs and basis sets,[17] with an added polarisation function for P (ζ = 0.387).[18] The flexible double-ζ polarised basis sets, 6-31G**,[19] were used for all

other atoms (H, B, C, N and O). Harmonic frequencies were used to confirm stationary points and transition states, and compute free energies. Intrinsic reaction coordinate calculations and subsequent geometry optimisations were used to confirm the identity of transition states along the reaction pathway. Corrected free energies were also calculated that include an additional dispersion description from a single point BP86-D31[20] calculation using G09, and a polarisable continuum model was used to obtain solvation free energies with fluorobenzene, ε = 5.42, (G09).

## 7.5 References


(1) *CrysAlisPro (Agilent Technologies, Oxford)* **2011**.
(2) Cosier, J.; Glazer, A. M. *J. Appl. Crystallogr.* **1986**, *19*, 105.
(3) Otwinowski, Z.; Minor, W. In *Methods Enzymol.*; Charles W. Carter, Jr., Ed.; Academic Press: 1997; Vol. Volume 276, p 307.
(4) Altomare, A.; Cascarano, G.; Giacovazzo, C.; Guagliardi, A.; Burla, M. C.; Polidori, G.; Camalli, M. *J. Appl. Crystallogr.* **1994**, *27*, 435.
(5) Palatinus, L.; Chapuis, G. *J. Appl. Crystallogr.* **2007**, *40*, 786.
(6) Betteridge, P. W.; Carruthers, J. R.; Cooper, R. I.; Prout, K.; Watkin, D. J. *J. Appl. Crystallogr.* **2003**, *36*, 1487.
(7) Blaquiere, N.; Diallo-Garcia, S.; Gorelsky, S. I.; Black, D. A.; Fagnou, K. *J. Am. Chem. Soc.* **2008**, *130*, 14034.
(8) Jaska, C. A.; Temple, K.; Lough, A. J.; Manners, I. *J. Am. Chem. Soc.* **2003**, *125*, 9424.
(9) Sloan, M. E.; Staubitz, A.; Clark, T. J.; Russell, C. A.; Lloyd-Jones, G. C.; Manners, I. *J. Am. Chem. Soc.* **2010**, *132*, 3831.
(10) Nöth, H.; Thomas, S. *Eur. J. Inorg. Chem.* **1999**, *1999*, 1373.
(11) Johnson, H. C.; Robertson, A. P. M.; Chaplin, A. B.; Sewell, L. J.; Thompson, A. L.; Haddow, M. F.; Manners, I.; Weller, A. S. *J. Am. Chem. Soc.* **2011**, *133*, 11076.
(12) Pawley, R. J.; Moxham, G. L.; Dallanegra, R.; Chaplin, A. B.; Brayshaw, S. K.; Weller, A. S.; Willis, M. C. *Organometallics* **2010**, *29*, 1717.
(13) Torry-Harris, R., University of Oxford, 2013.
(14) Pawley, R. J., University of Oxford, 2012.
(15) gNMR 5.1, Budzelaar, P. H. M., marketed by Adept Scientific until May 2005.
(16) Huertos, M. A.; Weller, A. S. *Chem. Sci.* **2013**, *4*, 1881.
(17) Andrae, D.; Häußermann, U.; Dolg, M.; Stoll, H.; Preuß, H. *Theor. Chim. Acta* **1990**, *77*, 123.
(18) Höllwarth, A.; Böhme, M.; Dapprich, S.; Ehlers, A. W.; Gobbi, A.; Jonas, V.; Köhler, K. F.; Stegmann, R.; Veldkamp, A.; Frenking, G. *Chem. Phys. Lett.* **1993**, *208*, 237.
(19) Hariharan, P. C.; Pople, J. A. *Theor. Chim. Acta* **1973**, *28*, 213.
(20) Grimme, S.; Antony, J.; Ehrlich, S.; Krieg, H. *J. Chem. Phys.* **2010**, *132*.

# 8 Appendices

## 8.1 Crystallographic data

**Table 8.1** Crystallographic data for **3**, **6** and **8**.

| | **3** | **6** | **8** |
|---|---|---|---|
| CCDC number | 932612 | 932613 | 932614 |
| Formula | $C_{74}H_{58}B_2F_{24}NOP_2Rh$ | $C_{80}H_{74}B_2F_{24}NOP_2Rh$ | $C_{77}H_{66}B_3F_{24}N_2OP_2Rh$ |
| $M$ | 1619.71 | 1701.85 | 1688.62 |
| Crystal system | Monoclinic | Monoclinic | Monoclinic |
| Space group | Cm | P 21/a | P 21/a |
| $T$ [K] | 150(2) | 150(2) | 150(2) |
| $a$ [Å] | 19.1077(2) | 20.2339(2) | 20.5150(2) |
| $b$ [Å] | 31.5349(4) | 19.7975(3) | 19.6068(2) |
| $c$ [Å] | 14.4478(2) | 21.5211(3) | 21.4091(2) |
| $\alpha$ [°] | 90 | 90 | 90 |
| $\beta$ [°] | 117.1444(6) | 115.2527(8) | 117.3098(5) |
| $\gamma$ [°] | 90 | 90 | 90 |
| $V$ [Å$^3$] | 7746.81(17) | 7797.08(19) | 7651.61(13) |
| $Z$ | 4 | 4 | 4 |
| Density [g cm$^{-3}$] | 1.389 | 1.45 | 1.466 |
| $\mu$ [mm$^{-1}$] | 0.361 | 0.363 | 0.369 |
| $\theta$ range [°] | 5.116 ≤ θ ≤ 27.467 | 5.123 ≤ θ ≤ 27.495 | 5.103 ≤ θ ≤ 27.486 |
| Reflns collected | 16274 | 17714 | 17407 |
| $R_{int}$ | 0.019 | 0.067 | 0.034 |
| Completeness | 98.90% | 99.00% | 99.20% |
| Data/restr/param | 16272/1164/1120 | 12269/1368/1168 | 17406/912/1099 |
| $R_1$ [I > 2σ(I)] | 0.0467 | 0.0618 | 0.0642 |
| $wR_2$ [all data] | 0.1196 | 0.1476 | 0.1628 |
| $GoF$ | 0.9785 | 0.9482 | 1.0066 |
| Largest diff. pk and hole [e Å$^{-3}$] | 0.83, -0.77 | 2.85, -0.72 | 2.04, -1.73 |

**Table 8.2** Crystallographic data for **9**, **10** and **15**.

| | **9** | **10** | **15** |
|---|---|---|---|
| CCDC number | 1001382 | - | 1001383 |
| Formula | $C_{79}H_{68}B_2F_{24}NOP_2RhSi$ | $C_{86}H_{72}B_2F_{26}NOP_2Rh$ | $C_{89}H_{77}BF_{24}NOP_3Rh$ |
| $M$ | 1717.93 | 1815.94 | 1825.18 |
| Crystal system | Triclinic | Triclinic | Triclinic |
| Space group | P -1 | P -1 | P -1 |
| $T$ [K] | 150(2) | 150(2) | 150(2) |
| $a$ [Å] | 16.6243(5) | 13.0463(4) | 12.90760(10) |
| $b$ [Å] | 16.8939(5) | 16.1249(5) | 17.8030(2) |
| $c$ [Å] | 17.7667(7) | 19.9993(8) | 19.9590(3) |
| $\alpha$ [°] | 110.6501(11) | 73.8261(10) | 87.9991(5) |
| $\beta$ [°] | 107.1873(12) | 85.7523(12) | 74.6948(5) |
| $\gamma$ [°] | 106.290(2) | 86.867(2) | 87.0039(6) |
| $V$ [Å$^3$] | 4026.5(3) | 4027.1(2) | 4416.68(9) |
| $Z$ | 2 | 2 | 2 |
| Density [g cm$^{-3}$] | 1.417 | 1.497 | 1.372 |
| $\mu$ [mm$^{-1}$] | 0.366 | 0.36 | 0.343 |
| $\theta$ range [°] | 5.113 ≤ θ ≤ 25.018 | 5.352 ≤ θ ≤ 25.057 | 5.099 ≤ θ ≤ 27.491 |
| Reflns collected | 36954 | 29693 | 61434 |
| $R_{int}$ | 0.078 | 0.058 | 0.05 |
| Completeness | 98.70% | 96.60% | 98.80% |
| Data/restr/param | 11566/ 2846/ 1186 | 13788/3192/1240 | 20022/ 456/ 1128 |
| $R_1$ [I > 2σ(I)] | 0.086 | 0.1055 | 0.051 |
| $wR_2$ [all data] | 0.2043 | 0.2376 | 0.1393 |
| $GoF$ | 0.9482 | 1.0361 | 0.9426 |
| Largest diff. pk and hole [e Å$^{-3}$] | 3.32, -1.68 | 1.46, -1.25 | 1.18, -0.85 |

**Table 8.3** Crystallographic data for **22**, **24** and **26**.

| | **22** | **24** | **26** |
|---|---|---|---|
| CCDC number | 993785 | - | - |
| Formula | $C_{79}H_{63}B_2F_{24}N_2OP_2Rh$ | $C_{136}H_{102}B_4F_{48}N_2O_2P_4Rh_2$ | $C_{156}H_{102}B_2F_{48}O_2P_6Rh_2$ |
| $M$ | 1698.81 | 3081.17 | 3333.71 |
| Crystal system | Monoclinic | Monoclinic | Monoclinic |
| Space group | P 21/n | C 2/c | P 21/n |
| $T$ [K] | 150(2) | 150(2) | 150(2) |
| $a$ [Å] | 13.86840(10) | 32.5926(3) | 14.6815(2) |
| $b$ [Å] | 14.9780(2) | 24.6249(3) | 16.8673(2) |
| $c$ [Å] | 39.1771(3) | 19.6743(2) | 58.7574(5) |
| $\alpha$ [°] | 90 | 90 | 90 |
| $\beta$ [°] | 94.9953(8) | 108.2170(5) | 90.9227(8) |
| $\gamma$ [°] | 90 | 90 | 90 |
| $V$ [Å$^3$] | 8106.99(14) | 14999.0(3) | 14548.6(3) |
| $Z$ | 4 | 4 | 4 |
| Density [g cm$^{-3}$] | 1.392 | 1.364 | 1.522 |
| $\mu$ [mm$^{-1}$] | 2.955 | 0.369 | 3.48 |
| $\theta$ range [°] | 3.160 ≤ θ ≤ 76.351 | 5.110 ≤ θ ≤ 27.489 | 3.115 ≤ θ ≤ 76.171 |
| Reflns collected | 34352 | 105008 | 167693 |
| $R_{int}$ | 0.0352 | 0.058 | 0.052 |
| Completeness | 99.80% | 99.20% | 99.30% |
| Data/restr/param | 16827/1020/1140 | 17080/1140/1032 | 30115/1140/2085 |
| $R_1$ [I > 2σ(I)] | 0.0454 | 0.0644 | 0.0596 |
| $wR_2$ [all data] | 0.1093 | 0.171 | 0.1578 |
| $GoF$ | 0.9908 | 0.9446 | 1.0967 |
| Largest diff. pk and hole [e Å$^{-3}$] | 1.13, -0.90 | 1.33, -1.13 | 1.17, -1.18 |

**Table 8.4** Crystallographic data for **27** and **28**.

| | **27** | **28** |
|---|---|---|
| CCDC number | - | - |
| Formula | $C_{97}H_{68}BF_{24}OP_4Rh$ | $C_{106.8}H_{91.2}B_3F_{24.6}NO_2P_4Rh_2$ |
| $M$ | 1943.17 | 2250.19 |
| Crystal system | Triclinic | Triclinic |
| Space group | P -1 | P -1 |
| $T$ [K] | 150(2) | 150(2) |
| $a$ [Å] | 17.1288(3) | 13.6309(2) |
| $b$ [Å] | 26.8243(6) | 16.5228(3) |
| $c$ [Å] | 30.9536(5) | 22.7975(4) |
| $\alpha$ [°] | 68.6578(17) | 94.0197(16) |
| $\beta$ [°] | 80.7508(14) | 95.2079(14) |
| $\gamma$ [°] | 85.2274(16) | 91.9282(14) |
| $V$ [Å$^3$] | 13069.9(5) | 5096.56(15) |
| $Z$ | 6 | 2 |
| Density [g cm$^{-3}$] | 1.481 | 1.466 |
| $\mu$ [mm$^{-1}$] | 3.162 | 4.039 |
| $\theta$ range [°] | 3.118 ≤ θ ≤ 76.229 | 3.200 ≤ θ ≤ 76.090 |
| Reflns collected | 149488 | 61481 |
| $R_{int}$ | 0.093 | 0.051 |
| Completeness | 98.50% | 98.80% |
| Data/restr/param | 53738/5244/3541 | 20971/4136/1622 |
| $R_1$ [I > 2σ(I)] | 0.0545 | 0.0618 |
| $wR_2$ [all data] | 0.149 | 0.173 |
| $GoF$ | 1.0004 | 1.0316 |
| Largest diff. pk and hole [e Å$^{-3}$] | 1.49, -1.41 | 3.36, -1.87 |